8-1-2006

Analytical Investigation of Fire Loads for Precast Concrete parking Structures

Jonathan L. Bayreuther

Stephen P. Pessiki

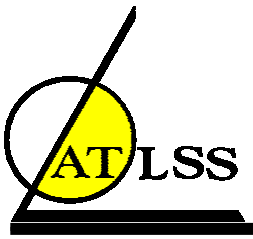

LEHIGH UNIVERSITY

ANALYTICAL INVESTIGATION OF FIRE LOADS FOR PRECAST CONCRETE PARKING STRUCTURES

by

Jonathan L. Bayreuther

Stephen Pessiki

ATLSS Report No. 06-19

August 2006

ATLSS is a National Center for Engineering Research on Advanced Technology for Large Structural Systems

117 ATLSS Drive
Bethlehem, PA 18015-4729

Phone: (610)758-3525
Fax: (610)758-5902

www.atlss.lehigh.edu
Email: inatl@lehigh.edu

ANALYTICAL INVESTIGATION OF FIRE LOADS FOR PRECAST CONCRETE PARKING STRUCTURES

by

Jonathan L. Bayreuther
Graduate Research Assistant
Department of Civil and Environmental Engineering

Stephen Pessiki
Professor and Chairperson
Department of Civil and Environmental Engineering

ATLSS Report No. 06-19

August 2006

ATLSS is a National Center for Engineering Research on Advanced Technology for Large Structural Systems

117 ATLSS Drive
Bethlehem, PA 18015-4729

Phone: (610)758-3525
Fax: (610)758-5902

www.atlss.lehigh.edu
Email: inatl@lehigh.edu

ACKNOWLEDGEMENTS

This research was funded by the Pennsylvania Infrastructure Technology Alliance, the Precast/Prestressed Concrete Institute, and the Center for Advanced Technology for Large Structural Systems (ATLSS) at Lehigh University. The support provided is gratefully acknowledged. The findings and conclusions included in this report are those of the author and do not necessarily reflect the views of the sponsors.

TABLE OF CONTENTS

LIST OF TABLES

LIST OF FIGURES

ABSTRACT

In most regions of the U.S., current practice for protecting structures from fire is governed by the International Building Code. The code requires fire resistance ratings baed on occupancy, type of construction, etc. Fire resistance ratings are obtained from standardized tests.

Design practice in the United States is moving toward performance-based design, and more information about fire loading is needed for full implementation. The broad objective of this research is the development of realistic fire loads for structures. More specifically, this research focuses on fire loads for precast concrete parking structures, and investigates the influence of structure geometry and fire characteristics in the resulting fire loading.

Fire analyses were run on nine simplified parking garage models using the computer program, Fire Dynamics Simulator. Analysis parameters were systematically varied to explore the impact of a range of geometry and fire characteristics on the resulting fire loading.

Results shows that openings in the center wall have a significant impact on the heat transmission through the structure. The relative position of the opening with respect to the floor slabs may trap heat on one side of the garage or allow to flow freely from one side to the other or from one floor to the next. Fires on lower floors create a preheating effect on upper floors if the heat is allowed to flow from floor-to-floor by the center wall openings. This preheating increases the concrete temperature over the course of the fire. The peak gas temperature may not be influenced by preheating, so the increased concrete temperature is due in part to the longer heating duration. The ASTM E119 standard time-temperature curve is not representative of the time-temperature curve that is produced by a single or multiple vehicle fire in a precast concrete parking garage. For the fire scenarios considered, vehicle fires do not cause the temperature of the prestressing strand in the concrete to increase significantly. Vehicle fires cause the strength of the prestressing steel to reduce to as low as 85 percent of room temperature strength.

CHAPTER 1

INTRODUCTION

Fire science is relatively new field, and though the general concepts that govern fire spread and energy release have been understood for some time, the study of fire behavior in structures is a relatively recent development. There are a number of factors that have contributed to the surge in interest in fire studies in structures in recent years. Among them: the availability of high-speed computing to run the complex calculations required to model fire, and a number of high-profile structure fires, the jet fuel driven fires in the World Trade Towers after the attacks of September 11, 2001, being the most prominent example.

In most regions of the U.S., current practice for protecting structures from fire is governed by the *International Building Code* (2003). The basic approach taken in the IBC is to prescribe a specific fire endurance time (e.g. 2 hours) for the structure or structural element. The required fire-resistance rating depends principally on the type of construction, the type of building element, the use and occupancy of the structure, and the fire separation distance between the subject structure and adjacent structures. The fire resistance rating is obtained from a standardized test (ASTM E-119) or from alternative methods that are based on the E-119 test.

Perceived advantages of this prescriptive approach are simplicity in design and enforcement, and generality in scope which permits the approach to cover a broad range of conditions (e.g. structure types, occupancies, sizes, etc.). Perceived limitations of this approach are that it in some instances it is overly conservative, unnecessarily expensive, restricts innovation and provides an uncertain level of safety (or in some instances a lack of safety). While the standardization for prescriptive codes makes structural design for fire much simpler, the variability of environmental and fire behavioral conditions cast doubt as to the effectiveness of this standard for comprehensive design.

At present, the direction of design practice in the United States is toward performance-based design. Perceived advantages of performance-based design are the encouragement of (or at least a tolerance for) innovation, integrated approach to facility design, and better understood factors of safety. Perceived limitations of performance-based design include insufficient knowledge of fire behavior and loading as well as a lack of usable tools to implement this design approach, though these tools are becoming more readily available. Full implementation of performance-based design of structures for fire requires more information about fire loading.

1.1 Objectives

The work described in this report is part of a broader program of research at Lehigh University that focuses on fire performance of structures and structural elements. The broad objective of this research is the development of realistic fire loads (time-temperature or time-heat flux relationships) for structures. More specifically, this research focuses on fire loads for precast concrete parking structures, and investigates the influence of structure geometry and fire characteristics in the resulting fire loading.

1.2 Summary of Approach

A typical precast concrete parking structure, in this case the Campus Square Parking Garage at Lehigh University, was analyzed for a series of fires, and the resulting fire loads at various points in the structure were determined. A parking garage was chosen as the model for the fire analyses because of its simple repeating geometry, uniform non-combustible construction, well-controlled ventilation conditions, and well-defined fuel loading. Variables treated in the analyses include structure geometry and fire characteristics.

Fire analyses were run on nine simplified parking garage models. Analysis parameters were systematically varied to explore a range of geometry and fire characteristic parameters. The first seven analyses were single-vehicle fires, and the final two analyses were sequential, multiple-vehicle fires. Analysis computations were performed using the computer program, Fire Dynamics Simulator (FDS), a computational fluid dynamics (CFD) program developed by the National Institute for Standards and Technology (NIST).

All analyses were performed on Hades, an 8-node 64-bit AMD cluster of computer processors at the Center for Advanced Technology for Large Structural Systems (ATLSS) at Lehigh University.

1.3 Summary of Findings

The following summarize the findings of this project:

The geometric effects of openings in the center wall have a significant impact on the heat transmission through the structure. Depending on the relative position of the opening to the floor slabs, heat may be trapped on one side of the garage or allowed to flow freely from one side to the other or from one floor to the next.

Fires on lower floors can create a preheating effect on upper floors if the heat is allowed to flow from floor-to-floor by the center wall openings. This preheating effect causes an

increase in the concrete temperature over the course of the fire. The peak gas temperature may not show a significant difference, so the increased concrete temperature is due in part to the longer heating duration.

The webs of the double-tee in a precast concrete construction trap the heat from the vehicle fires and "channel" it away from the fire.

The ASTM E119 standard time-temperature curve is not representative of the time-temperature curve that is produced by a single or multiple vehicle fire in a precast concrete parking garage.

For the fire scenarios considered, vehicle fires do not cause the temperature of the prestressing strand in the concrete to increase significantly. Vehicle fires cause the strength of the prestressing steel to vary from $0.99f_{pu}$ to $0.85f_{pu}$.

1.4 Outline of Report

The remainder of this report is divided into five chapters. Chapter 2 presents relevant background information including a review of basic fire concepts and definitions aimed specifically at a structural engineer that may have little knowledge of fire behavior. Chapter 3 describes the fire analysis methodogy including the analysis matrix, model details, and instrumentation. This chapter also includes the logic behind the development of the fire, vehicle, and parking garage models, and the assumptions made. A selection of the results of the analyses are presented in Chapter 4 and analyzed in Chapter 5. Lastly, Chapter 6 presents the conclusions and potential implications of this research. A series of recommendations for future research areas based on the findings of this work is also included in Chapter 6.

1.5 Notation

The following notation is used in this report:

A	=	Surface area of enclosure
A_o	=	Area of openings
E	=	Rate of thermal radiation
EB	=	Established burn
f_{pu}	=	Ultimate steel strength at ambient temperature
f_{puo}	=	Ultimate steel strength at elevated temperature
H_o	=	Average height of ventilation openings
HRR	=	Heat release rate (Heat flux)
h	=	Local heat transfer coefficient
h'_{net}	=	Net heat flux
IG	=	Ignition
m_f	=	Fuel mass

$\dot{Q}$ = Heat flux of fire
$\dot{q}_c''$ = Convective heat flux
$\dot{q}_r''$ = Convective heat flux
T = Temperature
T_g = Gas temperature (also T_f and Θ_g)
T_{gm} = Maximum compartment gas temperature
T_s = Surface temperature (also T_w and Θ_m)
t = Time
t_g = Growth time
α = Convection coefficient
α_s = Surface absorbtivity
ε = Surface emmisivity (also ε_m and ε_s)
ε_f = Gas emmisivity
Θ_r = Effective radiation temperature
Φ = Configuration factor
Ψ = Fuel mass and compartment area coefficient

1.6 Unit Conversion Factors

This report is presented in SI units. All measurements have been converted to SI if they were not originally presented as such. The following unit conversions were used:

1 in. = 25.4 mm
1 ft = 0.3048 m
1 in^2 = 645 mm^2

CHAPTER 2

BACKGROUND AND LITERATURE REVIEW

Vehicle fire is a topic about which little is known, both about the fire behavior as the vehicle burns, as well as total energy released over the course of the fire. The lack of knowledge is due in part to the prohibitively high cost of conducting fire analyses on vehicles. Despite this, there have been a number of combustion studies in recent years, among them are: Mangs and Keski-Rahkonen (1994a,b), Zhao and Kruppa (2004), Shipp and Spearpoint (1995), and Khono et al. (2005).

Parking garage fires are also a relatively little studied phenomenon, again partially due to high cost. Several studies have been conducted on steel parking structures to investigate the need for fireproofing on steel members in parking structures. These, in addition to a few documented fires in actual parking garage structures provide background research in this area.

This chapter begins with a basic discussion of fire and heat transfer in Section 2.1, then presents the concepts of the fire behavior and modeling theory in Sections 2.2 and 2.3 respectively. Finally, Section 2.4 summarizes the relevant vehicle and structure fire analyses.

2.1 Fire Primer

Because the intended audience for this project is the structural engineering community and not fire scientists, this section is included to establish a base of basic fire knowledge for the reader. The section begins with a discussion of basic definitions and mechanisms of heat transfer as well as code treatment of the same. Following the heat transfer discussion, a survey of fire types and fuel loading, and fire behavior is included.

The reader is assumed to have a basic knowledge of fluid mechanics that might be obtained from an introductory course or text such as Prandtl's Essentials of Fluid Mechanics (Oertel, 2004), which is cited in this report.

2.1.1 Definition of Fire Terms

In the most general sense fire is the breaking of molecular bonds in a fuel source through combustion to release energy in the form of heat and light and combustion product in the form of smoke and gas. The energy released when a fuel combusts is transferred to the surrounding environment via three basic heat transfer mechanisms: radiation, conduction, and convection. These mechanisms transfer energy to the environment an energy release

rate, referred to as heat flux and measured in watts, and in some total quantity measured in joules.

Thermal radiation heat transfer is the transfer of electromagnetic radiation during combustion from a body as the subatomic charged particles accelerate in both rotational and vibrational motion (Thomas, 1999). This general definition may be simplified to consider thermal radiation as the energy emitted to the environment by the light produced by combustion.

Thermal radiation is absorbed at different rates depending on the surface properties such as color and roughness of the material. Generally speaking, darker colors absorb higher proportions of thermal radiation. The governing law for radiant heat transfer to a surface is the Stephen-Boltzmann Law:

$$E = \varepsilon \sigma T_s^4$$

where:

E = rate of thermal radiation emitted per unit surface area

ε = surface emissivity (0-1.0 depending on character of surface;
1.0 for perfect absorbtion; 0.0 for perfect reflection)

σ = Stephen-Boltzmann constant $\left(= 5.670E-8\left(\frac{W}{m^2 K^4} \right) \right)$

T = surface temperature in degrees Kelvin

Equation 2-1: Stephen-Boltzmann Law.

Most surfaces in a structure may be described as graybodies. A graybody is a solid material with an emissivity less than one, therefore, not all radiant energy is transferred to the material. For the purposes of many engineering analyses, however, surfaces may be considered blackbodies, where the emissivity is 1.0, meaning all thermal radiant energy is transferred to the surface. The blackbody approximation takes into account the buildup of soot on the surfaces of structure, which increases the emmisivity. Most structural fires involve large amounts of soot because of the nature of the fuel, and because of incomplete combustion, surfaces are often coated with soot shortly after the fire begins. This phenomenon supports the blackbody assumption.

Conduction is the transfer of energy through the physical interaction of particles in a stationary material (Thomas, 1999). For the purpose of simplicity, conduction is considered to be the energy transfer within a solid, although it is noted that conduction also may describe the heat transfer within a stationary fluid.

Convection is the transfer of heat from a solid surface through a moving fluid (Thomas, 1999). In a well ventilated space such as a parking garage, the air is assumed to be moving, thus convection is the mechanism of heat transfer from the fire to the air, as well as the transfer of energy through the air itself. Convection is governed by Newton's Second Law of Cooling:

$$\dot{q}_r'' = h(T_g - T_s)$$

$where$:

$\dot{q}_r''$ = rate of convection energy transfer

T_g = fluid temperature

T_s = surface temperature

h = coefficient of convection $\left(\frac{W}{m^2 K}\right)$

Equation 2-2: Newton's Second Law of Cooling (Equation modified from Thomas, 1999).

2.1.2 Code Treatment of Heat Transfer

Eurocode 1: Actions on Structures (2002), Section 3 is entitled, "Thermal actions for temperature analysis" and outlines methods for applying thermal loading to structural members. More specifically, Section 3.1 General Rules, Part 1, reads: "Thermal actions are given by the net heat flux [W/m^2] to the surface of the member." Essentially, the actual thermal load applied to the surface of a member is the net energy (heat flux) getting into the surface of the member. The net heat flux is comprised of a combination of the convective heat flux and the radiative heat flux.

The convective heat flux is given as:

$$\dot{h}_{net,c} = \alpha_c \cdot (\Theta_g - \Theta_m)$$

$where$:

α_c = convection coefficient

Θ_g = gas temperature in vicinity of exposed member

Θ_m = surface temperature of the member

Equation 2-3: Convective heat flux in Eurocode 1.

The convection coefficient depends on the fire environment and is specified in the Eurocode as ranging from 4 W/m^{2}K on the unexposed side of separating members to 50 W/m^{2}K for members exposed to a hydrocarbon fire.

The radiative heat flux is given as:

$$\dot{h}_{net,r} = \Phi \cdot \varepsilon_m \cdot \varepsilon_t \cdot \sigma \cdot [(\Theta_r + 273)^4 - (\Theta_m + 273)^4]$$

where:

Φ = configuration factor (=1 unless otherwise specified)

ε_m = surface emissivity

ε_t = fire emissivity

σ = Boltzman constant (=5.67E-8 W/m$^2K^4$)

Θ_r = effective radiation temperature of fire environment

Equation 2-4: Radiative heat flux in Eurocode 1.

The configuration factor takes into account the geometry of the fire and affected surfaces. It is taken to be equal to 1.0 but may range from 0 to 1.0 to allow for position and shadow effects. A value of 1.0 is a conservative value and is recommended for use in most cases. The emissivity of the surface is specific to the material, but a value of 0.8 may be used unless otherwise specified. The fire emissivity is taken to be 1.0, which means that the fire temperature and gas temperature are taken to be the same.

Substituting the convective and radiative heat flux equations into the net heat flux equation and changing the temperature from Celsius to Kelvin:

$$\dot{h}_{net} = \alpha_c \cdot (\Theta_g - \Theta_m) + \Phi \cdot \varepsilon_m \cdot \varepsilon_t \cdot \sigma \cdot ({\Theta_r}^4 - {\Theta_m}^4)$$

Equation 2-5: Substituting convective (Equation 1-2) and radiative (Equation 1-3) terms into the net heat flux equation (Equation 1-1) and changing from Celsius to Kelvin.

The SFPE Engineering Guide – Fire Exposures to Structural Elements (Quintiere, 2004), hereafter referred to as the SFPE Engineering Guide, is a document prepared by the SFPE Task Group on Fire Exposures to Structural Elements with the purpose of providing the engineer with information and methodology in order to predict thermal boundary conditions for a fire over time. The SFPE Engineering Guide provides several prediction methods for both plume and compartment fires.

The governing boundary condition for a fire impinging on a surface is the net heat flux into the surface and is given in the SFPE Engineering Guide as:

$$q''_{net} = \alpha_s \cdot \varepsilon_f \cdot \sigma \cdot T_f^{\,4} + h \cdot (T_f - T_s) - \varepsilon_s \cdot \sigma \cdot T_s^{\,4}$$

where:

$\alpha_s =$ surface absorbtivity

$\varepsilon_f =$ gas emissivity

$\sigma =$ Stephen Boltzman constant

$h =$ local heat transfer coefficient

$T_f =$ Temperature of gas

$T_s =$ Temperature of surface

$\varepsilon_s =$ surface emissivity

Equation 2-6: Governing boundary heat flux equation in the SFPE Engineering Guide.

Like Eurocode 1, the SFPE net heat flux equation is takes into account the net convective and radiative heat flux into the surface. Comparing the SFPE and Eurocode 1 equations, it is seen that the two treat the net heat flux in the same manner. The similarity between the two becomes clear when the following are considered:

$\alpha_s = \varepsilon_m$; Surface absorbtivity and surface emissivity are equal and the terms are used interchangeably in the Eurocode 1 and SFPE Engineering Guide.

$\Phi = 1.0$; The configuration factor in the Eurocode 1 equation is considered to be equal to 1.0, and thus is not a difference between the two equations.

$\varepsilon_f = \varepsilon_t = 1.0$; Fire emissivity is taken as 1.0.

Substituting the above values into the Eurocode 1 and SFPE equations results in identical equations, therefore, the heat flux boundary condition is treated in the same manner in both guides.

2.1.3 Fire Types and Fuel Loading

For the purposes of structural fires in parking garages, two types of fires need to be considered: compartment fires and plume fires (localized fires). While the line separating plume fires a compartment fires may blur at times, a distinction may be drawn between the two using a ratio of fuel availability to the volume of the space in which the fire is contained. When the amount of fuel available is large compared to the volume of the space, the fire may be considered to be a compartment fire. Conversely, when the amount of fuel available is low compared to the volume of the space, the fire may be considered

to be a plume fire. To illustrate, a fire in a bedroom would likely be considered a compartment fire, whereas a campfire in the middle of a field would be a plume fire. The key difference for analysis purposes between these two types of fires is the temperature distribution throughout the environment and around the fire itself. In a compartment fire the gas temperature distribution in the space as a function of time is essentially uniform, whereas pool fires result in a non-uniform temperature distribution as a function of time (Eurocode 1, 2002).

Prescriptive codes such as the Eurocode and IBC (2203) are based on fully involved compartment fires, allowing for a standard fuel density for a given building type, and, taking into account the standard fire load, prescribe a minimum endurance limit for the structure. Recent advances in performance-based codes show promising improvements in fire resistance design, but may result in a much broader range of fire endurance based on owner specifications and design methods used by the engineer.

For this project, fire plumes are considered exclusively, since the only significant fuel source in a parking garage is the vehicles themselves. Fully involved compartment fires are not applicable because of the large openings intrinsic to open parking garages, and a uniform temperature distribution is highly improbable. Additionally, the nature of vehicle fires allows some significant simplifications to be made in terms of fire geometry as discussed in the next section.

2.1.4 Fire Stages

For the purposes of engineering analysis of structures, fire behavior may be simplified into the following five stages: Ignition, Established Burning, Fire Growth, Fully Developed Fire, and Decay (See Figure 2-1). These stages are discussed in the following paragraphs.

Ignition is the first appearance of flame in a fire. There is little heat release from this small flame and many fires actually extinguish during this stage. In reality, room or structure fires may have a pre-ignition stage, where smoldering or overheating may occur, but it is generally recognized that fire does not actually begin until ignition (Fitzgerald, 2002).

Established burning is an assumed threshold level that begins a fire analysis and varies depending on the analysis being performed. It may be defined by flame height, heat flux, fire diameter, etc. For example, a building fire analysis performed by a fire protection engineer while designing the fire prevention systems in an office building might consider established burn to be a flame height of about 250mm or a heat flux of about 20kW, which correspond to a small waste paper basket fire as illustrated in Figure 2-2 (Fitzgerald, 2002).

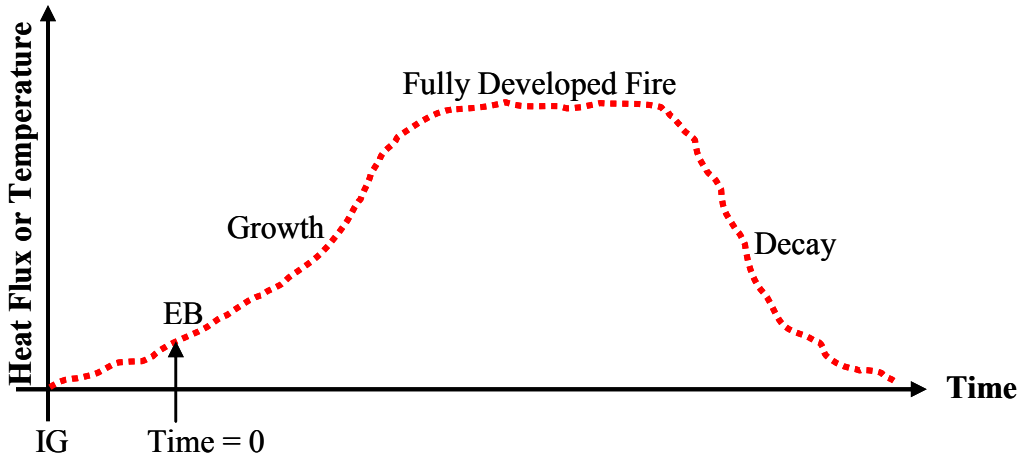

Figure 2-1: Stages of fire.

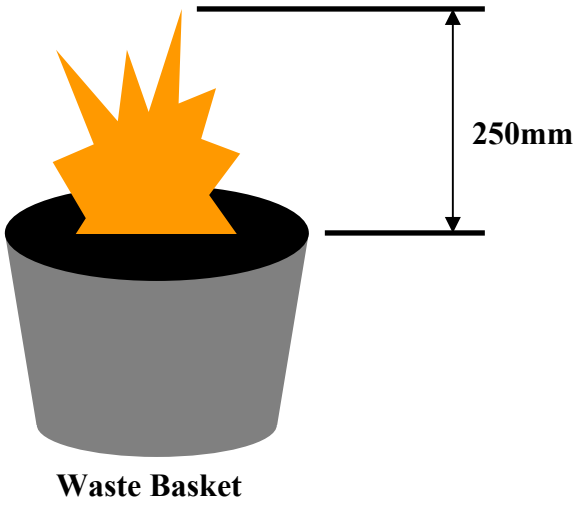

Figure 2-2: Waste paper basket fire; scale of fire at established burn stage (250mm).

Fire growth describes the period of time between established burning and the fire becoming fully developed. Heat flux and temperature trend upward throughout this stage.

A fully developed fire burns with a generally uniform heat flux and at some uniform temperature for some period of time until the majority of the fuel is consumed. The duration of this stage of the fire may be very short or may be drawn out for an extended

period of time depending on the availability of fuel. In addition, the assumption of constancy during this period is based on a single fuel source; in cases where more than one fuel is present and may be available at different times during the fire, variation may occur. This is the stage of fire that results in the most sustained heat transfer to a structure and thus may have a significant affect on structural behavior (Fitzgerald, 2002).

As the fuel reaches a point when the majority has been consumed, the heat flux decreases until no energy is released at all and the fire is out. This decay period is highly variable depending on fuel source and insulation, and is noted that, depending on conditions, significant continued heating of structural elements may still occur during this stage. This continued heating is a result of the ongoing, but diminishing energy release during the decay period.

2.2 Fire Histories

There are many ways that an engineer might characterize a fire depending on the analysis being performed, from types of gas released, to temperature, to dimensions of the flames. For a structural analysis of a building subjected to fire loading, however, two key parameters are used: gas time-temperature histories or fire heat flux histories, which describe the temperature and heat flux over time.

Section 2.1.4 of this report described the five stages of fire, from ignition to decay. The reader is again referred to Figure 2-1, but instead of individual stages of fire behavior, the entire history of the fire should now be considered to be a single event. This single event is a record of the heat flux or temperature as a function of time over the entire duration of the fire and is defined as a fire history. When analyses are conducted to evaluate the combustion characteristics of objects, heat flux and temperature are recorded versus time.

2.2.1 Time-Temperature Curves

Now that the basic form of fire histories are understood, the concept of design curves logically follows. As mentioned previously, the heat flux, total energy release, and temperature of a fire depend upon fuel source and are also affected by environmental conditions such as wind, oxygen availability, and location within a structure. The potential combinations of these effects are infinite, which for design purposes demands that some simplification be made. To that end, two major time-temperature curves are specified by building codes and are used by engineers in building design: ISO 834 which is essentially the same curve as the 2002 Eurocode Standard Compartment Curve and ASTM E119 (IBC, 2003). These standard curves are shown in Figure 2-3. For reference, the ASTM E119 curve represents the combustion of approximately 50kg of wood (with a energy potential of 8.44MJ/kg) per square meter of exposed area per hour of analysis" (Gustaferro, 1987).

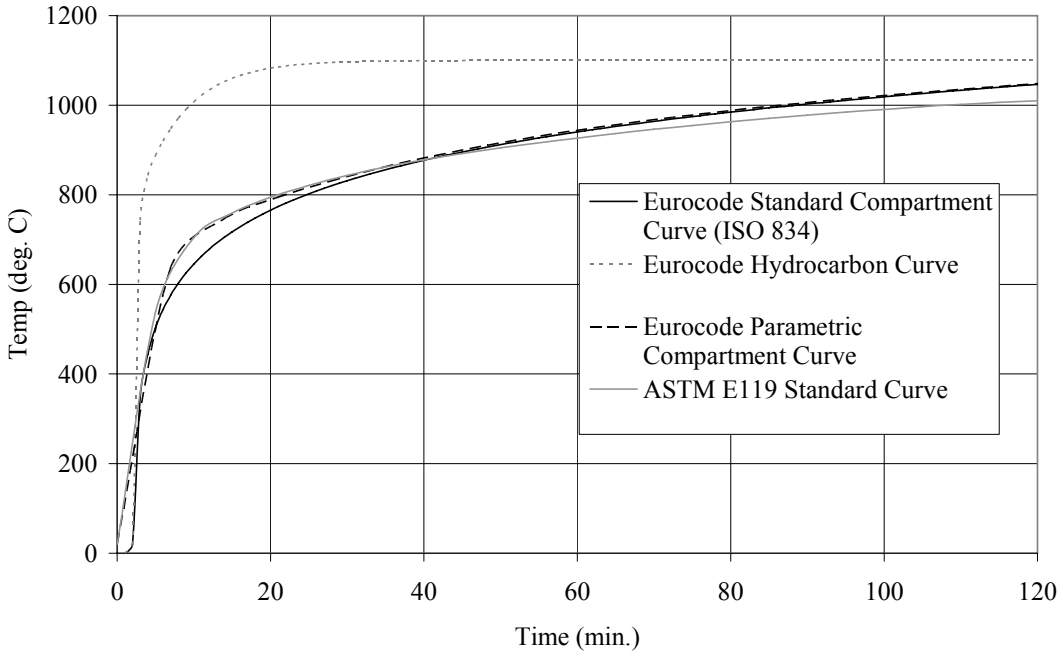

Figure 2-3: Standard time-temperature comparisons; Eurocode Standard (ISO834), ASTM E119, Eurocode Hydrocarbon, Eurocode Parametric Curve for parking garage model.

These standard curves are often used in the fire testing of structural components, where the component is placed in a furnace and the temperature of the fire is varied according to the applicable time-temperature curve. As implied by the name, however, standard time-temperature curves are generalizations, which are made to allow for performance comparisons between tested structural elements. The curves are agreed-upon approximations by the governing code bodies, and are considered representative of typical compartment fires. The standard curves do not consider specific compartment size, fuel load, material properties, etc., and thus are to be used for comparative purposes and not to be used to represent any particular fire.

The standard time-temperature curves represent the gas temperatures within a compartment because compartment fires assume a uniform temperature distribution throughout, therefore the fire and gas are assumed to be of the same temperature. Figure 2-3 shows the ASTM E119 and ISO 834 Time-Temperature curves plotted on the same graph. As shown, it is clear that the curves are similar, in fact, Harmathy (1988) showed, using a series of furnace analyses, that the ISO 834 curve specifies a slightly less severe fire, but the differences in the overall fire endurance by structural members exposed to either curve are not expected to be more than approximately 5 minutes. In comparing the two curves, some important characteristics are noted:

1. Both curves experience a period of rapid fire growth in the first 30 – 40 minutes, which then slows down considerably from about 30 minutes – 1 hour. After the first hour, the fire growth rate is relatively slow and nearly linear for the remainder of the analysis duration.

2. Neither curve includes a decay period. It is assumed that, when all the fuel is consumed, the fire is immediately extinguished, and the time-temperature curve terminates at that point.

3. Numerically, as Harmathy showed, the two curves are very similar. The largest difference between the two occurs at about the four minute mark, which is still less than 5%. For this reason these two curves are treated as essentially the same for the rest of this report.

A general procedure for applying the standard curves in a structural analysis based on thermal loading highlights the nature of the fire approximation. A standard curve might be used as gas temperature input for a finite elements model such as ABAQUS. In such a model, material properties such as emissivity of the gas and model surfaces, thermal conduction and specific heat (which are temperature dependent), and density would be entered. Boundary conditions such as the convection coefficient, ambient temperature, and initial surface temperature would also be specified. From the analysis, surface temperature values as well as interpolated convective and radiative heat flux data might be obtained. The key in this analysis is that the heat flux is a calculated value based on uniform gas temperature throughout the compartment.

In addition to the standard time-temperature curves in the Eurocode and ASTM standard, a wealth of parametrically and analytically derived time-temperature curves are available. The SFPE Engineering Guide (2004) provides a survey and relative comparison of a number of these curves. For compartment fires, the SFPE Engineering Guide concludes that Law's method is the best for use in "all roughly cubic compartments (compartment width to depth ratio within the range of 0.5 to 2.0) (Quintiere, 2004)." This aspect ratio roughly describes the entire campus square parking garage (See Equations 2-7 to 2-9).

$$T = T_{gm}\left(1 - e^{-0.05\Psi}\right)$$

where:

T = compartment temperature

T_{gm} = maximum compartment gas temperature

Ψ = fuel mass and compartment area coefficient

Equation 2-7: Law's Equation for maximum temperature reached in a compartment (Quintiere, 2004).

$$\Psi = \frac{m_f}{\sqrt{A \times A_0}}$$

where:

Ψ = fuel mass and compartment area coefficient

m_f = fuel mass

A = surface area of enclosure in square meters

A_0 = area of openings in square meters

Equation 2-8: Law's equation for fuel mass and compartment area coefficient equation (Quintiere, 2004).

$$T_{gm} = 6000\left(\frac{1-e^{-0.1\frac{A}{A_0\sqrt{H_0}}}}{\sqrt{\frac{A}{A_0\sqrt{H_0}}}}\right)$$

where:

T_{gm} = maximum compartment temperature

A = surface area of the compartment in square meters

A_0 = area of the ventilation openings in square meters

H_0 = average height of ventilation openings

Equation 2-9: Law's equation for finding maximum compartment temperature (Quintiere, 2004).

It is noted that the SFPE Engineering Guide only recommends Law's Method for use with wood-based fuels. Since this project uses motor vehicles, and consequently hydrocarbons, as the only fuel source, Law's method is not applicable. Also, it is important to reiterate that Law's Method as well as the ASTM E119 and ISO 834 curves are designed for compartment fires only.

2.2.2 Time-Heat Flux Curves

While the protocols for design time-temperature curves are well established, those for time-heat flux histories are not. Code treatment of fire to this point has focused almost exclusively on gas temperature in compartments, thus little attention has been paid to the development of design time-heat flux curves other than the T-squared fires addressed in the next paragraph. Some work has been done by Mangs and Keski-Rahkonen (1994, 2004) at VTT Building Technology in Finland, and Jannsens (2004) at Southwest

Research Institute in Texas, USA, in order to characterize the burning of motor vehicles, which is discussed later in this report.

The T-squared heat flux curve focuses exclusively on the growth stage of fire history and is still used as a base for growth rate comparison to many actual fires (See Equation 2-10). It was introduced in the 1980's as a way to approximate the change in heat-release rate over time as a fire grew. There are four T-squared fire curves: slow, medium, fast, and ultra-fast, which describe the amount of time each fire takes to reach 1055 kW (Fleming, 2003).

$$Q = 1055\left(\frac{t}{t_g}\right)^2$$

where:

Q = *h*eat flux of fire in kW

t = time after ignition in seconds

t_g = growth time in seconds

Equation 2-10: Heat flux equation for T-Squared fires (Equation modified from Klote, 2005).

Table 2-1 shows the range of t_g values set out in the NFPA 92B: Guide for Smoke Management Systems in Malls, Atria, and Large Areas (2005), and Figure 2-4 shows the T-Squared fires plotted versus time.

Fire Type	t_g sec.(NFPA 92B)
Slow	600
Medium	300
Fast	150
Ultra-Fast	75

Table 2-1: t_g range from NFPA 92B (2005).

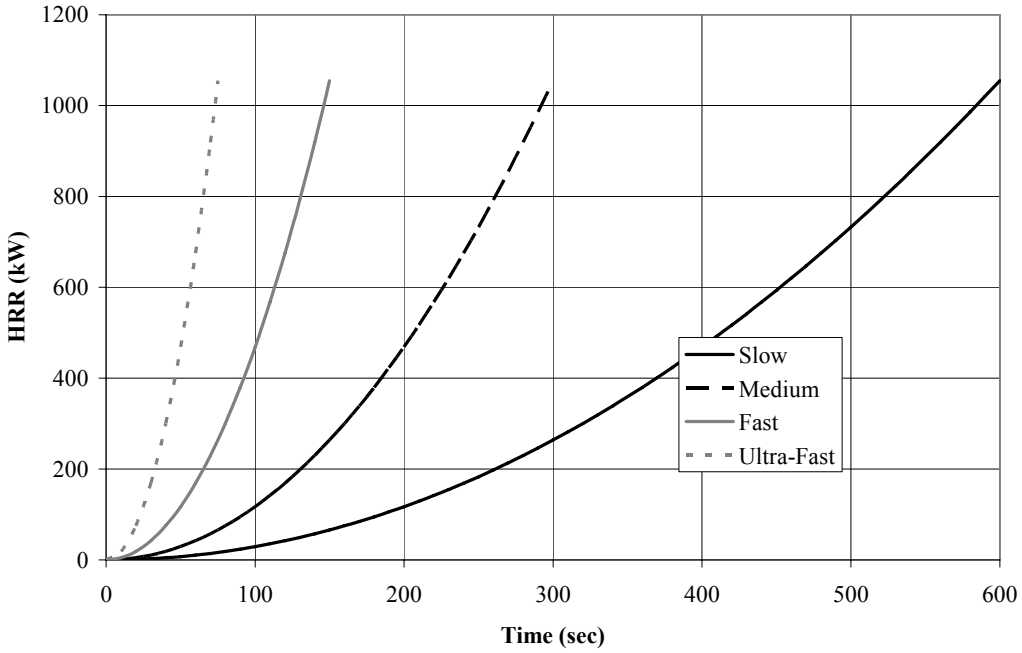

Figure 2-4: T-Squared fires from NFPA 92B (2005).

2.3 Fire Modeling with FDS

While the mechanisms of heat transfer from a fire have been understood for some time, the computing power required to numerically model fire behavior has only recently become available. Concurrent with this increase in computing power, a number of fire computer modeling programs have been developed. Fire Dynamics Simulator is the program used for this project. FDS was developed at NIST and is made publicly available free of charge through their website (http://fire.nist.gov/fds/). FDS uses a Computational Fluid Dynamics model to simulate fire-driven fluid flow (McGratten, 2005b).

The FDS program calculates the net heat flux into a surface as a combination of the radiative and convective heat flux. The convective heat flux is given by the same equation as in the Eurocode 1 and SFPE Engineering Guide:

$$\dot{q}''_c = h(T_g - T_w)$$

where:

$\dot{q}''_c$ = convective heat flux

h = convection coefficient

T_g = gas temperature

T_w = wall temperature

Equation 2-11: FDS Net Heat Flux Equation.

The fluid flow (convection) in FDS is governed by a version of the Navier-Stokes equations for low-speed (incompressible) flow. The Navier-Stokes Equations are a set of five, non-linear second-order partial differential equations that are derived from the conservation of mass, momentum, and energy equations, the ideal gas law, and the equation for density in any particular volume element. Given the low-speed flow constraint, which is defined by flow that is small in comparison to the speed of sound, the fluid is assumed to be incompressible. By assuming low-speed flow, the fifth Navier-Stokes equation is dropped. Therefore, in vector notation, the Navier-Stokes equations are:

$$\rho \cdot \left(\frac{\partial v}{\partial t} + (v \cdot \nabla)v \right) = F - \nabla p + \mu \cdot \Delta v$$

Equation 2-12: Vector Notation of the Navier-Stokes Equations (For derivation and variable definitions see Oertel, 2004).

The FDS radiative heat flux calculations are conducted following a version of the finite volume method for convective transport. The finite volume method is used to solve the radiation transport equations for gray gas. A thorough discussion is included in Section 3.3 of the FDS Technical Reference Guide (McGratten, 2005a).

2.4 Summary of Relevant Fire Analyses

This discussion is broken into five sections. The first three (Sections 2.4.1-2.4.3) examine the characteristics of individual vehicle fires, summarize past vehicle fire experiments, and design fires for motor vehicles. Sections 2.4.4 and 2.4.5 examine multiple vehicle fire analyses in parking structures.

2.4.1 Vehicle Fire Characteristics

Recent experimental analyses of burning vehicles have been performed on a variety of vehicles manufactured between 1970 and 2000, with the majority being earlier model year vehicles due to cost constraints. The analyses have addressed a range of issues, from fire geometry to heat flux, and some beginning work has been conducted in an attempt to create a design fire for burning vehicles (Li, 2004; Mangs, 1994a,b).

In a modern vehicle, materials can generally be divided into two categories: combustibles and incombustibles. Combustible materials are almost exclusively some variety of hydrocarbons, but relatively small quantities of organics, such as leather and wood may also be present. Incombustibles are nearly all metals. The combustible materials are considered the fuel for a vehicle fire.

Fire is a complicated phenomenon to model, partially due the large quantity of variables that must be taken into consideration. In general, the heat flux from a fire can be modeled more accurately than the flame geometry, which is acceptable for this investigation. It was assumed that all that was required for this study was a good estimation of flame height and location, as the important data are heat flux, total energy released, and temperature.

According to Mangs (2004) the fuel sources may be divided initially into seven groups by location within the vehicle: engine, front tires, front half of the passenger compartment, fuel tank, rear tires, trunk, rear half of the passenger compartment. Using these seven fuel groupings, two fire plumes may be modeled as follows:

Front Plume:
- Location: emerging through front windshield
- Fuel Groups: engine, front tires, front half of passenger compartment

Rear Plume:
- Location: emerging through rear window
- Fuel Groups: vehicle fuel tank, rear tires, trunk, rear half of passenger compartment

Figure 2-5 shows the front and rear fire plumes and the fuel groups contributing to those plumes.

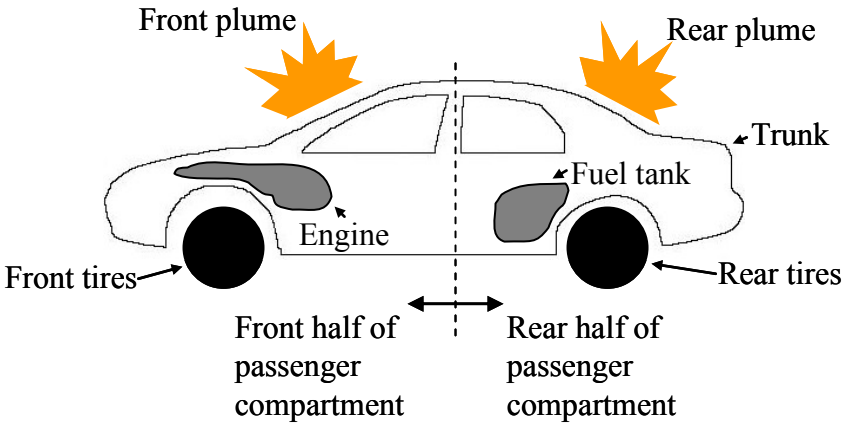

Figure 2-5: Vehicle fire geometry according to Mangs (2004).

Vehicle fire analyses conducted by Khono et al. (2005) show similar behavior to the characterization by Mangs. Different sections of the vehicle are seen to burn at different times and with varying intensity, generally adhering to the dual plume concept shown in Figure 2-5. The delineation between front and rear plumes, however, does not appear as clear as Mangs indicates, and flames are observed to emerge from side windows and the wheel wells in addition to the front and rear windshields. An example of one of the analyses performed by Khono et al. (2005) is shown in Figure 2-6.

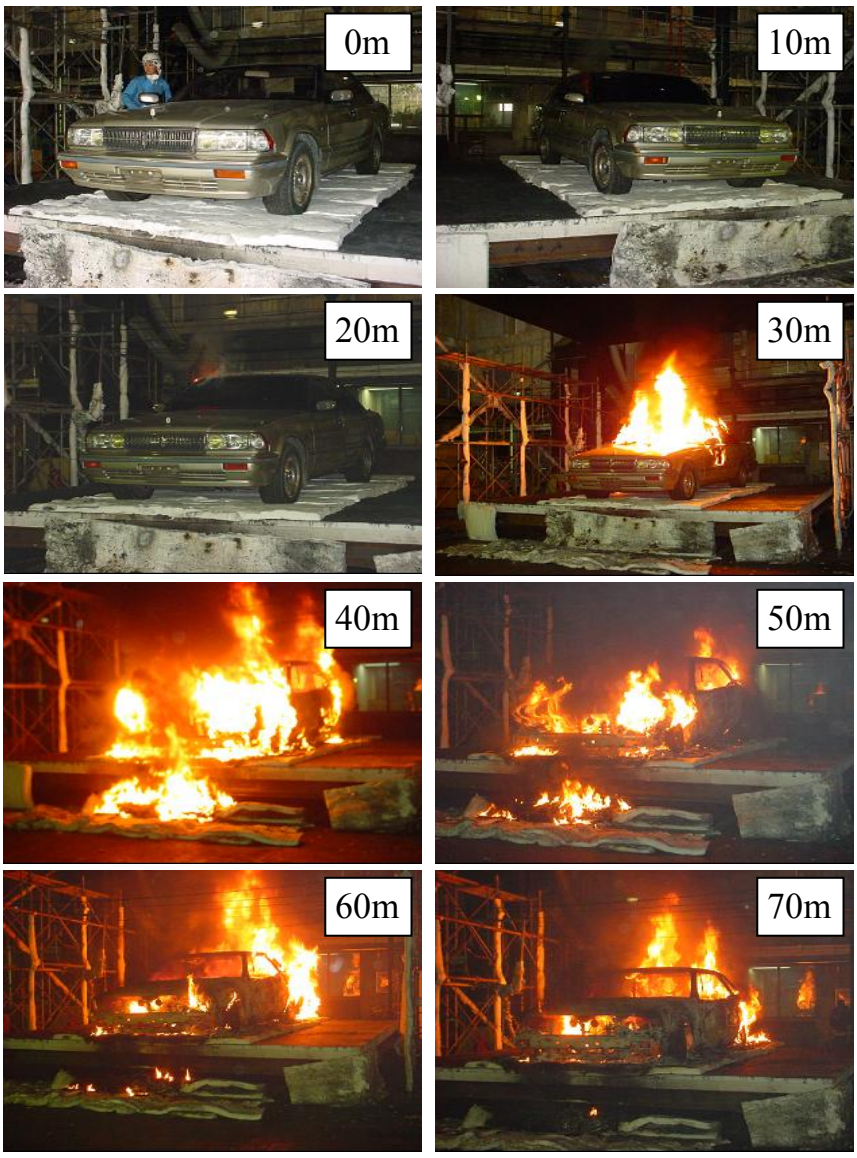

Figure 2-6: Images of Khono et al. (2005) vehicle burn analysis at 10 minute intervals (Midsize 4-door with 3L engine).

2.4.2 Vehicle Fire Experiments

As mentioned previously, several analyses of burning vehicles have been conducted in recent years. These analyses were all conducted in large calorimeters to capture the combustion products and record gas temperatures, and the vehicles were weighed during testing. From this data, heat flux and total heat release were calculated using oxygen consumption calorimetry, though in some cases, this was not performed for the entire

record. Table 2-2 summarizes the analyses and the following paragraphs briefly describe each.

Mangs and Keski-Rahkonen (1994a,b) performed a series of analyses on three vehicles, all of which were manufactured in the late 1970's and contained typical passenger effects such as luggage, maps, tissues, etc. The vehicles were ignited via a heptane tray either under the engine or in the passenger compartment. Heat flux data was collected for all three analyses yielding a peak heat flux of about 2 MW for all three analyses and total heat release ranging from 3 to 3.88 GJ.

Shipp and Spearpoint (1995) conducted analyses on two vehicles manufactured in the early to mid 1980's. Only one analysis was allowed to burn completely, but heat flux values were recorded for both analyses, yielding peak values of 7.5 and 4.5 MW and a total heat releas value for the one completed burn of about 5 GJ.

Type of Vehicle	Year of Vehicle	Peak Heat Flux (MW)	Total Heat Release (GJ)	Reference
Ford Taurus 1.6	Late 1970's	2	3.32	Mangs and Keski - Rahkonen (1994)
Datsun 160J	Late 1970's	2	3	Mangs and Keski - Rahkonen (1994)
Datsun 180B	Late 1970's	2	3.88	Mangs and Keski - Rahkonen (1994)
Unknown	1970-1980	2	Unknown	Zhao and Kruppa
Unknown	1990	8.5	Unknown	Zhao and Kruppa
Austin Maestro	1982	7.5	(Extinguished @ 17 min)	Shipp and Spearpoin (1995)
Citroen BX	1986	4.5	5	Shipp and Spearpoin (1995)
Minivan	1995	2.4	(Extinguished @ 4 min)	Stroup (2001)
Trabant	Unknown	3.8	3.1	Steinert (2000)
Austin	Unknown	1.9	3.2	Steinert (2000)
Citroen	Unknown	4.6	8	Steinert (2000)
Compact 4-door (2L Engine)	Mid-1990's	2.44	4.47	Khono et. al. (2004)
Compact 4-door (2L Engine)	Mid-1990's	3.21	5.12	Khono et. al. (2004)
Midsize 4-door (3L Engine)	Early-1990's	4.93	8.51	Khono et. al. (2004)
Midsize 4-door (3L Engine)	Early-1990's	3.76	6.99	Khono et. al. (2004)
Minivan	Early-1990's	4.66	5.53	Khono et. al. (2004)
Midsize SUV (3L Engine)	Early-1990's	3.36	5.67	Khono et. al. (2004)
Midsize SUV (3L Engine)	Mid-1990's	5.11	7.39	Khono et. al. (2004)
Full-size Mercedes (5.6L Engine)	Early-1990's	6.76	8.11	Khono et. al. (2004)

Table 2-2: Summary of vehicle burn analyses.

Zhao and Kruppa (2005) conducted a series of ten experiments, five with one vehicle involved and five with two vehicles. The vehicles were either older 1970-1980's models or a newer 1990's model. The vehicles were placed in varying positions in relation to a simulated wall or ceiling and heat flux and temperature data were collected. The peak heat flux ranged from 2 to 8.5 MW.

Stienert (2000) also conducted a series of ten experiments, primarily to study fire spread from one vehicle to another. Three analyses were performed on one vehicle, six on two vehicles, and one on three vehicles. The single vehicle analyses yielded peak heat flux values from 1.9 to 4.6 MW and total heat release values ranging from 3.1 to 8 GJ. The multiple vehicle analyses involved vehicles placed either 0.4 or 0.8 meters apart and showed that fire spread from one vehicle to the next ranged from 12 to 52 minutes.

Stroup et al. (2001) conducted analyses on a single passenger minivan to evaluate the hazard associated with a fire in such a vehicle. The final analysis involved a burn of the vehicle with windows down and two liters of gasoline used as an accelerant in the passenger cabin. The passenger compartment become untenable less than one minute after ignition, and the fire was extinguished after four minutes. A peak heat flux of 2.4 MW was recorded prior to extinguishment.

Khono et al. (2005) conducted a series of eight experiments on vehicles of varying size, all of which were manufactured in the early to mid 1990's. Each was placed under a cone-calorimeter, ignited, and allowed to burn completely. Peak heat flux values ranged from 2.44 to 6.76 MW and total heat release ranged from 4.47 to 8.51 GJ.

Shipp and Spearpoint (1995), Li (2004), and Zhao and Kruppa (2005), all agree that newer vehicles contain higher amounts of combustible plastics relative to organics or incombustible metals, thus higher peak heat flux are recorded for newer vehicles as compared to older vehicles. Additionally, vehicle weight for newer vehicles is significantly higher due to more extensive safety equipment and amenities, consequently quantity of fuel available is greater in newer vehicles as well, contributing to higher total heat flux values. A plot showing the general trend toward higher total energy release for newer vehicles in shown in Figure 2-7.

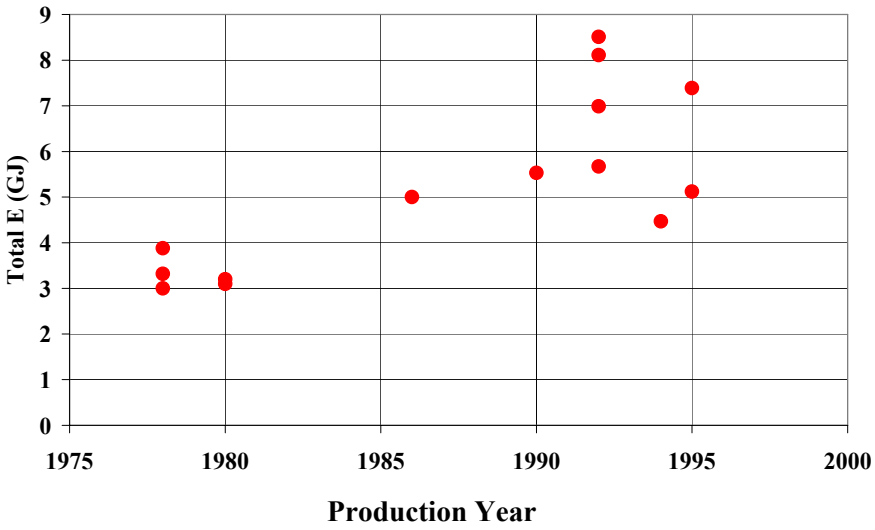

Figure 2-7: Summary of total energy release of vehicle fire analyses in Table 2-2, plotted as total energy output vs. production year.

2.4.3 Design Fire for Motor Vehicles

Work has been done by both Li (2004) and Mangs and Keski-Rahkonen (1994a,b) to characterize the heat flux histories of burning vehicles into a simplified form that might be applicable to design.

According to Li (2004), the growth period of the heat flux curve falls somewhere in between a slow and medium growth rate T-squared fire, which are defined by Equation 1-13. Experimental data from Shipp and Spearpoint (1995), Schleich et al. (1999), Steinert (2000), and Mangs and Keski-Rahkonen (1994a), all support this conclusion, as evidenced by the comparison of the HRR curves shown in Figure 2-8, which is taken from Li (2004).

The decay of fire is an area often overlooked, particularly in building codes, as it is generally considered to be of significantly lesser importance than growth or peak heat flux. It may have great influence, however, if the duration and intensity of HRR during the decay is long and high enough. Therefore, it is not ignored for this investigation. As seen in Figure 2-8, the duration of the majority of fire decay may take between one and two times the duration of the growth phase. For the nearly all of the analyses shown in Figure 2-8, heat flux reaches below 1000 kW between 40 and 50 minutes after ignition. The low heat flux after this point is negligible in relation to the peak heat flux, which is as much as 20 to 30 times the value apparent after 40-50 minutes.

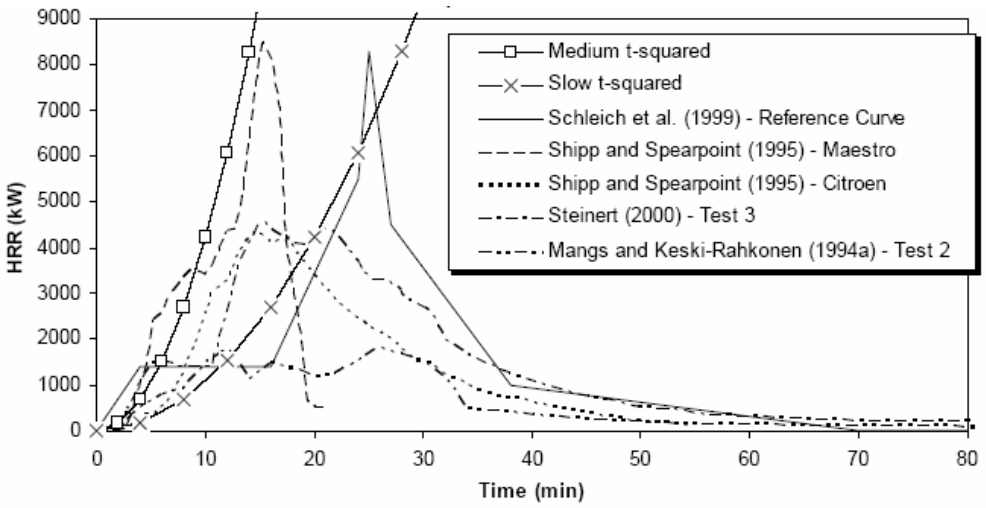

Figure 2-8: Comparison of T-squared fires to several actual fire analyses (reproduced from Li, 2004).

Mangs and Keski-Rahkonen (1994a,b) present a parameterization of their experimental findings that combines a single Boltzmann curve to describe the growth period, superimposed with three Gaussian curves to describe the burning of various portions of the vehicle. The limited data set (only three analyses) did not provide a enough information to justify the use of one curve over another, and the curves used were chosen because they worked for the analyses performed. While the curves presented fit the available data, no recommendations are made for more general use.

2.4.4 Parking Garage Fire Experiments

Several analyses have been performed in steel frame parking garages, some with composite decks. The focus of much of this work was to determine the fire protection measures necessary in such structures, such as sprinkler systems, spray-on fire proofing, etc.

Bennetts et al. (1985) performed two fire analyses on a two story, open-deck, unprotected steel parking garage with composite deck and precast concrete wall panels. In each of the analyses, five vehicles were parked on the lower floor between 0.4 and 0.5 meters apart. All vehicles were compact vehicles manufactured between 1973 and 1982. In the first analysis, only the analysis vehicle burned, and in the second analysis, the adjacent vehicles ignited at 14 and 35 minutes. Both gas and surface temperature readings were taken over the course of the analyses at several locations. Peak gas temperatures measured directly over the burning vehicle were about 750 degrees Celsius in the first analysis and 575 degrees Celsius in the second analysis. Maximum surface temperature for the steel beams above the burning vehicles was 285 degrees Celsius for the first

analysis and 340 degrees Celsius for the second. No attempt to record the heat flux from the vehicle fires was reported.

Kitano et al. (2000) performed an experiment with passenger vehicles in a four-story parking garage in a similar configuration of steel members, composite concrete deck, and precast wall panels to that of Bennetts et al. Once again temperatures were recorded for the gas and steel, but no attempt to measure heat flux was reported.

Zhao and Kruppa (2004) performed a series of fire analyses on model parking garage constructed of steel columns and beams with a full scale composite slab. The two main analyses involved three vehicles clustered together at a normal parking distance with the center vehicle igniting first in both analyses. Analysis conditions included a strong wind that varied in direction through both analyses, and though all three vehicles burned in both analyses, time for fire spread from one vehicle the next varied widely due to the wind. As in the Bennetts et al. analyses, Zhao and Kruppa recorded gas and surface temperatures at several locations in the structure. Peak gas and steel surface temperatures were 1000 degrees Celsius and 700 degrees Celsius respectively, and no attempt to record heat flux was recorded.

2.4.5 Parking Garage Fire Analysis

Chow (1995) performed a series of analyses modeling an underground, closed parking garage using the CFAST and CCFM VENTS programs from NIST. The volumes ranged from 2000 to 50,000 cubic meters with square footprints from 25.8 to 129.1 meters in side length and ceiling heights from 3 to 5 meters. A 3m x 3m fire with a constant heat flux of 5MW and duration of 60 minutes was assumed. Chow concluded that the assumed fire in any closed parking garage larger than 1000 cubic meters is unlikely to reach an average gas temperature of greater than 300 degrees Celsius.

CHAPTER 3

FIRE ANALYSIS METHODOLOGY

This chapter explains the methodology used in this research including the procedures for assembling the fire analysis models and the tools utilized for analysis. Section 3.1 descibes the prototype structure that the analysis models were based on. Section 3.2 then explains the variables addressed in the analyses and presents the analysis matrix. Section 3.3 presents the analysis model that was developed based on the prototype structure. Section 3.4 provides details of the vehicle fire model. Sections 3.5 and 3.6 present the analysis parameters and instrumentation scheme respectively, and finally Section 3.7 explains the tools used to process the results.

3.1 Prototype Structure

The analysis models are based on the Campus Square Parking Garage on the Lehigh University campus, shown in Figures 3-1 and 3-2.

Figure 3-1: Lehigh University Campus Square Parking Garage (Southwest corner).

Figure 3-2: Lehigh University Campus Square Parking Garage (Southeast corner).

The Campus Square Parking Garage is located on a sloping lot with three floors above grade on the south side and four on the north side. The floor height varies from 3.8m on the ground floor to 3.1m for each of the upper floors. Overall dimensions are 45m from east to west and 36m north to south.

The garage is constructed of precast, prestressed concrete double-tees that are oriented longitudinally north-to-south, and three double-tees are placed side-by-side in between each column forming bays. The typical double-tee used is similar to the 15DT34 design from the PCI Handbook (2004), which is 4.6m wide, 18.4m long, and 0.87mm in total depth (See Figure 3-3). The double-tees are simply supported on the interior walls by inverted-tee girders (See Figure 3-5) or corbels (See Figure 3-4) protruding from the center shear wall.

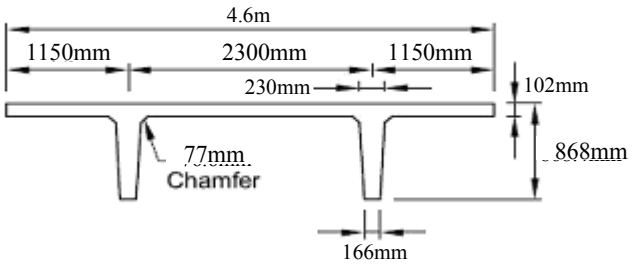

Figure 3-3: 15DT34 Double-tee from PCI Handbook (2004).

Figure 3-4: Corbels supporting double-tee.

Figure 3-5: Inverted-tee spandrel supporting double-tee.

The exterior ends of the double-tees are supported by a spandrel beam with pockets to allow the webs at the end of the double-tee to rest in a simply supported manner (See Figure 3-6).

Figure 3-6: Exterior spandrel beam supporting double-tee.

Precast sections also comprise the center shear wall, which includes a series of larger openings. Driving ramps to allow vehicles to move between floors are created by inclining the double-tee sections. An as built drawing or one floor of the Campus Square Parking Garage is shown in Figure 3-7.

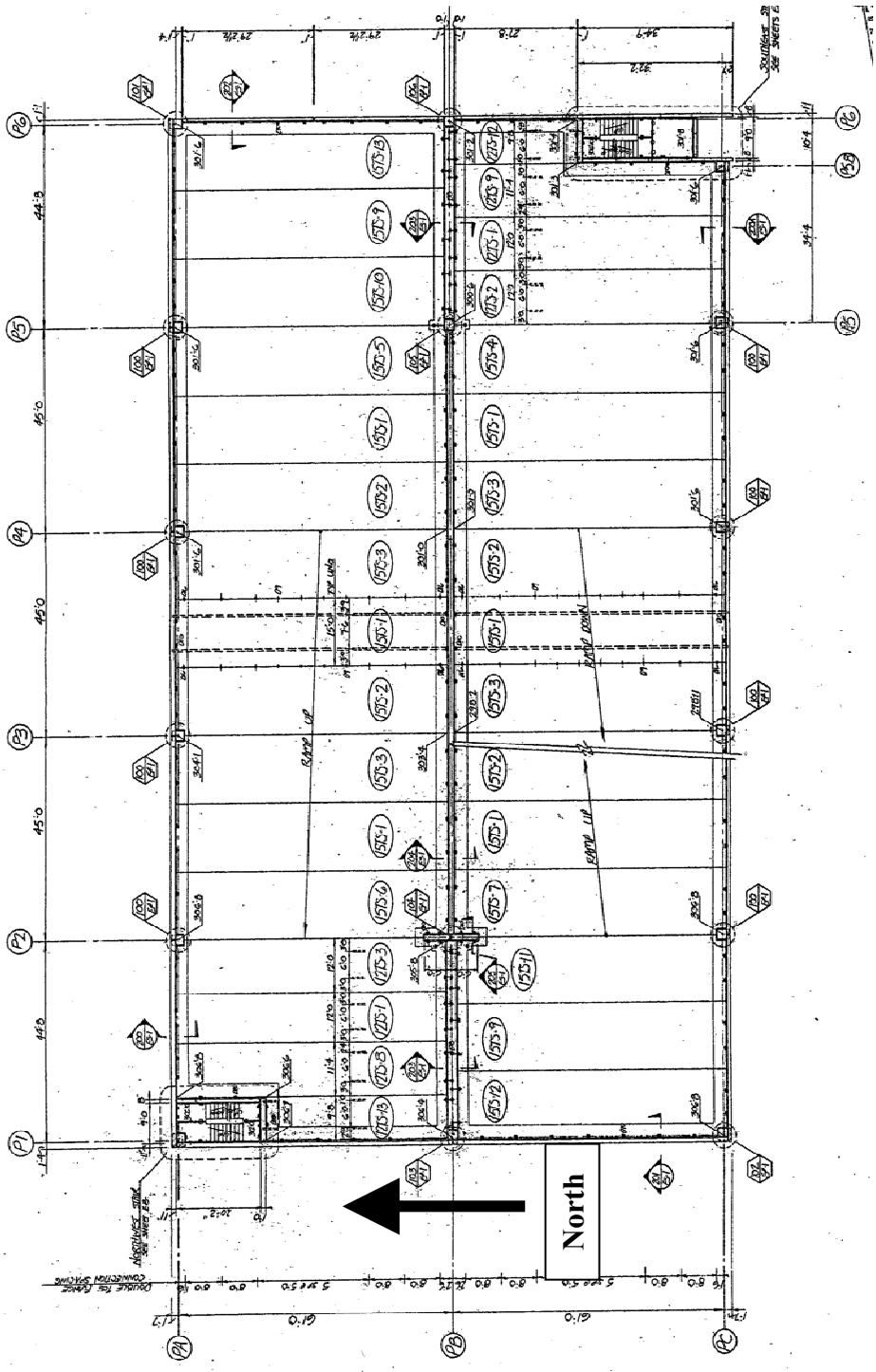

Figure 3-7: As-built drawing of a typical floor of the Lehigh University Campus Square Parking Garage.

3.2 Analysis Matrix and Analysis Variable Explanations

Based on the prototype parking garage a number of a variables were identified that might contribute to different effects of fire on the structure. This section presents the analysis matrix and explains each of the variables that were addressed in this project.

3.2.1 Analysis Matrix

In total, nine fire analyses were performed to address four variables. Table 3-1 summarizes the analyses, which are then explained in Sections 3.2.2 to 3.2.5.

Analysis		Floor Elevation		Center Wall Opening Position				Vehicle Type		Vehicle Fire Characteristics		
#	Name	Level	Staggered	Top	Bottom	Chimney	Staggered	1	2	Floor	Position	Ignition Time (Min.)
1	Top	X		X				X		1	23	0
2	Bottom	X			X			X		1	23	0
3	Chimney 1	X				X		X		1	23	0
4	Chimney 2	X				X			X	1	23	0
5	Stagger 1		X				X	X		1	23	0
6	Stagger 2		X				X	X		2	14	0
7	Stagger 3		X				X	X		3	23	0
8	Stagger 123		X				X	X		1	23	0
										2	14	+12
										3	23	+24
9	Spread	X			X			X		1	23	0
										1	22	+12
										1	24	+12
										1	21	+24
										1	25	+24
										1	20	+36
										1	26	+36

Table 3-1: Analysis matrix for FDS analyses.

3.2.2 Analysis Variable: Floor Elevation

The driving ramps in the Campus Square Parking Garage have the effect of varying the elevation of the floors relative to each other. At either end of the structure, the north and

south sides of the garage are at the same elevation, but through the middle the floors are inclined at opposite angles. This geometry may allow combustion products to spread from one floor to another. In order to capture this behavior, two floor elevations were chosen, described here as *level* and *staggered*. The level elevation represents the ends of the garage where the north and south sides are even, and in the staggered elevation the north and south sides are offset by one half story height. Both of these cases are shown in Figure 5-8. As shown in Table 3-1, Analyses 1-4 and 9 treat the level floor elevation, and Analyses 5-8 treat the staggered floor elevation.

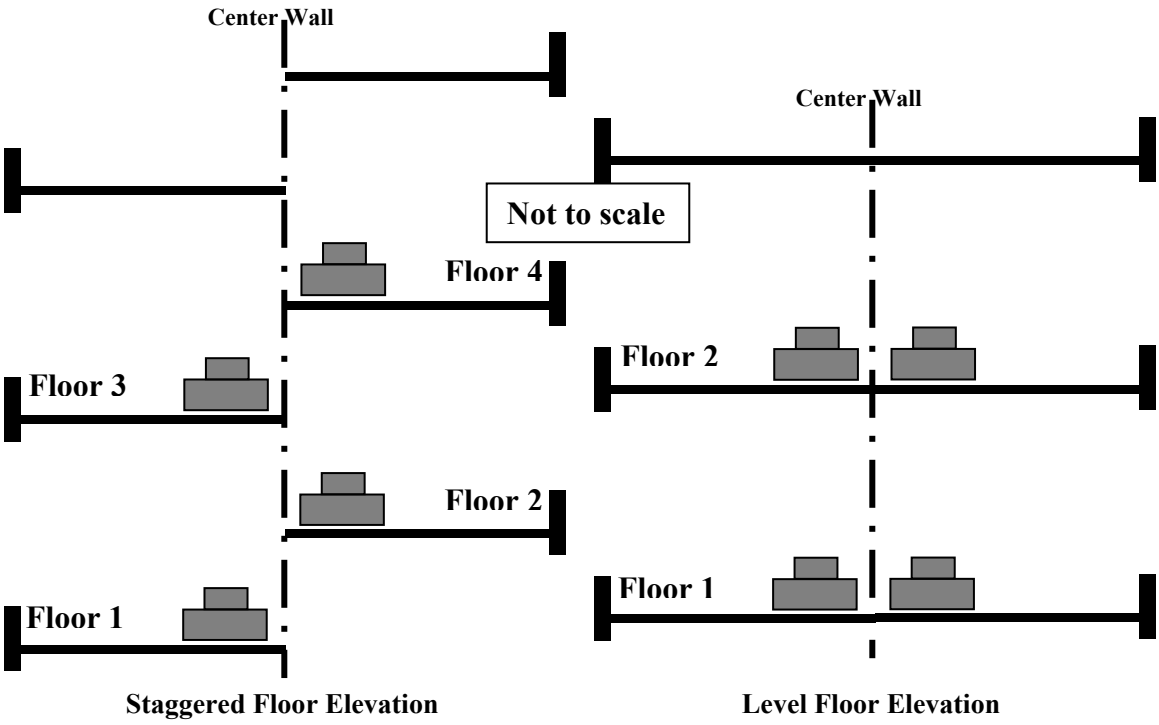

Figure 3-8: Staggered and level floor elevations.

3.2.3 Analysis Variable: Center Wall Opening Position

As explained previously, the center wall of the prototype garage is comprised of precast concrete sections with large openings spaced at regular intervals. Because the double-tees are inclined to create driving ramps, the relative position of the center wall openings varies in relation to the floor slab along the length of the garage. An example of this is shown in Figure 3-9.

Figure 3-9: Photograph of the center wall of the prototype garage.

These openings in the center wall allow combustion gases to pass from one side of the garage to the other and potentially from one floor to the next depending on the elevation of the double-tees relative to the openings. In order to capture this variability, and to investigate its effect on heat travel through the structure, the four different positions of the center wall opening in relation to the floor slab were modeled, referred to here as *top*, *bottom*, *chimney*, and *staggered*. The top, bottom, and chimney opening positions were all used when the floors were at the level elevation as explained in Section 3.2.2. The top opening position places the top of the center wall opening flush with the bottom of the floor slab that forms the ceiling. The bottom opening position puts the bottom center wall opening flush with the top of the floor slab. These two situations are shown in Figure 3-10.

For the chimney analysis opening position, the center wall opening was placed so it straddles the floor slab, with roughly half of the opening above and half below the slab (See Figure 3-10). This position creates a "chimney" opening in the floor where the two slabs from the north and south sides meet at the center wall (See Figure 3-11). This "chimney" simulates the instance where the two ramped sides of the parking garage cross in front of a center wall opening and the floors are at essentially the same level. It is noted that neither one of these conditions are present in the prototype garage, but nonetheless are possible in such a structure.

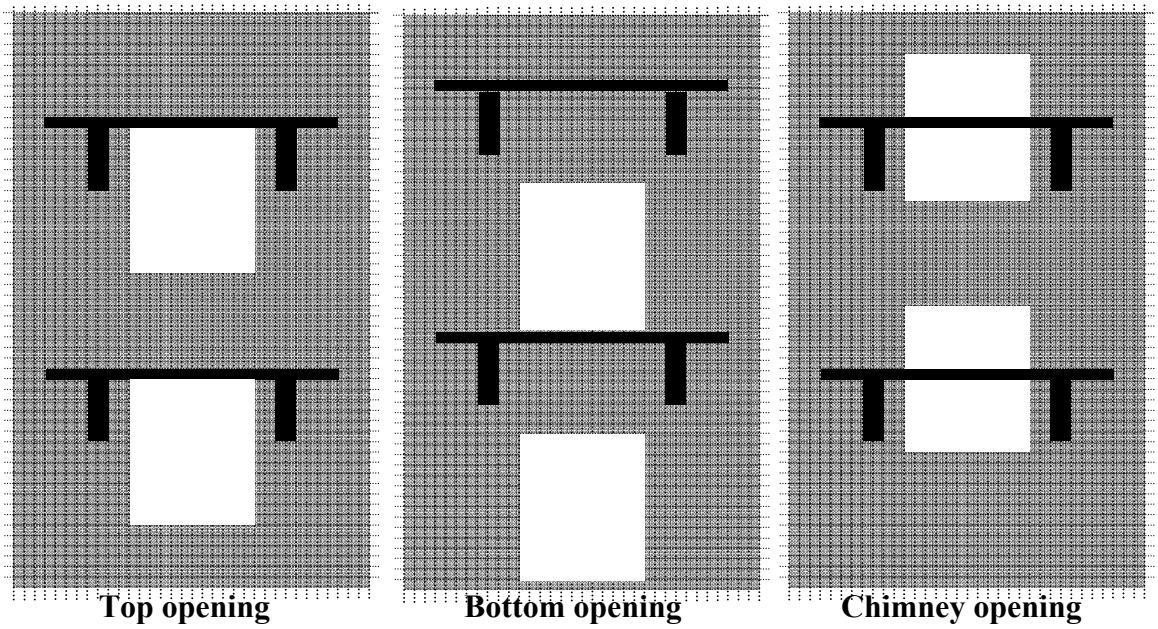

Figure 3-10: Center wall opening positions for level floors.

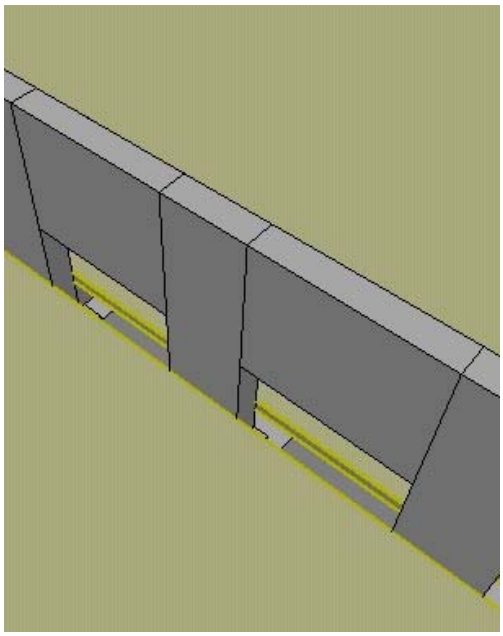

Figure 3-11: "Chimney" opening in center wall between slabs.

Finally, the staggered center wall opening position simulates the effects of the driving ramps. Because the floors are offset by one-half the floor height, identical center wall opening position relative to each floor is impossible to achieve. The center wall openings were therefore placed in the top opening position relative to the first and third floors, creating a new position on the second and fourth floors. Figure 3-12 shows the staggered opening position with the openings in white, the first and third floors in dotted gray, and the second and fourth floors in black.

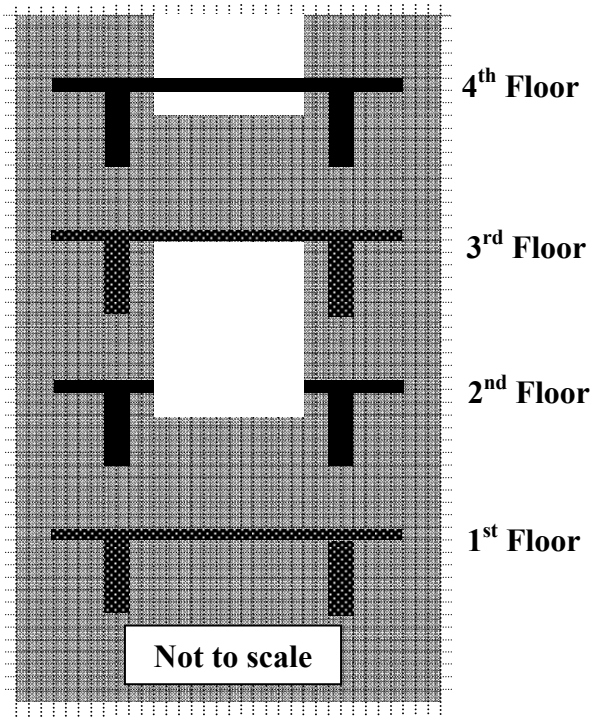

Figure 3-12: Center wall opening position for staggered floors.

Another way to visualize the staggered opening position is shown in Figure 3-13 where the concrete structure is shown in black and the arrows represent the potential direction of gas or heat flow through the center wall openings. The arrows are shown in different sizes to emphasize the difference in opening position.

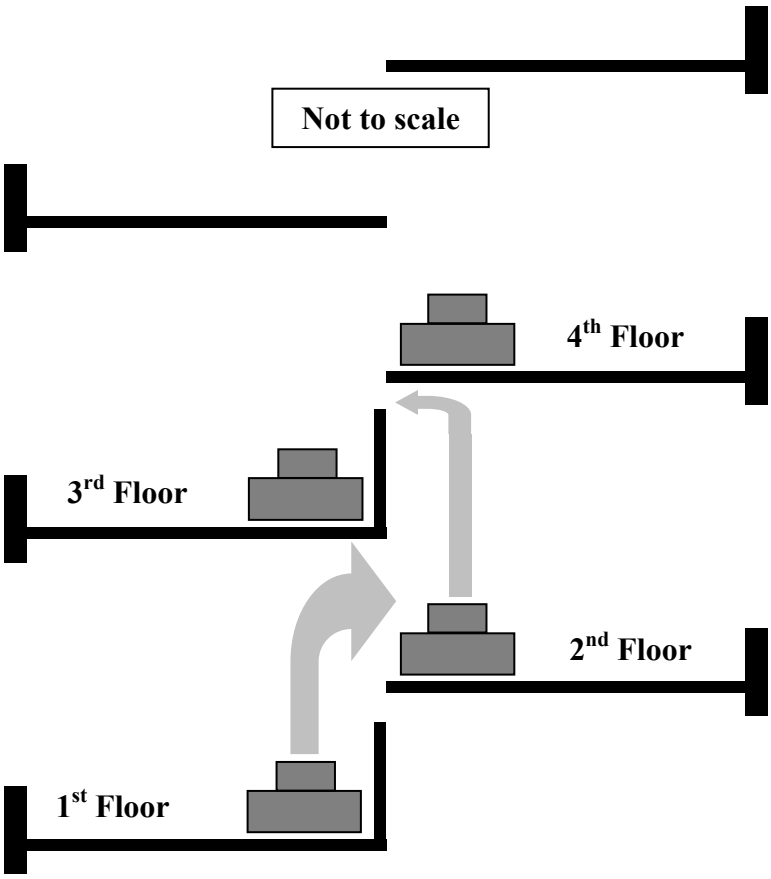

Figure 3-13: Staggered floor configuration with center wall opening positions shown.

3.2.4 Analysis Variable: Vehicle Type

The vehicles modeled in this project were based on two of the vehicles burned by Khono et al., namely an early 1990's Toyota 4Runner SUV labeled 3000cc 4WD No.2 (hereafter called Vehicle 1) and a full-size early 1990's sedan labeled 5600cc (hereafter called Vehicle 2) (See Figure 3-14).

Figure 3-14: Photographs of vehicles 1 and 2.

The heat flux release records from these two vehicle fire analyses are shown in Figure 3-15. These two records were used as inputs for the models (See Figure 3-15). These specific records were chosen rather than a more general approximation of a typical heat flux record for a vehicle fire. The reason for this choice was that the limited amount of current data available does not support a heat flux curve shape that approximates a range of vehicle fires. These two specific vehicles were chosen because their heat flux records differ greatly in shape and have a total energy release and peak heat flux in the upper range of the data shown previously in Figure 2-7. Vehicle 1 has a total energy release of 7.4 GJ and a peak heat flux of 5100 kW while Vehicle 2 has a total energy release of 8.1 GJ and a peak heat flux of 6800 kW.

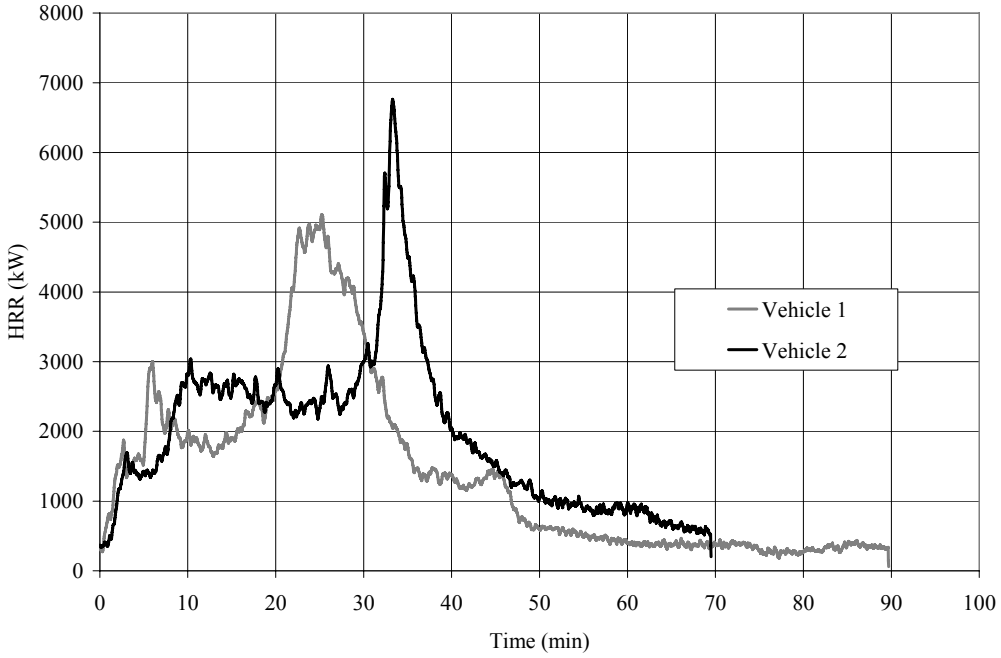

Figure 3-15: Comparison of heat flux records for Vehicles 1 and 2.

3.2.5 Analysis Variable: Vehicle Fire Characteristics

The title of this analysis variable, 'vehicle fire characteristics,' is used to describe the position of the burning vehicle in the model and ignition time of each vehicle for the multiple-vehicle analyses. The model was populated with vehicles in a typical parking pattern for the prototype garage, which causes the relative position of the vehicles in relation to the double-tees to vary (See Figure 3-16). For the single vehicle analyses, the fires occurred at position 23 or 14 in Figure 3-16. These two positions are mirrors of each other across the center wall and locate the vehicle roughly in the center between the double-tee webs.

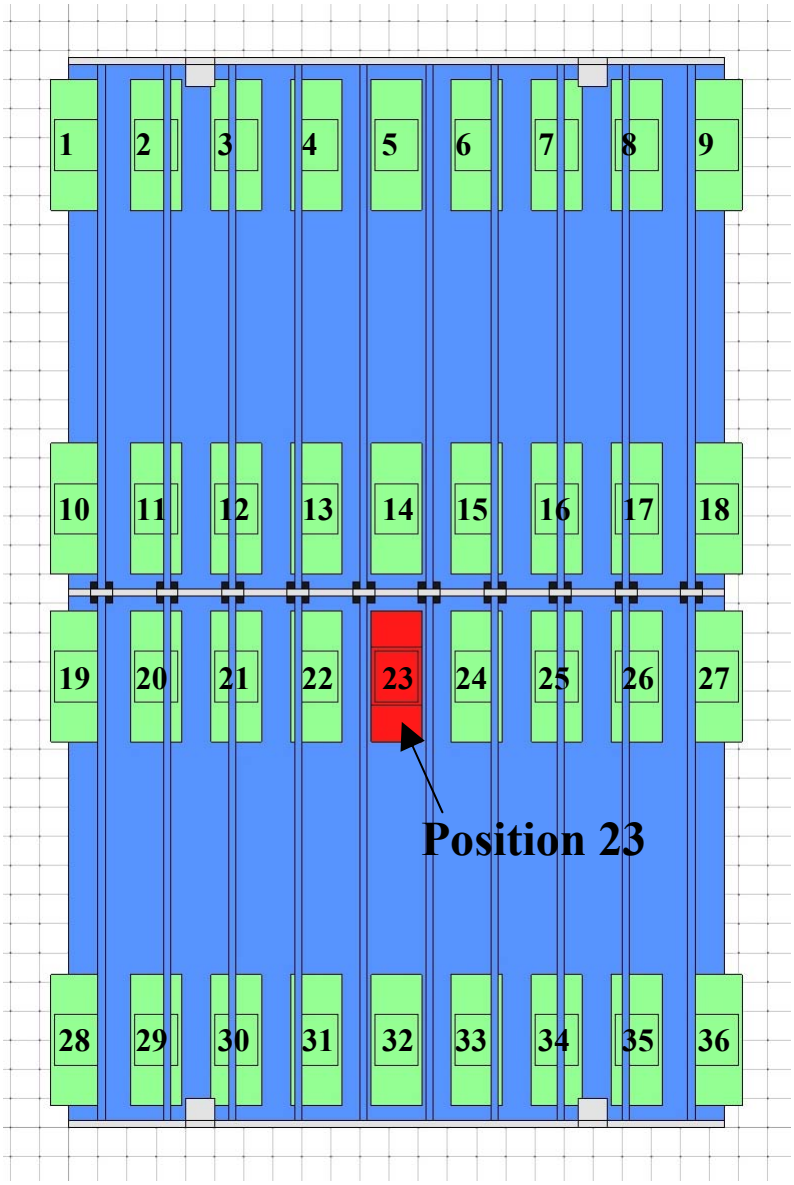

Figure 3-16: Vehicle position.

The two multi-vehicle analyses address two different patterns of ignition. Analysis 8 is a three-vehicle fire wherein the vehicle in position 23 on the first floor ignites at time 0, the vehicle in position 14 on the second floor ignites at time +12 minutes, and the vehicle in position 23 on the third floor ignites at time +24 minutes. Analysis 9 addresses fire spread on a single floor with five vehicles involved. The first vehicle is in position 23 again and ignites at time 0, followed by vehicles at positions 22 and 24 at time +12 minutes, vehicles at positions 21 and 25 at time +24 minutes, and vehicles at positions 20

and 26 at time + 36 minutes. Analysis 8 focuses on the flow of combustion gases between floors, whereas Analysis 9 looks at a larger total thermal input on just one floor.

3.3 Parking Garage Analysis Model

The model used for the analyses was based on the prototype structure modified to conform to a major constraint of the FDS program: a uniform computational mesh. In general, building scale models in FDS requires cell sizes of 0.100m to 0.150m for reasonable accuracy. Smaller cells can detract from the effectiveness of the Large Eddy Simulation used by FDS to model convection, and larger cells are not fine enough to capture radiative effects of fire (Meeting with D. Carpenter 11 January 2006). Cell sizes of 0.100m, 0.125m, and 0.150m were compared to the dimensions of the prototype structure, and the 0.125m cells were found to most accurately capture the geometry, and, as a result a 0.125m cubic mesh was used to create the model. In order to adhere to this 0.125m square mesh, every measurement in the model was constrained to 0.125m increments. Figure 3-7 shows cross-sections of a single double-tee overlaid with a 0.125m mesh.

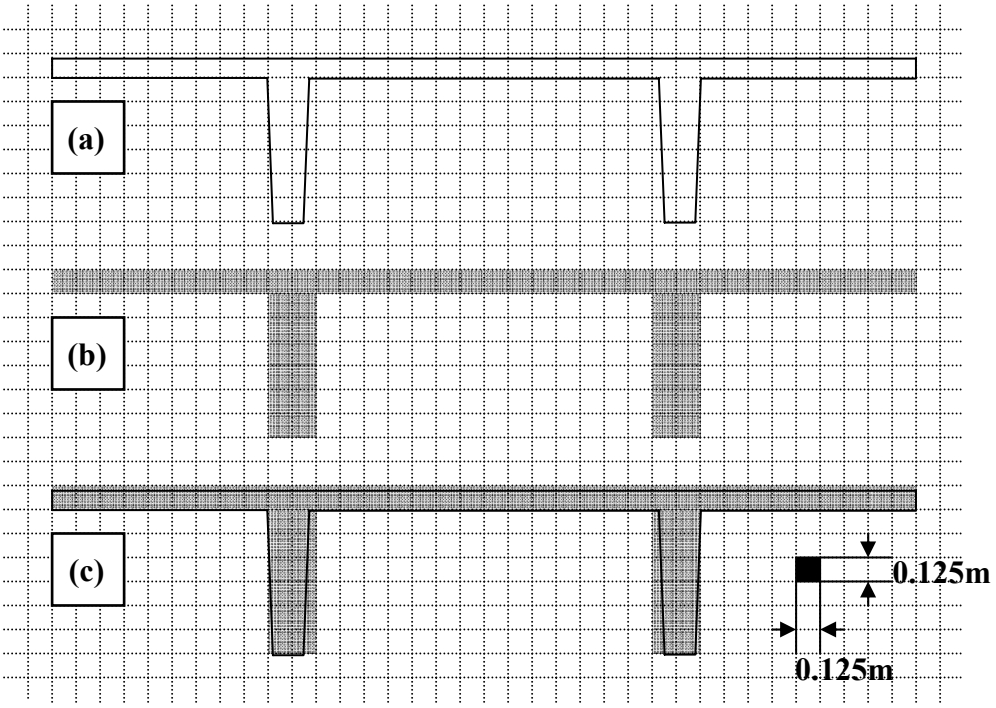

Figure 3-17: Double-tee approximation for 0.125m cell size. (a) Actual 15DT34; (b) 0.125m approximation; (c) Overlay of actual and 0.125m approximation.

All other elements: columns, corbels, floor height, etc., also adhere to the 0.125m mesh, and are approximated to the nearest 0.125m from the as-built drawings. Figures 3-18 through 3-23 show dimensioned drawings of the model used for the FDS analyses.

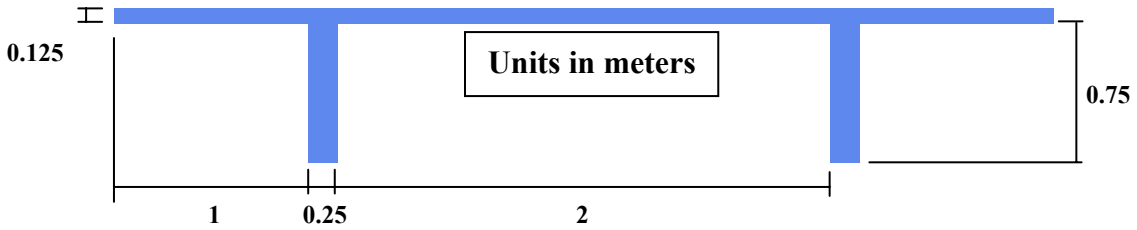

Figure 3-18: Single double-tee approximation used in the FDS model with dimensions shown.

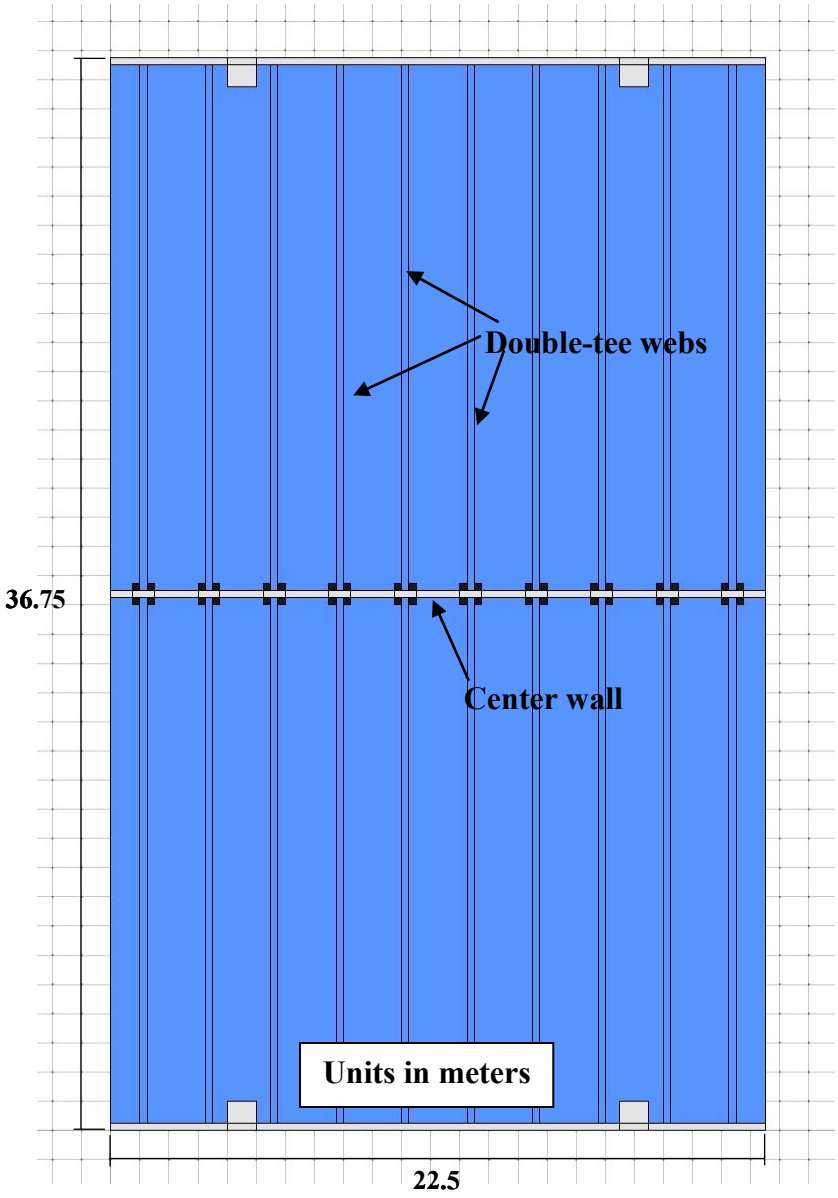

Figure 3-19: Plan view of FDS model.

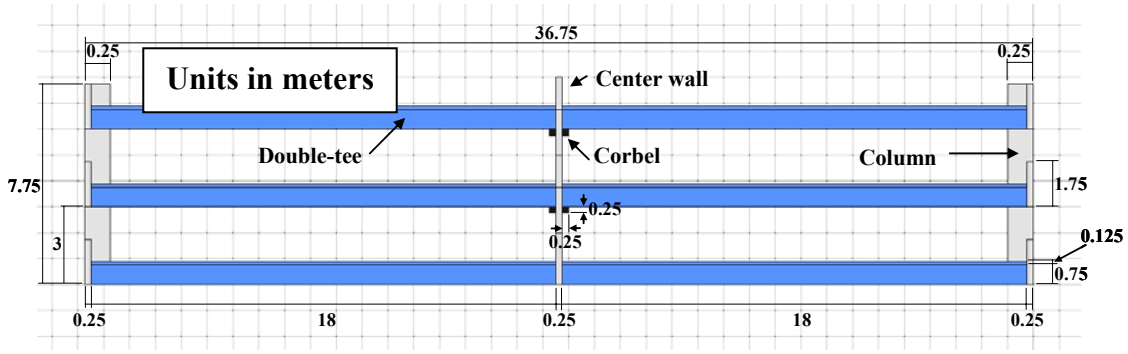

Figure 3-20: East-west elevation view of FDS model with level floor elevation.

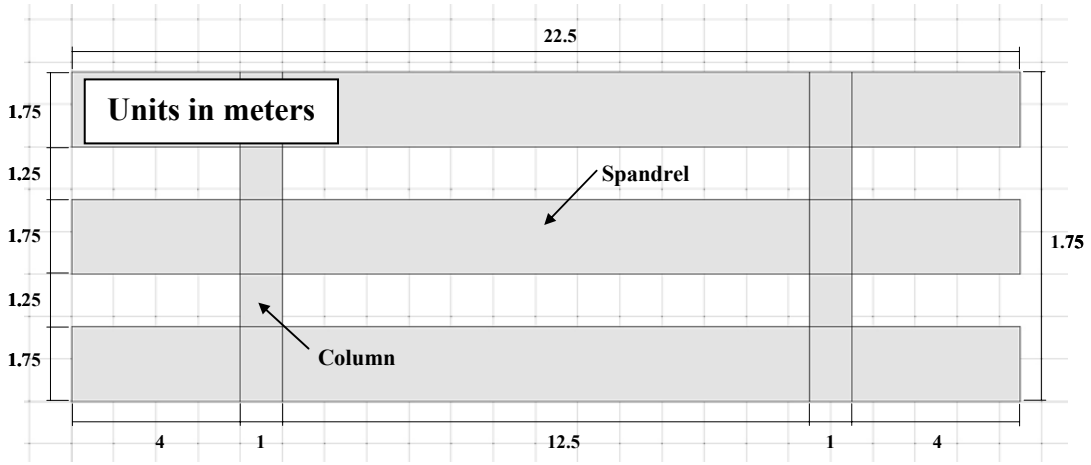

Figure 3-21: North-south elevation view of FDS model showing outer spandrels and columns.

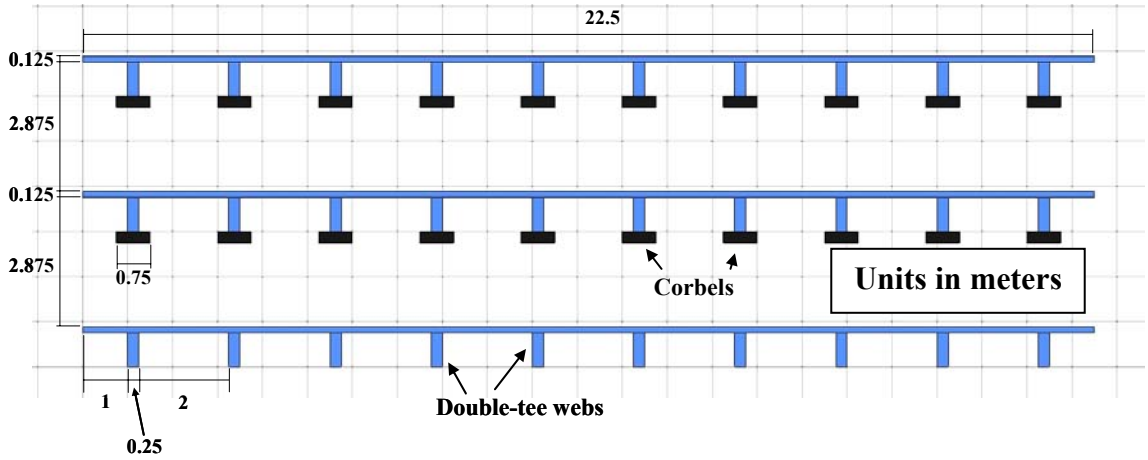

Figure 3-22: North-south elevation view of FDS model showing double-tees and corbels.

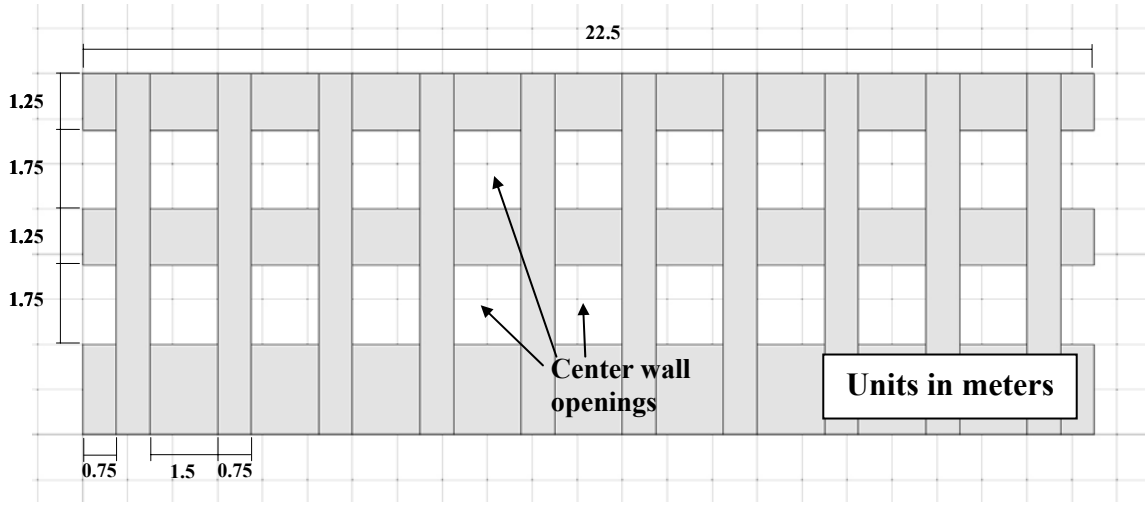

Figure 3-23: North-south elevation view of FDS model showing center wall.

3.4 Vehicle Model

Like the approximations that were made to create the model of the parking garage, the vehicle model geometry was also simplified in order to conform to the 0.125m mesh and to match the fire behavior exhibited during actual testing performed by Khono et al. (2004). The vehicle model is intended to represent a typical midsize passenger vehicle, and all surfaces in the model are considered to be inert. The dimensions are approximations of a 2004 Ford Taurus. Other vehicles in this class include: Toyota Camry, Honda Accord, Dodge Stratus, and BMW 5-Series.

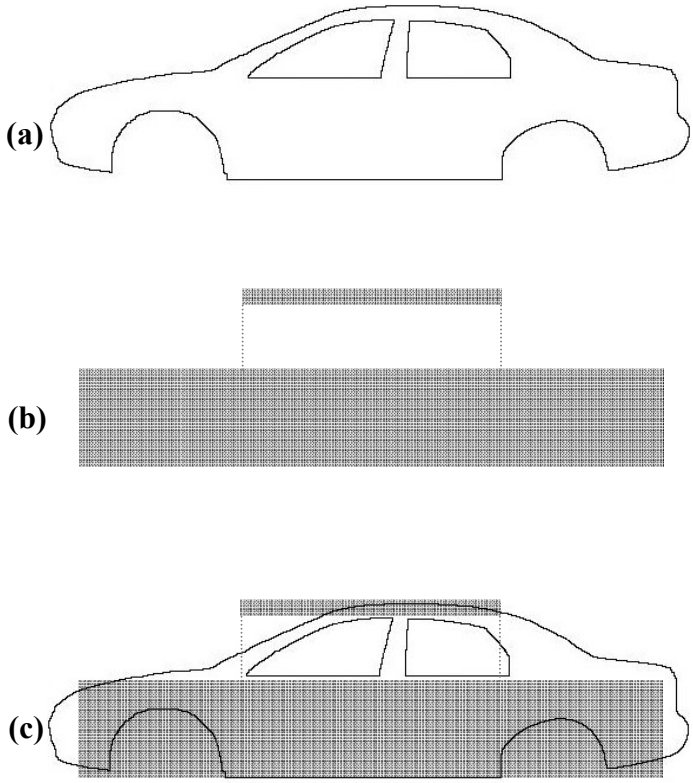

Figure 3-24: Vehicle model geometry: (a) Actual outline of a 2000 Ford Taurus; (b) 0.125m approximation used for FDS modeling; (c) Overlay of (a) and (b).

As shown in Figures 3-24 and 3-25, the body of the vehicle is approximated by a rectangular prism, 4.5m long, 1.75m wide, and 1m high. A 0.125m thick plate 1.75m long and 1.5m wide is centered 0.5m over the body to represent the roof of the cab of the vehicle.

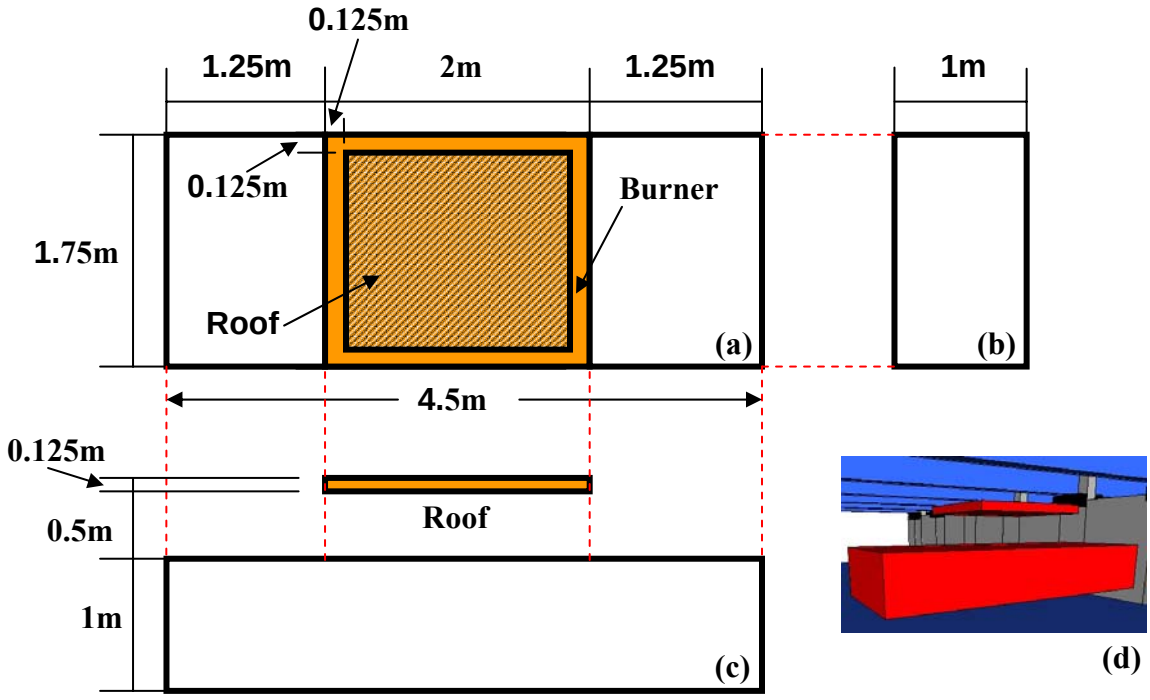

Figure 3-25: Dimensioned drawings of burning vehicle model: (a) Plan view; (b) Front/rear elevation view; (c) Side elevation view; (d) PyroSim screenshot of burning vehicle model against center wall with opening position 3.

The heat flux records for Vehicles 1 and 2 are discussed in Section 3.2.4 and shown in Figure 3-15. Vehicle 1 is an early 1990's Toyota 4Runner that is designated as 3000cc 4WD No.2 in the data obtained from Khono et al. Two distinct peaks are observed at approximately 6 and 25 minutes of 3000 and 5100 kW respectively. The area under the time-heat release curve is defined as the total energy output recorded during the analysis, which for this vehicle is 7387 MJ. Vehicle 2 was a full sized Mercedes sedan. The heat release increases from 0 to 10 minutes to about 2500 kW, plateaus from 10 to 30 minutes at about 2500 kW, and peaks at about 6700 kW at about 37 minutes before dropping off rapidly. The total energy output and is 8110 MJ for this vehicle.

The fire is modeled in FDS as a flat surface called a burner, and is distributed over the area that would be taken up by the cab in a real vehicle as shown in the model. The burner was modeled as a flammable solid vent with a given maximum heat flux. The actual heat flux was varied by input of a table of fractions of that maximum heat flux. This table represented one of the eight real fire heat flux records provided by Khono et al.

In order to make sure that the FDS vehicle model was a reasonably accurate representation of the vehicle fires being modeled, the images of the projected flame pattern were captured from PyroSim and compared to photos from the actual fire analysis

of the 3000cc vehicle in Khono et al. (See Figure 3-26 and 3-27). It is seen that, while the shape of the flame is different, the location and size match quite well. This, in addition to the identical heat flux file, were enough to be confident of the vehicle model for the objectives of this project.

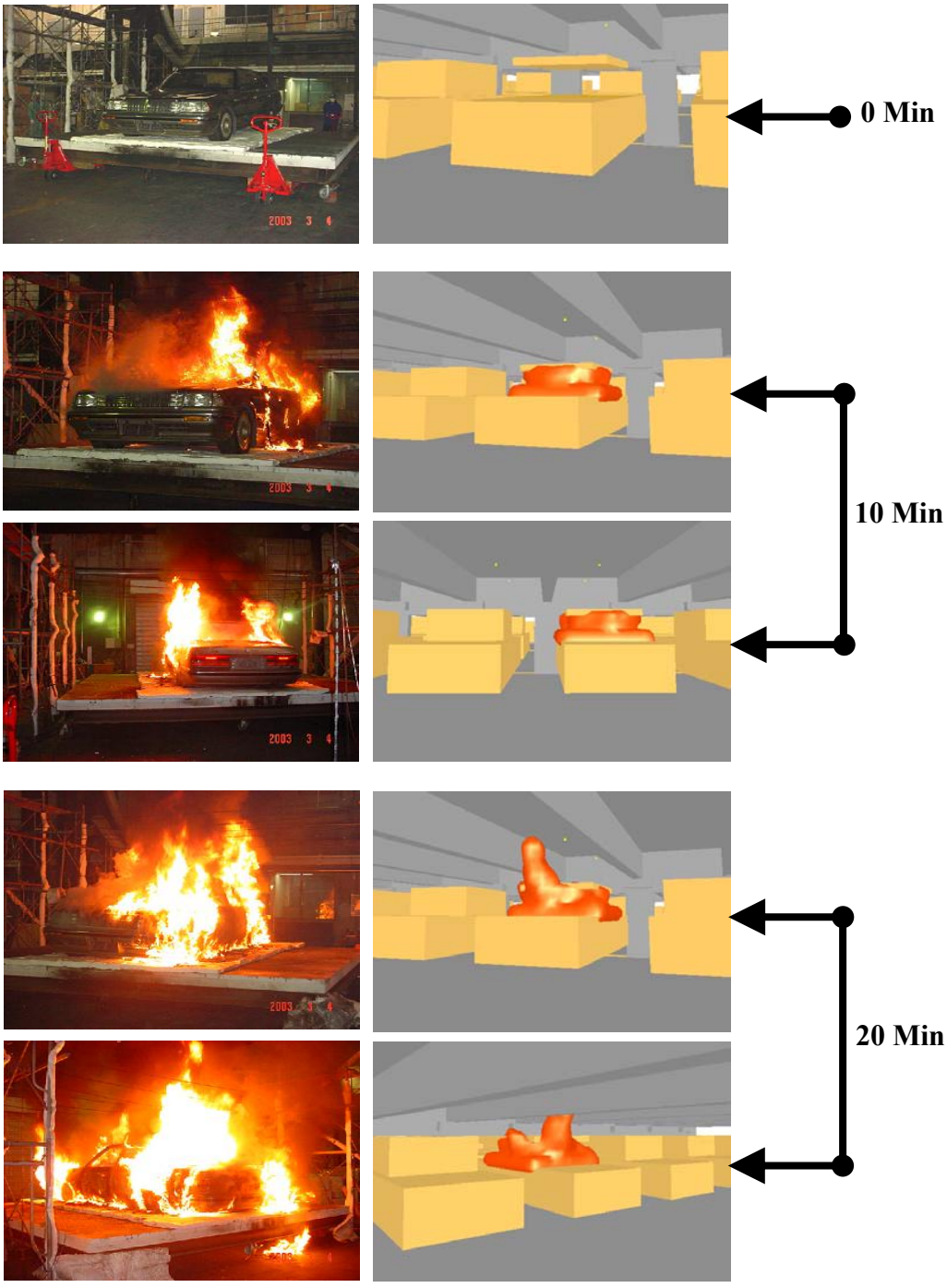

Figure 3-26: Comparison of actual 3000cc No. 2 fire analysis from Khono et al. to FDS vehicle fire analysis using simplified vehicle model at 0, 10, and 20 minutes.

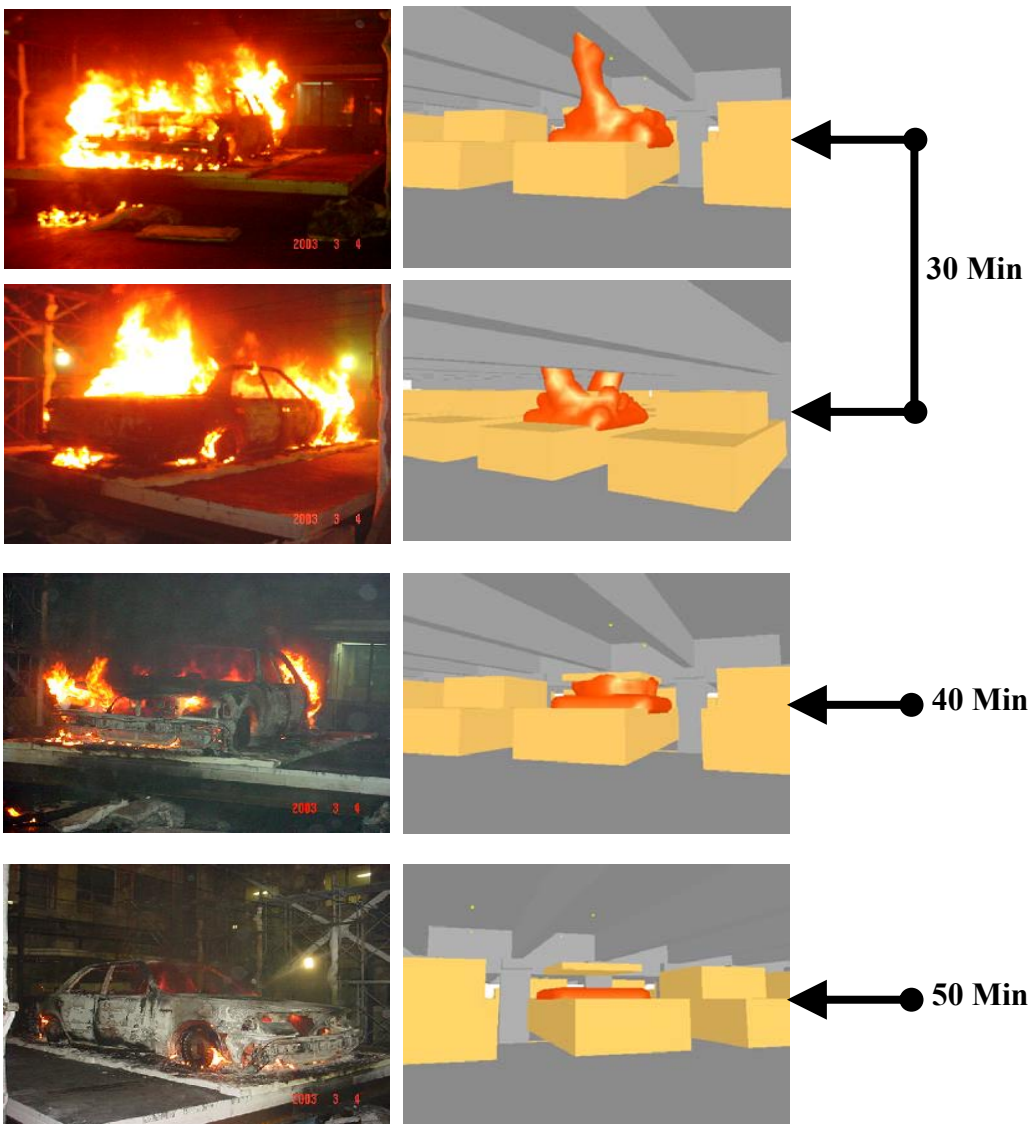

Figure 3-27: Comparison of actual 3000cc No. 2 fire analysis from Khono et al. to FDS vehicle fire analysis using simplified vehicle model at 30, 40, and 50 minutes.

3.5 Analysis Parameters

The following sections describe the parameters used for the FDS analyses. They are presented in a format that would allow the reader to move through the various menus and tabs in PyroSim and enter these specifications as written.

3.5.1 Concrete Material Properties

The entire model of the parking garage was assigned the properties of concrete as explained below.

Surface Type: Non-Flammable Solid
Properties:

Emmisivity: 0.6

Backing: Exposed – FDS allows three backing conditions: (1) *Air-gap*, which is used for hollow walls such as gypsum board over wood studs. (2) *Insulated*, which is used for similar situation as the Air-gap condition but includes insulation in the void. In both of these first two cases, FDS does not compute heat transfer through the obstruction. (Note: Any solid object in FDS is referred to as an obstruction.) (3) *Exposed*, which is used when the back of the obstruction is exposed and allows a one dimensional heat transfer though the thickness of the obstruction as long as the obstruction is only one cell thick. If the backing-exposed obstruction is more than one cell thick, FDS assumes that heat does not transfer through the obstruction similar to the air-gap and insulated cases.

Boundary Conditions:

Surface Type: Thermally Thick – FDS allows four thermal boundary conditions, fixed temperature solid surface, fixed heat flux solid surface, thermally thick solid, or thermally thin sheet. The thermally thick condition allow for the user to prescribe thermal properties of the material.

Thermal Conductivity: Apply a Ramp – The thermal conductivity of concrete varies with temperature. (See Figure 3-28).

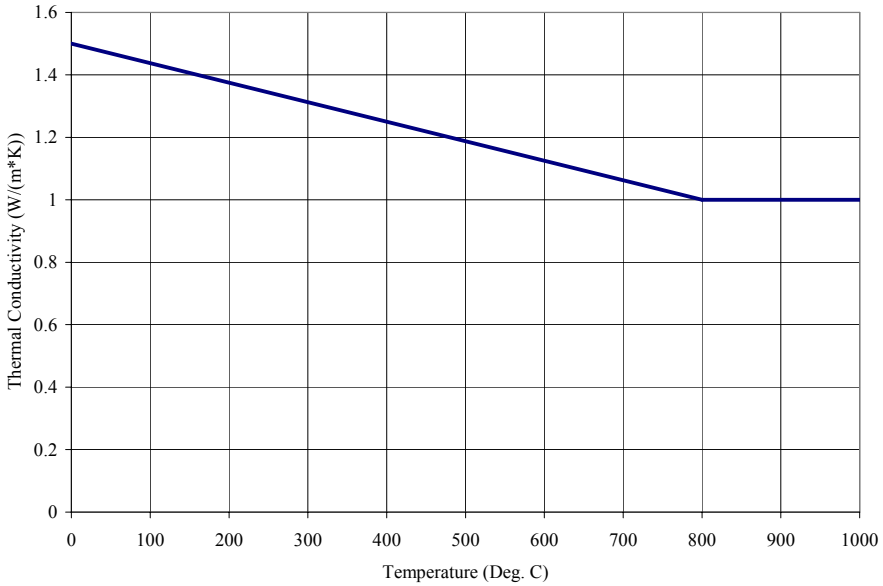

Figure 3-28: Thermal conductivity of concrete (Wang, 2002).

Specific Heat: Apply a Ramp – The specific heat of concrete also varies with temperature. (See Figure 3-29)

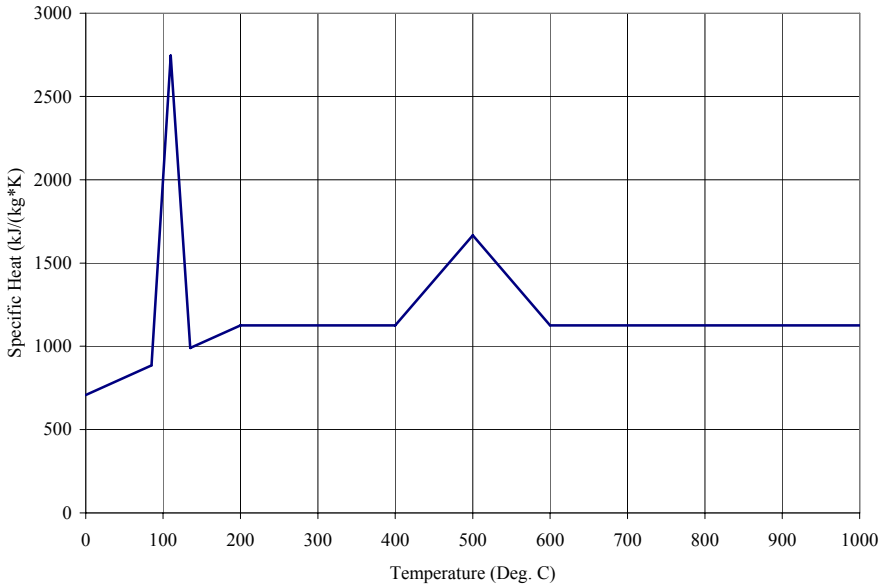

Figure 3-29: Specific heat of concrete (Wang, 2002).

Density: 2100.00 kg/m3

3.5.2 FDS Analysis Parameters

In addition to the material properties, there are a number of parameters that must be selected in order to completely set up the FDS fire analysis.

Time:

Duration: 3600 seconds – The duration of the single vehicle FDS analysis was chosen as 3600 seconds (1 hour) because all of the vehicle burn analyses that the HRR data were taken from are essentially over at about one hour. The multiple vehicle burns were constructed of a series of 3600 second single vehicle burns with a ΔT offset of 12 minutes (720 seconds). 12 minutes was chosen because the fire SPREAD in both Steinert and Mangs generally fell within 4 to 15 minutes. Again, like the vehicle fire records, the literature did not provide enough data to point to a conclusive ΔT, and a choice was made to estimate the time at 12 minutes.

Initial Time Step: 1E-02 seconds – This is the FDS solver default value.

Number of output frames: 1000 – This is the FDS default value.

Environment:

Ambient Temperature: 20 degrees C – This is the FDS default value, but is also a standard value used in many analyses.

Ambient Pressure: 1.01325E5 – This is the FDS default value, but is also a standard value representing atmospheric pressure at sea level.

Initial Wind Velocity: No wind was included in this study.

Simulator:

Non-Isothermal Calculation (YES)

Enable Radiation Transport Solver (YES) – In FDS, one has the option of turning off the radiation transport solver within the program in order to speed up compute times if the radiation quantity is not needed. For this project radiation was a critical computed quantity, thus the solver was turned on.

Simulation Type: Large Eddy (LES) – FDS can run fluid dynamics calculations using either Direct Numerical Simulation, which is only useful for very fine meshes (usually 1mm or less), and Large Eddy Simulation. Large Eddy Simulation was chosen for this project.

Boundary Conditions:

Boundaries for the model are defined in the FDS model as large, open vents that allow heat and combustion materials to exit the model but not return. They define the extents of the computational domain and are placed on all six sides of the model.

3.5.3 Multi-Processor Computing with FDS

Multi-blocking, or the use of multiple computer processors to run an FDS analysis significantly decreases the amount of time required to run each model. Multi-blocking divides the model into essentially separate sections that are coupled together in the FDS code. Each section or 'block' is run on a separate processor, so a model of 2000 cells run on 4 processors might be blocked evenly into 4 blocks of 500 cells. Uneven multi-blocking is also possible and may be used to create finer meshes in critical sections of a model while using more coarse meshes in other portions. A thorough explanation of multi-blocking schemes is available in the FDS User's Guide, and Minkowycz (2000) also discusses the mathematical implications of CFD model division.

It is important to note that multi-blocking in FDS introduces an error that is not well understood. The source of the error appears to be the heat transfer at the boundaries of each block from one block to the next because the heat transfer calculations within each cell of a mesh are more accurate than from one block to the next. These errors are affected by the aspect ratio of the block itself, though how and to what extent are also unknown. This is not a problem that is limited to FDS but appears in many multi-blocking CFD schemes. The error may be reduced by overlapping the blocks by several cells and averaging the values at the cell boundaries within the overlap. This solution is not possible with the FDS software as written, however, and therefore was not used for this project.

With the previous discussion in mind, the blocking scheme for the model was chosen to be simple while trying to keep block boundaries away from direct contact with flame wherever possible. Eight processors were available on the Hades cluster, so the model was divided into eight blocks as shown in Figure 3-30. It should be noted that the block dimensions, and consequently aspect ratio, remain unchanged from one model to the next to avoid compounding the error discussed previously. The placement of the blocks, however, does change from the models with level floor elevation to those with staggered floor elevations.

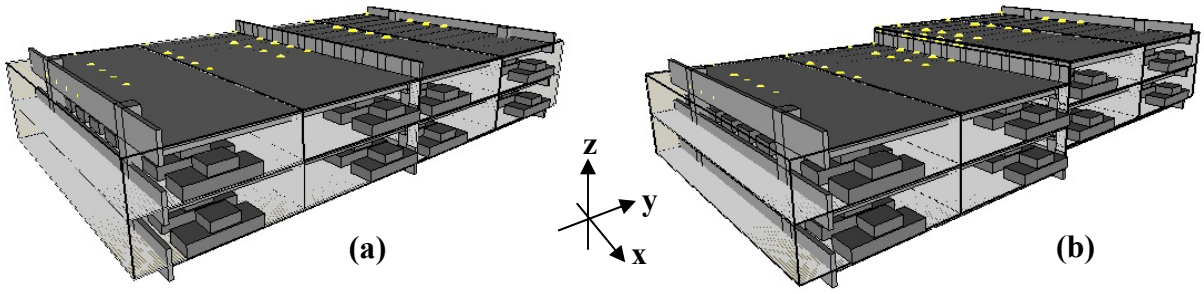

Figure 3-30: Blocking layout for FDS models ((a) Analysis 1-4, 9; (b) Analysis 5-8) 2 blocks in the z-direction, 4 blocks in the y-direction, and 1 block in the x-direction.

In order to accommodate the dimensions of the model, and conform to the FDS computational constraints, the block dimensions are restricted to cell multiples of 2, 3, and 5 because of the Fast Fourier Transforms used in part of the calculations. As a result, each block is 180 cells in the x-direction, 80 cells in the y-direction, and 24 cells in the z-direction for a cell subtotal of 345,600 cells for each block and a total of 2,764,800 cells for the entire model.

3.6 Instrumentation of the Model

In FDS analyses, "instrumentation" refers to the specification of what analysis output is saved. There are three specific ways that the model is instrumented: thermocouples and slice files to capture gas temperature, and boundary files to capture heat flux into solids.

3.6.1 Gas Temperature: Thermocouples and Slice Files

The term 'thermocouple' is used in FDS as a generic term to describe a sensor that records gas data at a specific point. For this project, thermocouples were placed throughout the model at key locations and set to capture gas temperature data. A diagram detailing the location of the thermocouples is shown in Figure 3-32 and Table 3-2 and 3-3 give a complete list of thermocouple coordinates.

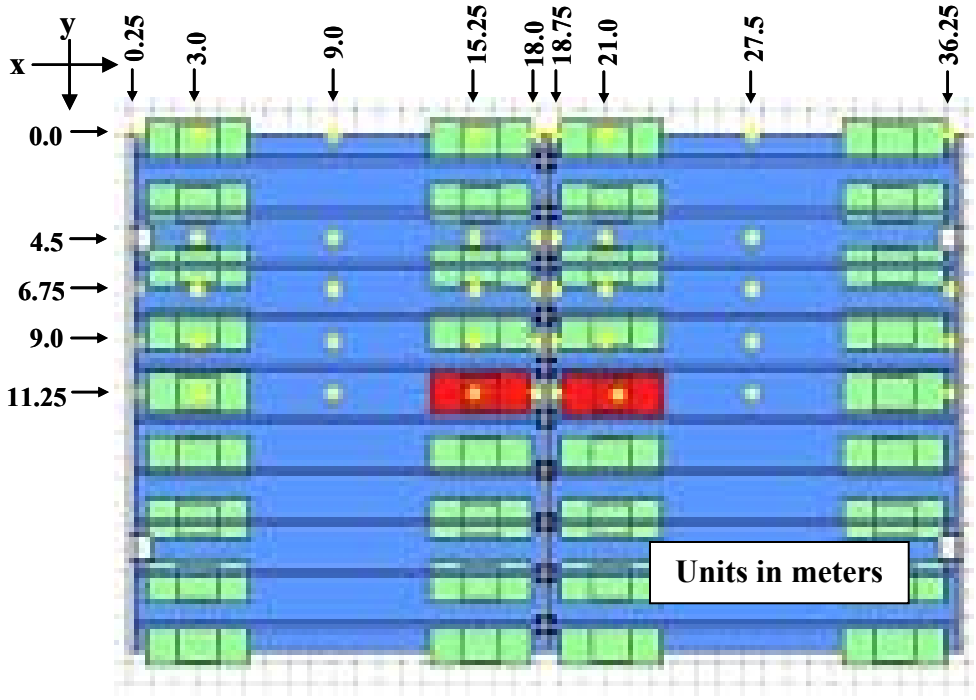

Figure 3-31: Plan view of thermocouple locations at z = 3.625 and 6.625 in Analyses 1-4, 9; and at z = 3.625, 5.125, 6.625, and 8.125 in Analysis 5-8 (0.125m below bottom of double-tee deck.).

Thermocouple	X(m)	Y(m)	Z(m)	Thermocouple	X(m)	Y(m)	Z(m)	Thermocouple	X(m)	Y(m)	Z(m)
1	11.25	0.25	3.625	***31***	4.5	15.25	3.625	***61***	9	21	6.625
2	11.25	3	3.625	***32***	4.5	18	3.625	***62***	9	27.5	6.625
3	11.25	9	3.625	***33***	4.5	18.75	3.625	***63***	9	36.25	6.625
4	11.25	15.25	3.625	***34***	4.5	21	3.625	***64***	6.75	0.25	6.625
5	11.25	18	3.625	***35***	4.5	27.5	3.625	***65***	6.75	3	6.625
6	11.25	18.75	3.625	***36***	4.5	36.25	3.625	***66***	6.75	9	6.625
7	11.25	21	3.625	***37***	0	0.25	3.625	***67***	6.75	15.25	6.625
8	11.25	27.5	3.625	***38***	0	3	3.625	***68***	6.75	18	6.625
9	11.25	36.25	3.625	***39***	0	9	3.625	***69***	6.75	18.75	6.625
10	9	0.25	3.625	***40***	0	15.25	3.625	***70***	6.75	21	6.625
11	9	3	3.625	***41***	0	18	3.625	***71***	6.75	27.5	6.625
12	9	9	3.625	***42***	0	18.75	3.625	***72***	6.75	36.25	6.625
13	9	15.25	3.625	***43***	0	21	3.625	***73***	4.5	0.25	6.625
14	9	18	3.625	***44***	0	27.5	3.625	***74***	4.5	3	6.625
15	9	18.75	3.625	***45***	0	36.25	3.625	***75***	4.5	9	6.625
16	9	21	3.625	***46***	11.25	0.25	6.625	***76***	4.5	15.25	6.625
17	9	27.5	3.625	***47***	11.25	3	6.625	***77***	4.5	18	6.625
18	9	36.25	3.625	***48***	11.25	9	6.625	***78***	4.5	18.75	6.625
19	6.75	0.25	3.625	***49***	11.25	15.25	6.625	***79***	4.5	21	6.625
20	6.75	3	3.625	***50***	11.25	18	6.625	***80***	4.5	27.5	6.625
21	6.75	9	3.625	***51***	11.25	18.75	6.625	***81***	4.5	36.25	6.625
22	6.75	15.25	3.625	***52***	11.25	21	6.625	***82***	0	0.25	6.625
23	6.75	18	3.625	***53***	11.25	27.5	6.625	***83***	0	3	6.625
24	6.75	18.75	3.625	***54***	11.25	36.25	6.625	***84***	0	9	6.625
25	6.75	21	3.625	***55***	9	0.25	6.625	***85***	0	15.25	6.625
26	6.75	27.5	3.625	***56***	9	3	6.625	***86***	0	18	6.625
27	6.75	36.25	3.625	***57***	9	9	6.625	***87***	0	18.75	6.625
28	4.5	0.25	3.625	***58***	9	15.25	6.625	***88***	0	21	6.625
29	4.5	3	3.625	***59***	9	18	6.625	***89***	0	27.5	6.625
30	4.5	9	3.625	***60***	9	18.75	6.625	***90***	0	36.25	6.625

Table 3-2: Thermocouple locations for level floor elevation analyses (Analyses 1-4, 9).

Thermocouple	X(m)	Y(m)	Z(m)	Thermocouple	X(m)	Y(m)	Z(m)	Thermocouple	X(m)	Y(m)	Z(m)
1	11.25	0.25	3.625	***31***	4.5	15.25	3.625	***61***	9	21	8.125
2	11.25	3	3.625	***32***	4.5	18	3.625	***62***	9	27.5	8.125
3	11.25	9	3.625	***33***	4.5	18.75	5.125	***63***	9	36.25	8.125
4	11.25	15.25	3.625	***34***	4.5	21	5.125	***64***	6.75	0.25	6.625
5	11.25	18	3.625	***35***	4.5	27.5	5.125	***65***	6.75	3	6.625
6	11.25	18.75	5.125	***36***	4.5	36.25	5.125	***66***	6.75	9	6.625
7	11.25	21	5.125	***37***	0	0.25	3.625	***67***	6.75	15.25	6.625
8	11.25	27.5	5.125	***38***	0	3	3.625	***68***	6.75	18	6.625
9	11.25	36.25	5.125	***39***	0	9	3.625	***69***	6.75	18.75	8.125
10	9	0.25	3.625	***40***	0	15.25	3.625	***70***	6.75	21	8.125
11	9	3	3.625	***41***	0	18	3.625	***71***	6.75	27.5	8.125
12	9	9	3.625	***42***	0	18.75	5.125	***72***	6.75	36.25	8.125
13	9	15.25	3.625	***43***	0	21	5.125	***73***	4.5	0.25	6.625
14	9	18	3.625	***44***	0	27.5	5.125	***74***	4.5	3	6.625
15	9	18.75	5.125	***45***	0	36.25	5.125	***75***	4.5	9	6.625
16	9	21	5.125	***46***	11.25	0.25	6.625	***76***	4.5	15.25	6.625
17	9	27.5	5.125	***47***	11.25	3	6.625	***77***	4.5	18	6.625
18	9	36.25	5.125	***48***	11.25	9	6.625	***78***	4.5	18.75	8.125
19	6.75	0.25	3.625	***49***	11.25	15.25	6.625	***79***	4.5	21	8.125
20	6.75	3	3.625	***50***	11.25	18	6.625	***80***	4.5	27.5	8.125
21	6.75	9	3.625	***51***	11.25	18.75	8.125	***81***	4.5	36.25	8.125
22	6.75	15.25	3.625	***52***	11.25	21	8.125	***82***	0	0.25	6.625
23	6.75	18	3.625	***53***	11.25	27.5	8.125	***83***	0	3	6.625
24	6.75	18.75	5.125	***54***	11.25	36.25	8.125	***84***	0	9	6.625
25	6.75	21	5.125	***55***	9	0.25	6.625	***85***	0	15.25	6.625
26	6.75	27.5	5.125	***56***	9	3	6.625	***86***	0	18	6.625
27	6.75	36.25	5.125	***57***	9	9	6.625	***87***	0	18.75	8.125
28	4.5	0.25	3.625	***58***	9	15.25	6.625	***88***	0	21	8.125
29	4.5	3	3.625	***59***	9	18	6.625	***89***	0	27.5	8.125
30	4.5	9	3.625	***60***	9	18.75	8.125	***90***	0	36.25	8.125

Table 3-3: Thermocouple locations for staggered floor elevation analyses (Analyses 5-8).

Slice files in FDS are used to gather the same information as thermocouples, but instead of outputting that data in a text file for a specific point, the slice file is used to graphically display the data on a specific plane (or slice). In this project, slice files were chosen at key planes in the model to gather gas temperature. These planes match up with several of the key thermocouple locations to provide continuity. (See Figure 3-32)

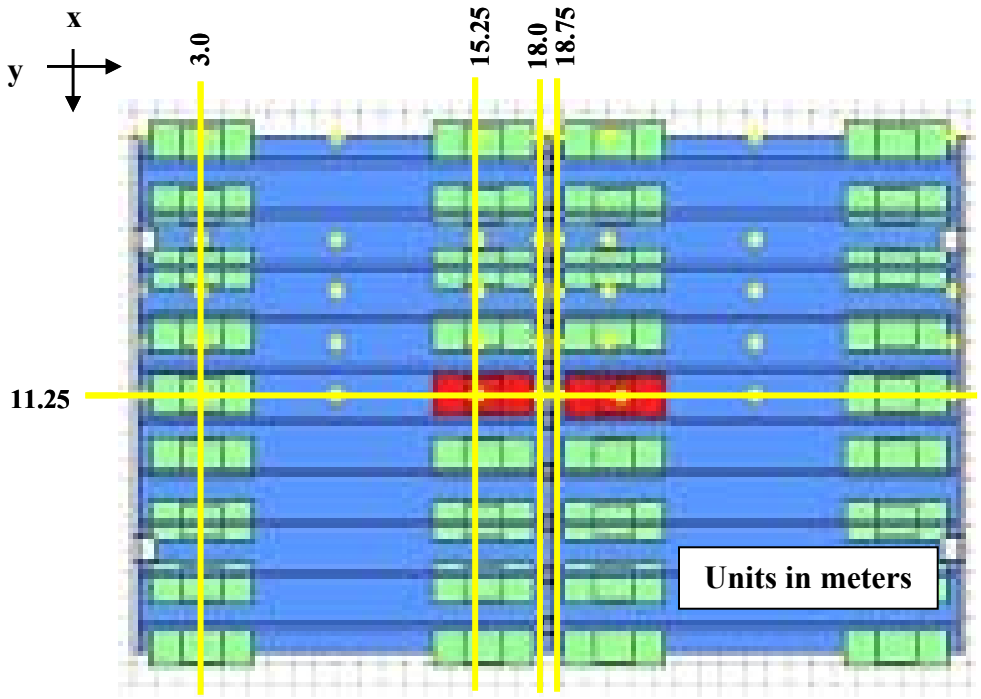

Figure 3-32: Plan view of slice file locations.

3.6.2 Heat Flux: Boundary Files

Heat flux data is gathered in FDS by using boundary files. These files record heat flux into solids using the specified material properties. For this project, heat flux data into solid surfaces were gathered for all surfaces in the model at 30 second intervals. A Fortran 90 program written at NIST called fds2ascii was then used to convert heat flux data at specific points of interest into text files that are used for analysis and comparison of the models. The procedure for non-linear heat flux analysis is explained in Section 3.7.

3.7 Non-Linear Heat Flux Analysis Procedure

In order to more fully understand the implications of vehicle fires as loads imposed on concrete structural members, knowledge of the temperature distribution within the member is critical to further analysis. Time-temperature curves, which represent the gas temperature at a specific point are useful for comparing different fires, but structural integrity is directly tied to the heat flux into the solid and the resulting temperature rise of the material. In the case of double-tees, the temperatures at the levels of the prestressing strands are particularly important, since high temperatures at those locations could mean a significant behavior degradation and modification of the stress-strain curve. Using the

net heat flux output from FDS and a non-linear heat transfer model based on the procedures explained in Okasha (2006) (See Section 3.7.2), the temperature distribution through the web of the double-tee at several locations throughout the structure is evaluated.

3.7.1 FDS Model

Net heat flux into a solid surface is one of the outputs that was taken from each of the FDS models for this project. The fds2ascii program discussed previously takes the raw data from the analysis and outputs net heat flux specified nodes using a tributary area for each node as shown in Figure 3-33.

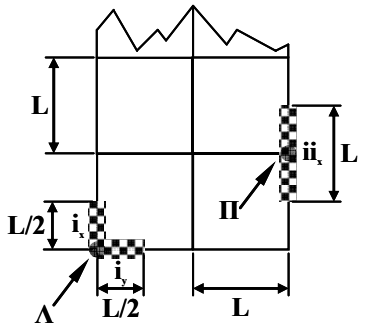

Figure 3-33: fds2ascii element and node diagram.

The example model in Figure 3-33 is made up of square elements with side length L and a unit thickness. Because nodes on corners such as Λ have surfaces on more than one plane, separate net heat flux files are created for each of the surfaces the node represents. In the case of Figure 3-33, Λ represents surfaces i_x and i_y, which both have a tributary area of L/2. Nodes in the middle of a surface such as Π represent single surfaces such as ii_x with a tributary area of L.

For the model used in this project, the web of the double-tee is modeled as explained previously with cubic elements with a side length of 0.125m. The slab is one element thick and the web is six elements deep by two elements wide. The FDS net heat flux outputs are recorded at seven nodes (labeled A-G) on the web of one of the double-tees as shown in the model in Figure 3-34.

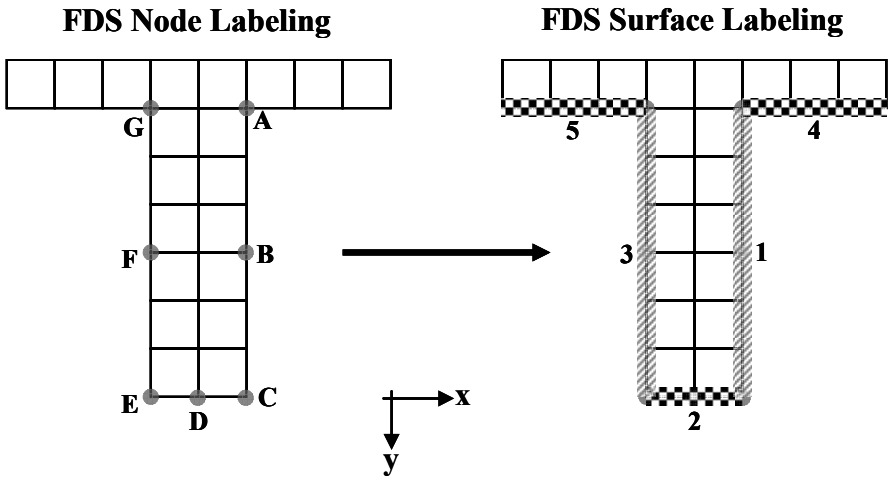

Figure 3-34: FDS double-tee model for heat flux averages with nodes labeled (left) and surfaces labeled (right).

To create an input file for the ABAQUS analysis, the nodal heat flux values on each surface are averaged to get a uniform net heat flux for each for surfaces 1-5. Table 3-4 distinguishes which nodes are used for those surfaces.

Surface:	**Nodes:**		
1	A_x	B_x	C_x
2	C_y	D_y	E_y
3	E_x	F_x	G_x
4	A_y		
5	G_y		

Table 3-4: Node and surface breakdown for FDS/ABAQUS heat transfer analysis.

The goal of the heat transfer analysis is to estimate the heat distribution within the double-tee web, therefore the net heat flux data is gathered for nodes on the web itself. It is seen from Figure 3-35 to 3-37 that the net heat flux on any specific surface in the model is essentially uniform, which allows the average of nodal heat flux values to be used. Surfaces 4 and 5 are included in the model to more accurately represent the actual double-tees and potential heat transfer from the slab down into the web.

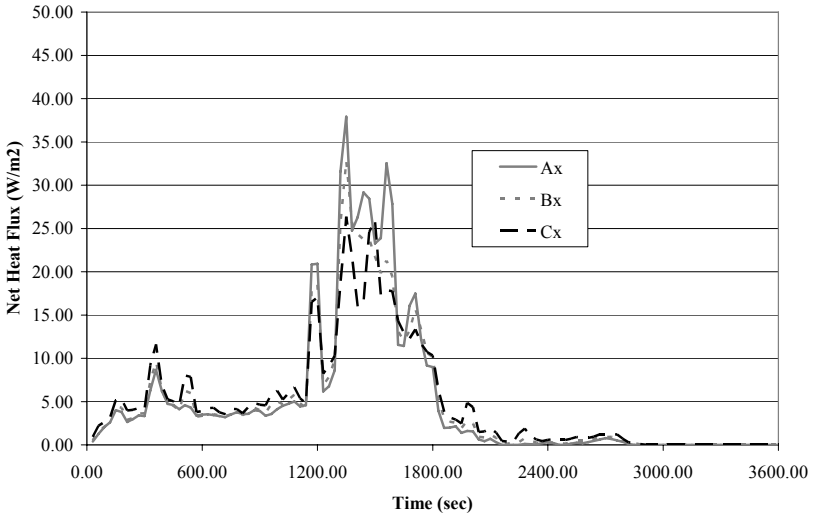

Figure 3-35: Heat flux on Surface 1 for Analysis 1.

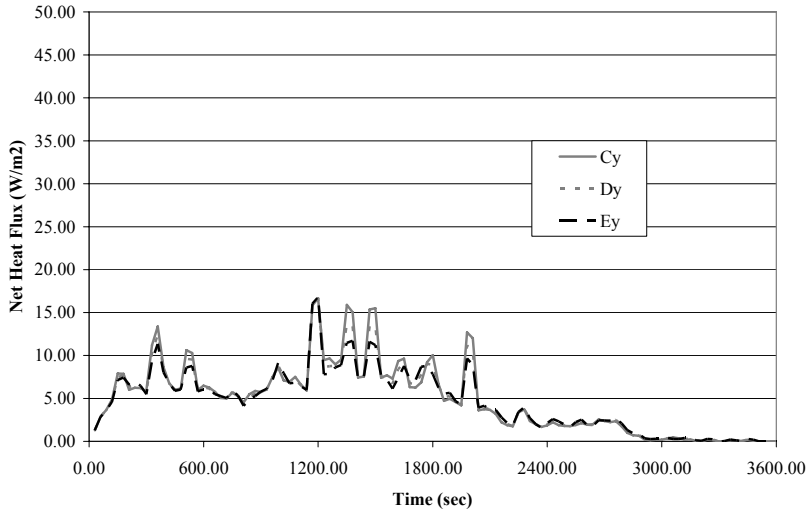

Figure 3-36: Heat flux on Surface 2 for Analysis 1.

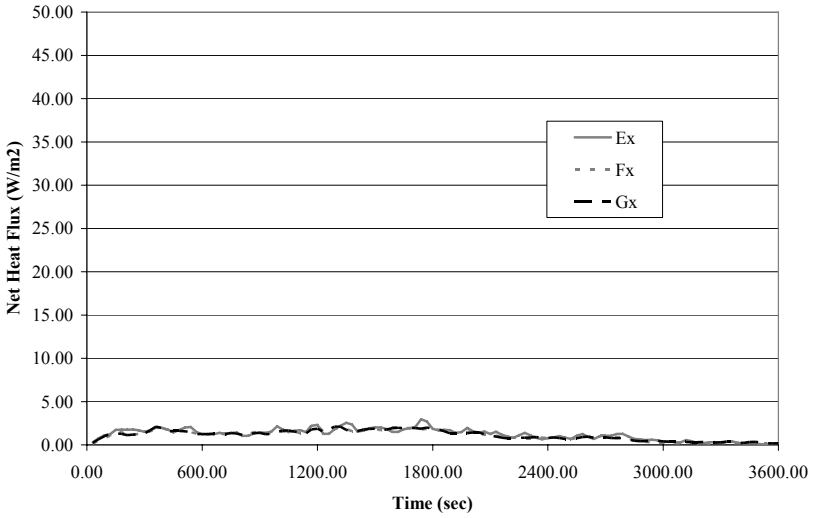

Figure 3-37: Heat flux on Surface 3 for Analysis 1.

The net heat flux averages for each surface are then used as input for the ABAQUS model explained in the next section.

3.7.2 ABAQUS Model

The non-linear finite element transient heat transfer analysis used in this project for purposes of results analysis was performed using the ABAQUS non-linear finite elements software package. A model of the double-tee web was constructed by Dr. Byoung-Jun Lee based on the procedures explained in Okasha (2006). The following section provides details of the model.

A three-dimensional unit-thickness slice of a double-tee web was constructed based on the dimensions of the 15DT34 double-tee from the PCI handbook and the 188-S strand pattern (18 strands of 8/16 inch diameter). The element type was a solid (continuum), first order (eight nodes), hexahedra (brick) element called DC3D8 in ABAQUS with full integration. The element mesh configuration is eight elements across the web and four through the thickness of the slab. This is finer than the configuration used in Okasha, which was four elements across the web and three through the slab thickness and was based on a convergence study for accuracy. The trend from the convergence study was that the finer mesh with similar element aspect ratio resulted in higher accuracy; therefore the configuration used for this project is at least as accurate as that used for Okasha. Figure 3-38 shows an elevation view of the ABAQUS model with dimensions and elements shown.

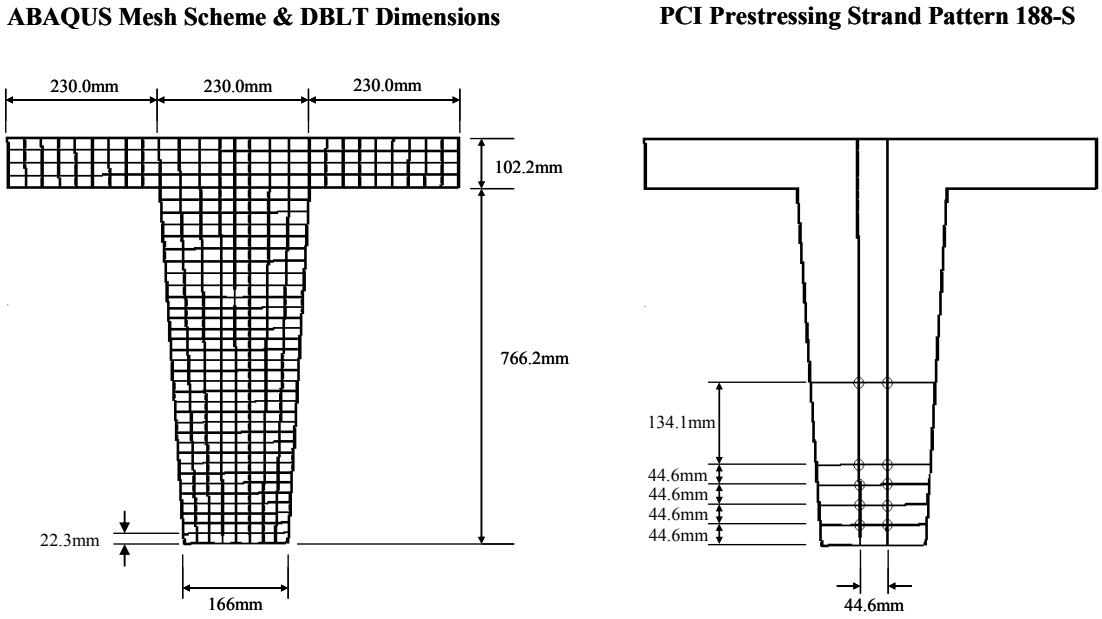

Figure 3-38: ABAQUS mesh scheme and double-tee model dimensions (left) and PCI prestressing strand pattern 188-S (right).

The element meshing configuration results in nodes located at the levels of the prestressing strands in the web. This allows nodal temperatures to be recorded directly and used in Chapter 5 to analyze the potential changes to the steel strength because of elevated temperatures.

The difference between the heat transfer analysis in Okasha and this project is the load input. Okasha uses the standard ASTM E119 time-temperature curve as the load, while this project uses the net heat flux output as described in the last section. In this case, the net heat transfer averages from FDS for the five surfaces in the model are defined as field inputs for the ABAQUS (See Figure 3-39). All other parameters are the same, including material and environmental properties, which are identical to those explained in Section 3.2.1.

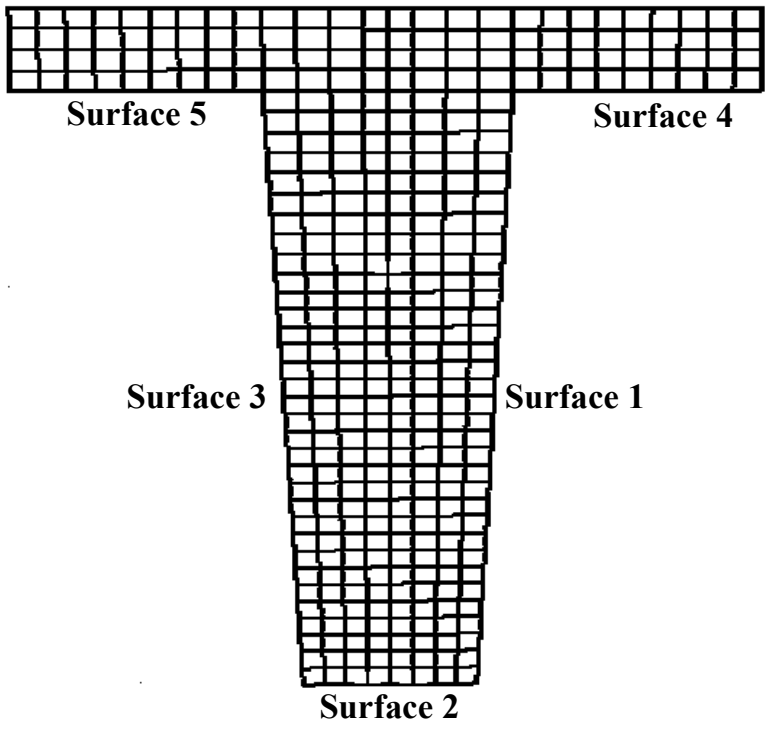

Figure 3-39: Surfaces 1-5 correlation between FDS and ABAQUS models.

CHAPTER 4

ANALYSIS RESULTS

This chapter presents detailed results of each of the analyses. An explanation of the analysis procedure is described in Section 4.1. Each of the analysis summaries is presented following a similar format, which is explained in Section 4.2. Section 4.3 contains the individual summaries for each of the nine different analyses that were performed.

4.1 Analysis Procedure

This project used several different computer programs to complete each analysis. Figure 4-1 is a flow chart of how the different computer programs were used.

The parking garage model was built using PyroSim, a graphical interface that serves as a preprocessor for FDS. The PyroSim software can be used to directly interface with the FDS software when a single processor is used, but for this project, where multiple processors were used, the PyroSim software was used only to create the input data file for FDS.

Once the FDS data file was created, it was run using the FDS software installed on Hades, an eight-node computing cluster. Hades is comprised of four dual processor machines with two AMD 64-bit processors in each running at 2.4 GHz and 1 GB RAM. Each analysis took between eight and twenty days to complete and progress was monitored via a dedicated computer running Linux Red Hat. After completion of each analysis, the data was backed up on a dedicated hard drive and transferred to computer running Microsoft Windows XP Professional for post-processing.

The thermocouple data for each analysis was processed using Microsoft Excel to create graphs of the time-temperature records. Slice files created by FDS were viewed with Smokeview, a graphical reader for FDS output files. Finally, the heat flux output data required several steps to be usable. First, the FDS heat flux boundary files were processed using the fds2ascii computer program. The heat flux data files were then compiled in Microsoft Excel and processed through ABAQUS using the procedures explained in Section 3.7 of this report.

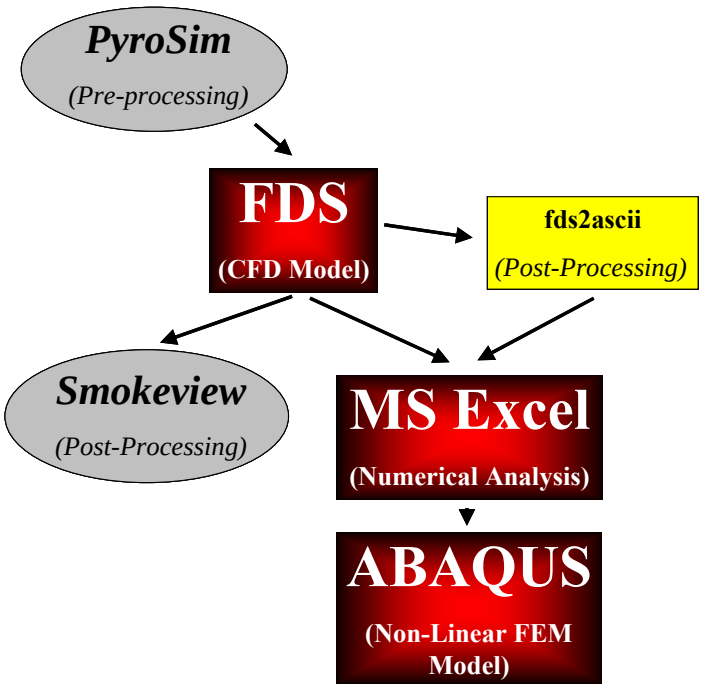

Figure 4-1: Analysis software flow chart.

4.2 Format of Analysis Summaries

Each individual analysis summary is presented in a similar format as described below. The reader should refer to Section 3.3 for the instrumentation plans.

1. A summary of the geometry and fire properties of the model.
2. A description of the heat distribution over the course of the analysis. This section includes several slice file images obtained from Smokeview detailing the heat distribution.
3. A selection of time-temperature records taken at thermocouples throughout each model. The plots presented show the thermocouple records for locations that experienced notable heating.

4.3 Individual Analysis Summaries

The following sections present the results of each of the individual analyses.

4.3.1 Analysis 1: Top Opening Analysis

The geometry of the Analysis 1 model is shown is Figures 4.2 and 4.3. Images are captured from PyroSim, and particular note should be taken of the opening position in the center wall shown in Figure 4.2 as it relates to the double-tee flanges, specifically that the top of the opening is flush with the bottom of the double-tee flange. The only structural obstructions to heat flow through the center wall are small protrusions into the cavity on either side of the openings. The burning vehicle is located on the lower floor of the model and is centered between the double-tee webs in position 23 as shown previously in Figure 3-16.

Figure 4.4 shows the Vehicle 1 fire heat release record used as an input for the FDS analysis for all models except Analysis 4. The record is for an early 1990's Toyota 4Runner that is designated as 3000cc 4WD No.2 in the data obtained from Khono et al. Two distinct peaks are observed at approximately 6 and 25 minutes of 3000 and 5100 kW respectively. The area under the time-heat release curve is defined as the total energy output recorded during the analysis, which for this vehicle is 7387 MJ.

Slice images showing temperature distribution through the structure are shown in Figures 4-5 to 4-10. Images are shown at 10 minute intervals, and the slice location is shown by the diagrams in Figures 4-5 and 4-8.

Figures 4-5 to 4-7 shows a temperature slice located just below the slab above the burning vehicle at z = 3.625m. It is observed that the heat builds up longitudinally between the double-tee webs with relatively little heat spilling over into adjacent double-tee cavities. As shown in the figure, the heat flows largely unimpeded through the center wall. Peak temperature is reached above the burning vehicle.

The second set of images in this series are Figure 4-8 to 4-10, showing a transversely oriented temperature slice located 0.125m from the center wall at y = 18m. This figure further reinforces the data shown in Figures 4-5 to 4-7 that the double-tee webs contain the majority of the heat released from the burning vehicle for the Analysis 1 model.

Time-temperature plots taken from thermocouples throughout the structure are shown in Figures 4-11 to 4-19 and are broken into three series: longitudinal time-temperature plots (Figures 4-3 to 4-15), transverse time-temperature plots (Figures 4-16 to 4-18), and a vertical time-temperature plot (Figures 4-19).

The longitudinal time-temperature plots are shown for thermocouple locations centered between the double-tee webs in the cavity above the burning vehicle. Figure 4-13 shows four thermocouples distributed from y = 0.25m to y = 18m. The highest temperature

recorded was 1019 degrees Celsius at y = 15.25m. Temperatures were generally lower as the distance from the center of the fire increased. Figure 4-14 shows a similar set of thermocouple time-temperature plots to Figure 4-13, but these are shown for the opposite side of the center wall. Once again, the temperature plot is generally lower as the distance from the center of the fire increases. Finally, Figure 4-15, shows two time-temperature curves, one on either side of the center wall. The thermocouple location closer to the fire at y = 18.0m shows slightly higher recorded temperatures than those at y = 18.75m.

The transverse time-temperature plots are shown in Figures 4-16 to 4-18 to show the how the heat spills under the double-tee webs from one cavity to the next. All three figures show that the majority of the heat is generally contained within the cavity above the burning vehicle, but, as the distance from the fire increases, the difference in temperature from one cavity to the next decreases.

The final time-temperature plot is shown in Figure 4-19, which shows the vertical temperature distribution along the center wall from one floor to the next. The two thermocouples are centered between the double-tee webs on above the burning vehicle at y = 18.0m and on both floors at z = 3.625m and 6.625m. Negligible temperature increase is observed on the upper floor.

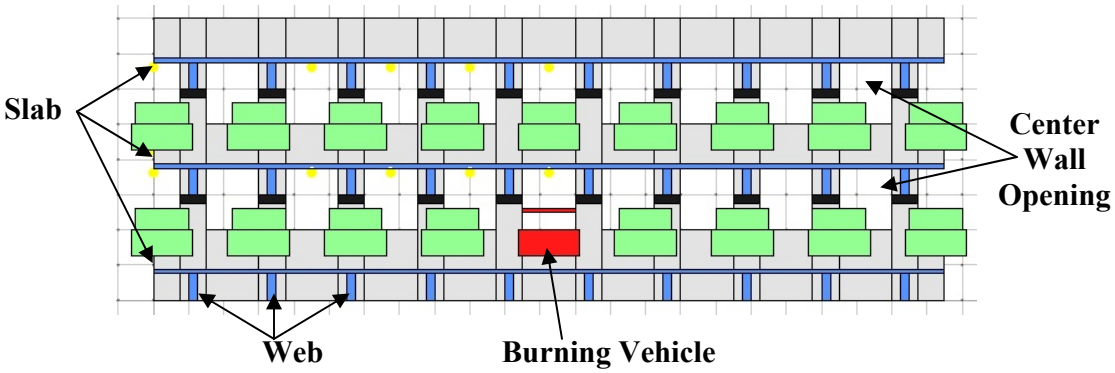

Figure 4-2: View of the center wall of Analysis 1 showing center wall opening position and the burning vehicle centered in between the double-tee stems.

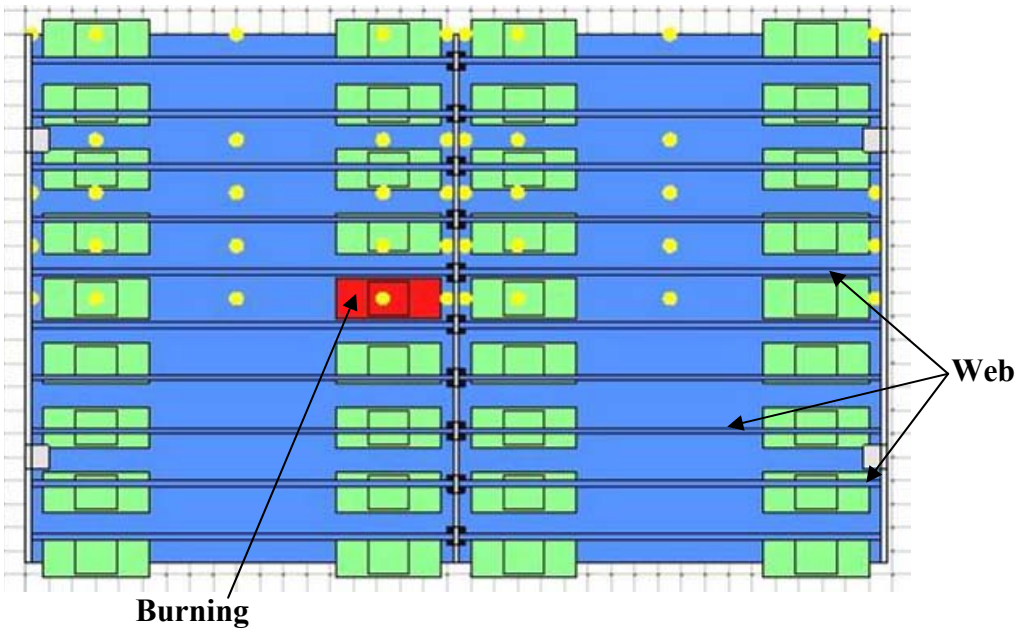

Figure 4-3: Plan view of Analysis 1 showing the burning vehicle position next to the center wall and centered between the double-tee stems.

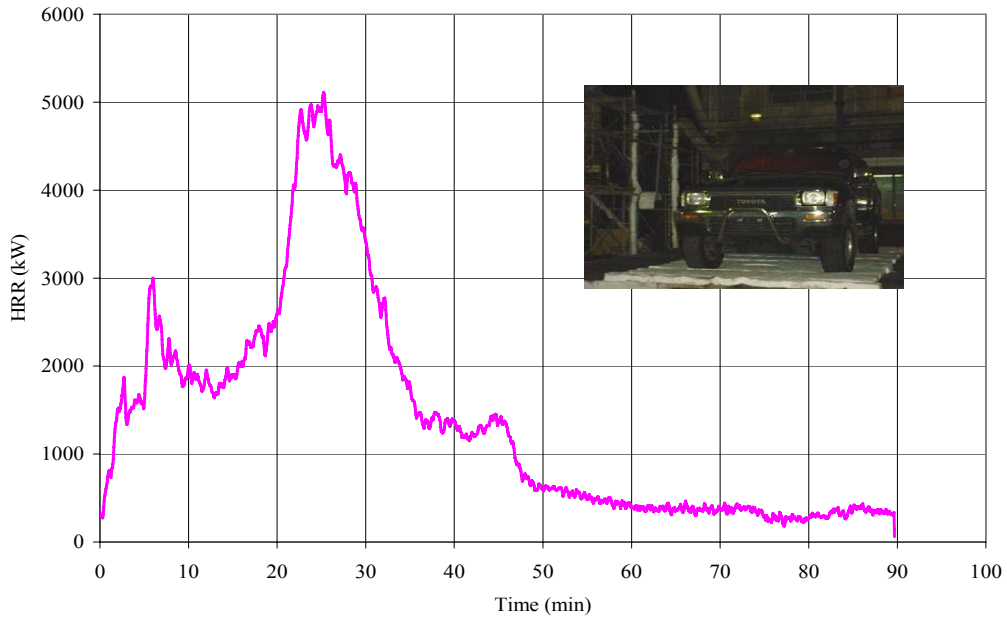

Figure 4-4: Heat release record for vehicle 1.

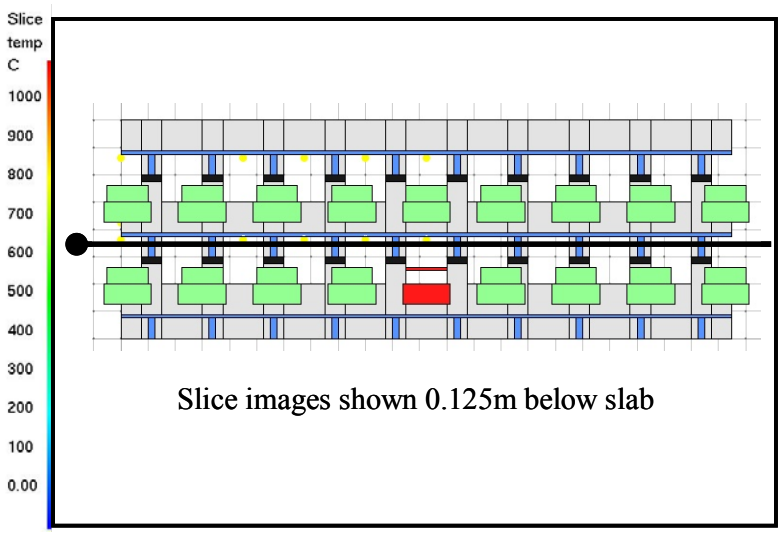

Figure 4-5: Slice images for Analysis 1 showing temperature distribution 0.125m below slab above burning vehicle (z = 3.625m). Images shown at 10 minute intervals (600sec) from time = 10 to 60 minutes (600-3600sec). Temperature scale in degrees Celsius. Continued in Figures 4-6 and 4-7.

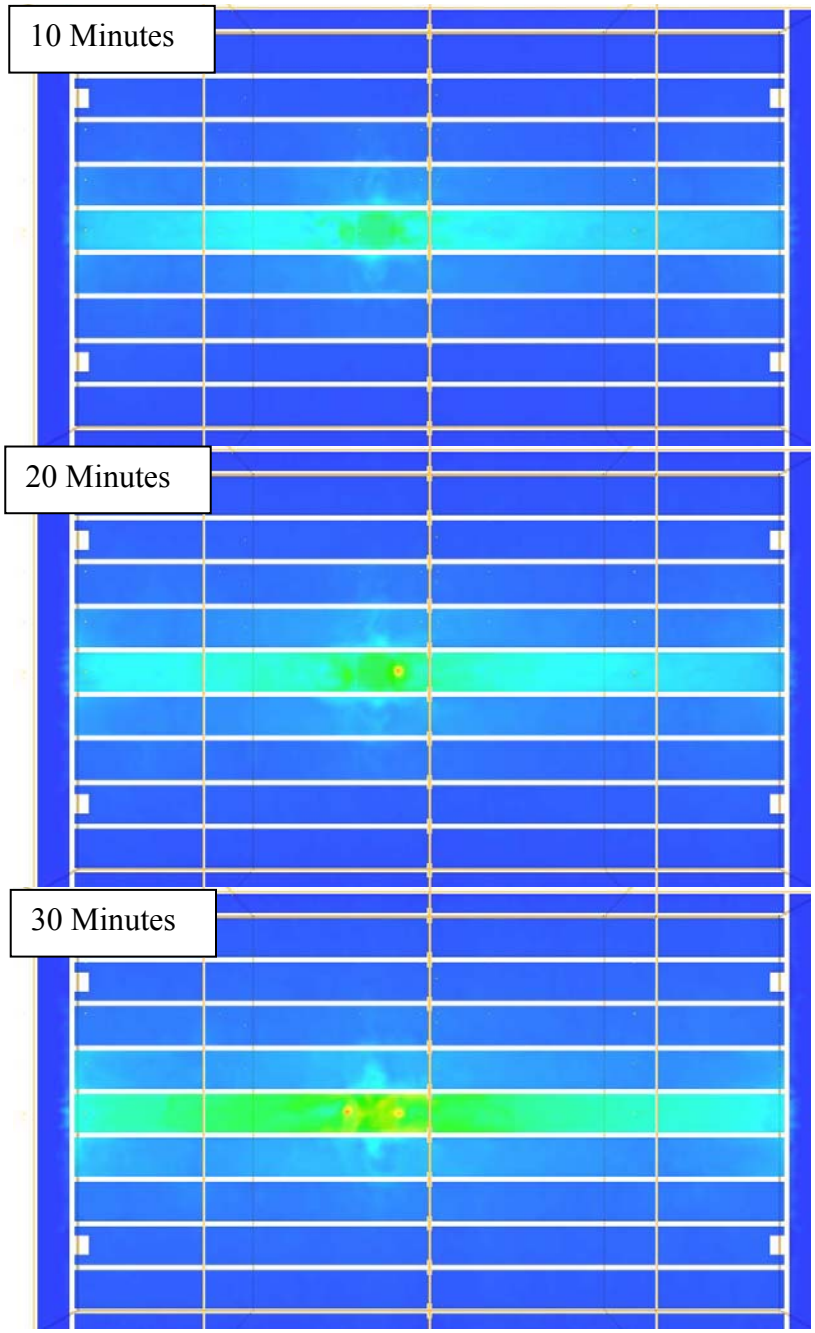

Figure 4-6: Continued from Figure 4-5.

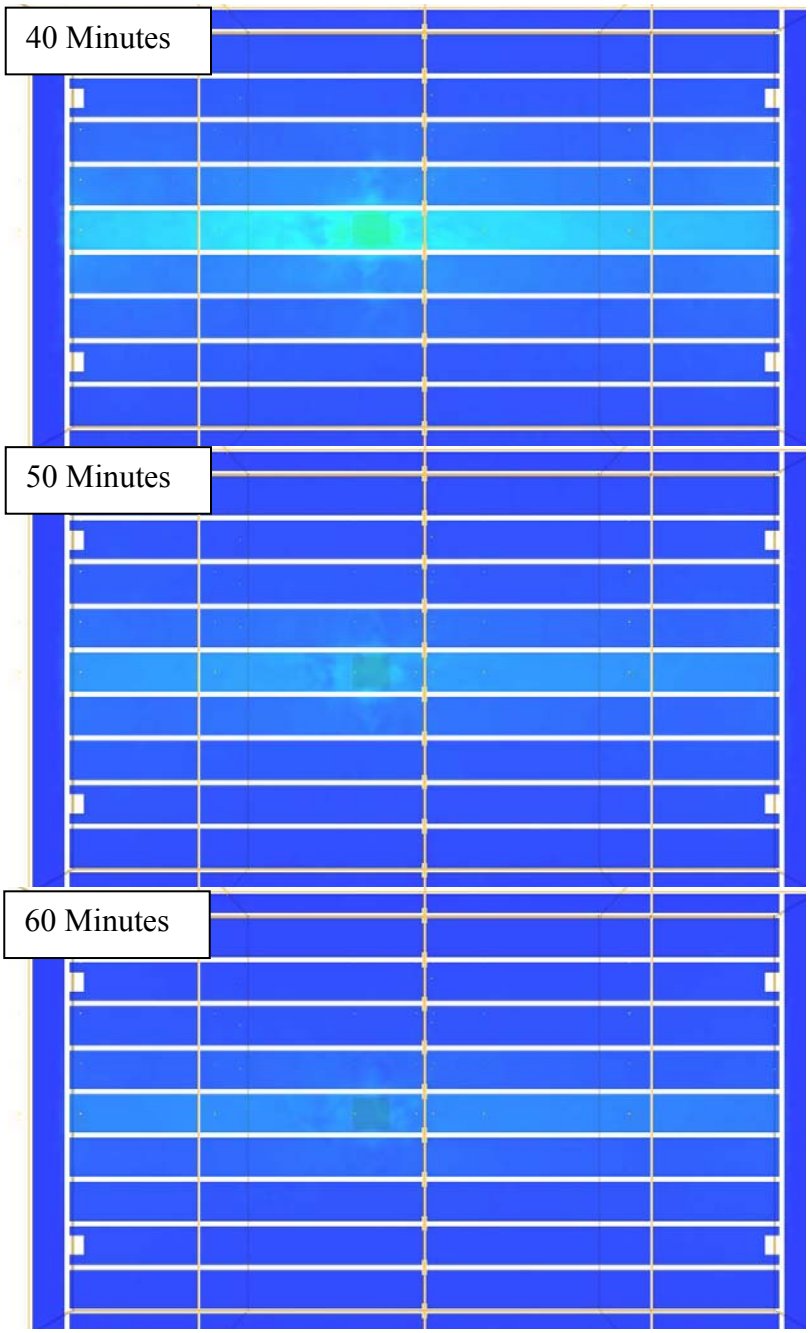

Figure 4-7: Continued from Figure 4-6.

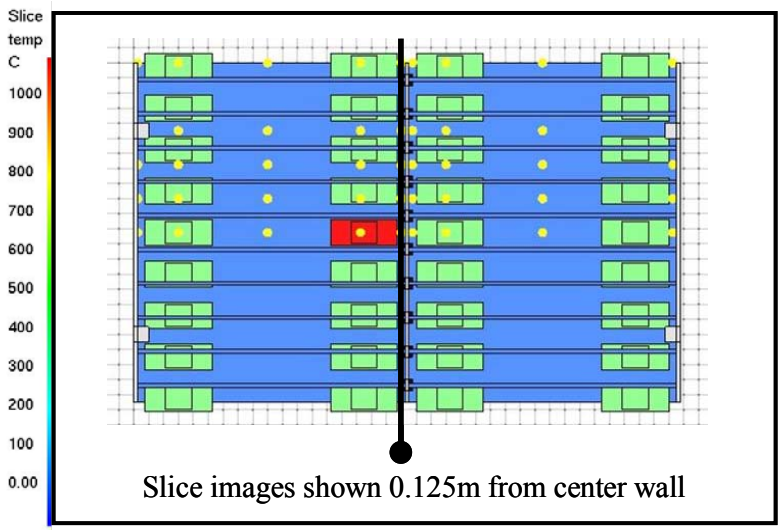

Figure 4-8: Slice images for Analysis 1 showing temperature distribution across double-tee webs next to the center wall (y = 18.0m). Images shown at 10 minute intervals (600sec) from time = 10 to 60 minutes (600-3600sec). Temperature scale in degrees Celsius. Continued in Figures 4-9 and 4-10.

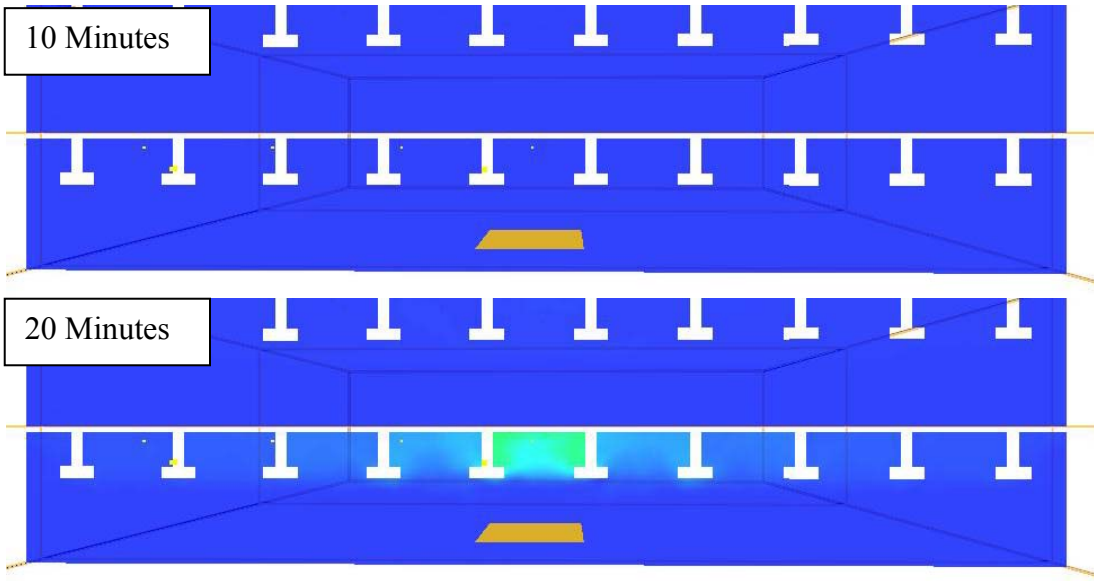

Figure 4-9: Continued from Figure 4-8.

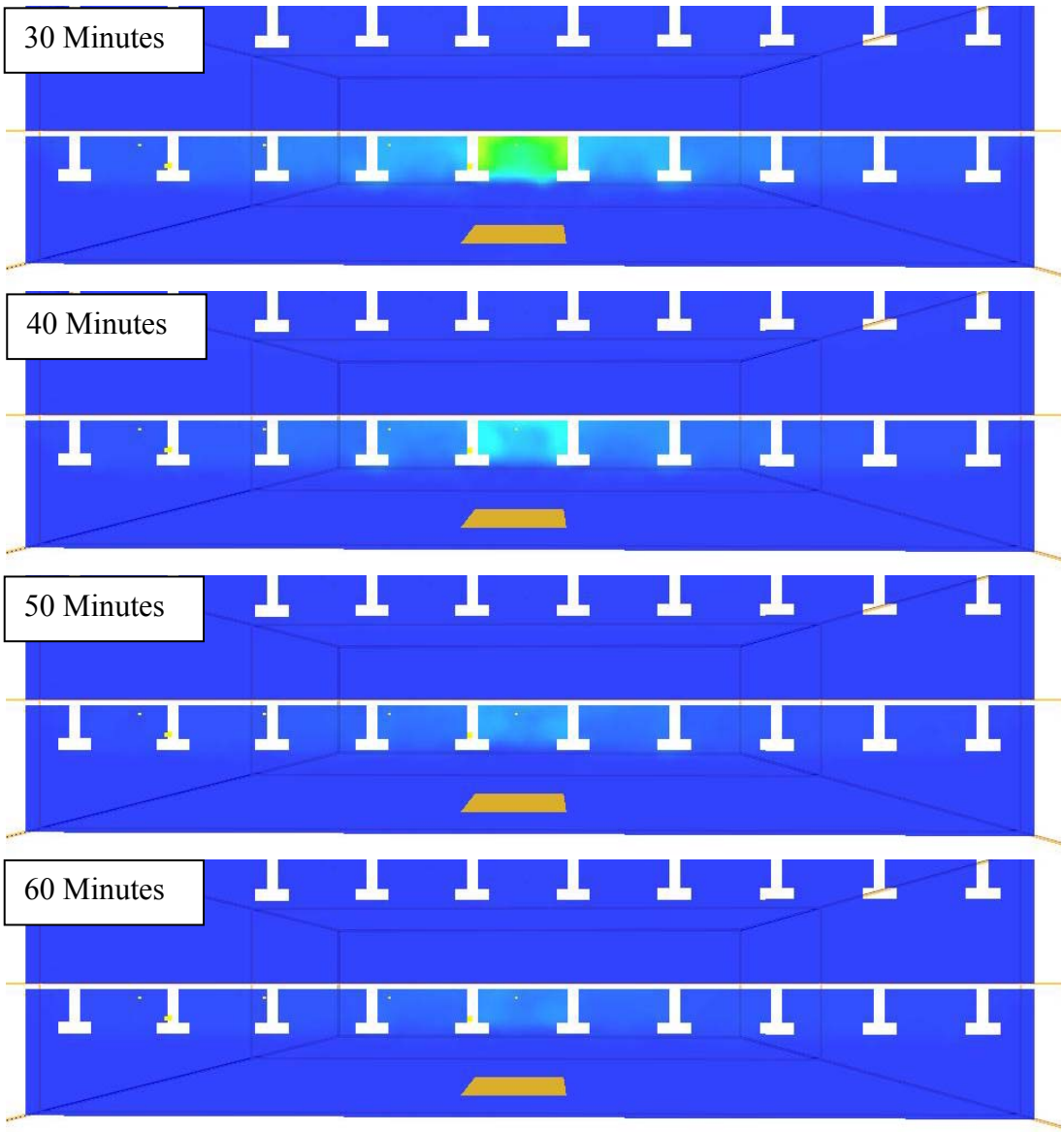

Figure 4-10: Continued from Figure 4-9.

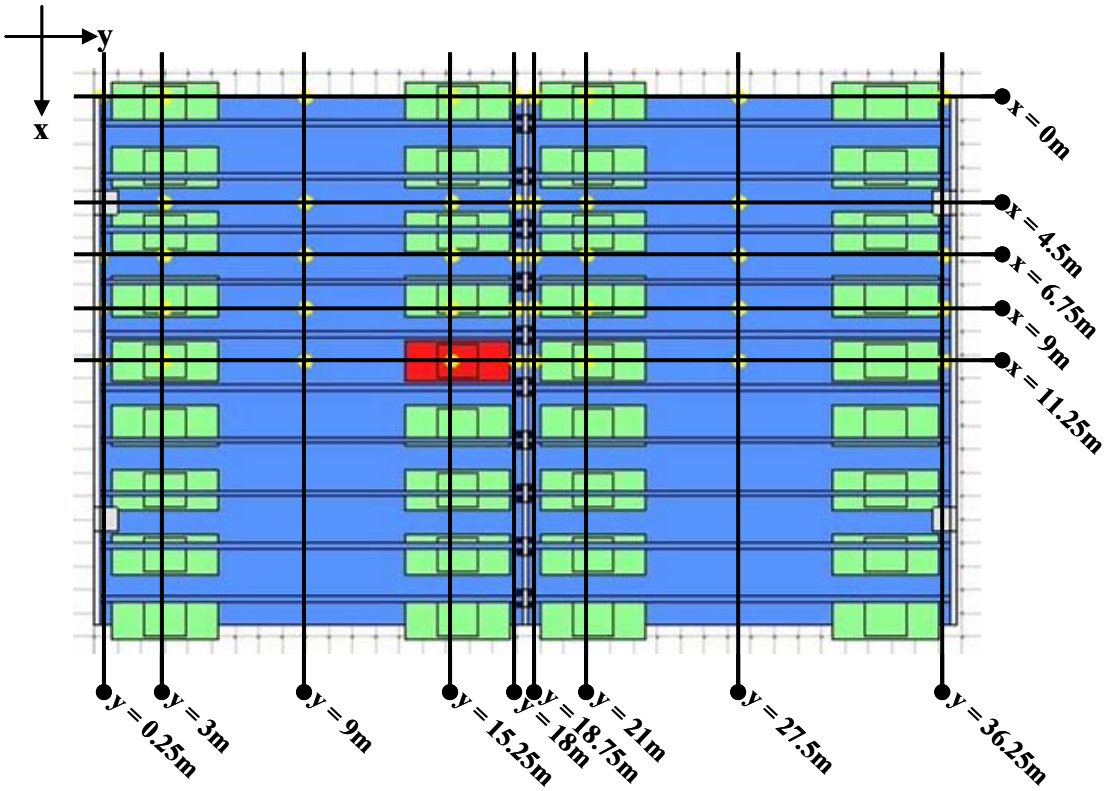

Figure 4-11: Plan view location key for thermocouples.

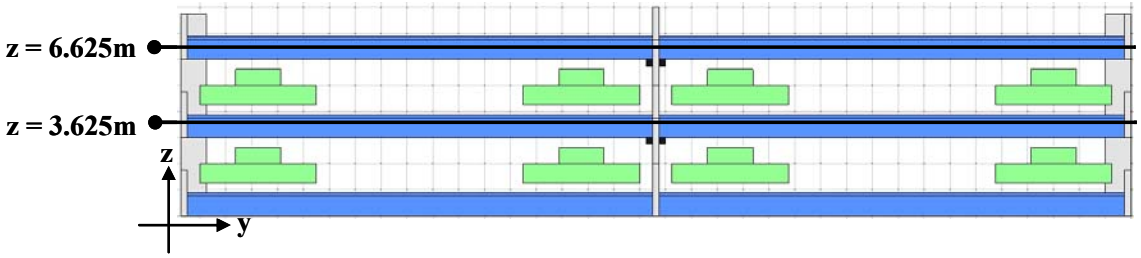

Figure 4-12: Elevation view location key for thermocouples.

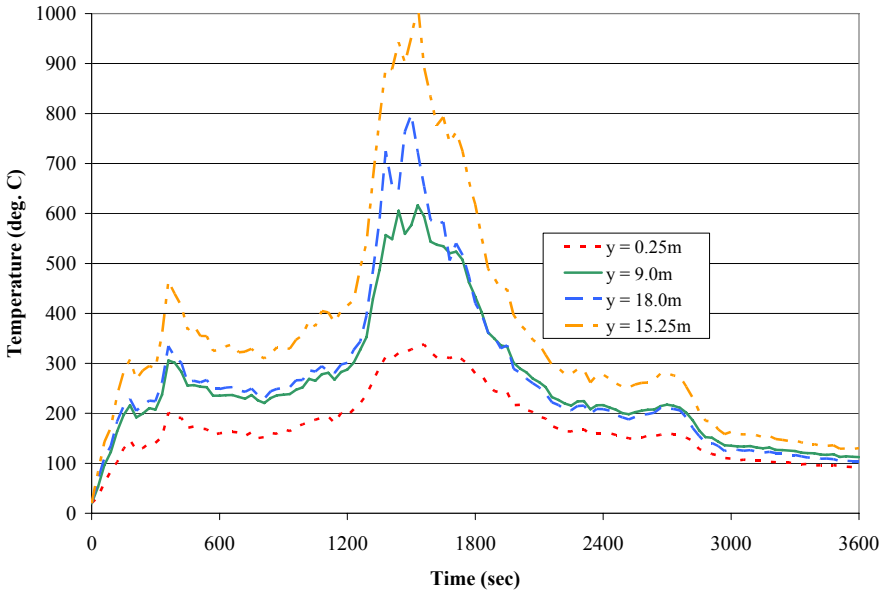

Figure 4-13: Time-temperature histories for Analysis 1 centered between double-tee webs above burning vehicle at x = 11.25m; y = 0.25m, 9.0m, 15.25m, 18.0m; z = 3.625m.

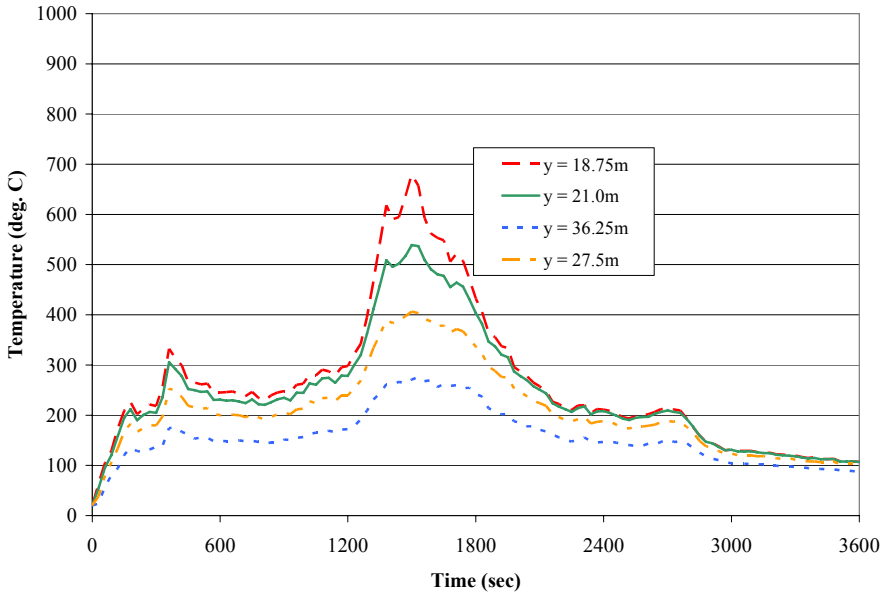

Figure 4-14: Time-temperature histories for Analysis 1 centered between double-tee webs above burning vehicle at x = 11.25m; y = 18.75m, 21.0m, 27.5m, 36.25m; z = 3.625m.

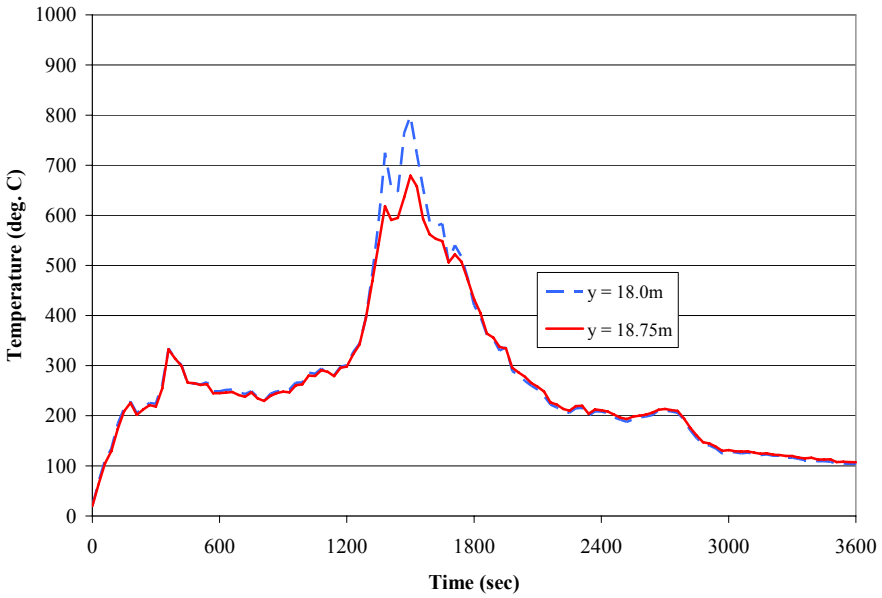

Figure 4-15: Time-temperature histories for Analysis 1 centered between double-tee webs above burning vehicle at x = 11.25m; y = 18.0m, 18.75m; z = 3.625m.

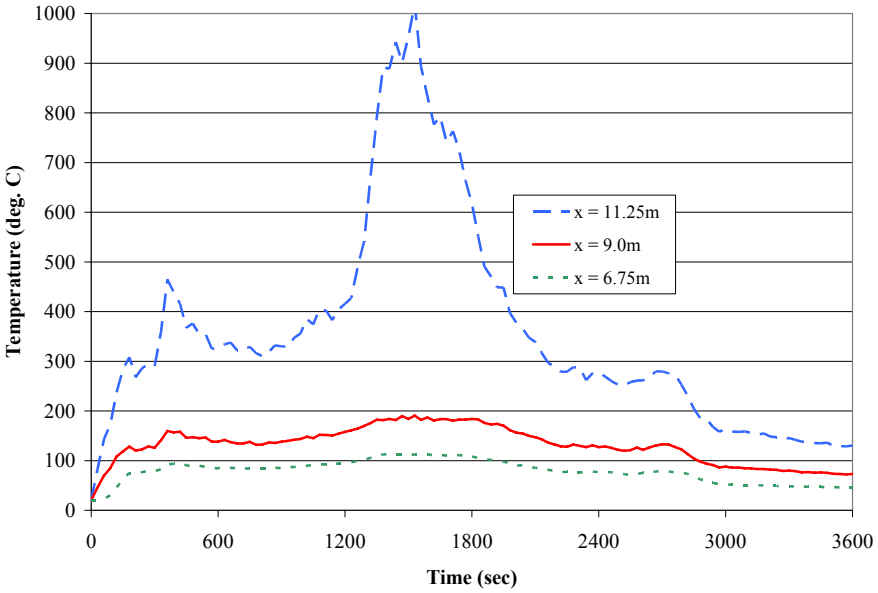

Figure 4-16: Time-temperature histories for Analysis 1 across double-tee webs at x = 11.25m, 9.0m, 6.75m; y = 15.25m; z = 3.625m.

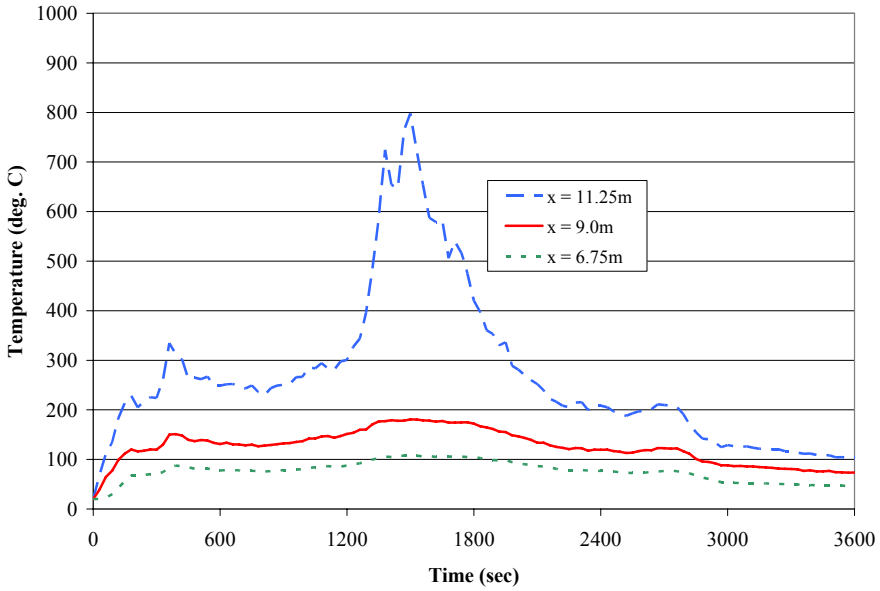

Figure 4-17: Time-temperature histories for Analysis 1 across double-tee webs at x = 11.25m, 9.0m, 6.75m; y = 18.0m; z = 3.625m.

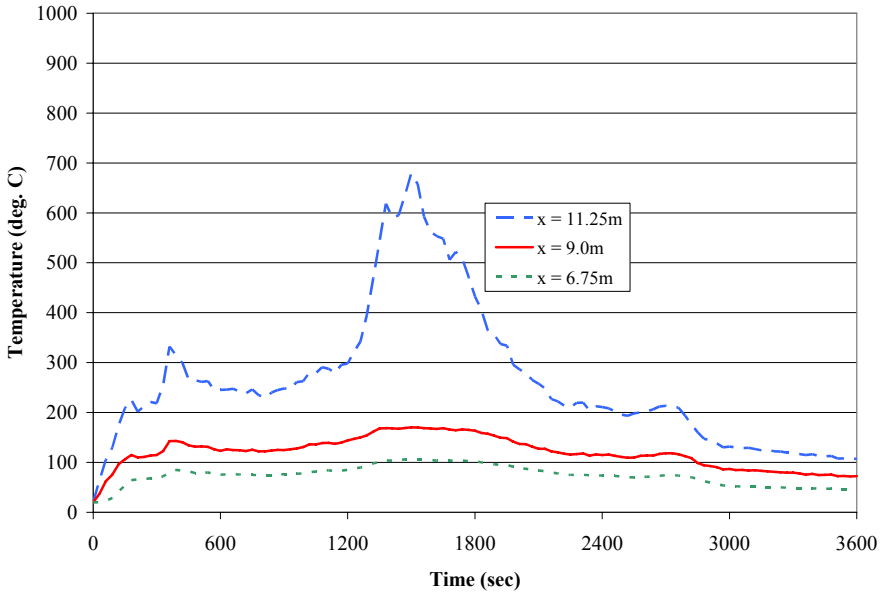

Figure 4-18: Time-temperature histories for Analysis 1 across double-tee webs at x = 11.25m, 9.0m, 6.75m; y = 18.75m; z = 3.625m.

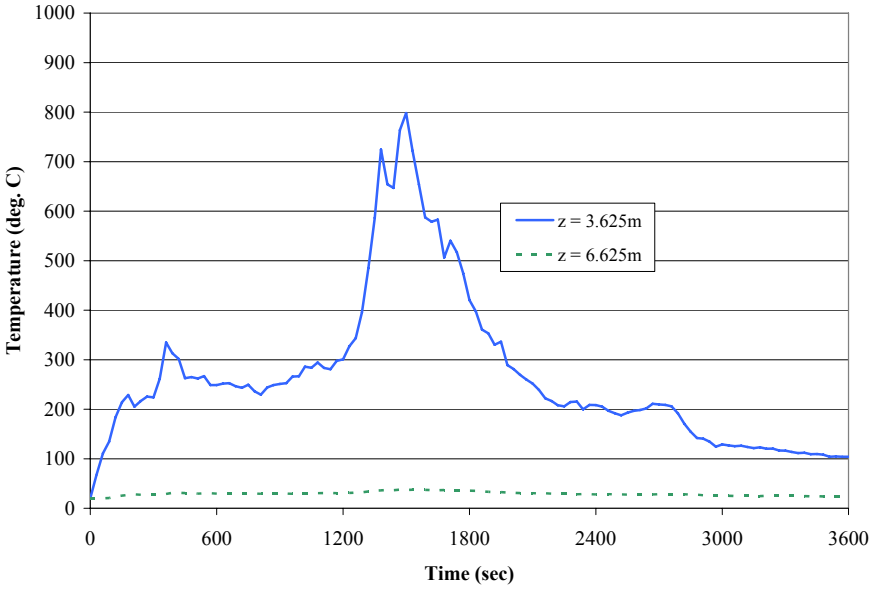

Figure 4-19: Time-temperature histories for Analysis 1 transferring from one floor to the next at x = 11.25m; y = 18.0m; z = 3.625m, 6.625m.

4.3.2 Analysis 2: Bottom Opening Analysis

Analysis 2 is similar to Analysis 1, except that the opening position in the center wall is flush with the top of the double-tee slab, thus a comparison of the results of Analysis 1 and Analysis 2 provides information about how the opening position influences heat transfer across the width of the structure.

The material properties and analysis parameters used conformed to those explained in Chapter 3. The burning vehicle is located on the lower floor of the model and is centered between the double-tee webs in location 23 as shown previously in Figure 3-16. The vehicle fire record used for this analysis is the same as the Analysis 1 and is shown previously in Figure 4-4.

The geometry of the Analysis 2 model is shown is Figures 4-20 and 4-21. Images are captured from PyroSim, and particular note should be taken of the opening position in the center wall shown in Figure 4-20 as it relates to the flange of the double-tee, specifically that the bottom of the opening is flush with the top of the double-tee slab. Particular note should also be taken that the top of the opening is located 0.375m, or three cells, below the bottom of the double-tee webs.

Slice images showing temperature distribution through the structure are shown in Figures 4-22 to 4-27. Images are shown at 10 minute intervals, and the slice location is shown by the diagram at the top of each figure. Figures 4-22 to 4-24 show a temperature slice located just below the slab above the burning vehicle at z = 3.625m. It is observed that the heat builds up longitudinally between the double-tee webs with some heat spilling over into adjacent double-tee cavities. Little or no heat is allowed to flow through the center wall, and, once again, peak temperature is reached above the burning vehicle. The second set of images in this series are Figures 4-25 to 4-27, showing a transversely oriented temperature slice located 0.125m from the center wall at y = 18m, and heat is seen to spill over into adjacent cavities.

As before, time-temperature plots taken from thermocouples throughout the structure are shown in Figures 4-28 to 4-36 and are broken into three series: longitudinal time-temperature plots (Figures 4-30 to 4-32), transverse time-temperature plots (Figures 4-33 to 4-35), and a vertical time-temperature plot (Figures 4-36).

The longitudinal time-temperature plots are shown for thermocouple locations centered between the double-tee webs in the cavity above the burning vehicle. Figure 4-30 shows four thermocouples distributed from y = 0.25m to y = 18m. The highest temperatures recorded were 975 and 971 degrees Celsius at y = 18.0m and y = 15.25m respectively. Temperatures were generally lower as the distance from the center of the fire increased.

Figure 4-31 shows a similar set of thermocouple time-temperature plots to Figure 4-30, but these are shown for the opposite side of the center wall. Very little heat transmission through the center wall is shown to have occurred, a characteristic that is further shown in Figure 4-32, which shows two time-temperature plots, one on either side of the center wall. The thermocouple location closer to the fire at y = 18.0m shows significantly higher recorded temperatures than those at y = 18.75m.

The transverse time-temperature plots are shown in Figures 4-33 to 4-35 to show the how the heat spills under the double-tee webs from one cavity to the next. All three figures show that the majority of the heat is generally contained within the cavity above the burning vehicle.

The final time-temperature plot is Figure 4-36, which shows the vertical temperature distribution along the center wall from one floor to the next. Two thermocouples are shown centered between the double-tee webs on above the burning vehicle at y = 18.0m and on both floors at z = 3.625m and 6.625m. Once again, negligible temperature increase is observed on the upper floor.

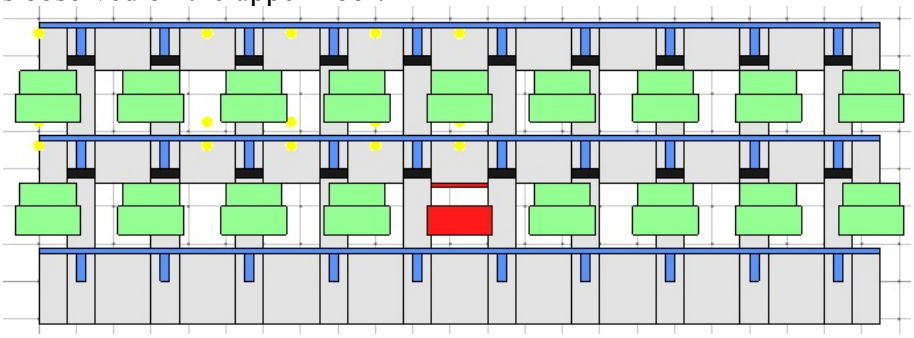

Figure 4-20: View of the center wall of Analysis 2 showing the bottom opening position and the burning vehicle centered in between the double-tee stems.

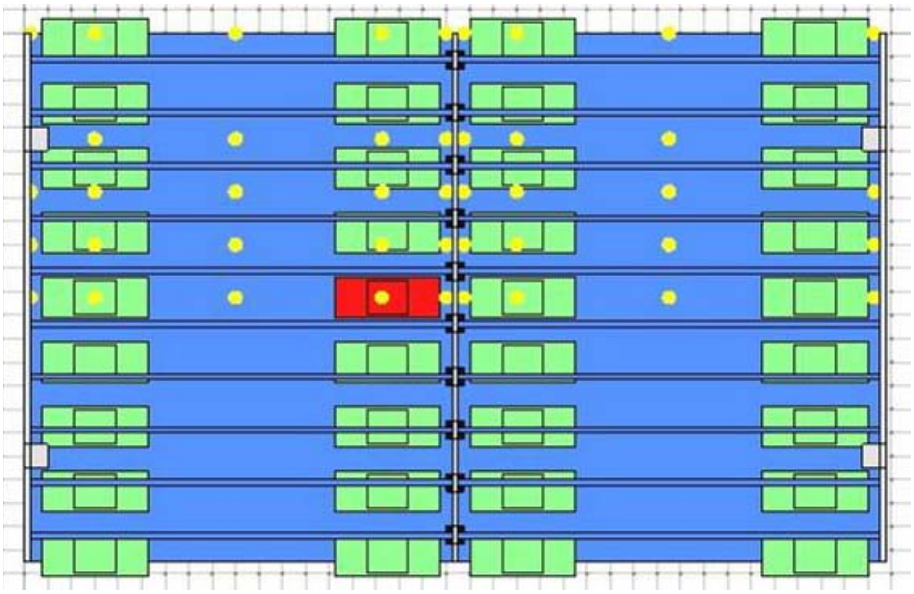

Figure 4-21: Plan view of Analysis 2 showing the burning vehicle position next to the center wall and centered between the double-tee stems.

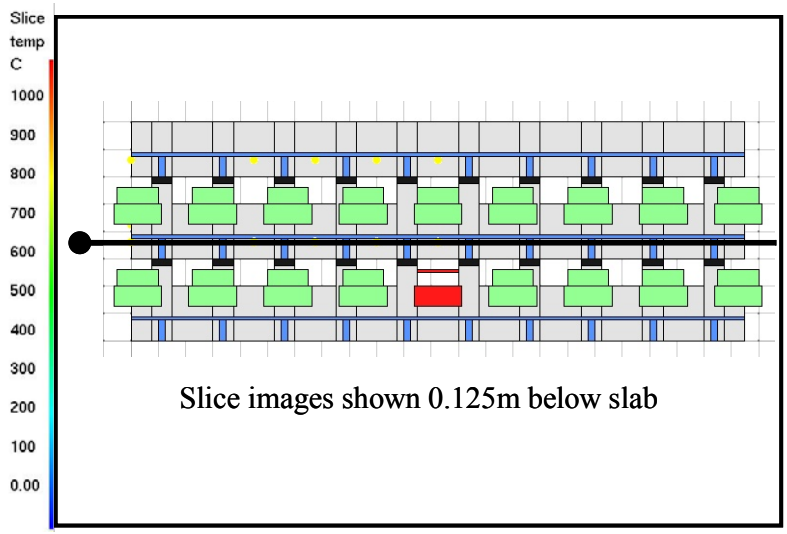

Figure 4-22: Slice images for Analysis 2 showing temperature distribution 0.125m below slab above burning vehicle (z = 3.625m). Images shown at 10 minute intervals (600sec) from time = 0 to 60 minutes. (0-3600sec) Temperature scale in degrees Celsius. Continued in Figures 4-23 and 4-24.

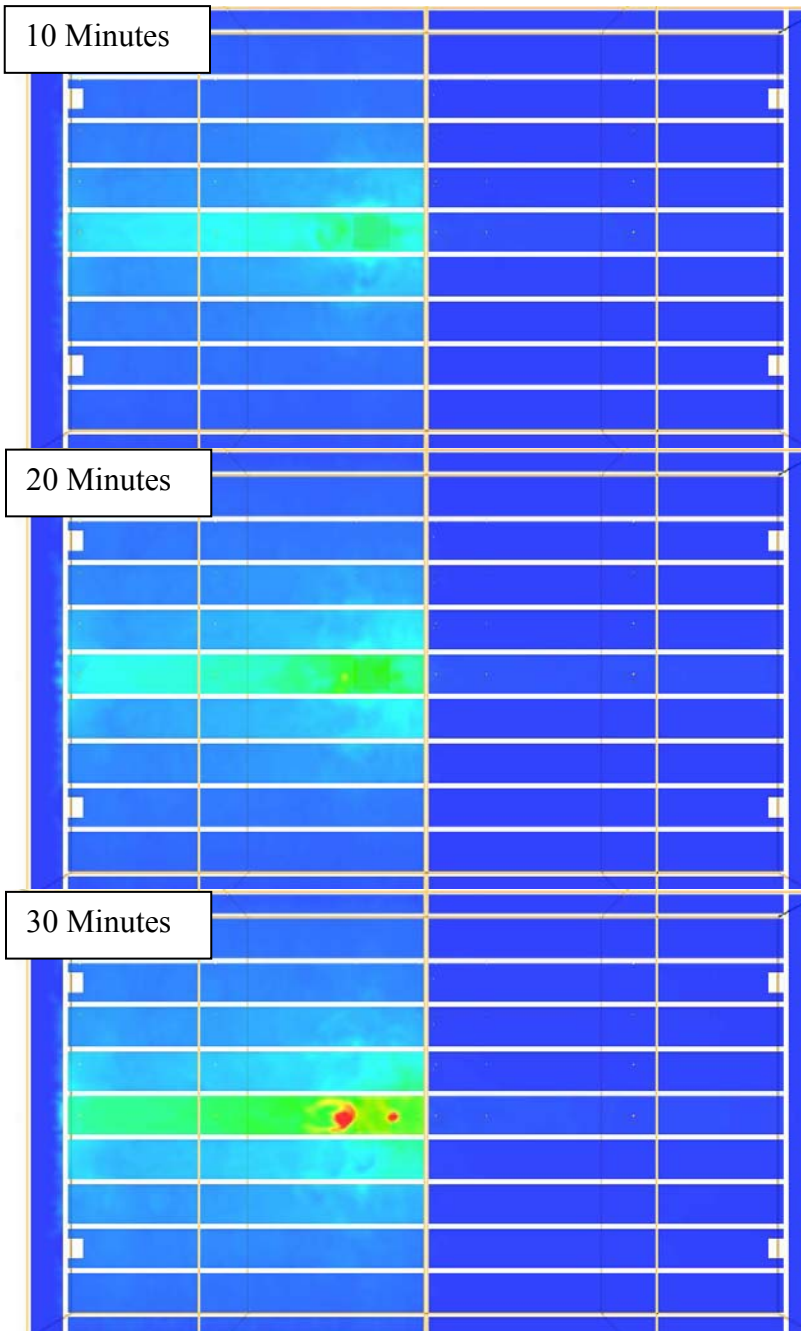

Figure 4-23: Continued from Figure 4-22.

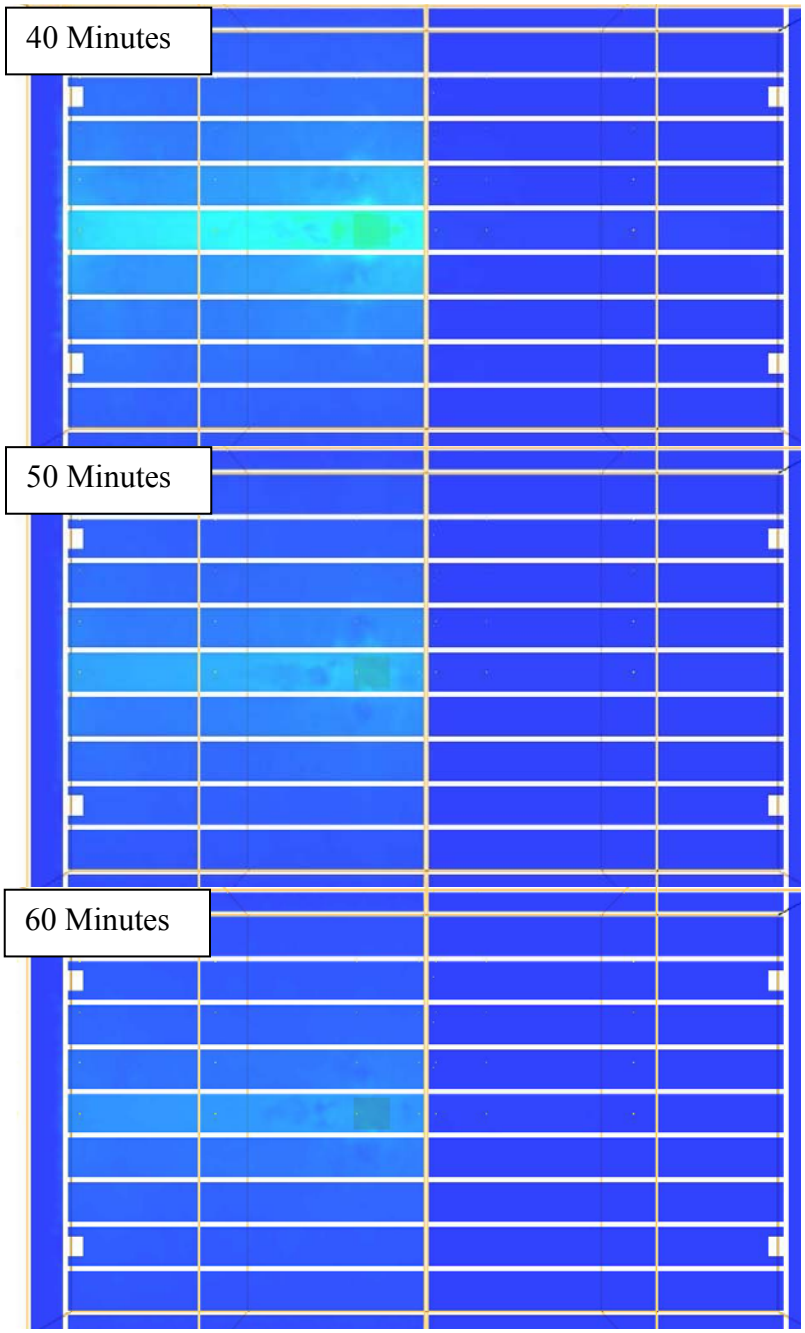

Figure 4-24: Continued from Figure 4-23.

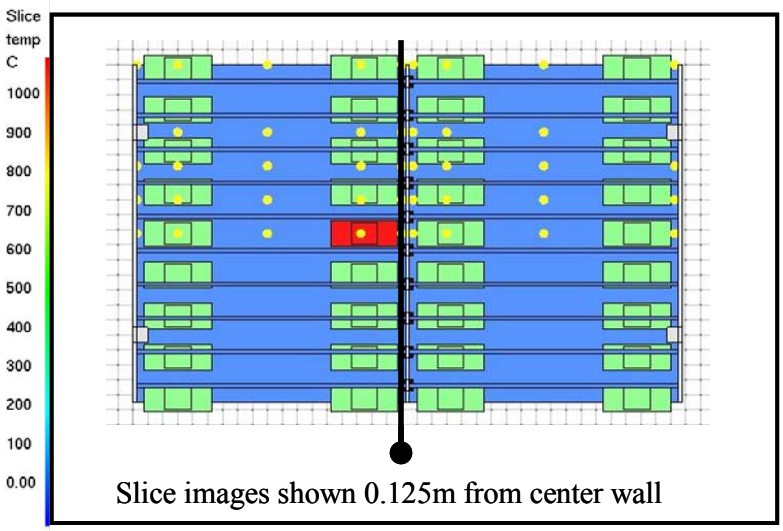

Figure 4-25: Slice images for Analysis 2 showing temperature distribution across double-tee webs next to the center wall (y = 18.0m). Images shown at 10 minute intervals (600sec) from time = 10 to 60 minutes (600-3600sec). Temperature scale in degrees Celsius. Continued in Figures 4-26 and 4-27.

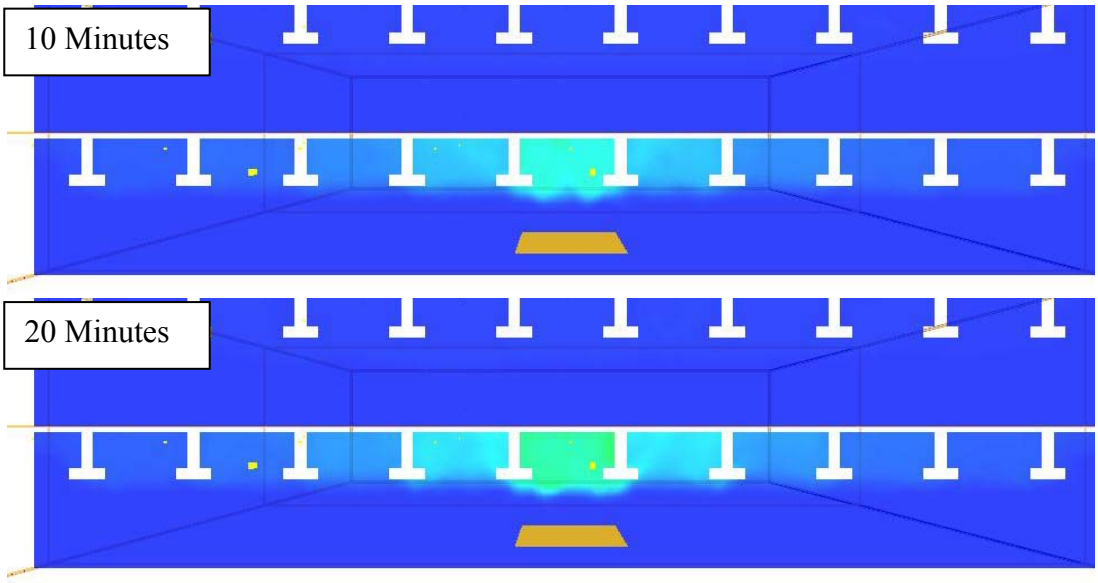

Figure 4-26: Continued from Figure 4-25

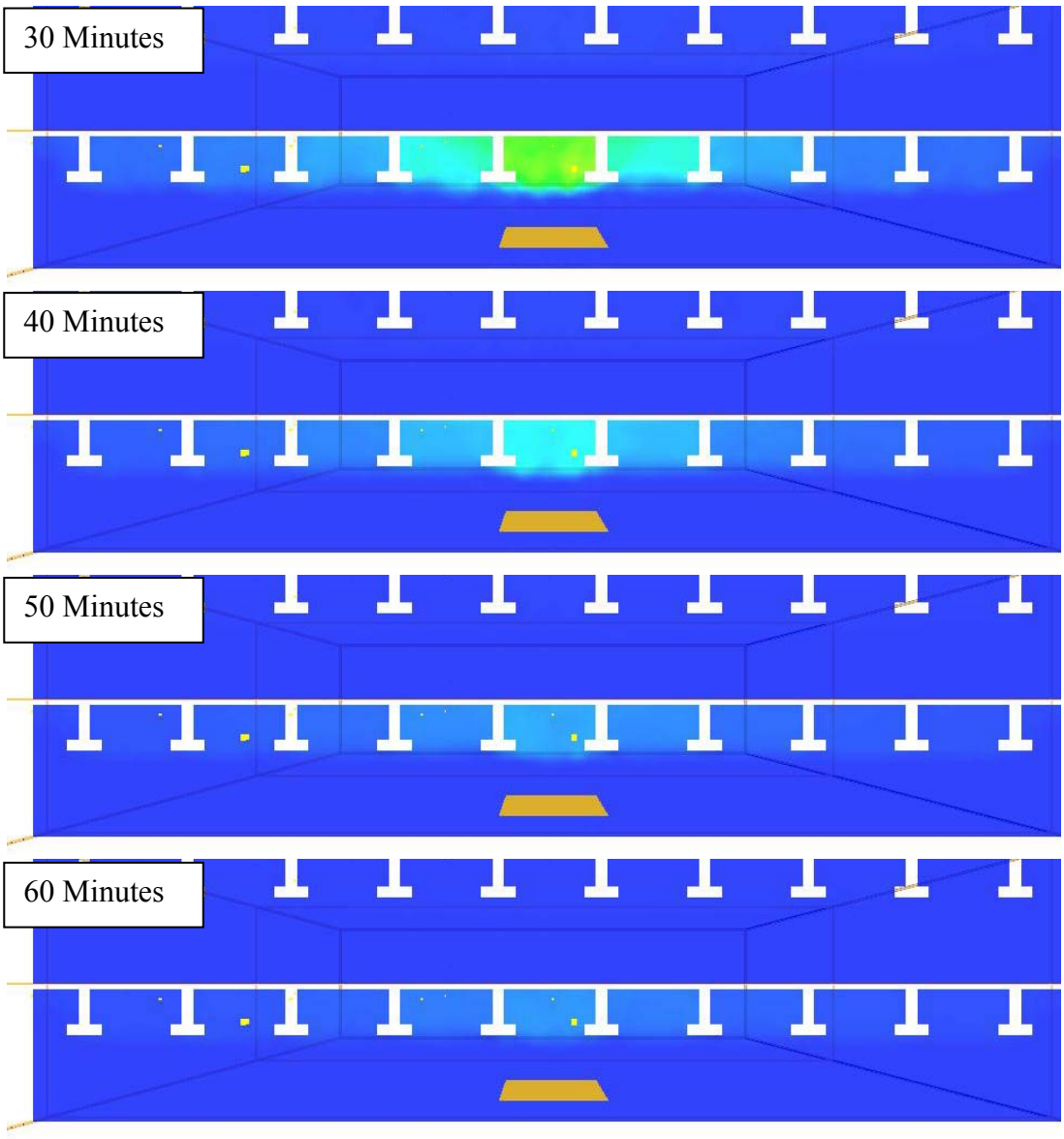

Figure 4-27: Continued from Figure 4-26.

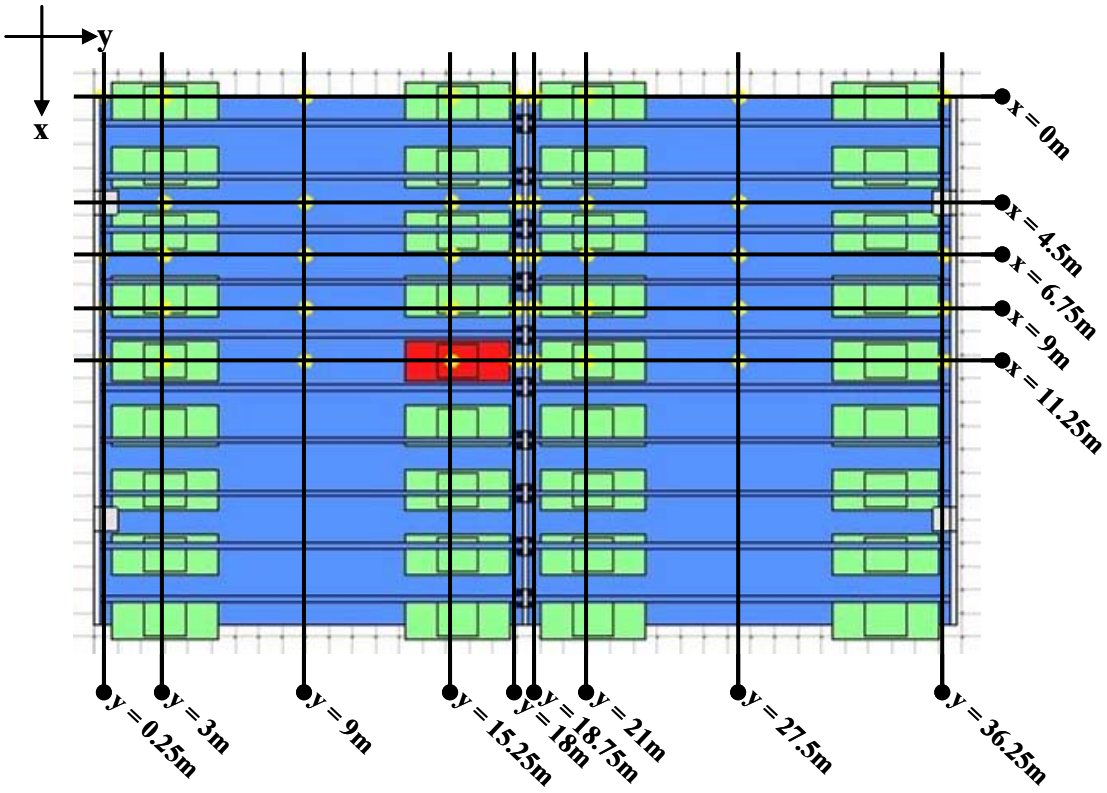

Figure 4-28: Plan view location key for thermocouples.

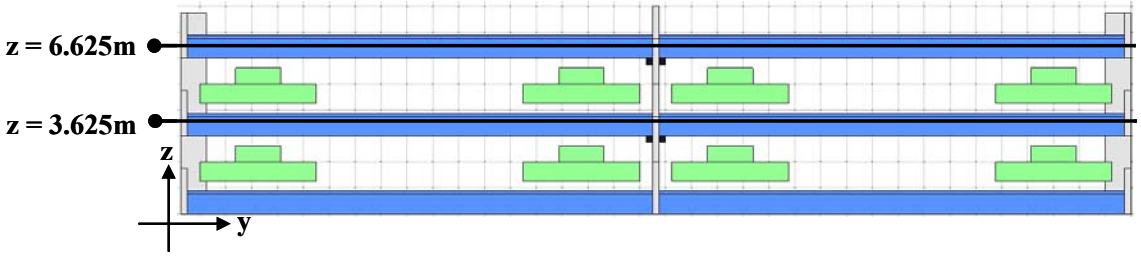

Figure 4-29: Elevation view location key for thermocouples.

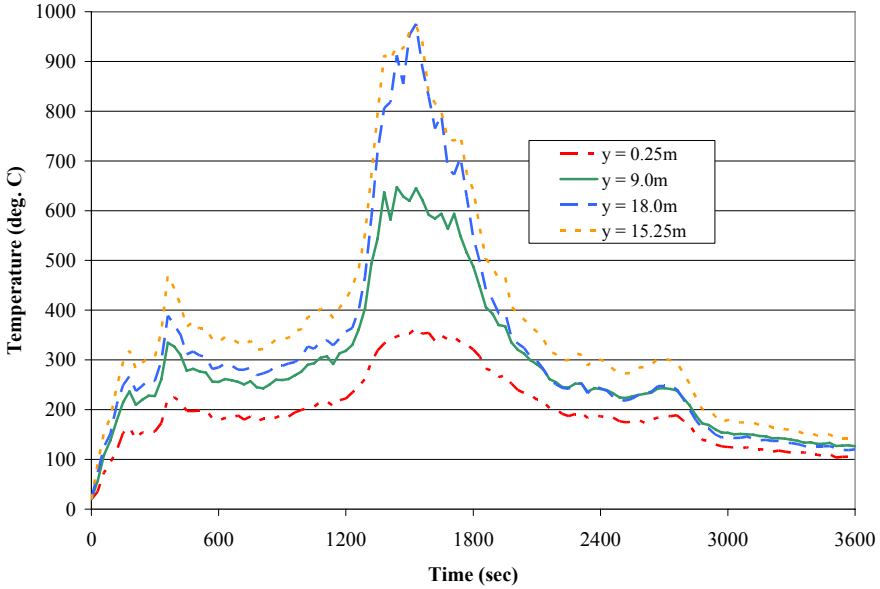

Figure 4-30: Time-temperature histories for Analysis 2 centered between double-tee webs above burning vehicle at x = 11.25m; y = 0.25m, 9.0m, 15.25m, 18.0m; z = 3.625m.

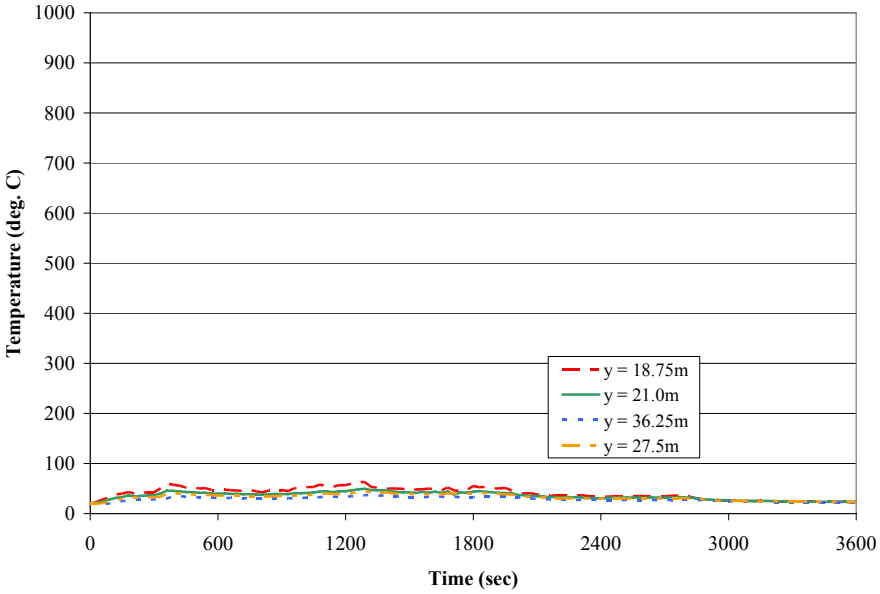

Figure 4-31: Time-temperature histories for Analysis 2 centered between double-tee webs above burning vehicle at x = 11.25m; y = 18.75m, 21.0m, 27.5m, 36.25m; z = 3.625m.

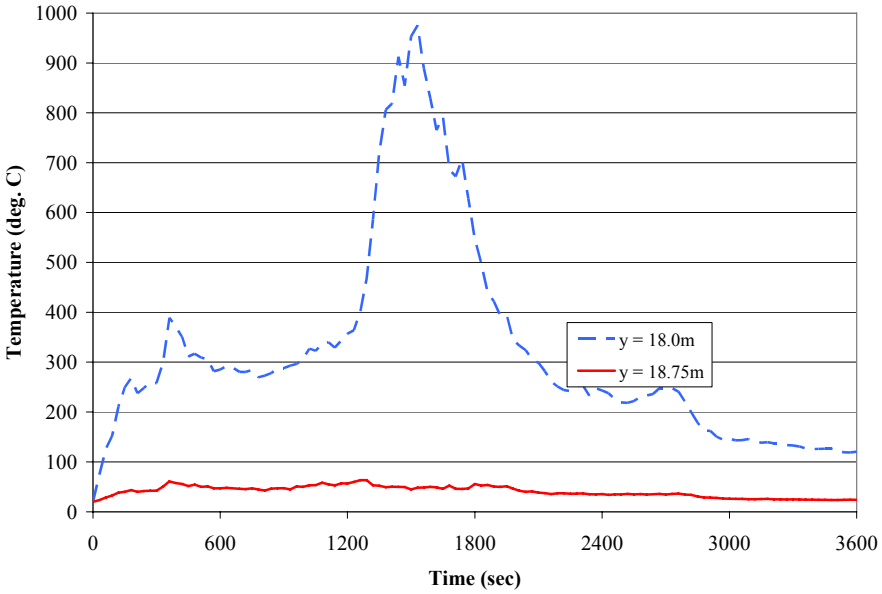

Figure 4-32: Time-temperature histories for Analysis 2 centered between double-tee webs above burning vehicle at x = 11.25m; y = 18.0m, 18.75m; z = 3.625m.

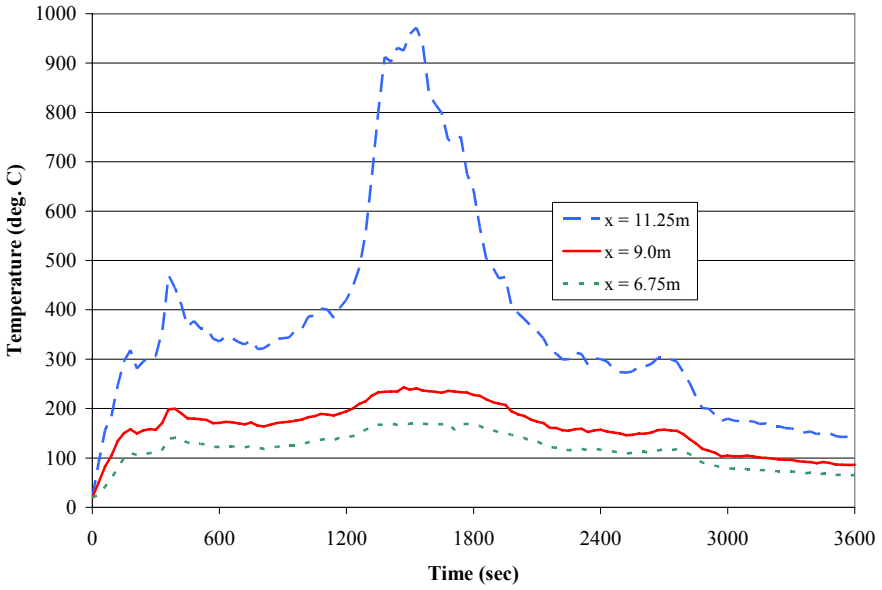

Figure 4-33: Time-temperature histories for Analysis 2 across double-tee webs at x = 11.25m, 9.0m, 6.75m; y = 15.25m; z = 3.625m.

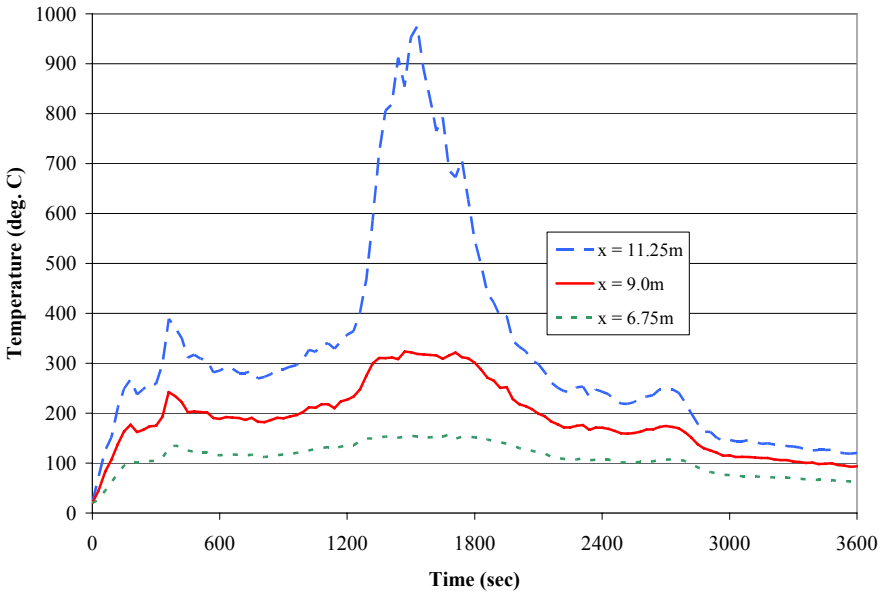

Figure 4-34: Time-temperature histories for Analysis 2 across double-tee webs at x = 11.25m, 9.0m, 6.75m; y = 18.0m; z = 3.625m.

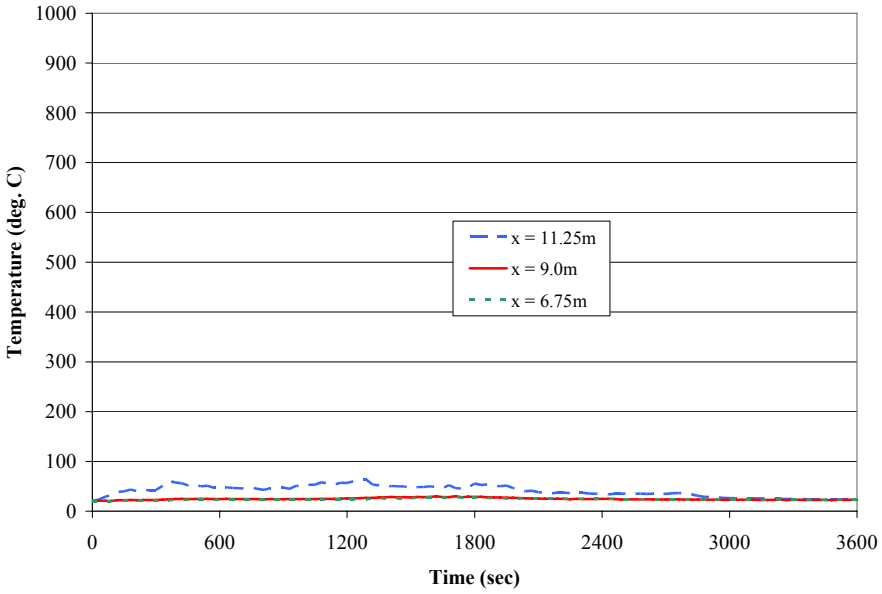

Figure 4-35: Time-temperature histories for Analysis 2 across double-tee webs at x = 11.25m, 9.0m, 6.75m; y = 18.75m; z = 3.625m.

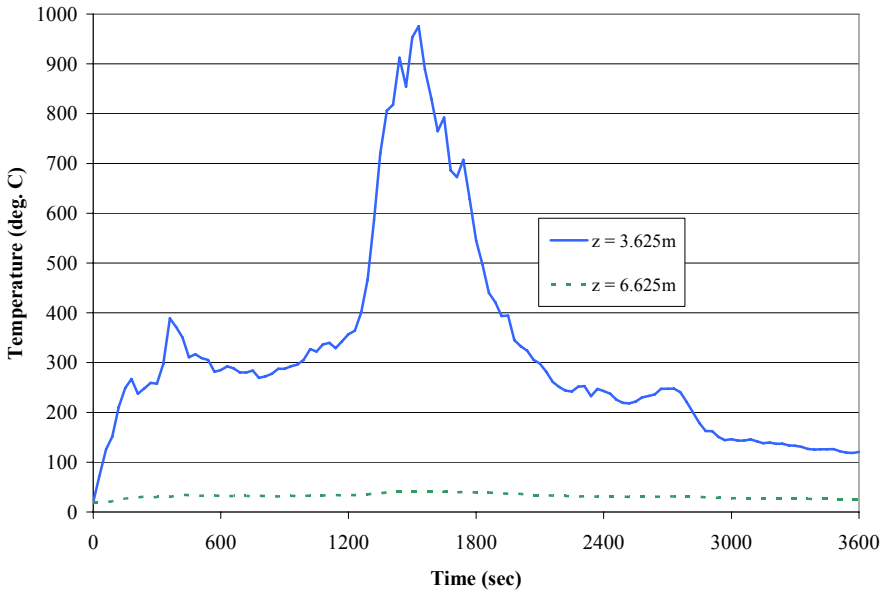

Figure 4-36: Time-temperature histories for Analysis 2 transferring from one floor to the next at x = 11.25m; y = 18.0m; z = 3.625m, 6.625m.

4.3.3 Analysis 3: Chimney 1 Analysis

The purpose of the Chimney Analyses was to investigate the effect of an opening of limited size in the slab to allow heat flow to the upper floor. Because of the dimensions of the opening, it was not possible to completely center the opening on the slab, therefore, 0.75m is open above the slab and 0.875m below. The opening or 'chimney' is the thickness of the center wall, which is 0.25m, and the width of the center wall used throughout this project, 1.5m wide. The material properties and analysis parameters used conformed to those explained in Chapter 3. The burning vehicle is located on the lower floor of the model and is centered between the double-tee webs in location 23 as shown previously in Figure 3-16. The vehicle fire record used for this analysis is the same as the Analyses 1 and 2 and is shown previously in Figure 4-4.

The geometry of the Analysis 3 model is shown in Figures 4-37 to 4-39. Images are captured from PyroSim, and particular note should be taken of the opening position in the center wall shown in Figure 4-37 as it relates to the slabs, specifically how the center opening straddles the double-tee slab. Figure 4-38 shows the 'chimney' opening in the center wall, and Figure 4-39 shows the location of the burning vehicle.

Slice images showing temperature distribution through the structure are shown in Figures 4-40 to 4-45. Images are shown at 10 minute intervals, and the slice location is shown by the diagram at the top of each figure. Figures 4-40 to 4-42 shows a temperature slice located just below the slab above the burning vehicle at z = 3.625m. It is observed that the heat builds up longitudinally between the double-tee webs with relatively little heat spilling over into adjacent double-tee cavities. Peak temperature is reached above the burning vehicle.

The second set of images in this series are Figures 4-43 to 4-45, showing a transversely oriented temperature slice located 0.125m from the center wall at y = 18m. This figure further reinforces the data shown in Figures 4-40 to 4-42 that the double-tee webs contain the majority of the heat released from the burning vehicle.

Time-temperature plots taken from thermocouples throughout the structure are shown in Figures 4-46 to 4-54 and are broken into three series: longitudinal time-temperature plots (Figures 4-48 to 4-50), transverse time-temperature plots (Figures 4-51 to 4-53), and a vertical time-temperature plot (Figures 4-54).

The longitudinal time-temperature plots are shown for thermocouple locations centered between the double-tee webs in the cavity above the burning vehicle. Figure 4-48 shows four thermocouples distributed from y = 0.25m to y = 18m. The highest temperature recorded was 1014 degrees Celsius at y = 15.25m. Temperatures on either side of the

vehicle at 9m and 18m follow very similar lines except at peak where the temperature against the center wall is higher. Temperatures were generally lower as the distance from the center of the fire increased.

Figure 4-49 shows a similar set of thermocouple time-temperature plots to Figure 4-48, but these are shown for the opposite side of the center wall. Once again, the temperature plot is generally lower as the distance from the center of the fire increases. Finally, Figure 4-50, shows two time-temperature plots, one on either side of the center wall. The thermocouple location closer to the fire at y = 18.0m shows a nearly identical record at lower temperatures, but a significantly higher temperature record than those at y = 18.75m.

The transverse time-temperature plots are shown in Figures 4-51 to 4-53 to show the how the heat spills under the double-tee webs from one cavity to the next. Once again, all five figures show that the majority of the heat is generally contained within the cavity above the burning vehicle, but, as the distance from the fire increases, the difference in temperature from one cavity to the next decreases.

The final time-temperature plot is Figures 4-54, which shows the vertical temperature distribution along the center wall from one floor to the next. Two thermocouples are centered between the double-tee webs on above the burning vehicle at y = 18.0m and on both floors at z = 3.625m and 6.625m. Despite the 'chimney' opening in the center wall, very little temperature rise is recorded in the upper floor.

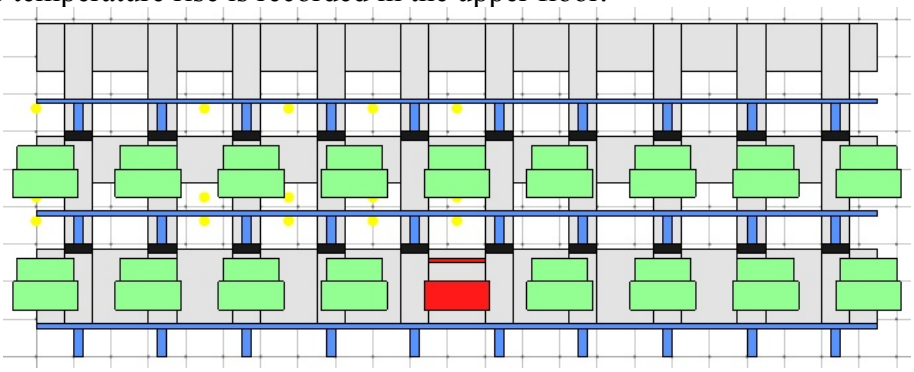

Figure 4-37: View of the center wall of Analysis 3 showing center wall opening position and the burning vehicle centered in between the double-tee stems.

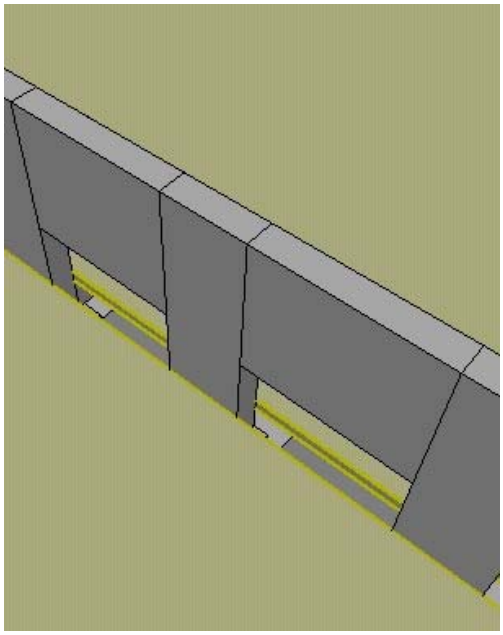

Figure 4-38: View of the 'chimney' openings in the center wall between the double-tee slabs in Analyses 3 and 4.

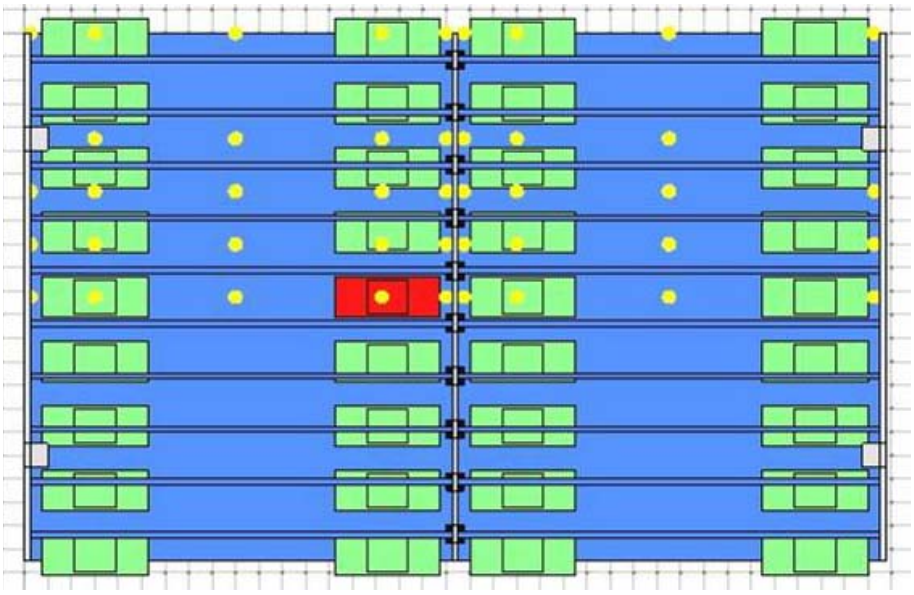

Figure 4-39: Plan view of Analysis 3 showing the burning vehicle position next to the center wall and centered between the double-tee stems.

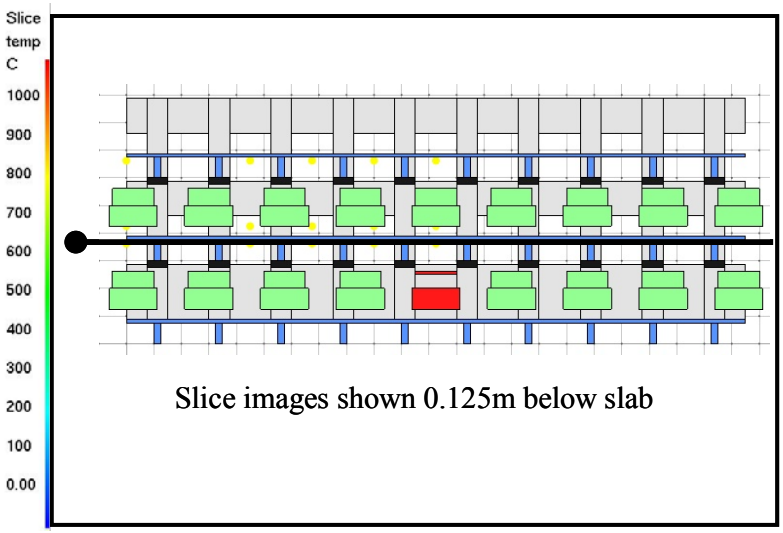

Figure 4-40: Slice images for Analysis 3 showing temperature distribution 0.125m below slab above burning vehicle (z = 3.625m). Images shown at 10 minute intervals (600sec) from time = 0 to 60 minutes. (0-3600sec) Temperature scale in degrees Celsius. Continued in Figures 4-41 and 4-42.

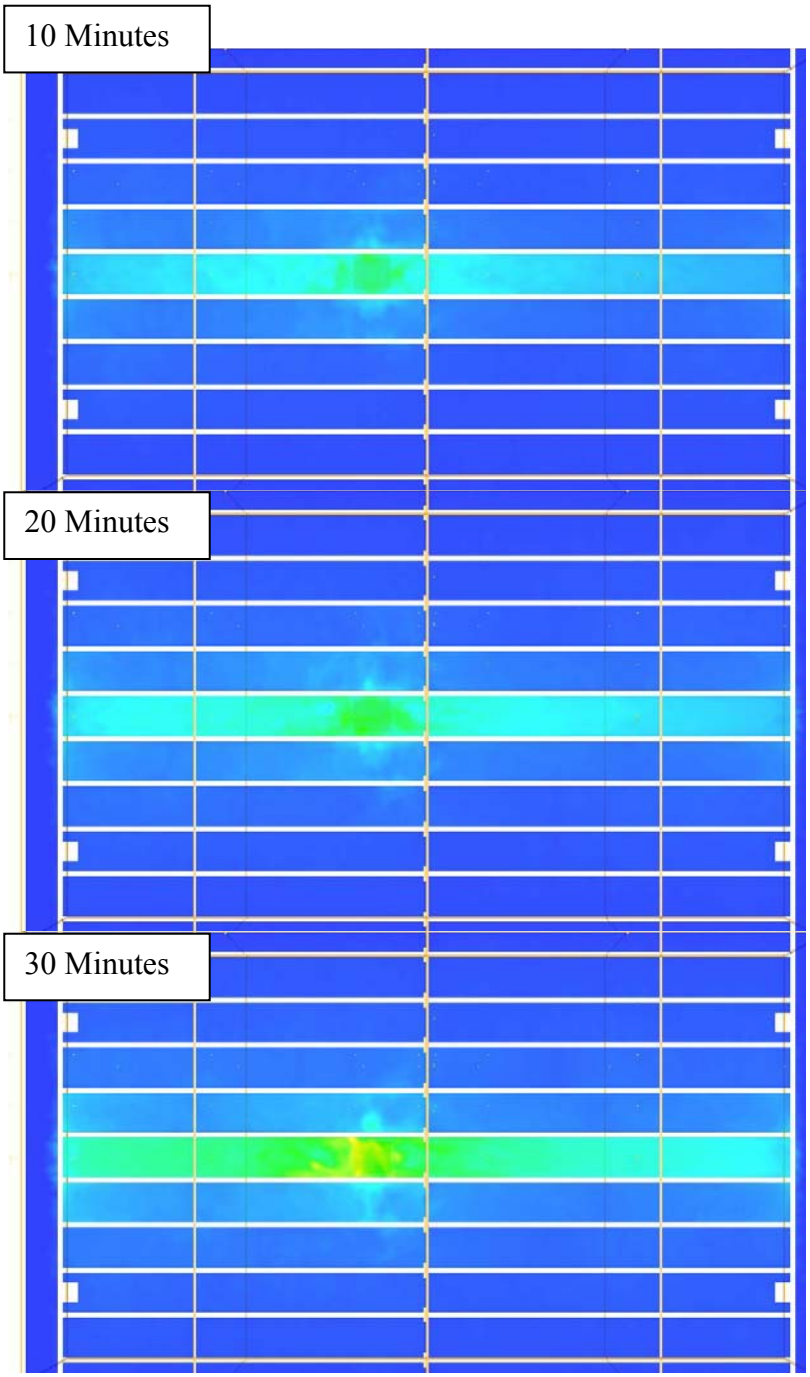

Figure 4-41: Continued from Figure 4-40.

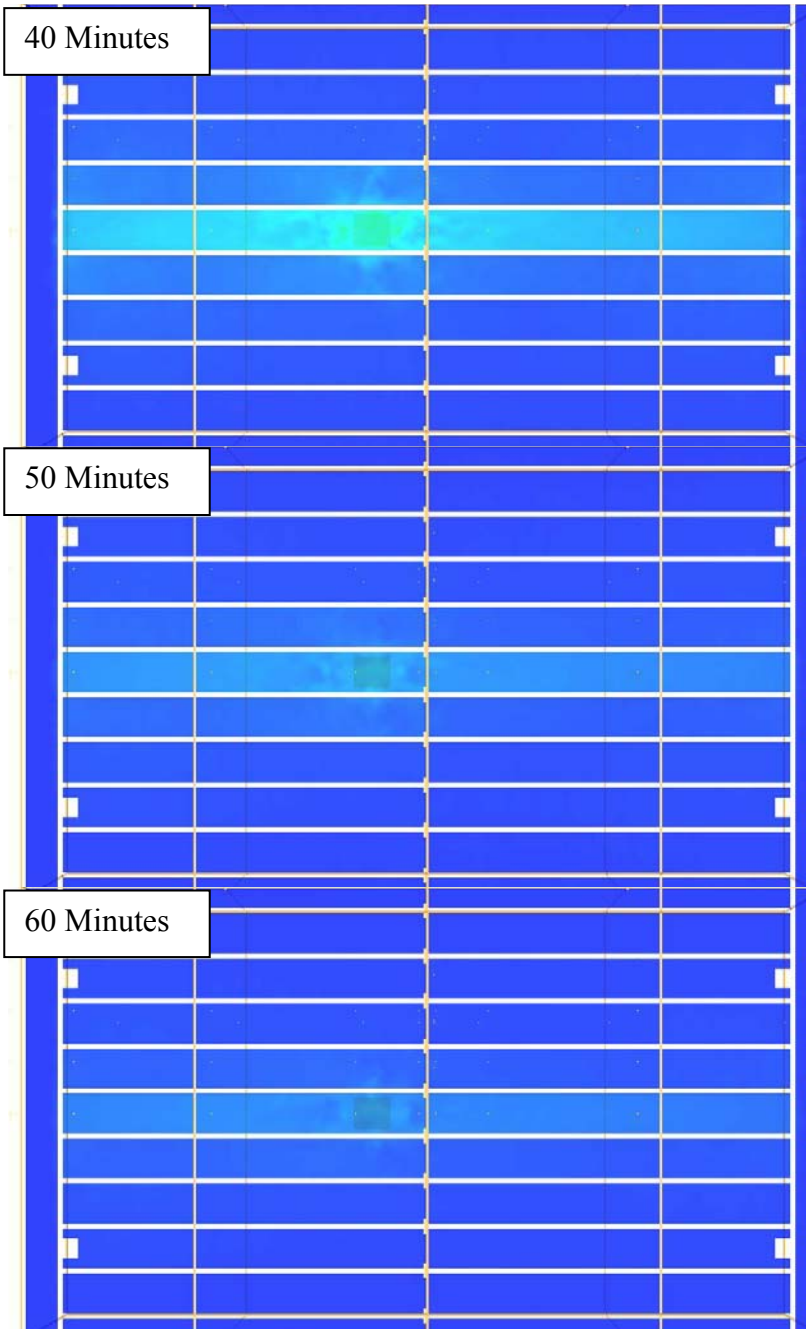

Figure 4-42: Continued from Figure 4-41.

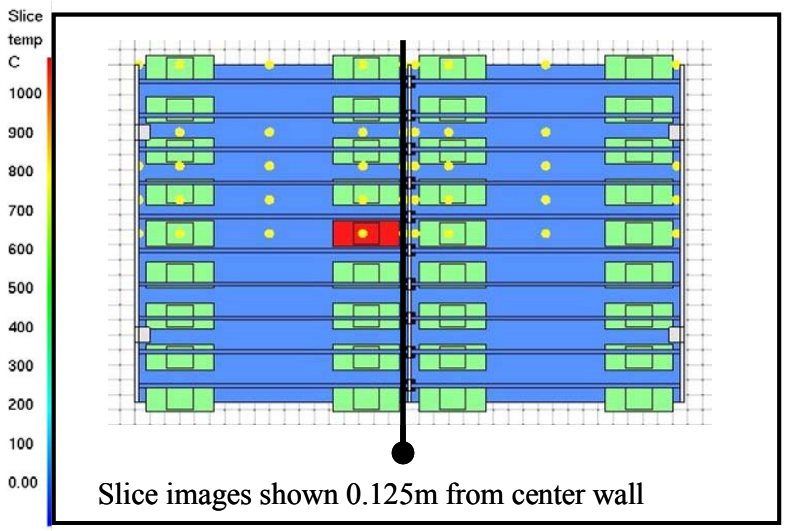

Figure 4-43: Slice images for Analysis 3 showing temperature distribution across double-tee webs next to the center wall (y = 18.0m). Images shown at 10 minute intervals (600sec) from time = 0 to 60 minutes. (0-3600sec) Temperature scale in degrees Celsius. Continued in Figures 4-44 and 4-45.

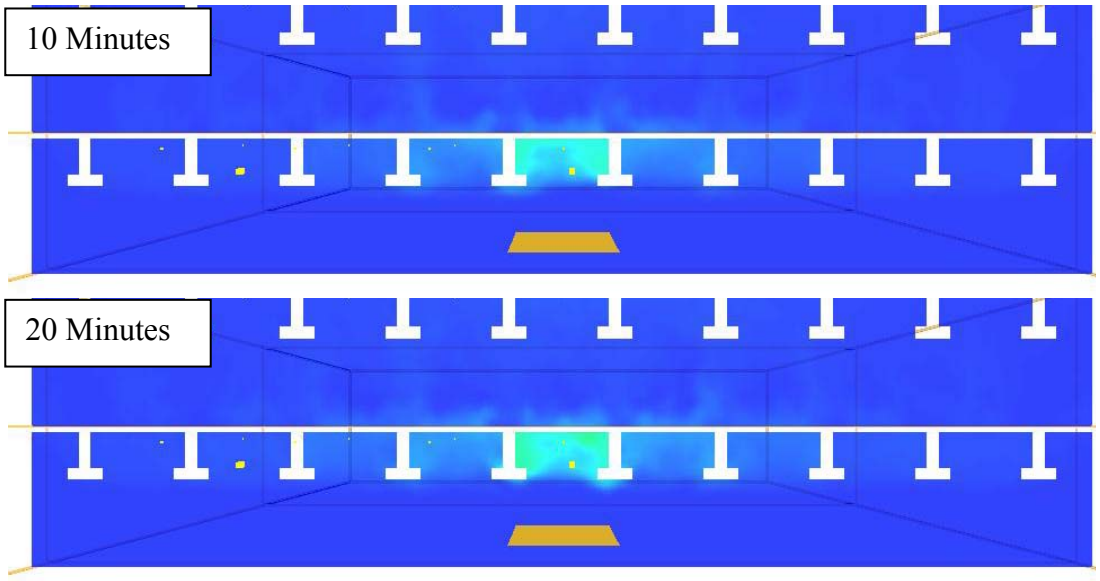

Figure 4-44: Continued from Figure 4-43.

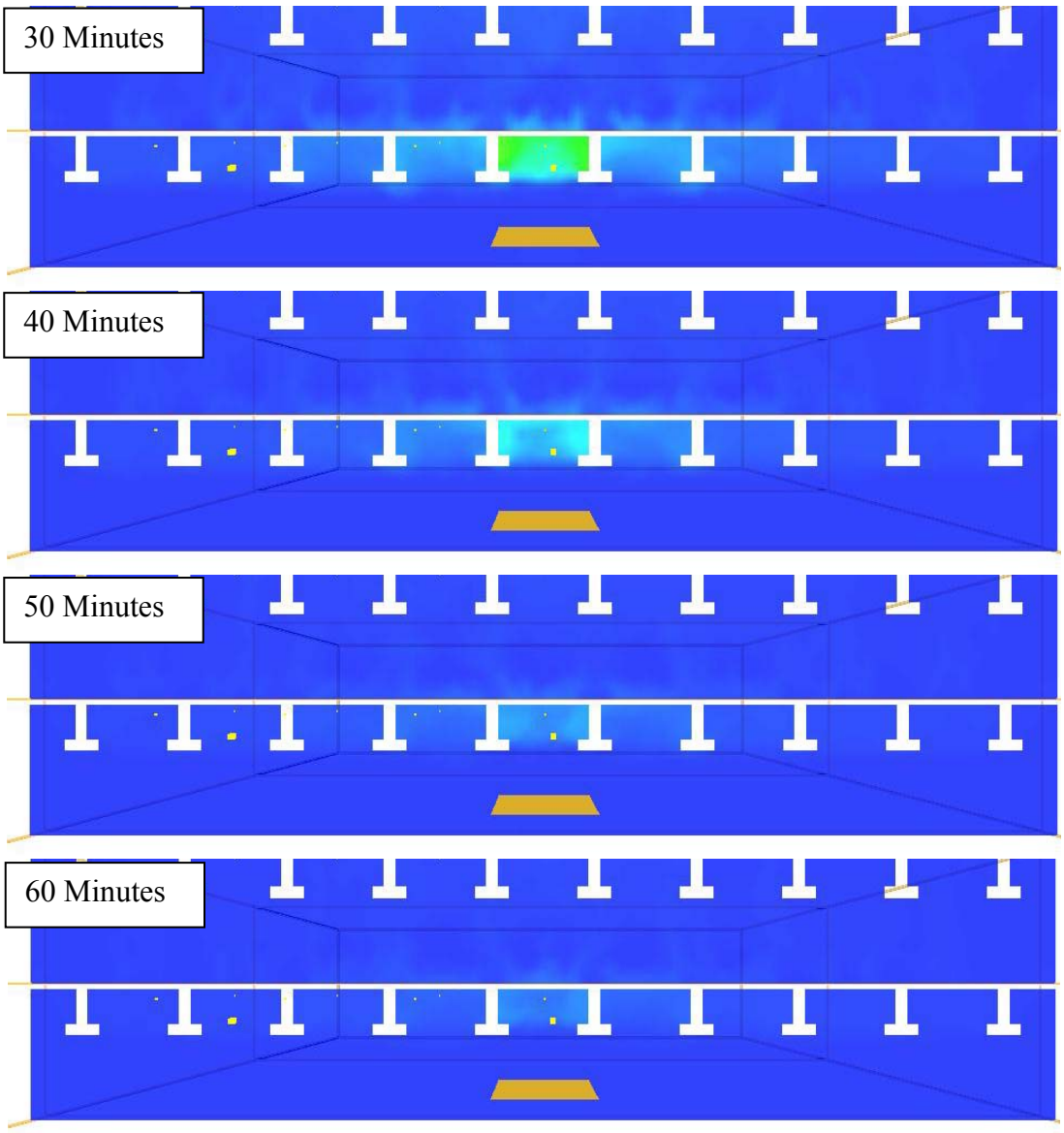

Figure 4-45: Continued from Figure 4-44.

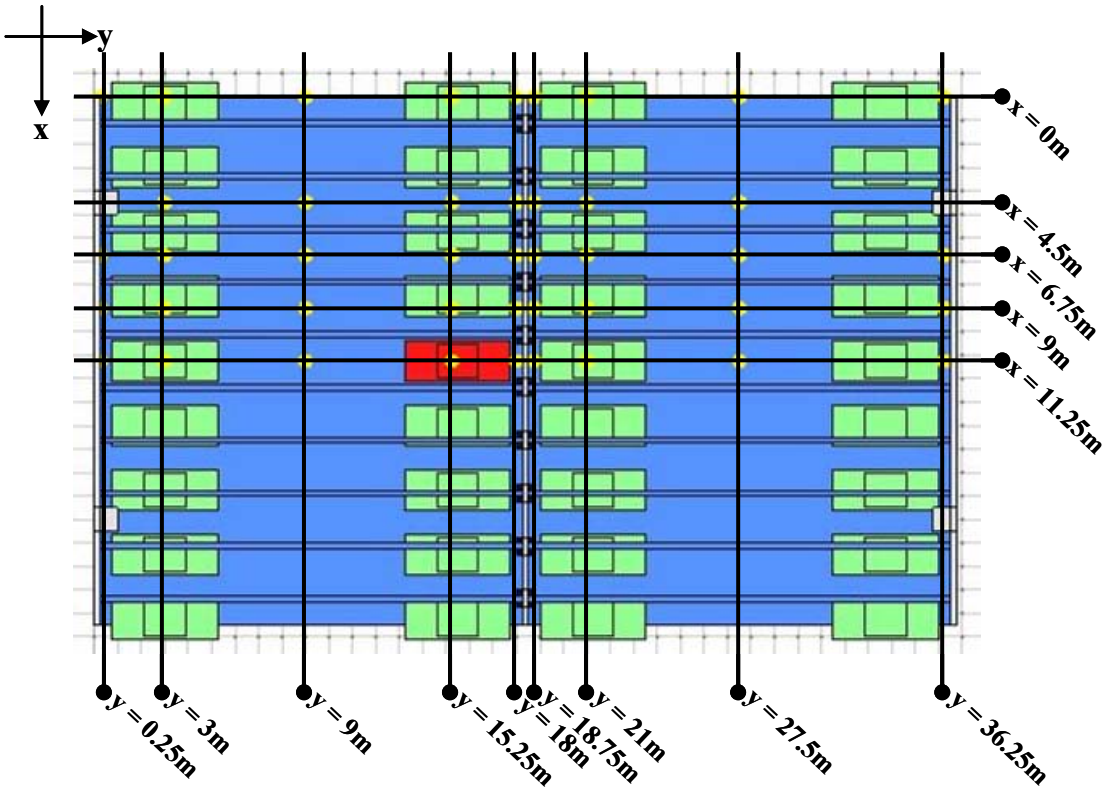

Figure 4-46: Plan view location key for thermocouples.

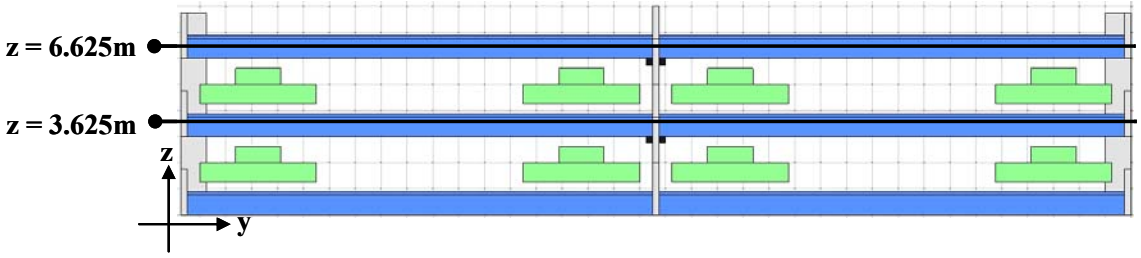

Figure 4-47: Elevation view location key for thermocouples.

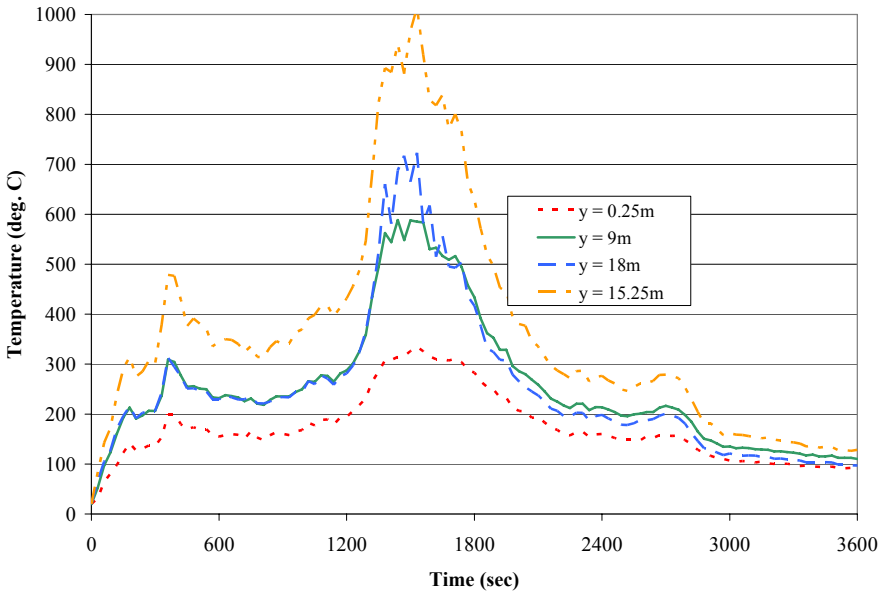

Figure 4-48: Time-temperature histories for Analysis 3 centered between double-tee webs above burning vehicle at x = 11.25m; y = 0.25m, 9.0m, 15.25m, 18.0m; z = 3.625m.

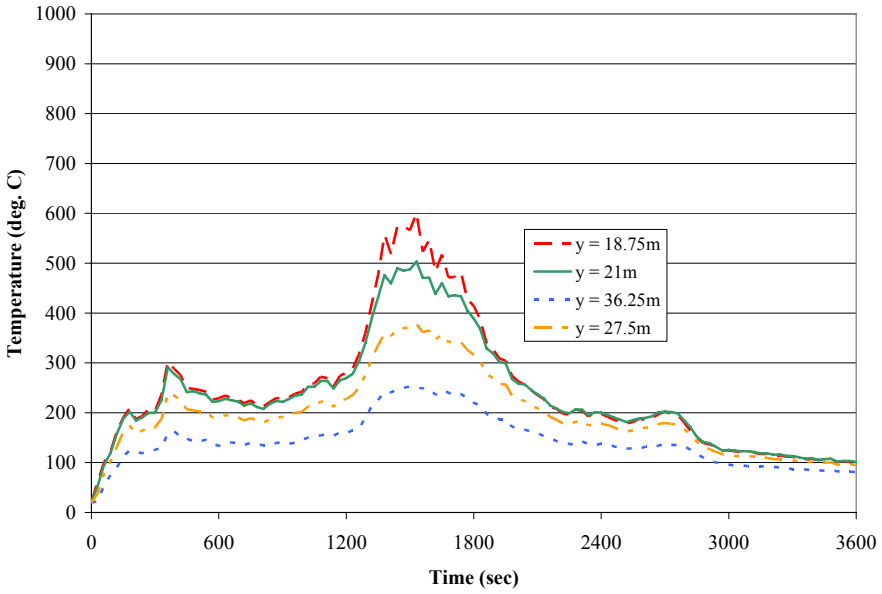

Figure 4-49: Time-temperature histories for Analysis 3 centered between double-tee webs above burning vehicle at x = 11.25m; y = 18.75m, 21.0m, 27.5m, 36.25m; z = 3.625m.

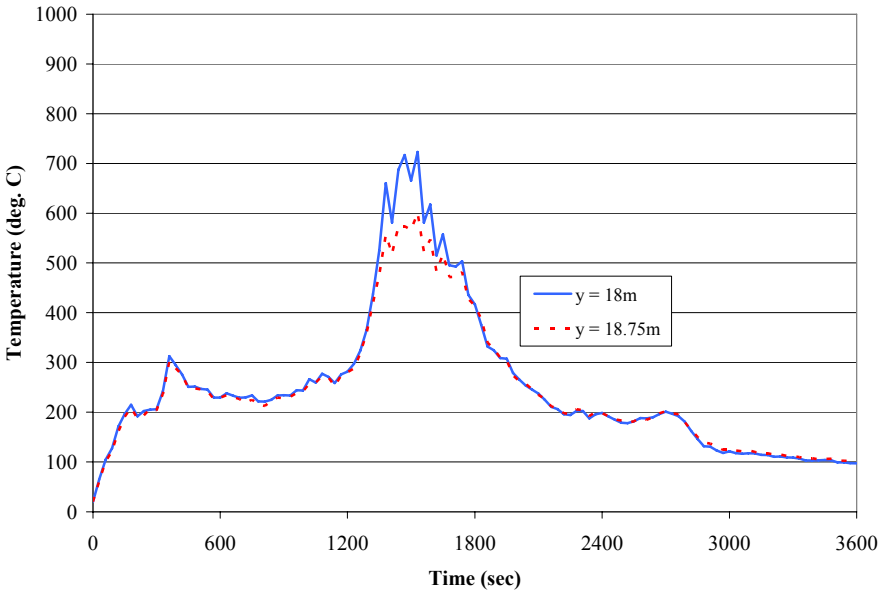

Figure 4-50: Time-temperature histories for Analysis 3 centered between double-tee webs above burning vehicle at x = 11.25m; y = 18.0m, 18.75m; z = 3.625m.

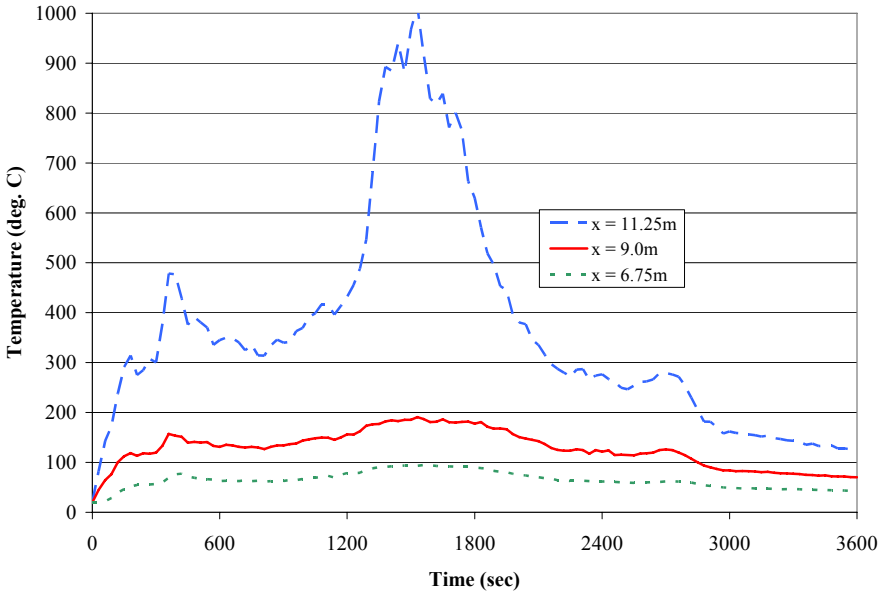

Figure 4-51: Time-temperature histories for Analysis 3 across double-tee webs at x = 11.25m, 9.0m, 6.75m,; y = 15.25m; z = 3.625m.

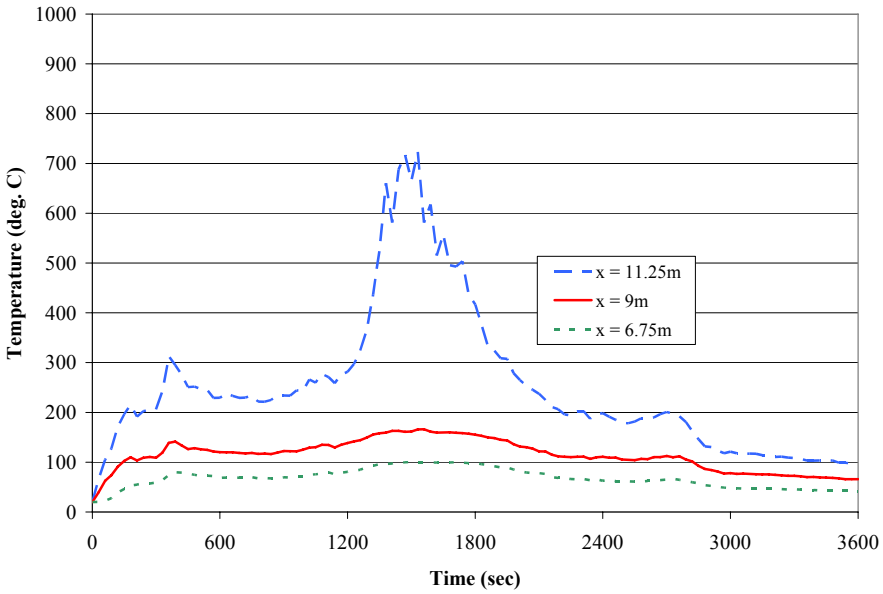

Figure 4-52: Time-temperature histories for Analysis 3 across double-tee webs at x = 11.25m, 9.0m, 6.75m; y = 18.0m; z = 3.625m.

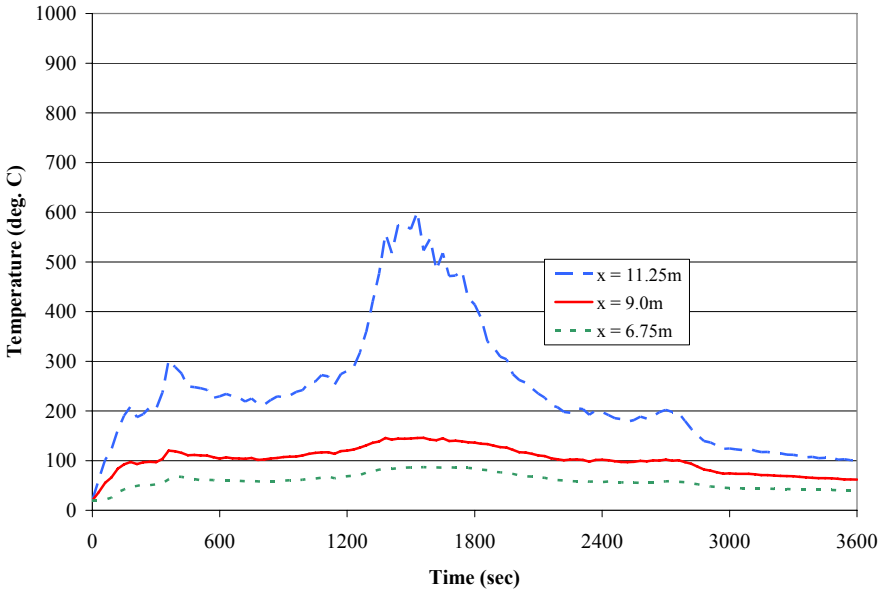

Figure 4-53: Time-temperature histories for Analysis 3 across double-tee webs at x = 11.25m, 9.0m, 6.75m,; y = 18.75m; z = 3.625m.

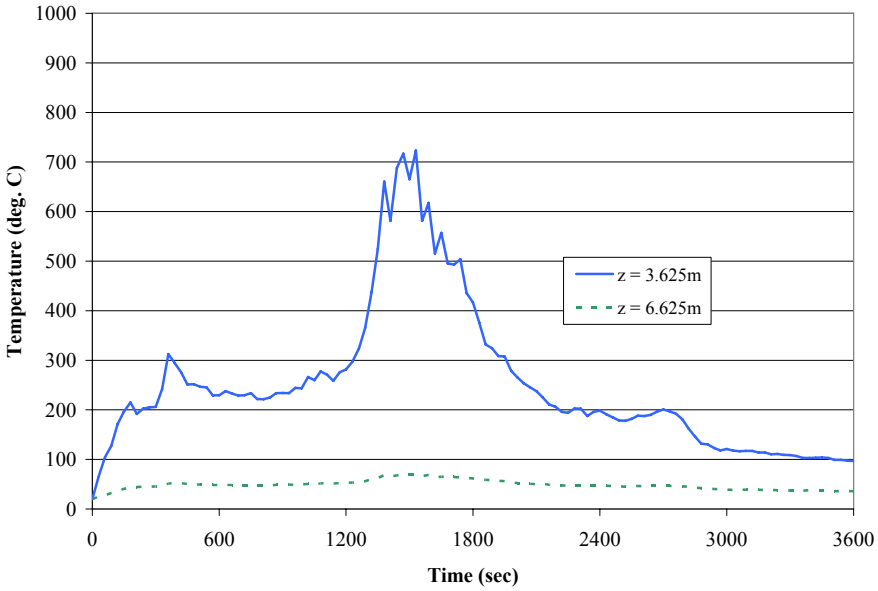

Figure 4-54: Time-temperature histories for Analysis 3 transferring from one floor to the next at x = 11.25m; y = 18.0m; z = 3.625m, 6.625m.

4.3.4 Analysis 4: Chimney 2 Analysis

The purpose of Analyses 3 and 4 was to investigate the effect of different vehicle fires on the heat flow and buildup through the structure. The geometry for both Analyses 3 and 4 is identical, with the opening in the center wall straddling the double-tee slab. Analysis 4 is the second of the two Chimney Analyses and uses a different vehicle fire heat release record from Analysis 3, namely the 5600cc heat release record from Khono et al. designated Vehicle 2, which was a full size Mercedes sedan from the early 1990's. The geometry of Analysis 4 is identical to Analysis 3.

Figure 4-55 shows the Vehicle 2 fire heat release record used as an input for Analysis 4. The heat release increases from 0 to 10 minutes to about 2500 kW, plateaus from 10 to 30 minutes at about 2500 kW, and peaks at about 6700 kW at about 37 minutes before dropping off rapidly. The total energy output and is 8110 MJ for this vehicle.

Slice images showing temperature distribution through the structure are shown in Figures 4-56 to 4-61. Images are shown at 10 minute intervals, and the slice location is shown by the diagram at the top of each figure. Figures 4-56 to 4-58 show a temperature slice located just below the slab above the burning vehicle at z = 3.625m. Once again it is observed that the heat builds up longitudinally between the double-tee webs with relatively little heat spilling over into adjacent double-tee cavities. Peak temperature is reached above the burning vehicle. The second set of images in this series are Figure 4-59 to 4-61, showing a transversely oriented temperature slice located 0.125m from the center wall at y = 18m.

Time-temperature plots taken from thermocouples throughout the structure are shown in Figures 4-62 to 4-70 and are broken into three series: longitudinal time-temperature plots (Figures 4-64 to 4-66), transverse time-temperature plots (Figures 4-67 to 4-69), and a vertical time-temperature plot (Figures 4-70).

The longitudinal time-temperature plots are shown for thermocouple locations centered between the double-tee webs in the cavity above the burning vehicle. Figure 4-64 shows four thermocouples distributed from y = 0.25m to y = 18m. The highest temperature recorded was 1149 degrees Celsius at y = 15.25m. Figure 4-65 shows a similar set of thermocouple time-temperature plots to Figure 4-64, but these are shown for the opposite side of the center wall. Once again, the temperature plot is generally lower as the distance from the center of the fire increases. Finally, Figure 4-66, shows two time-temperature plots, one on either side of the center wall. The thermocouple location closer to the fire at y = 18.0m shows higher recorded temperatures around the peak temperature than those at y = 18.75m but similar temperatures are recorded for the rest of the analysis.

The transverse time-temperature plots are shown in Figures 4-67 to 4-69 to show the how the heat spills under the double-tee webs from one cavity to the next. As before all five figures show that the majority of the heat is generally contained within the cavity above the burning vehicle, but, as the distance from the fire increases, the difference in temperature from one cavity to the next decreases.

The final time-temperature plot is Figures 4-70, which show the vertical temperature distribution along the center wall from one floor to the next. Figure 4-70 shows a plot of two thermocouples centered between the double-tee webs on above the burning vehicle at y = 18.0m and on both floors at z = 3.625m and 6.625m. Once again, despite the 'chimney' opening in the center wall, very little heat is shown to flow to the upper floor.

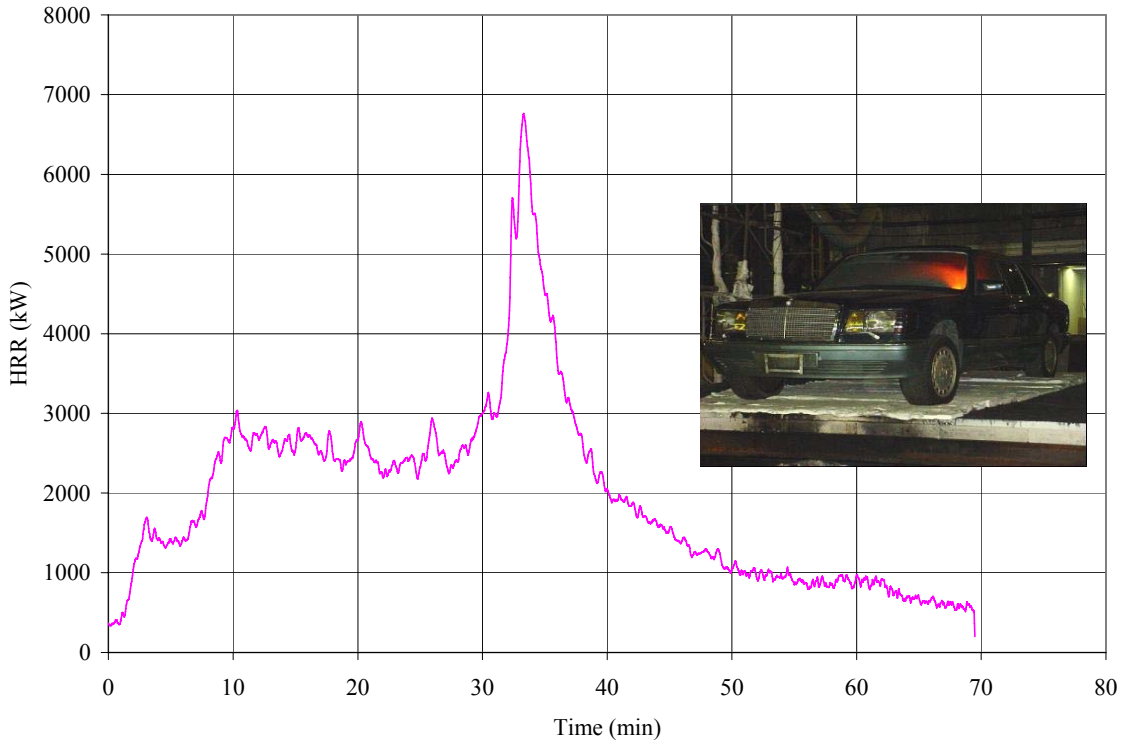

Figure 4-55: Heat release rate record for Vehicle 2.

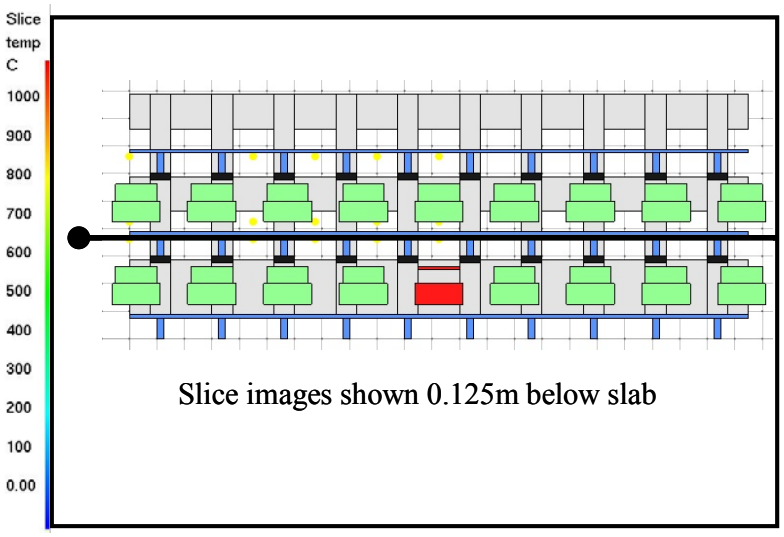

Figure 4-56: Slice images for Analysis 4 showing temperature distribution 0.125m below slab above burning vehicle (z = 3.625m). Images shown at 10 minute intervals (600sec) from time = 0 to 60 minutes. (0-3600sec) Temperature scale in degrees Celsius. Continued in Figures 4-57 and 4-58.

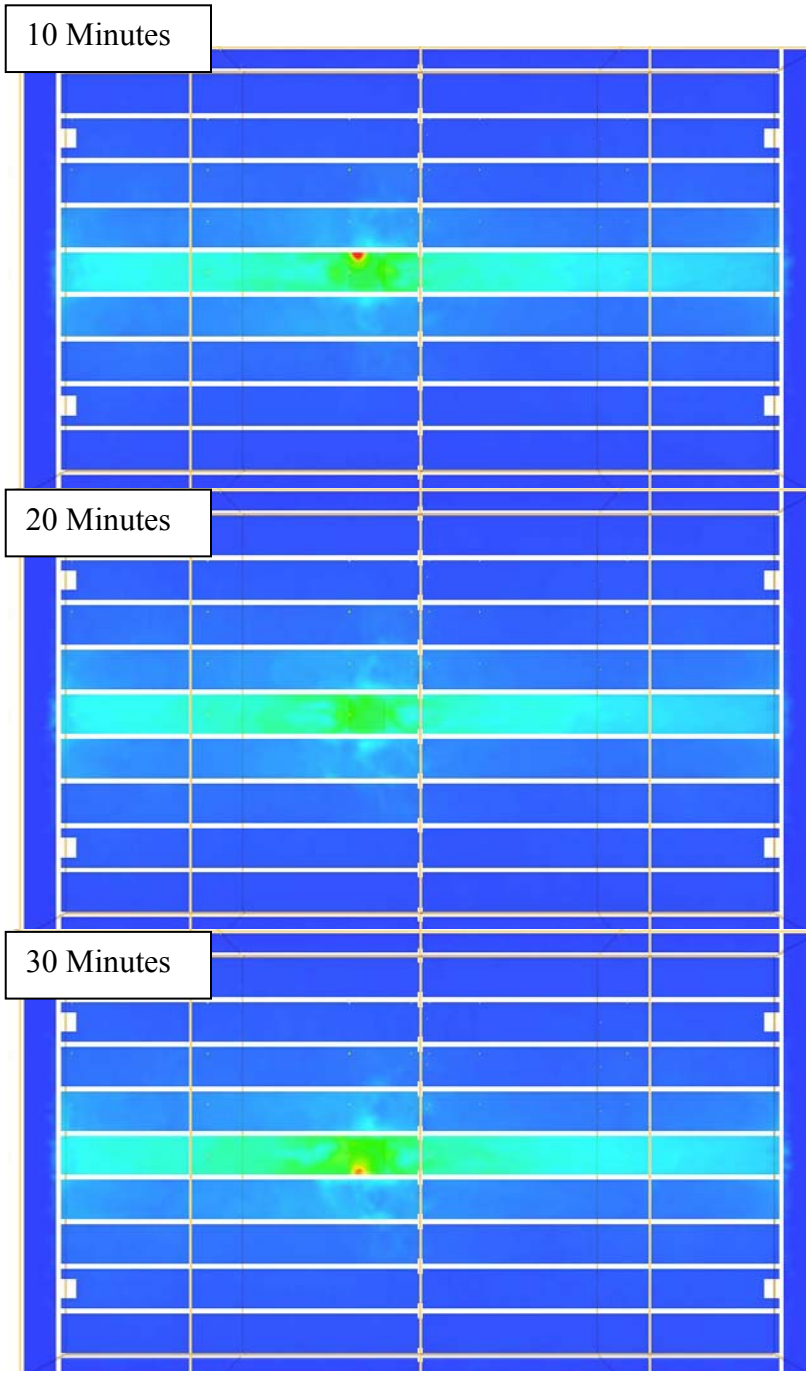

Figure 4-57: Continued from Figure 4-56.

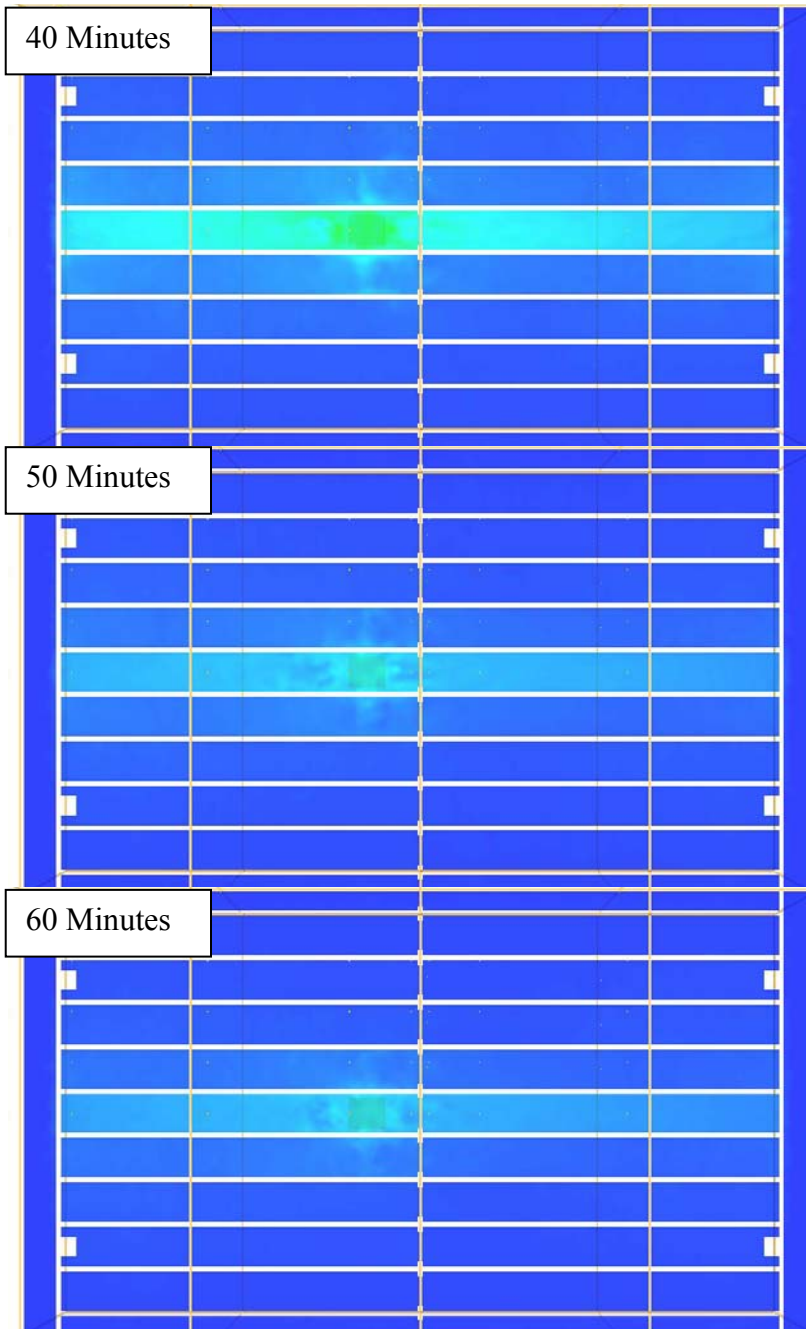

Figure 4-58: Continued from Figure 4-57.

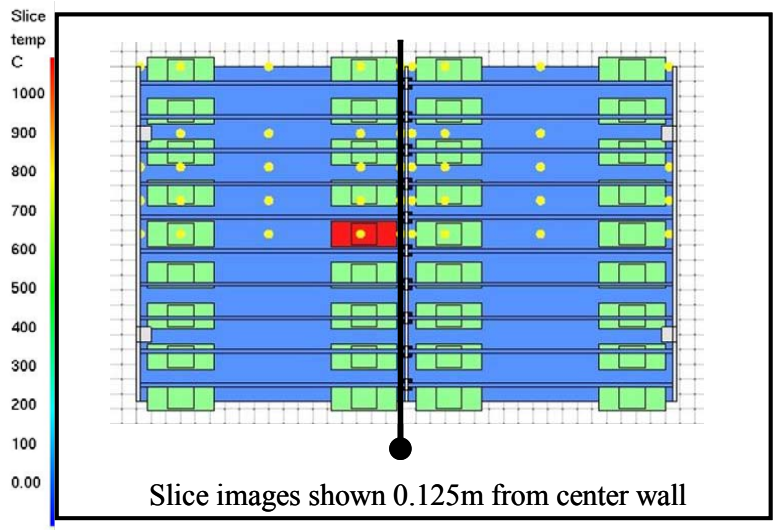

Figure 4-59: Slice images for Analysis 4 showing temperature distribution across double-tee webs next to the center wall (y = 18.0m). Images shown at 10 minute intervals (600sec) from time = 0 to 60 minutes. (0-3600sec) Temperature scale in degrees Celsius. Continued in Figures 4-60 and 4-61.

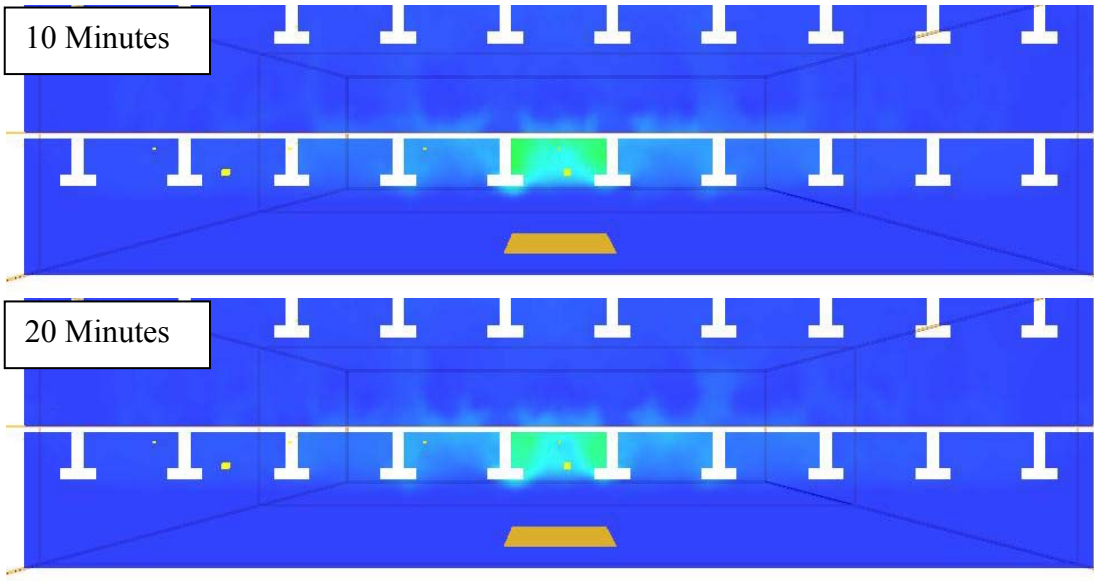

Figure 4-60: Continued from Figure 4-59.

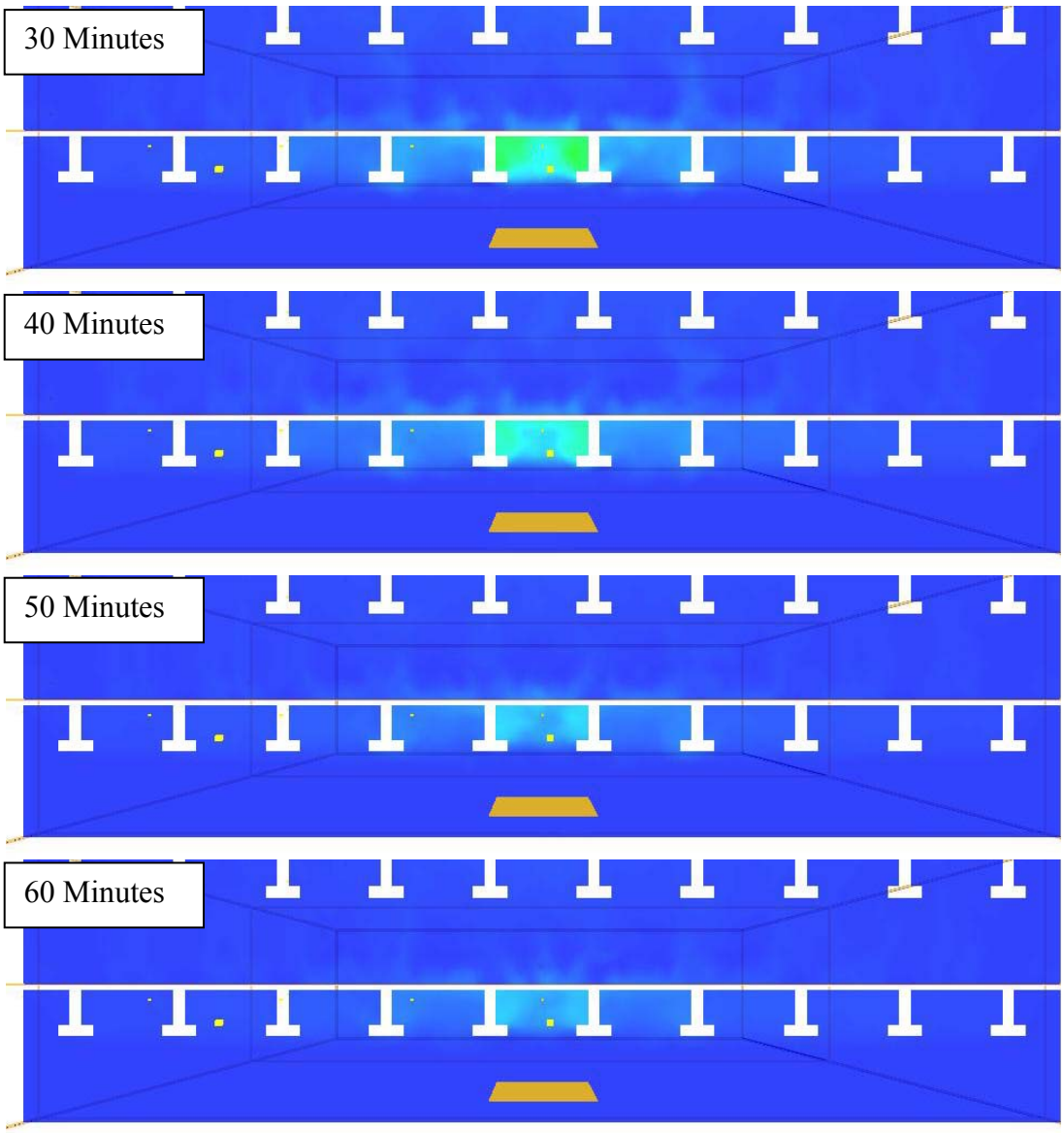

Figure 4-61: Continued from Figure 4-60.

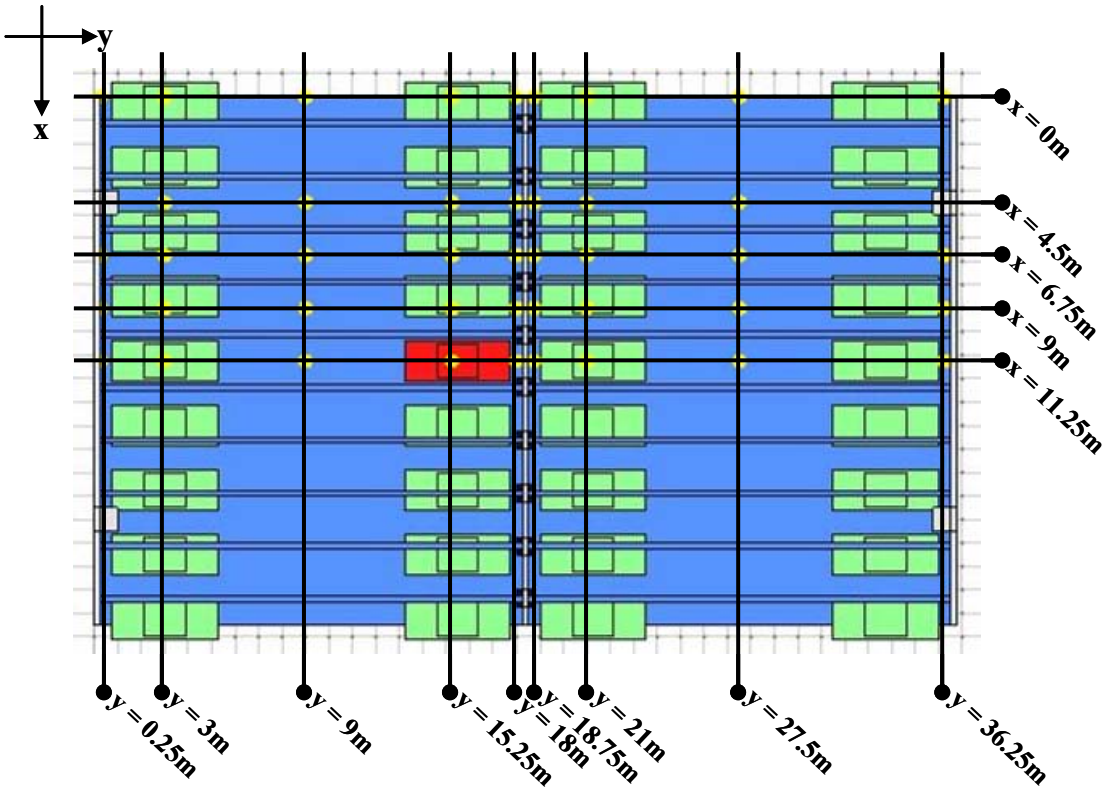

Figure 4-62: Plan view location key for thermocouples.

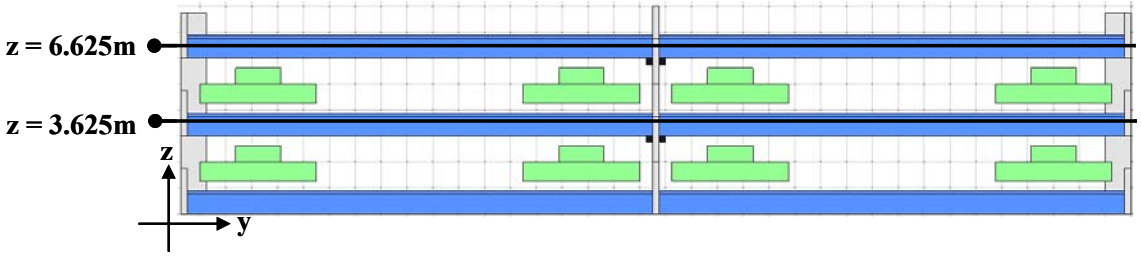

Figure 4-63: Elevation view location key for thermocouples.

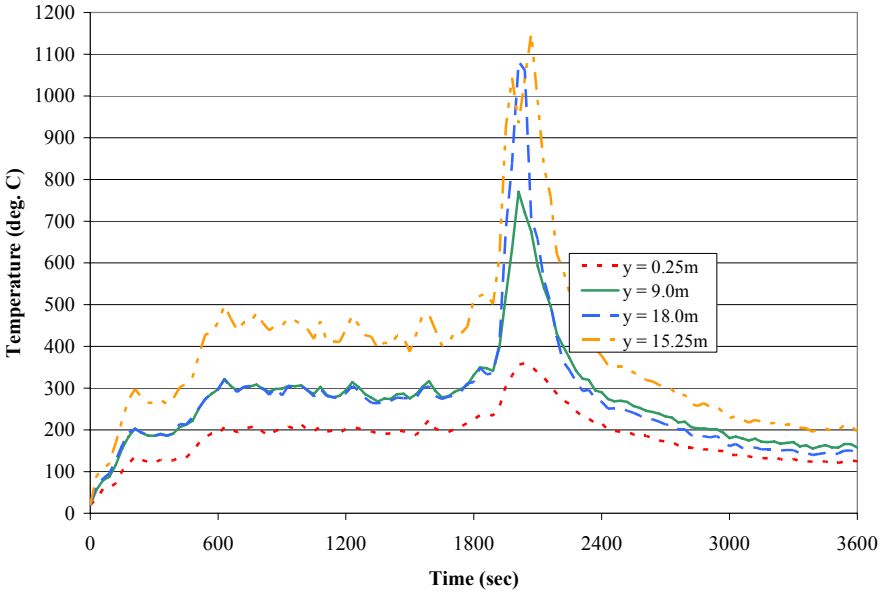

Figure 4-64: Time-temperature histories for Analysis 4 centered between double-tee webs above burning vehicle at x = 11.25m; y = 0.25m, 9.0m, 15.25m, 18.0m; z = 3.625m.

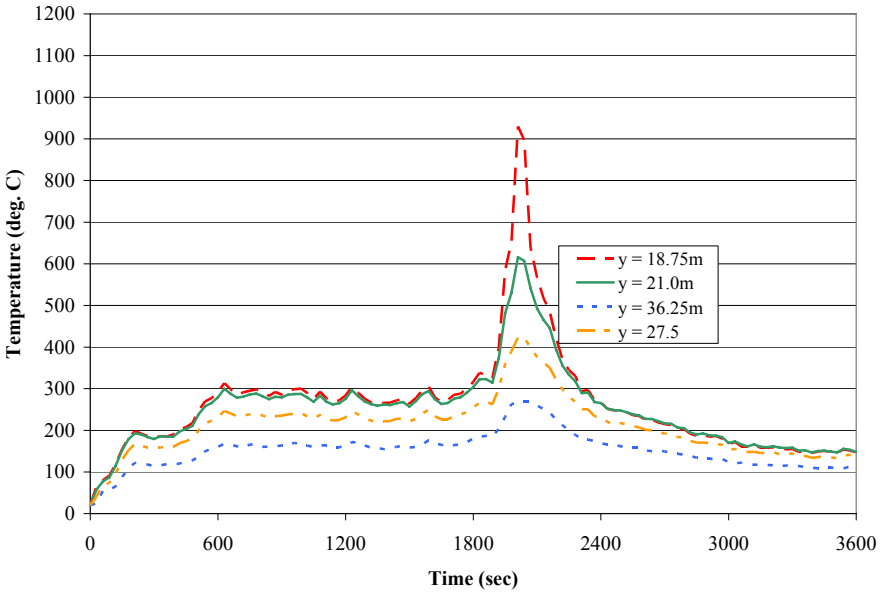

Figure 4-65: Time-temperature histories for Analysis 4 centered between double-tee webs above burning vehicle at x = 11.25m,; y = 18.75m, 21.0m, 27.5m, 36.25m; z = 3.625m.

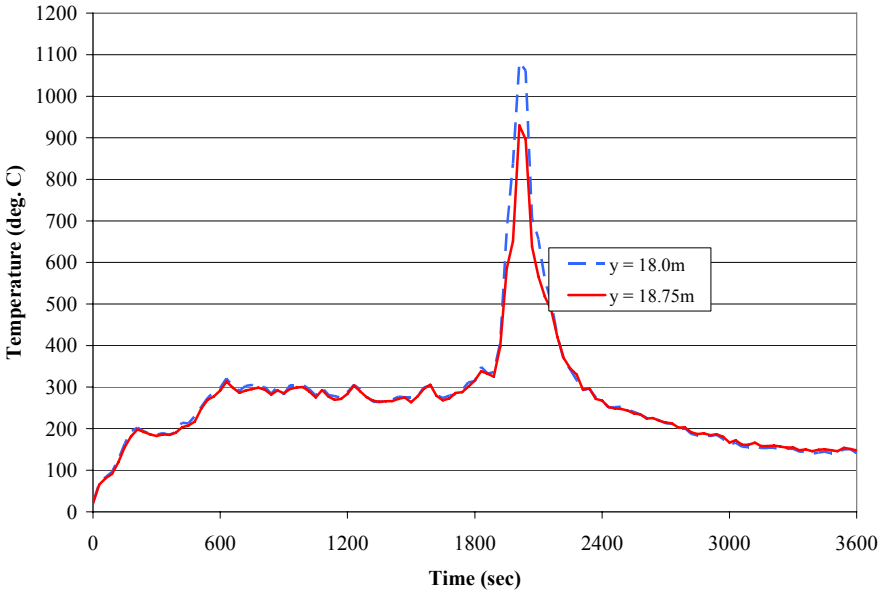

Figure 4-66: Time-temperature histories for Analysis 4 centered between double-tee webs above burning vehicle at x = 11.25m; y = 18.0m, 18.75m; z = 3.625m.

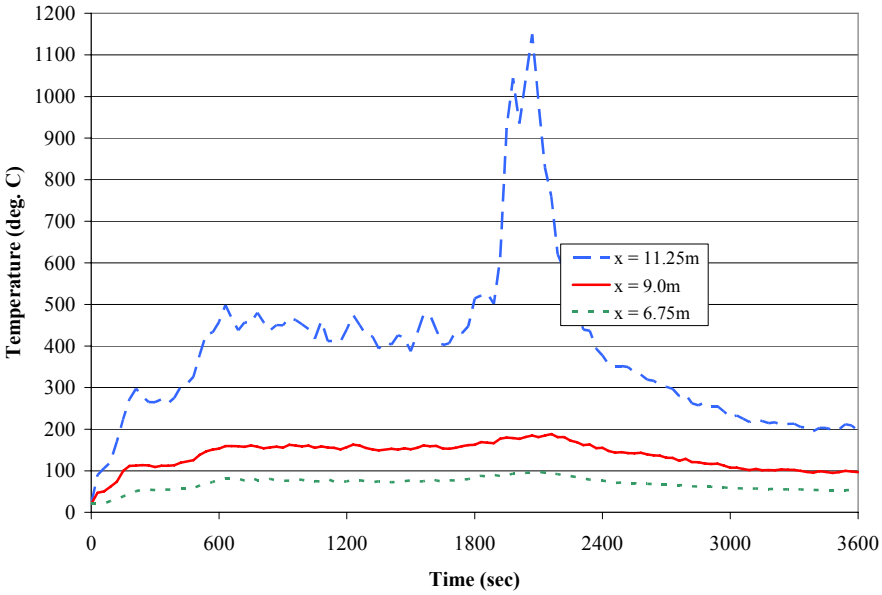

Figure 4-67: Time-temperature histories for Analysis 4 across double-tee webs at x = 11.25m, 9.0m, 6.75m; y = 15.25m; z = 3.625m.

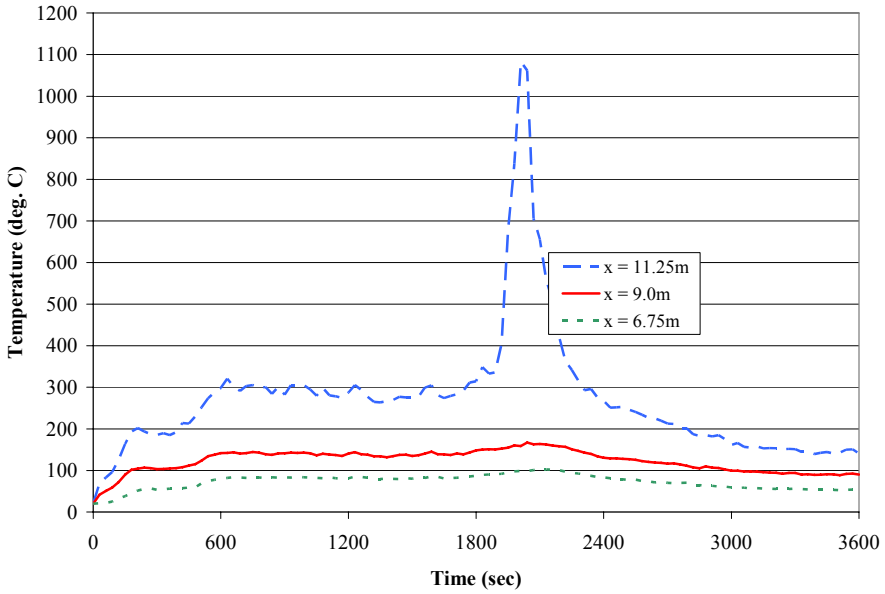

Figure 4-68: Time-temperature histories for Analysis 4 across double-tee webs at x = 11.25m, 9.0m, 6.75m; y = 18.0m; z = 3.625m.

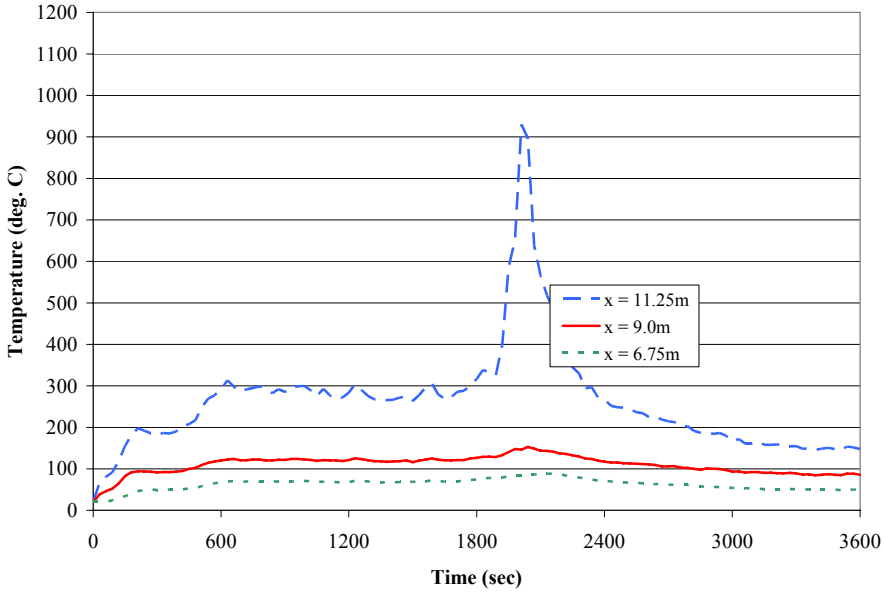

Figure 4-69: Time-temperature histories Analysis 4 across double-tee webs at x = 11.25m, 9.0m, 6.75m; y = 18.75m; z = 3.625m.

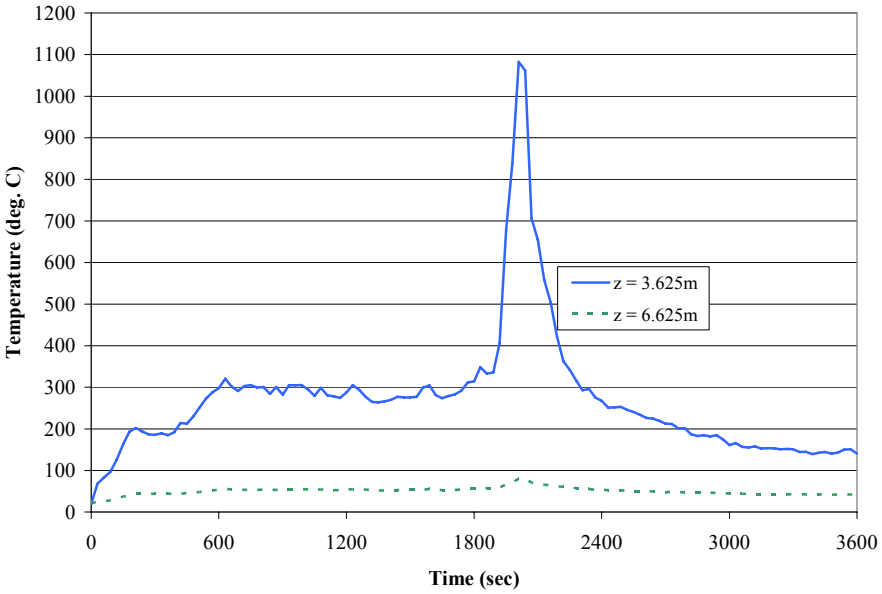

Figure 4-70: Time-temperature histories for Analysis 4 transferring from one floor to the next at x = 11.25m; y = 18.0m; z = 3.625m, 6.625m.

4.3.5 Analysis 5: Stagger 1 Analysis

The primary purpose of the Stagger Analyses was to investigate the potential heat spread from one floor to the next when the floors are evenly offset at the center wall. The secondary purpose was to examine the preheating of upper floors prior to ignition of the vehicle on those floors. Analysis 5 is the first analysis in this series with the only burning vehicle located on the first floor in the same position (23) as Analyses 1-4. The opening is located so that the top of the opening is flush with the bottom of the double-tee slab on the floor where the vehicle is burning as in the Analysis 1. The material properties and analysis parameters used conformed to those explained in Chapter 3.

The geometry of the Analysis 5 model is shown is Figures 4-71 and 4-72. Images are captured from PyroSim, and particular note should be taken of the opening position in the center wall shown in Figure 4-71 as it relates to the slabs, specifically that the top of the opening is flush with the bottom of the double-tee slab on the floor where the vehicle is burning and that the opposite slab is visible on the other side of the opening. Once again, the only structural obstructions to heat spread through the center wall are small protrusions into the cavity on either side of the openings.

Figures 4-73 to 4-75 show slice images of gas temperature distribution through the structure located just below the slab above the burning vehicle on the first floor at z = 3.625m and just below the slab on the other side of the center wall on the second floor at z = 5.125m. It may be observed that the heat flows through the center wall and up to the second floor with some heat loss as shown by the shading change from one side of the center wall to the other.

Additional slice images are shown in Figures 4-76 to 4-78. The slice is located directly above the burning vehicles centered between the double-tee webs at x = 11.25m and the heat flow from one floor to the next through the center wall is visible.

Time-temperature plots taken from thermocouples throughout the structure are shown in Figures 4-79 to 4-84 and are broken into two series: longitudinal time-temperature plots (Figures 4-81 to 4-83) and a single vertical time-temperature plot (Figure 4-84).

The longitudinal time-temperature plots are shown for thermocouple locations centered between the double-tee webs in the cavity above the burning vehicle. Figure 4-81 shows four thermocouples distributed on the first floor from y = 0.25m to y = 18m. The highest temperature recorded was 959 degrees Celsius at y = 15.25m. As before, temperatures were generally lower as the distance from the center of the fire increased. Figure 4-82 shows a similar set of thermocouple time-temperature plots to Figure 4-81, but these are shown for the opposite side of the center wall on the second floor with a peak recorded

temperature of 354 degrees Celsius at y = 18.75m. Once again, the temperature plot is generally lower as the distance from the center of the fire increases. Finally, Figure 4-83 shows another set of thermocouples arrayed on the third floor just as those on the first floor. The peak recorded temperature for the third floor was 104 degrees Celsius at y = 18.0m.

The final time-temperature plot shown for Analysis 5 is a comparison between thermocouple locations on the first, second, and third floors (See Figure 4-84). The readings were taken centered above the burning vehicle on the first floor and mirrored on the second and third floor in anticipation of comparison with data from Analyses 6-8. The heat flow from the first floor vehicle burn to the upper floors is clearly evident.

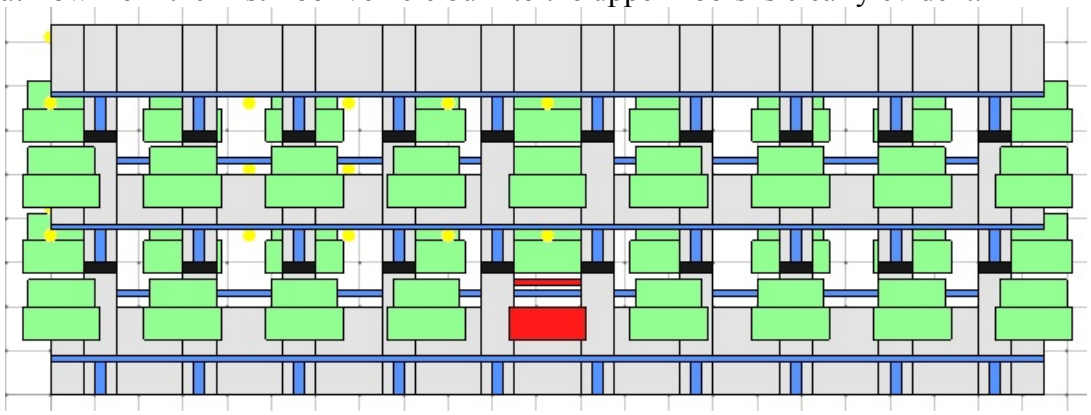

Figure 4-71: View of the center wall of Analysis 5 model.

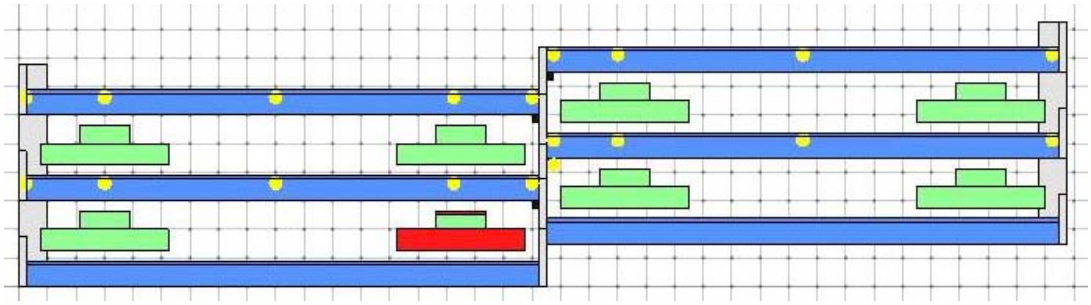

Figure 4-72: Elevation view of the Analysis 5 model showing the burning vehicle position next to the center wall on the first floor.

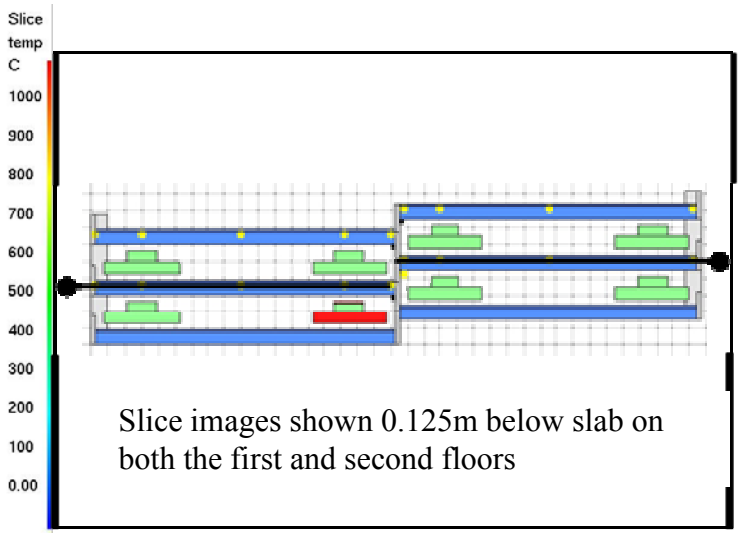

Figure 4-73: Slice images for Analysis 5 showing temperature distribution 0.125m below slab above burning vehicle on the first floor (z = 3.625m – left side) and 0.125m below slab on the second floor (z = 5.125m – right side). Images shown at 10 minute intervals (600sec) from time = 0 to 60 minutes. (0-3600sec) Temperature scale in degrees Celsius. Continued in Figures 4-74 and 4-75.

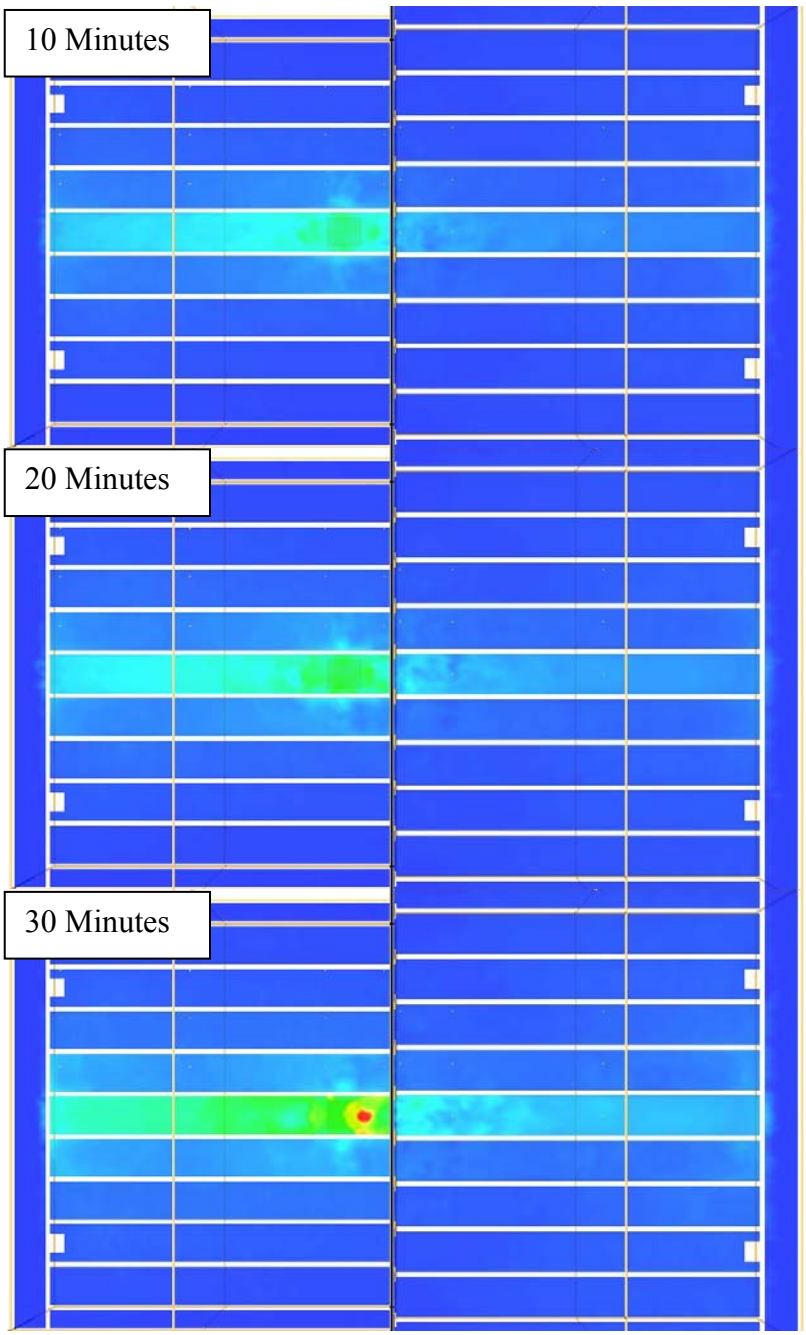

Figure 4-74: Continued from Figure 4-73.

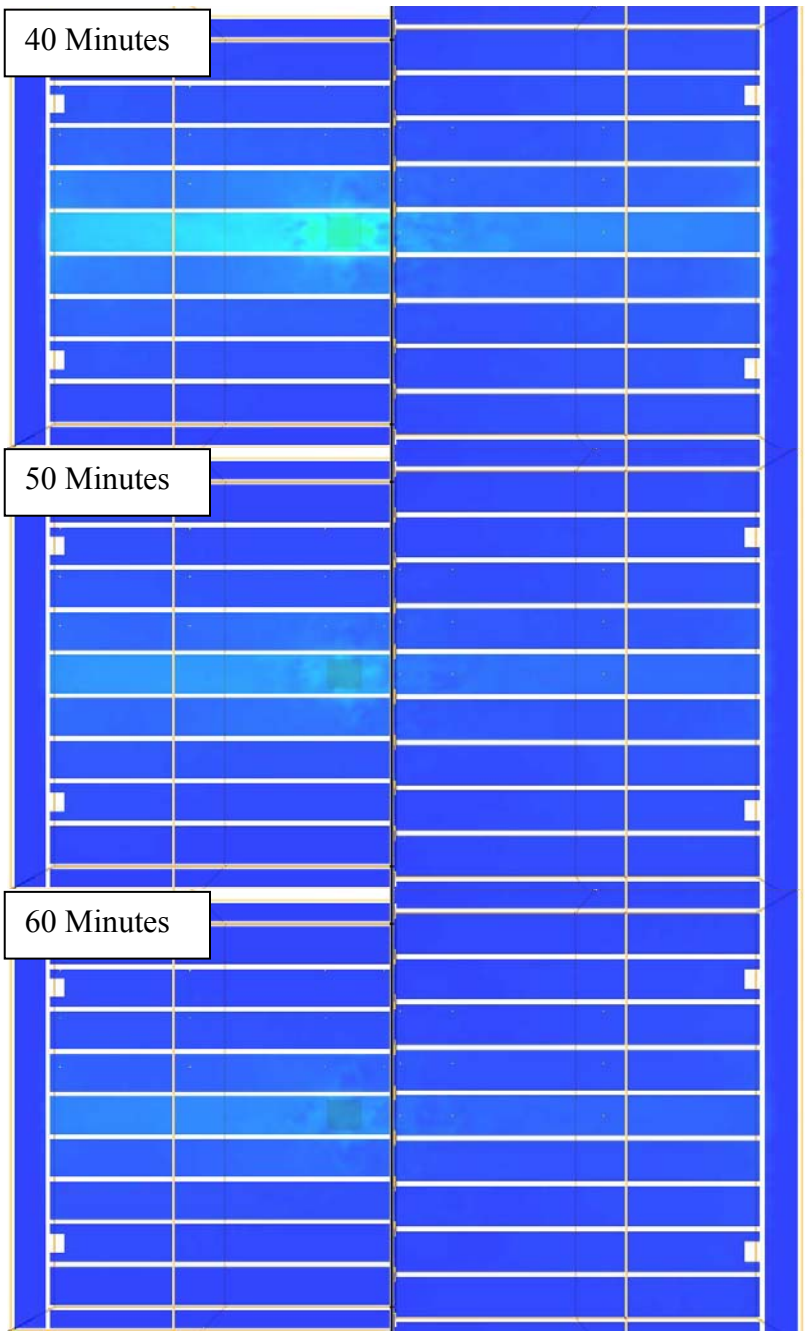

Figure 4-75: Continued from Figure 4-74.

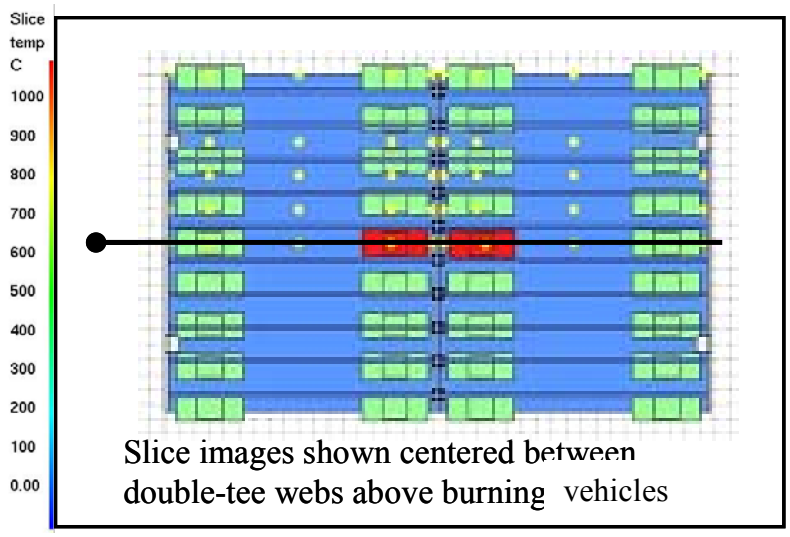

Figure 4-76: Slice images for Analysis 5 showing temperature distribution centered between double-tee webs above burning vehicles (x = 11.25m). Images shown at 6 minute intervals (360sec) from time = 6 to 60 minutes. (360-3600sec) Temperature scale in degrees Celsius. Continued in Figures 4-77 and 4-78.

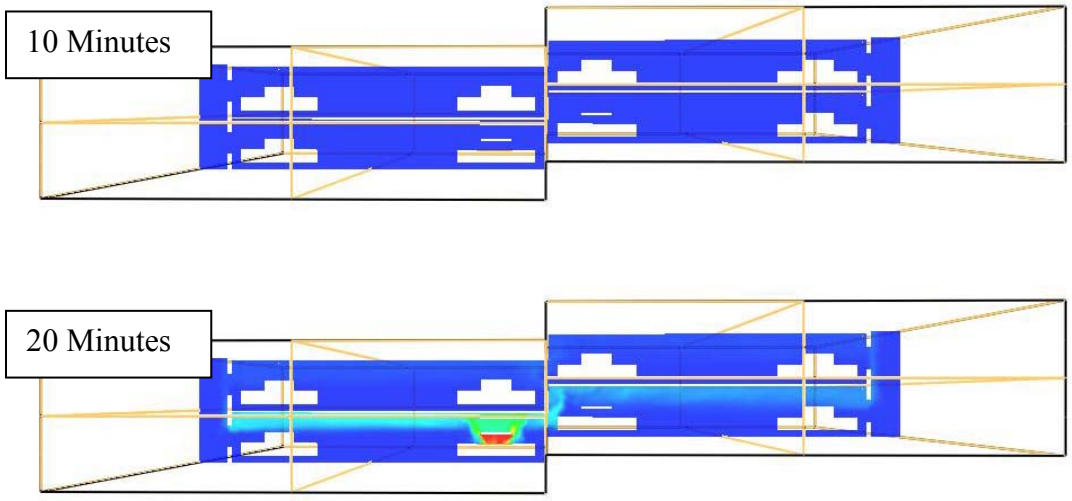

Figure 4-77: Continued from Figure 4-76.

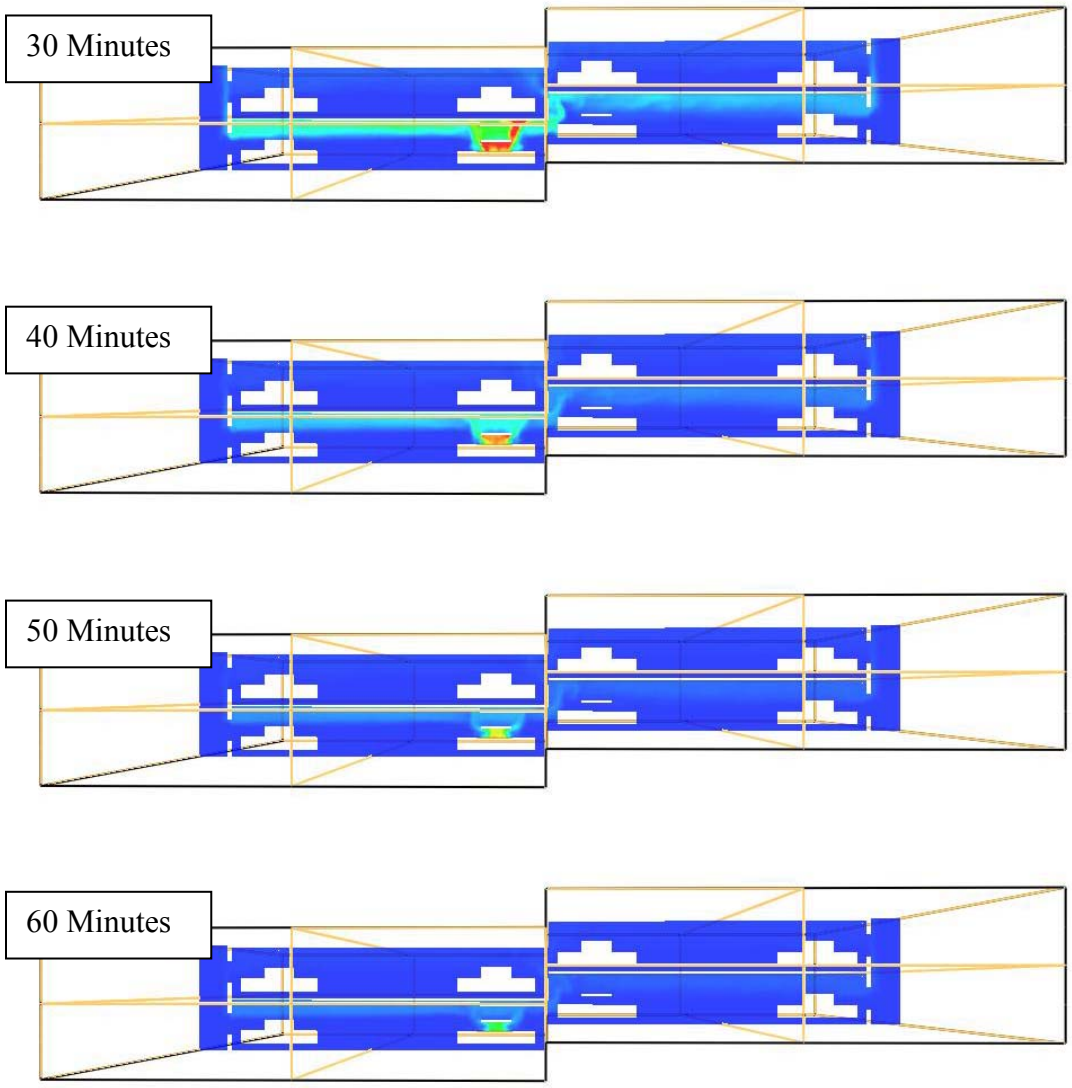

Figure 4-78: Continued from Figure 4-77.

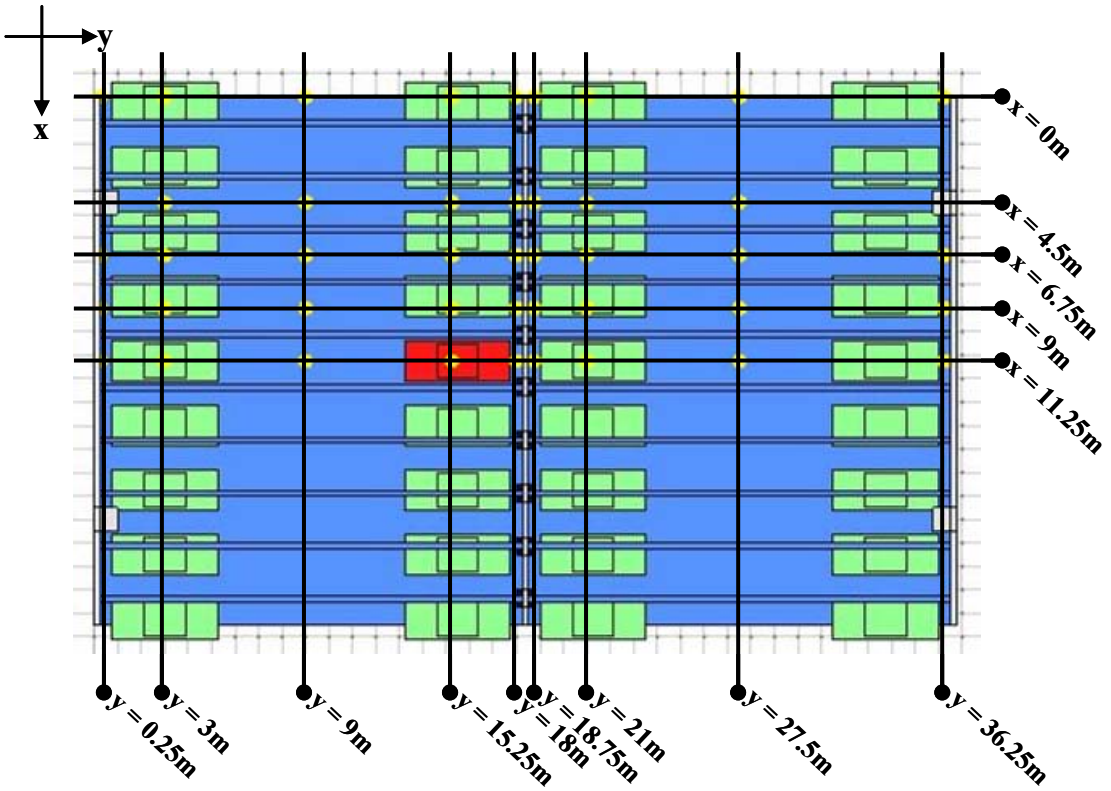

Figure 4-79: Plan view location key for thermocouples.

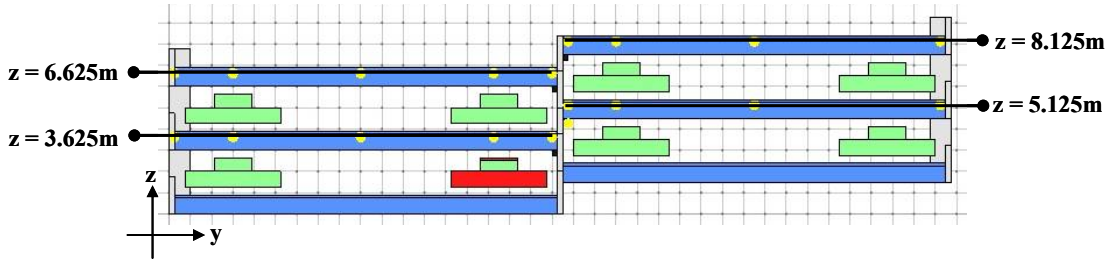

Figure 4-80: Elevation view location key for thermocouples.

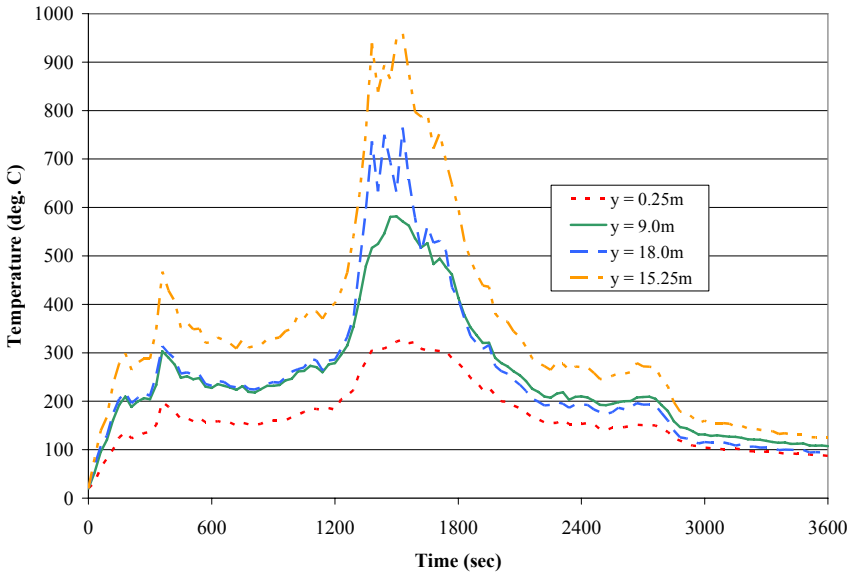

Figure 4-81: Time-temperature histories for Analysis 5 centered between double-tee webs above burning vehicle on floor 1 at x = 11.25m; y = 0.25m, 9.0m, 15.25m, 18.0m; z = 3.625m.

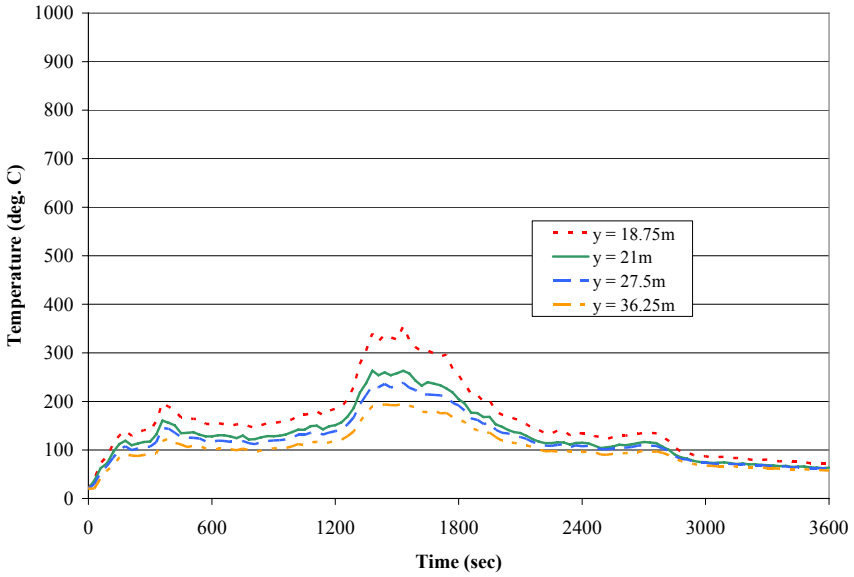

Figure 4-82: Time-temperature histories for Analysis 5 centered between double-tee webs on the opposite side of the center wall from vehicle on floor 2 at x = 11.25m; y = 18.75m, 21.0m, 27.5m, 36.25m; z = 5.125m.

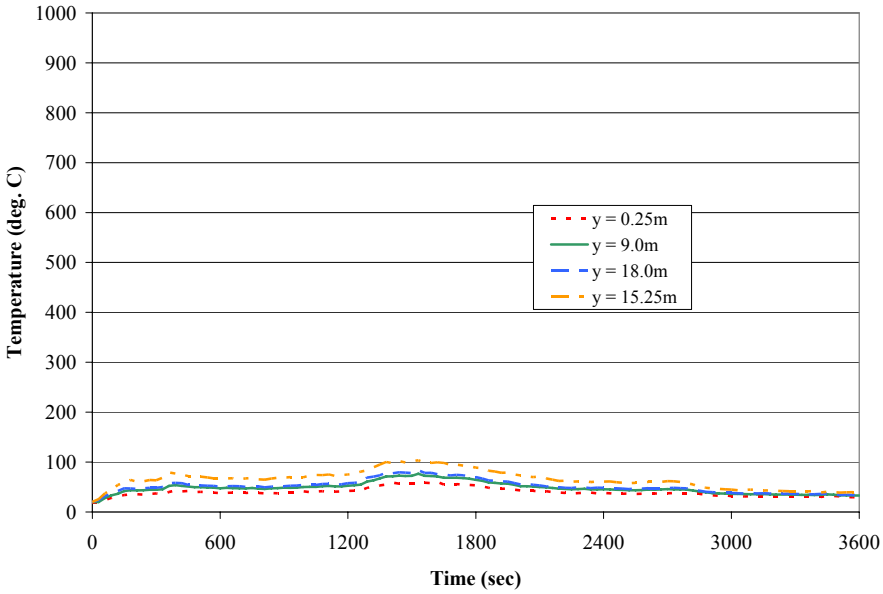

Figure 4-83: Time-temperature histories for Analysis 5 centered between double-tee webs on floor 3 at x = 11.25m; y = m, 18.75m; z = 3.625m.

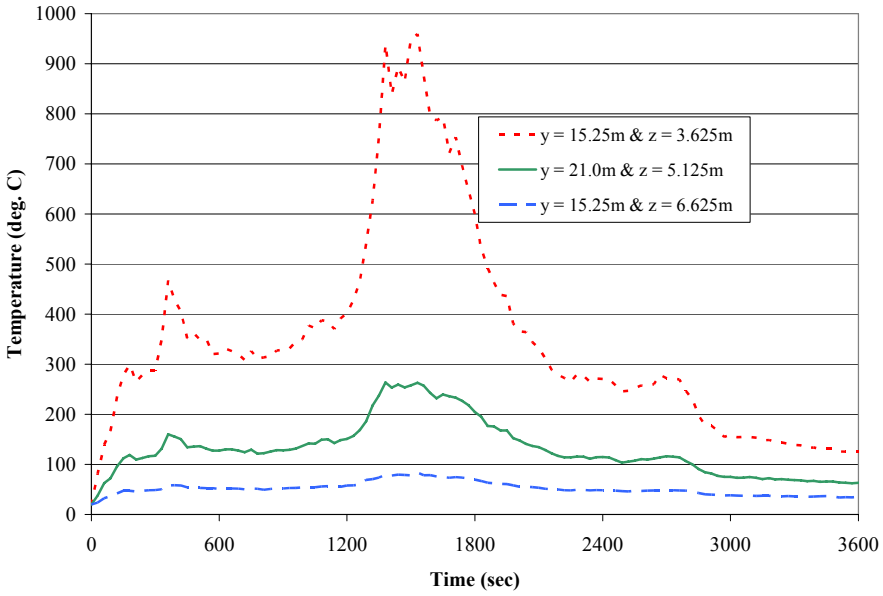

Figure 4-84: Time-temperature histories for Analysis 5 on floors 1, 2, and 3 at x = 11.25m; y = 15.25m/z = 3.625m, y = 21.0m/z = 5.125m; and y = 15.25m/z = 6.625m.

4.3.6 Analysis 6: Stagger 2 Analysis

Analysis 6 is the second analysis in the Stagger Analysis series with the only burning vehicle located on the second floor in the 14 position from Figure 3-16. For further details of the analysis geometry, see the discussion in Section 4.3.5. The material properties and analysis parameters used conformed to those explained in Chapter 3, and transverse and longitudinal elevation views are shown in Figures 4-85 and 4-86.

Slice images showing temperature distribution through the structure are shown in Figures 4-87 and 4-89. Images are shown at 10 minute intervals, and the slice location is shown by the diagram at the top of each figure. Figures 4-87 to 4-89 show a temperature slice located just below the slab above the burning vehicle on the second floor at z = 5.125m and just below the slab on the other side of the center wall on the third floor at z = 6.625m. As before, it may be observed that the heat flows through the center wall and up to the third floor with some heat loss as shown by the shading change from one side of the center wall to the other.

Additional slice images are shown in Figures 4-90 to 4-92. The slice is located directly above the burning vehicles centered between the double-tee webs at x = 11.25m and the heat flow from one floor to the next through the center wall is visible.

Once again, time-temperature plots taken from thermocouples throughout the structure are shown in Figures 4-93 to 5-98 and are broken into two series: longitudinal time-temperature plots (Figures 4-95 to 4-97) and a single vertical time-temperature plot (Figure 4-98). It should be noted that these plots show identical thermocouple locations to Analysis 5 for comparative purposes.

The longitudinal time-temperature plots are shown for thermocouple locations centered between the double-tee webs in the cavity above the burning vehicle. Figure 4-95 shows four thermocouples distributed on the first floor from y = 0.25m to y = 18m. The highest temperature recorded was 20 degrees Celsius at y = 18.0m showing no recorded temperature increase one floor down from the fire. Figure 4-96 shows a similar set of thermocouple time-temperature plots to Figure 4-95, but these are shown for the opposite side of the center wall on the second floor with a peak recorded temperature of 1024 degrees Celsius at y = 21.0m directly above the burning vehicle. Once again, the temperature plot is generally lower as the distance from the center of the fire increases. Finally, Figure 4-97 shows another set of thermocouples arrayed on the third floor just as those on the first floor. The peak recorded temperature for the third floor was 189 degrees Celsius at y = 18.0m.

As in Analysis 5, the final time-temperature plot shown for Analysis 6 is a comparison between thermocouple locations on the first, second, and third floors (See Figure 4-98). The readings were taken centered above the burning vehicle on the first floor and mirrored on the second and third floor in anticipation of comparison with data from Analyses 5, 7, and 8. The heat flow from the second floor vehicle burn to the third floor is shown, and the negligible heat flow to the first floor is also seen.

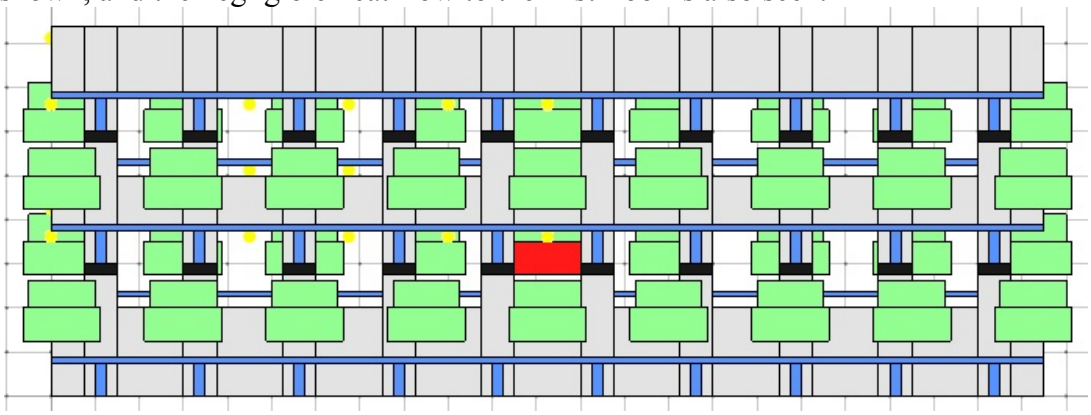

Figure 4-85: View of the center wall of Analysis 6 model showing center wall opening position and the burning vehicle centered in between the double-tee stems.

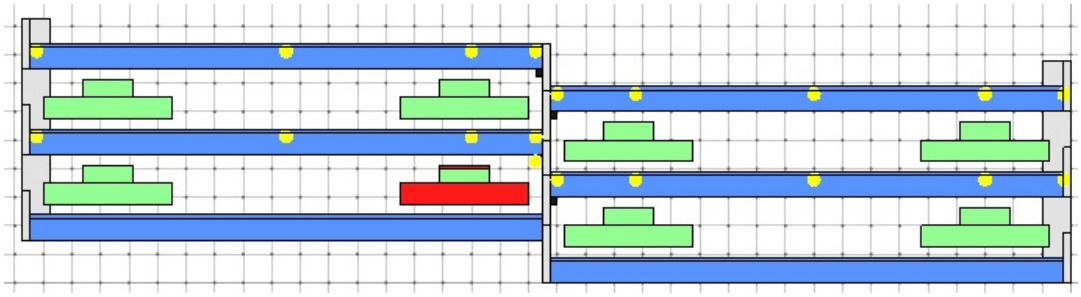

Figure 4-86: Elevation view of the Analysis 6 model showing the burning vehicle position next to the center wall on the second floor.

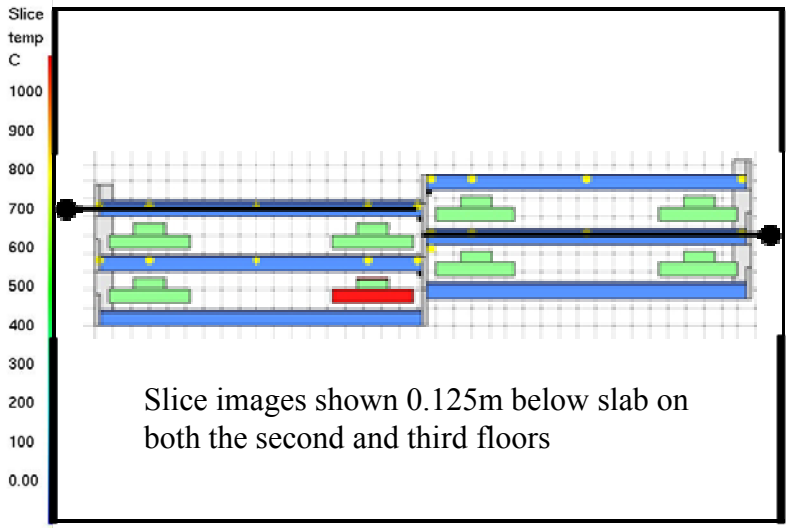

Figure 4-87: Slice images for Analysis 6 showing temperature distribution 0.125m below slab above burning vehicle on the second floor (z = 5.125m – right side) and 0.125m below slab on the third floor (z = 6.625m – left side). Images shown at 10 minute intervals (600sec) from time = 0 to 60 minutes. (0-3600sec) Temperature scale in degrees Celsius. Continued in Figures 4-88 and 4-89.

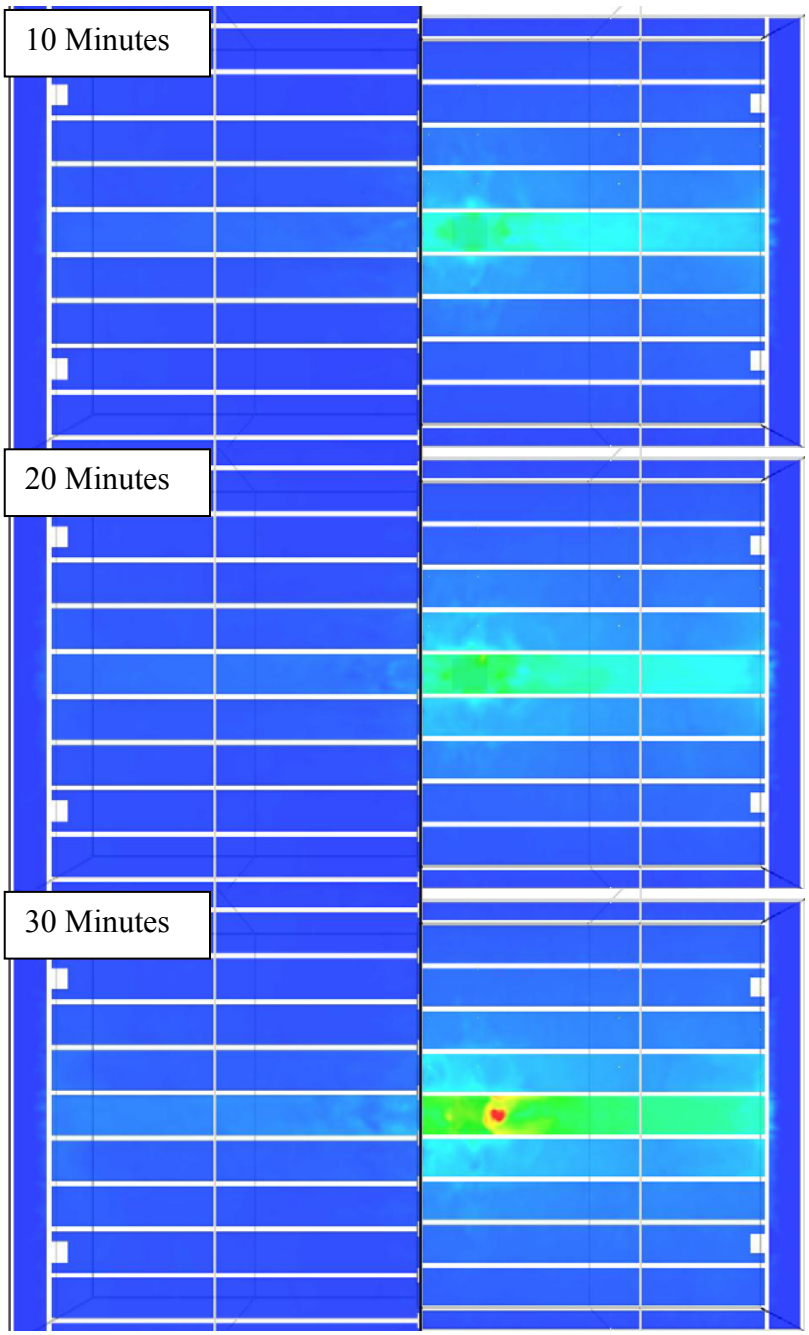

Figure 4-88: Continued from Figure 4-84.

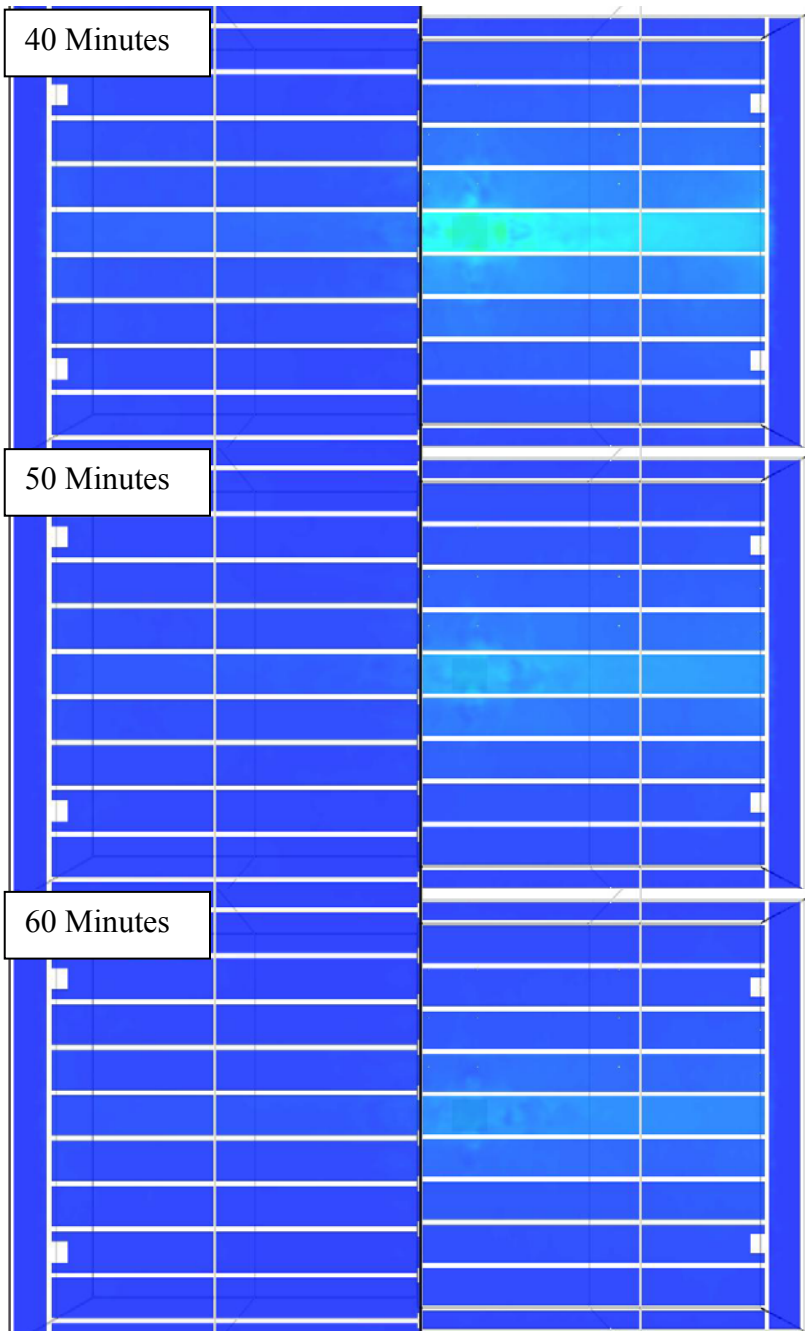

Figure 4-89: Continued from Figure 4-85.

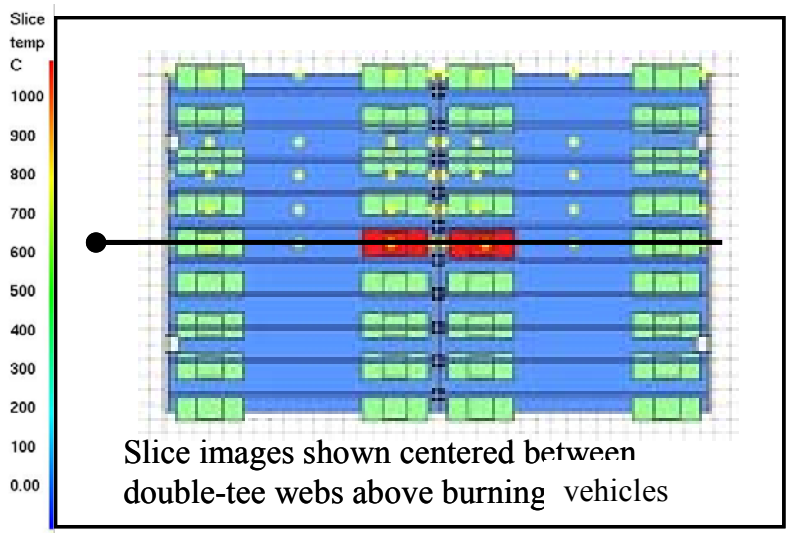

Figure 4-90: Slice images for Analysis 6 showing temperature distribution centered between double-tee webs above burning vehicles (x = 11.25m). Images shown at 6 minute intervals (360sec) from time = 6 to 60 minutes. (360-3600sec) Temperature scale in degrees Celsius. Continued in Figures 4-91 and 4-92.

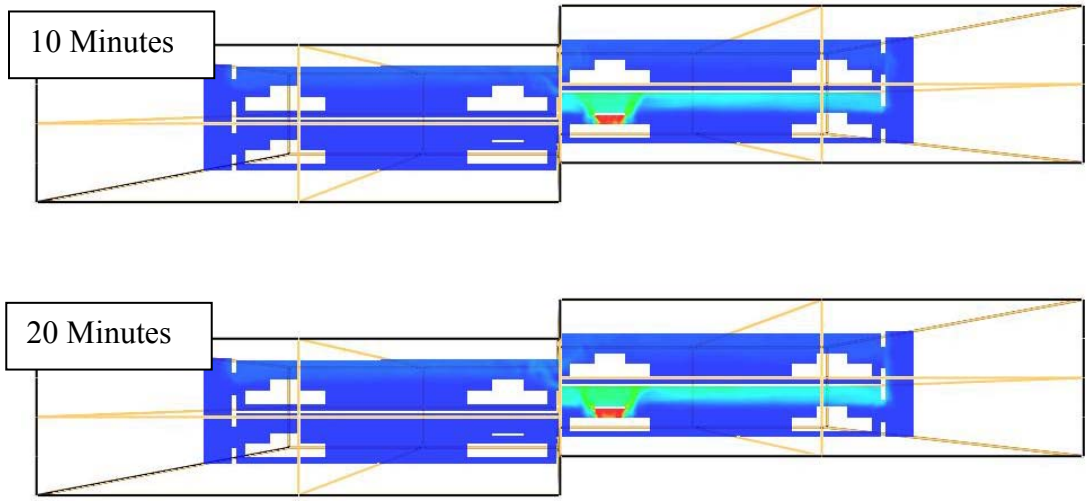

Figure 4-91: Continued from Figure 4-90.

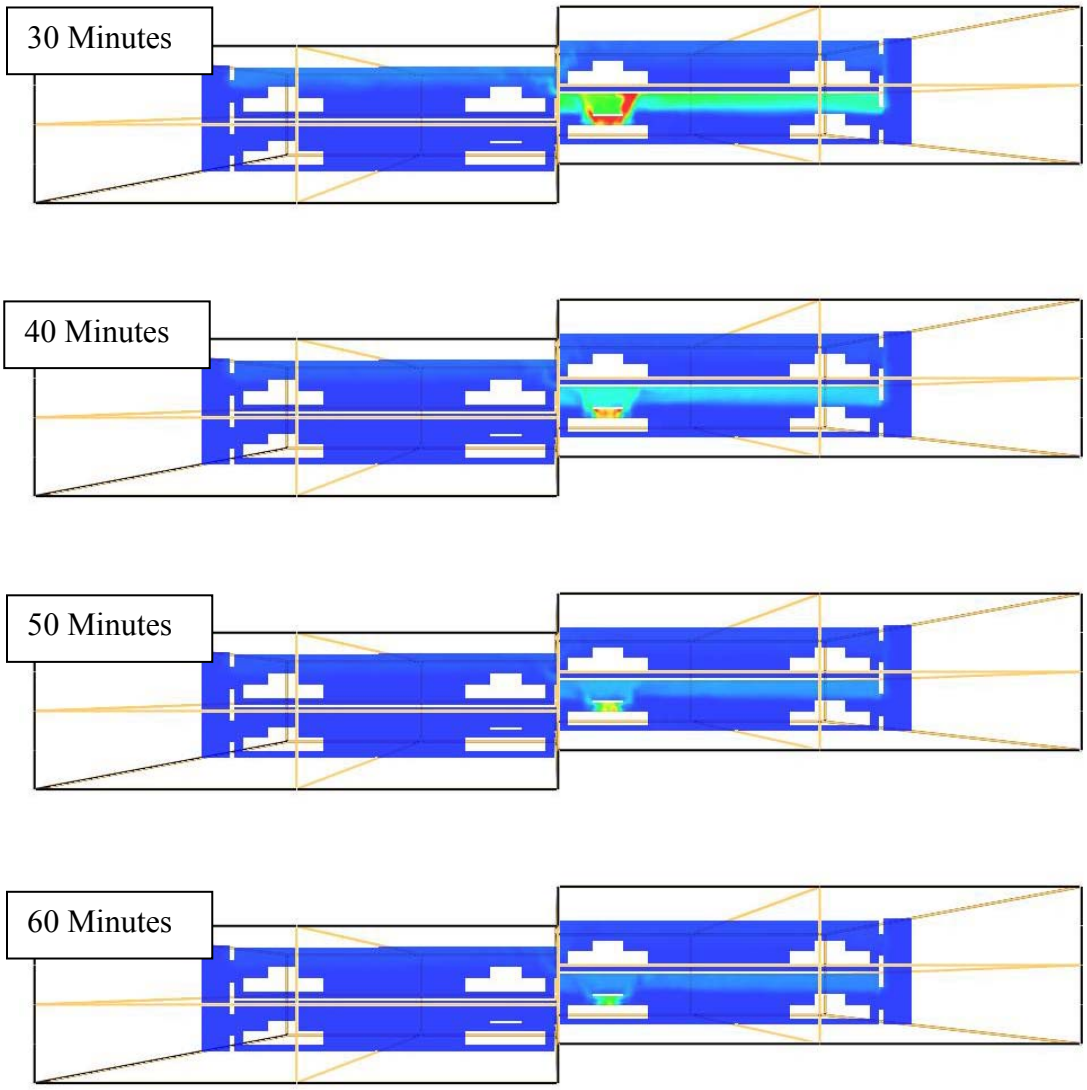

Figure 4-92: Continued from Figure 4-91.

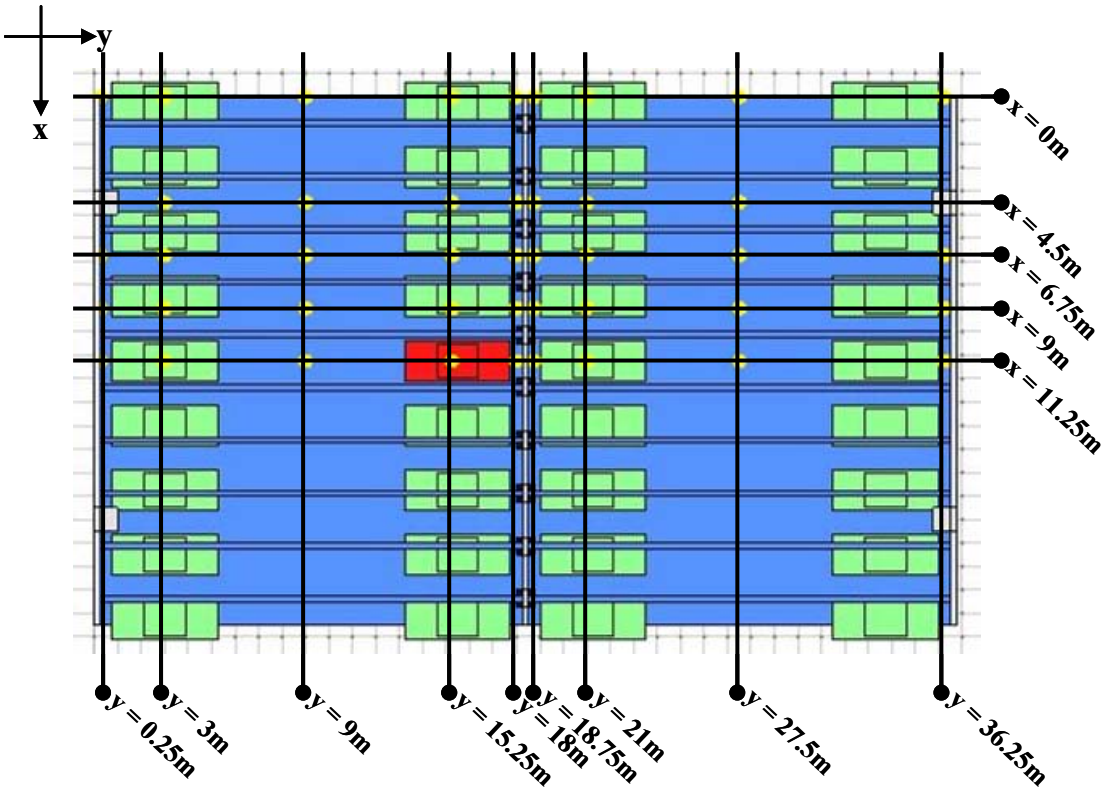

Figure 4-93: Plan view location key for thermocouples.

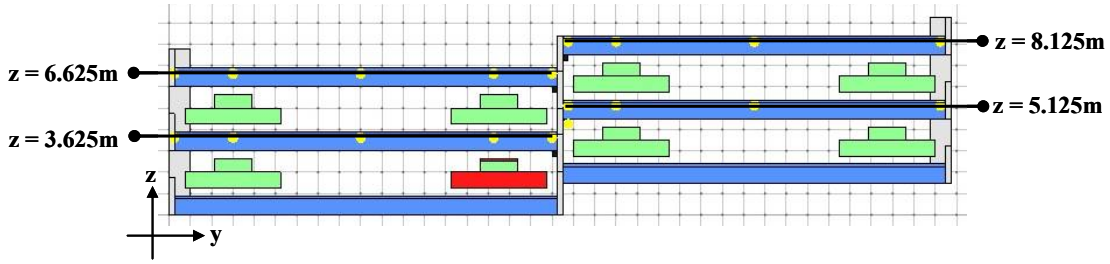

Figure 4-94: Elevation view location key for thermocouples.

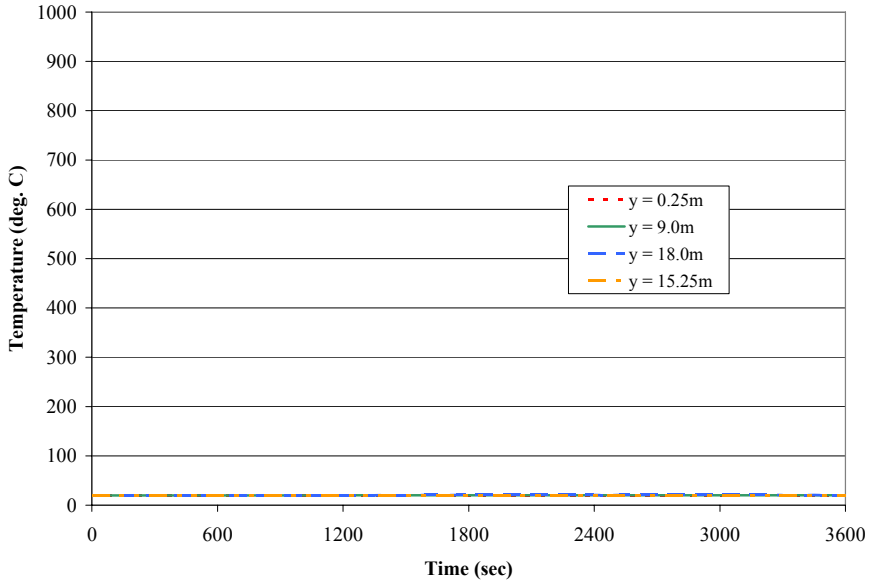

Figure 4-95: Time-temperature histories for Analysis 6 centered between double-tee webs above burning vehicle on floor 1 at x = 11.25m; y = 0.25m, 9.0m, 15.25m, 18.0m; z = 3.625m.

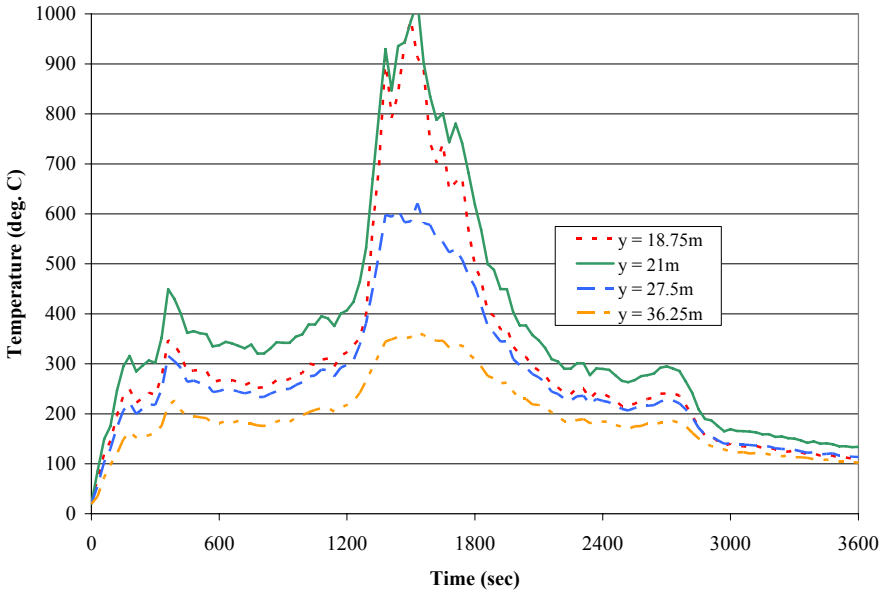

Figure 4-96: Time-temperature histories for Analysis 6 centered between double-tee webs on the opposite side of the center wall from the burning vehicle on floor 2 at x = 11.25m; y = 18.75m, 21.0m, 27.5m, 36.25m; z = 5.125m.

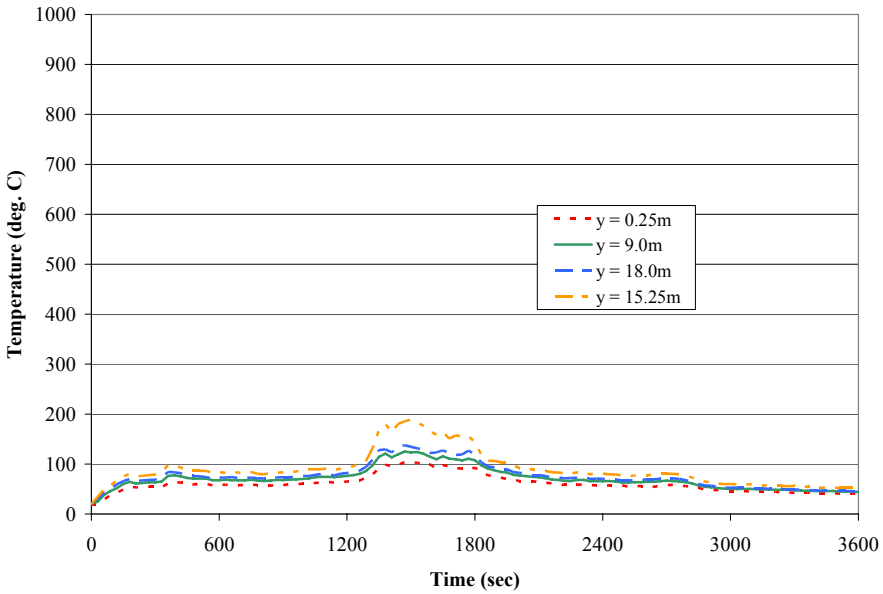

Figure 4-97: Time-temperature histories for Analysis 6 centered between double-tee webs on floor 3 at x = 11.25m; y = m, 18.75m; z = 3.625m.

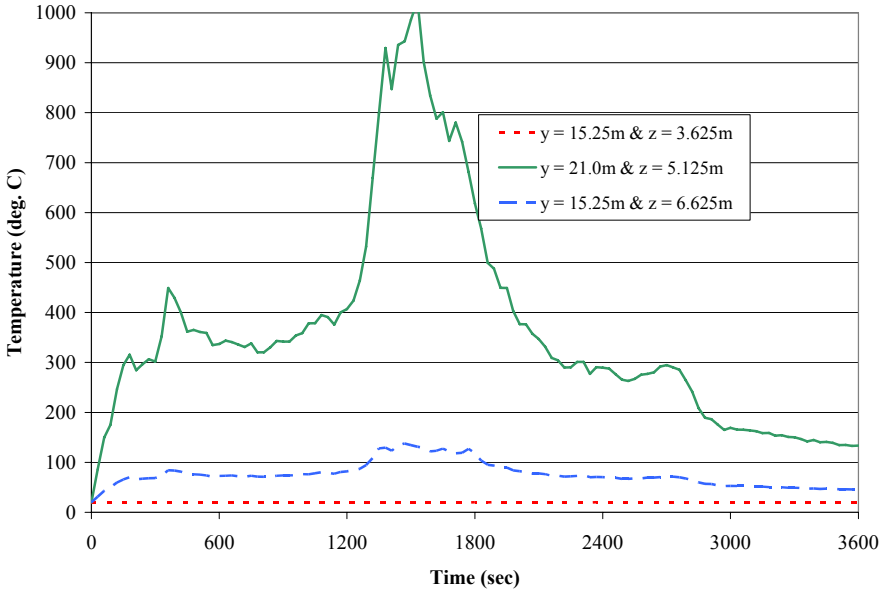

Figure 4-98: Time-temperature histories for Analysis 6 on floors 1, 2, and 3 at x = 11.25m; y = 15.25m/z = 3.625m, y = 21.0m/z = 5.125m; y = 15.25m/z = 6.625m.

4.3.7 Analysis 7: Stagger 3 Analysis

Analysis 7 is the third analysis in the Stagger Analysis series with the only burning vehicle located on the third floor in the position 23 from Figure 3-16. For details of the analysis geometry, see the discussion in Section 4.3.5. The material properties and analysis parameters used conformed to those explained in Chapter 3.

Slice images showing temperature distribution through the structure are shown in Figures 4-101 and 4-103. Images are shown at 10 minute intervals, and the slice location is shown by the diagram in Figure 4-101. The temperature is slice located just below the slab above the burning vehicle on the third floor at z = 6.625m and just below the slab on the other side of the center wall on the fourth floor at z = 8.125m. As before, it may be observed that the heat flows through the center wall and up to the fourth floor with some heat loss as shown by the shading change from one side of the center wall to the other.

Additional slice images are shown in Figures 4-104 to 4-106. The slice is located directly above the burning vehicles centered between the double-tee webs at x = 11.25m and the heat flow from one floor to the next through the center wall is visible.

Once again, time-temperature plots taken from thermocouples throughout the structure are shown in Figures 4-107 to 4-112 and are broken into two series: longitudinal time-temperature plots (Figures 4-109 to 4-111) and a single vertical time-temperature plot (Figure 4-112).

The longitudinal time-temperature plots are shown for thermocouple locations centered between the double-tee webs in the cavity above the burning vehicle. Figures 4-109 and 4-110 show four thermocouples distributed on the first and second floors respectively from y = 0.25m to y = 18m, and from y = 18.75m to y = 36.25m. No temperature increase was recorded one or two floors down from the fire. Finally, Figure 4-111 shows another set of thermocouples arrayed on the third floor just as those on the first floor. The peak recorded temperature for the third floor was 1001 degrees Celsius at y = 15.25m.

The final time-temperature plot shown for Analysis 7 is a comparison between thermocouple locations on the first, second, and third floors (See Figure 4-112). The readings were taken centered above the burning vehicle on the first floor and mirrored on the second and third floor in anticipation of comparison with data from Analyses 5, 6, and 8. The negligible heat flow to the first and second floors is seen.

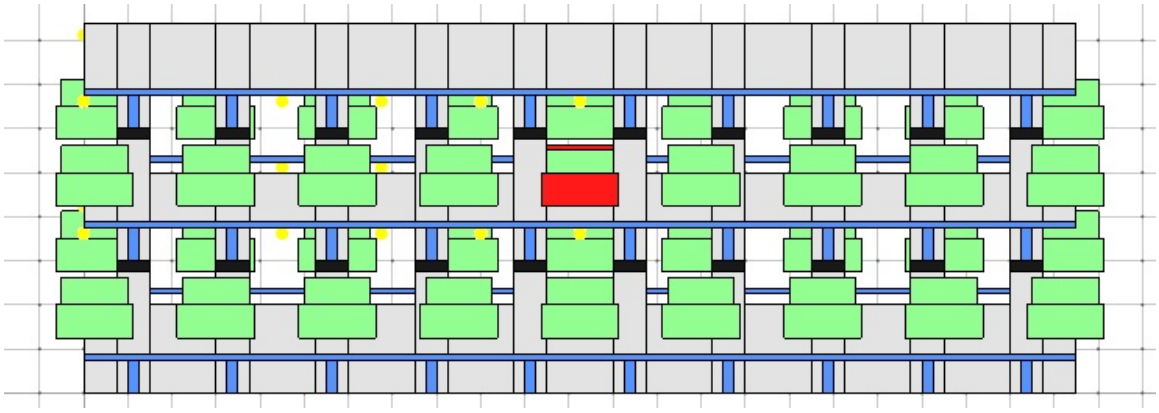

Figure 4-99: View of the center wall of Analysis 7 model showing opening the Top Opening position and the burning vehicle centered in between the double-tee stems.

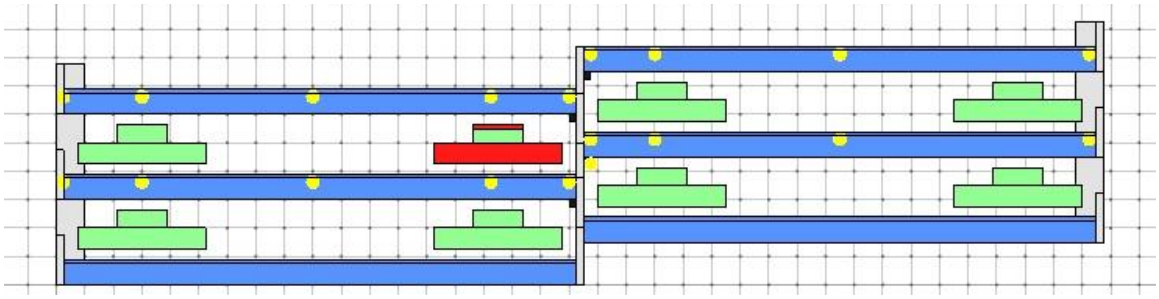

Figure 4-100: Elevation view of the Analysis 7 model showing the burning vehicle position next to the center wall on the second floor.

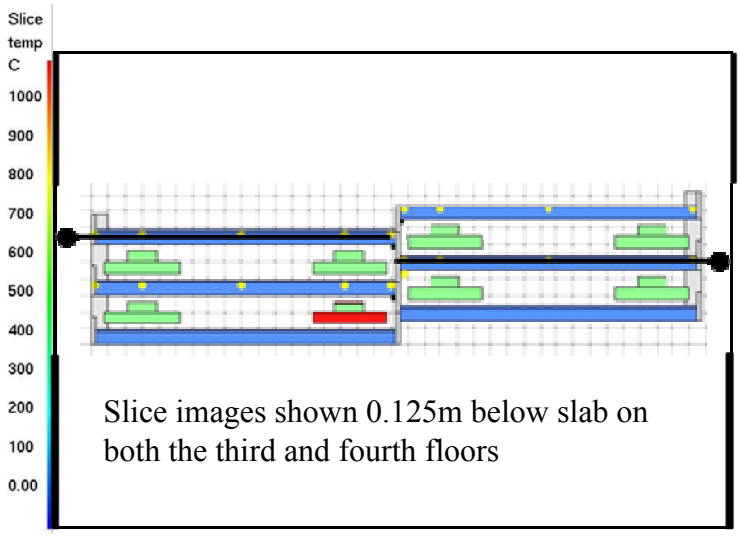

Figure 4-101: Slice images for Analysis 7 showing temperature distribution 0.125m below slab above burning vehicle on the third floor (z = 6.625m – left side) and 0.125m below slab on the fourth floor (z = 8.125m – right side). Images shown at 10 minute intervals (600sec) from time = 0 to 60 minutes. (0-3600sec) Temperature scale in degrees Celsius. Continued in Figures 4-102 and 4-103.

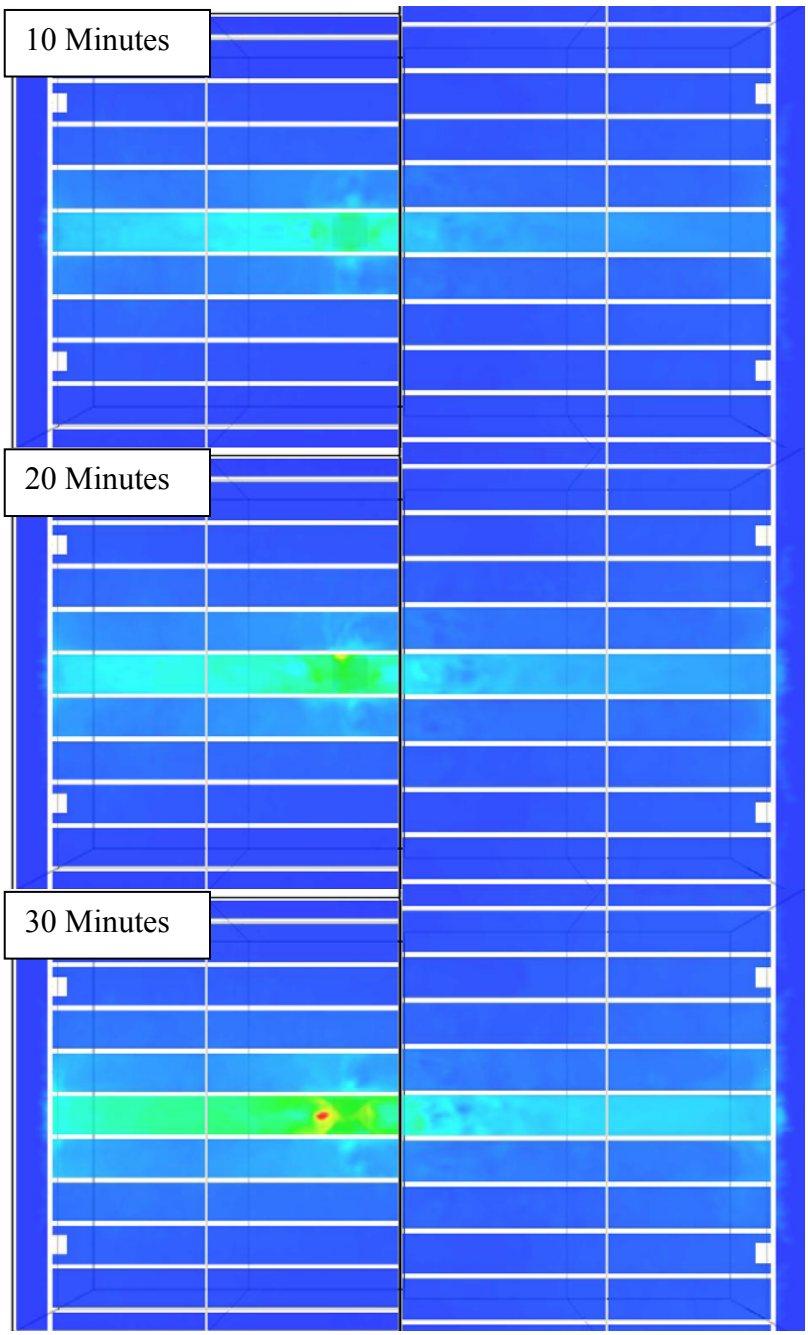

Figure 4-102: Continued from Figure 4-101.

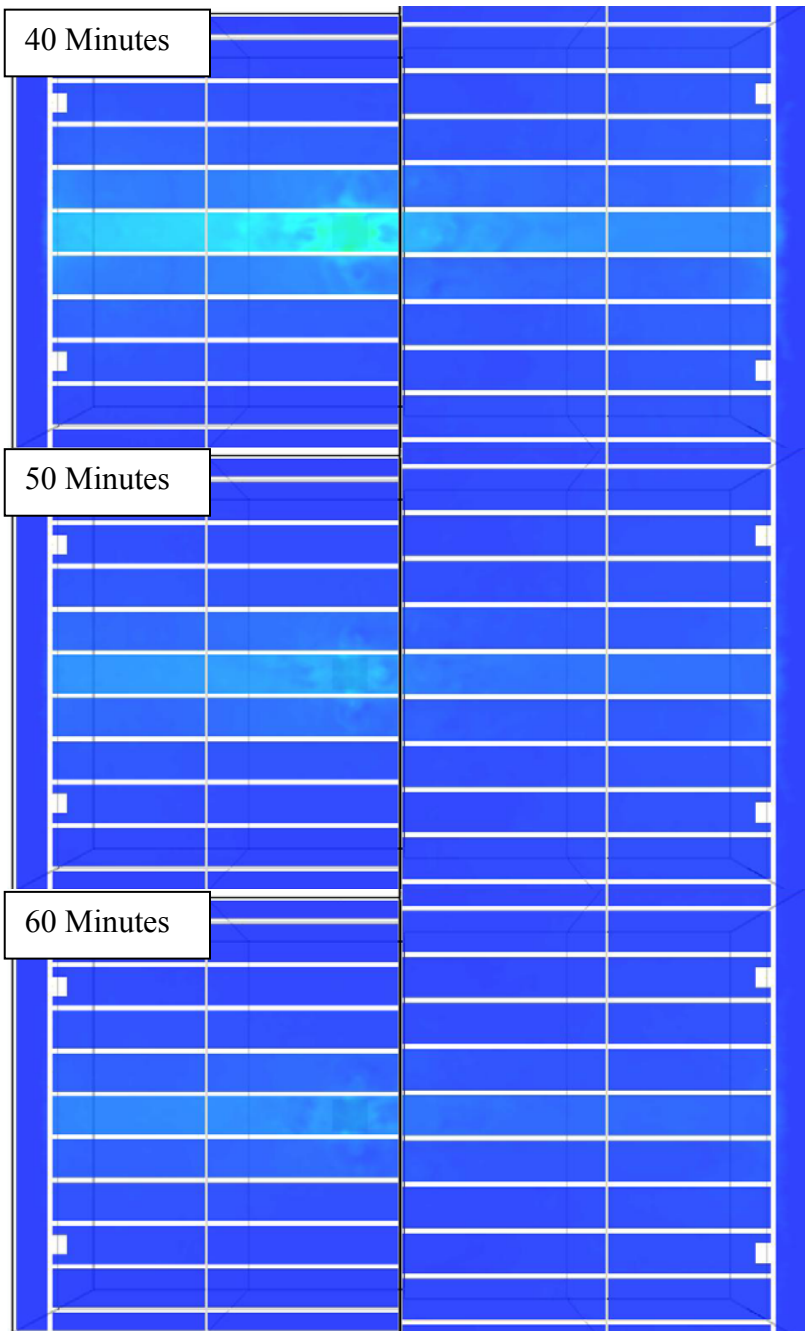

Figure 4-103: Continued from Figure 4-102.

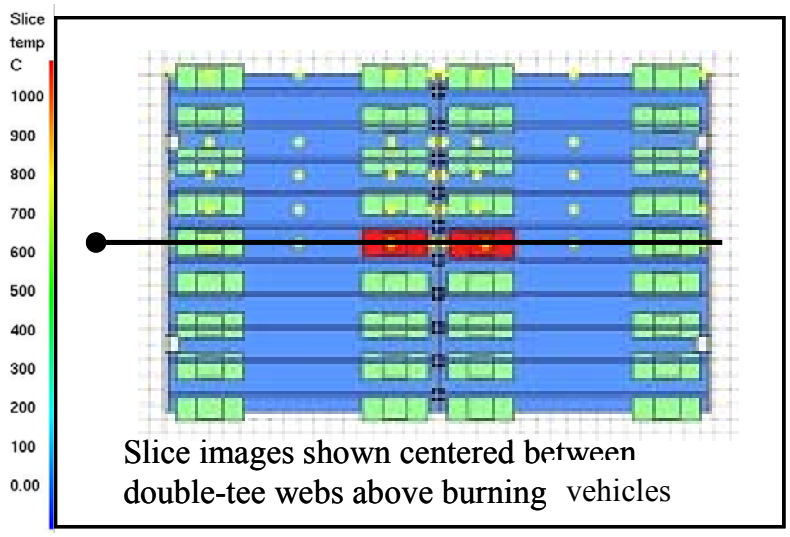

Figure 4-104: Slice images for Analysis 7 showing temperature distribution centered between double-tee webs above burning vehicles (x = 11.25m). Images shown at 6 minute intervals (360sec) from time = 6 to 60 minutes. (360-3600sec) Temperature scale in degrees Celsius. Continued in Figures 4-105 to 4-106.

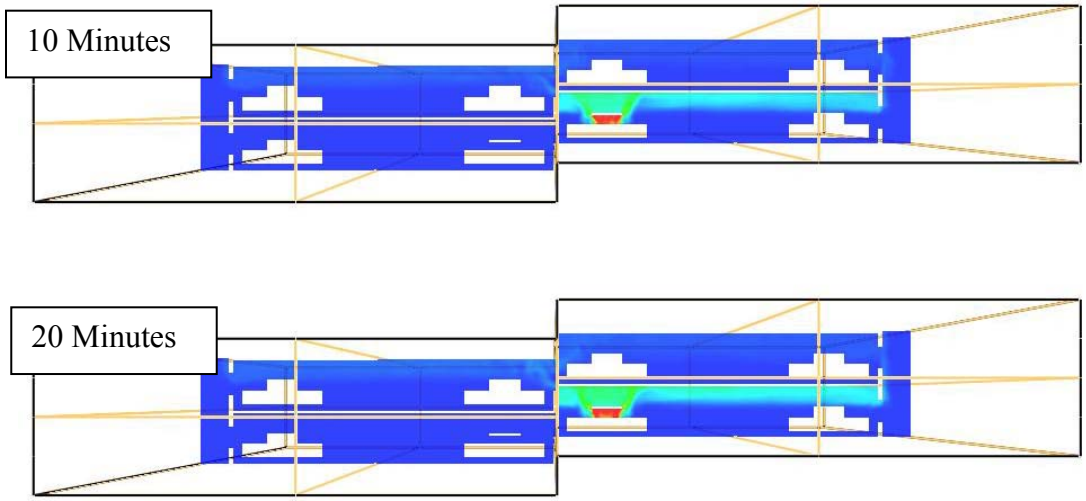

Figure 4-105: Continued from Figure 4-104.

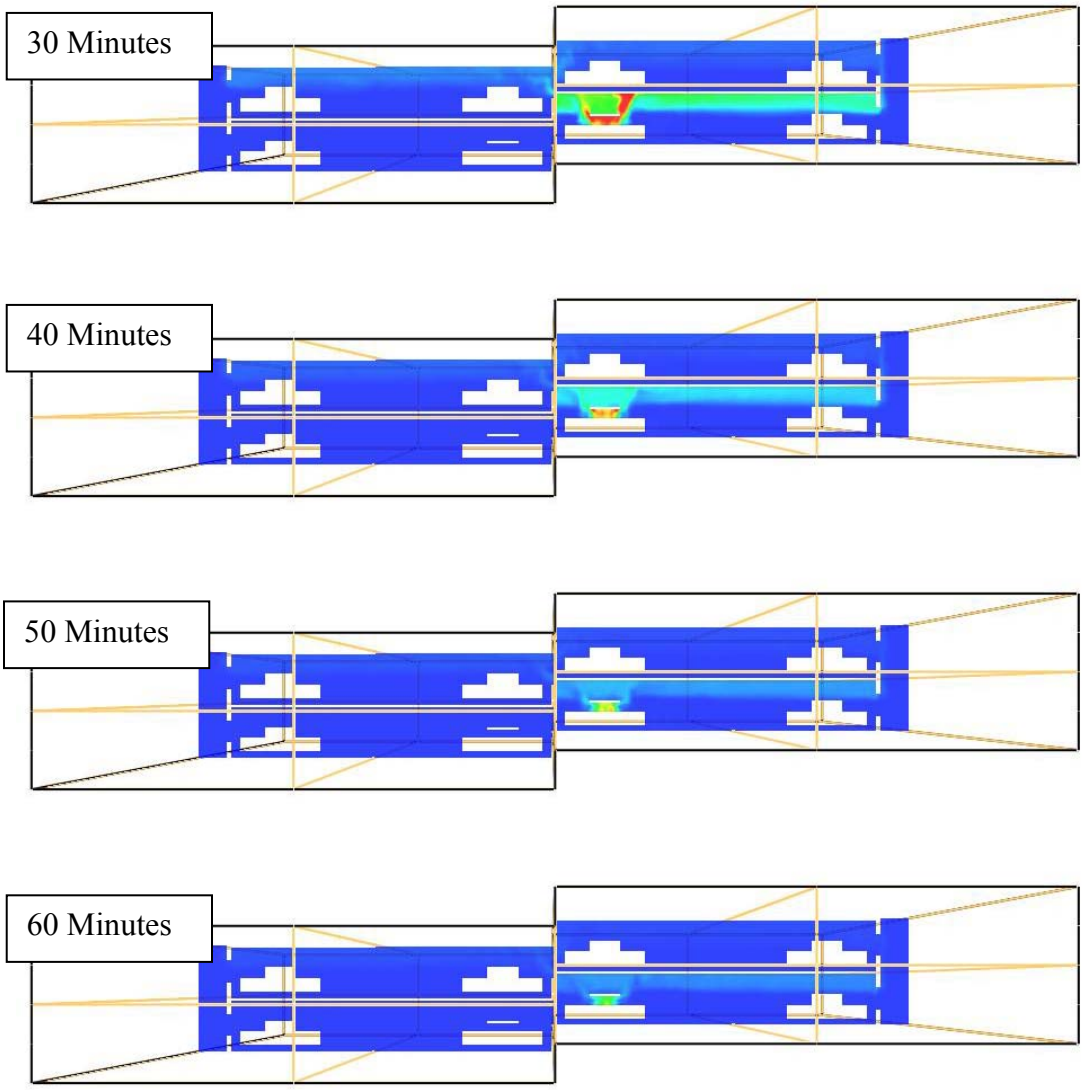

Figure 4-106: Continued from Figure 4-105.

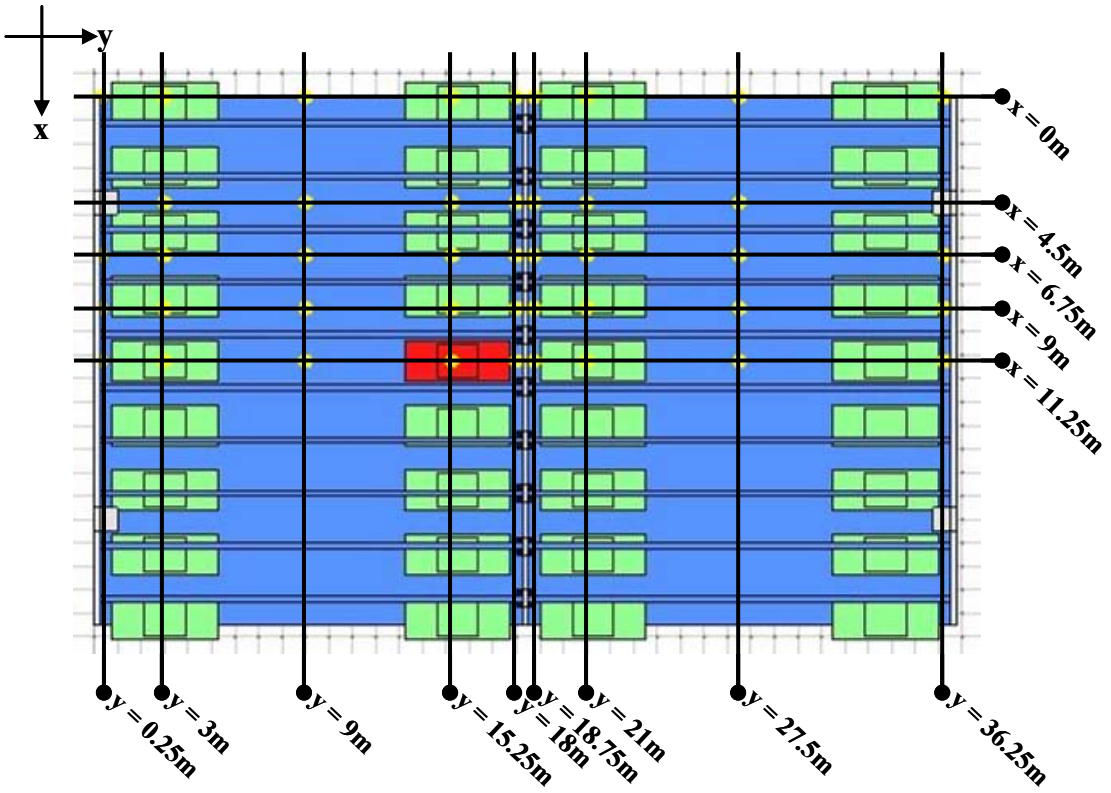

Figure 4-107: Plan view location key for thermocouples.

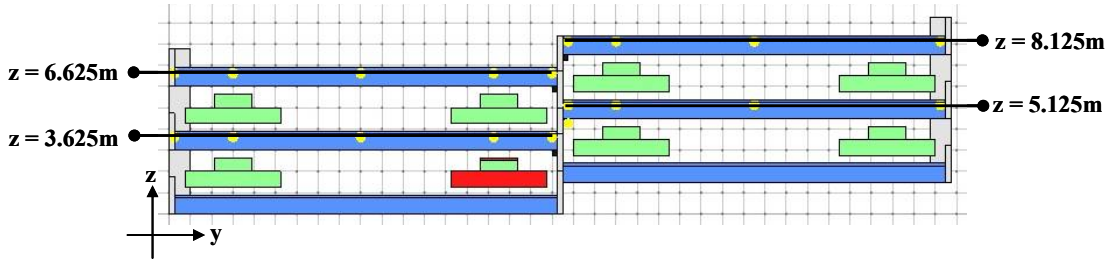

Figure 4-108: Elevation view location key for thermocouples.

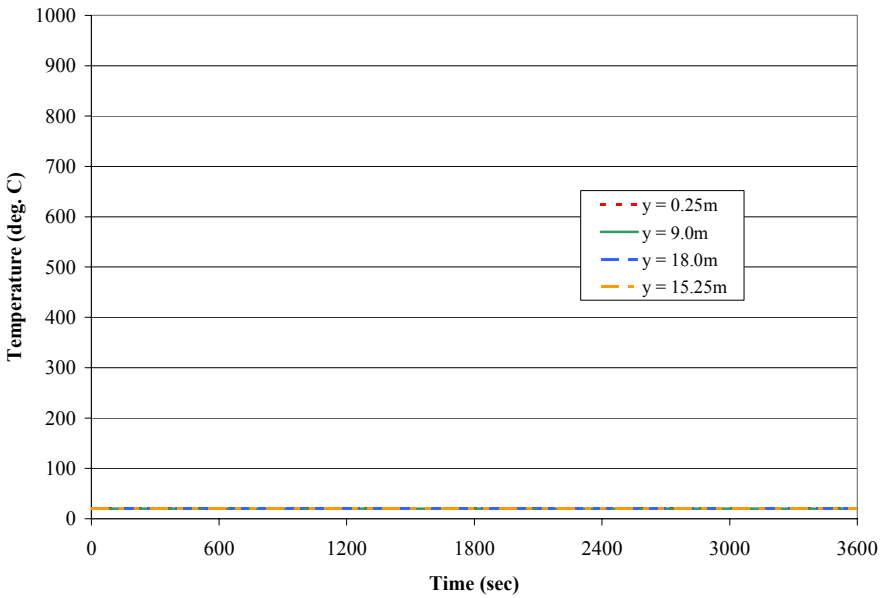

Figure 4-109: Time-temperature histories for Analysis 7 centered between double-tee webs above burning vehicle on floor 1 at x = 11.25m; y = 0.25m, 9.0m, 15.25m, 18.0m; z = 3.625m.

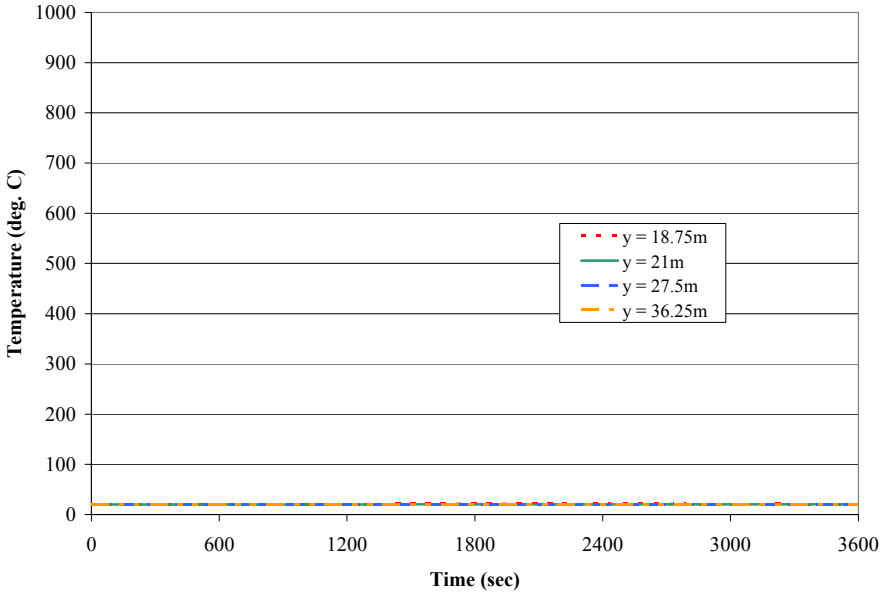

Figure 4-110: Time-temperature histories for Analysis 7 centered between double-tee webs on the opposite side of the center wall from the burning vehicle on floor 4 at x = 11.25m; y = 18.75m, 21.0m, 27.5m, 36.25m; z = 5.125m.

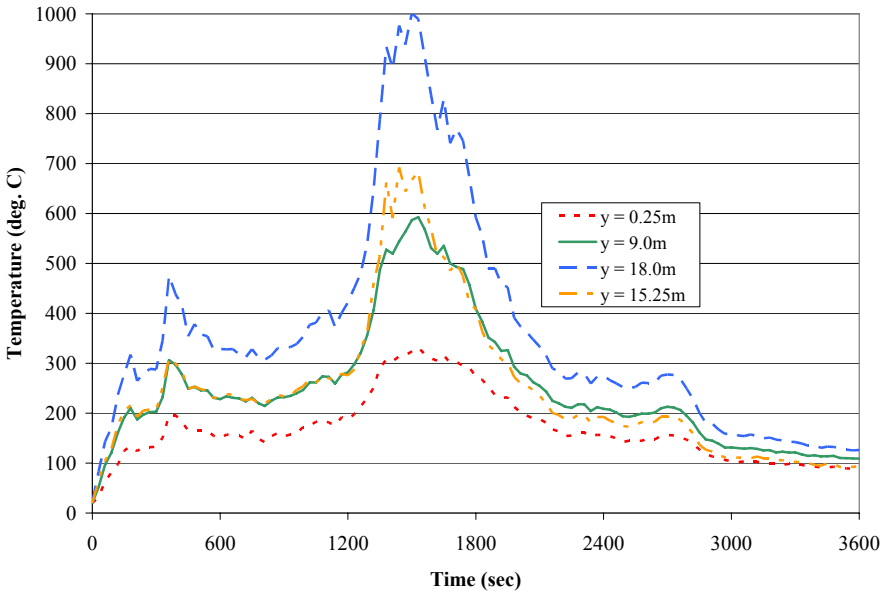

Figure 4-111: Time-temperature histories for Analysis 7 centered between double-tee webs on floor 3 at x = 11.25m; y = m, 18.75m; z = 3.625m.

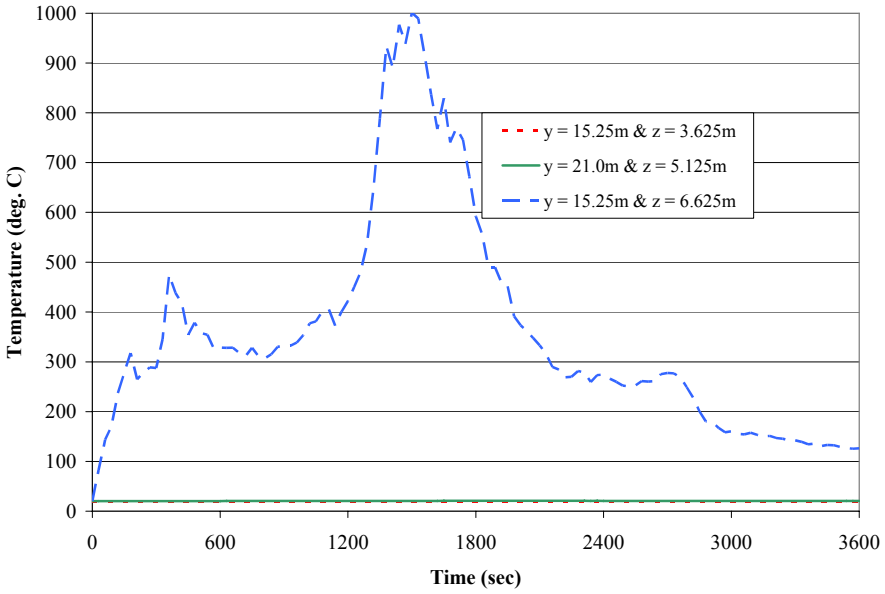

Figure 4-112: Time-temperature histories for Analysis 7 on floors 1, 2, and 3 at x = 11.25m; y = 15.25m/z = 3.625m, y = 21.0m/z = 5.125m; y = 15.25m/z = 6.625m.

4.3.8 Analysis 8: Stagger 123 Analysis

Analysis 8 is the final analysis in the Stagger Analysis series and includes three burning vehicles distributed on floors 1 (Position 23), 2 (Position 14), and 3 (Position 23) from Figure 3-16. The vehicles on floors 2 and 3 ignite at $\Delta T = +12$ minutes and $\Delta T = +24$ minutes respectively, resulting in a sequential burn from one floor to the next. For further details of the Stagger floor geometry, see the discussion in Section 4.3.5. The material properties and analysis parameters used conformed to those explained in Chapter 3.

It is noted that there was an error in the input file for this analysis, which caused the fire on the third floor at $\Delta T = +24$ minutes to have an incorrect heat flux output. The specified heat flux output for the fire should have been identical to the Vehicle 1 record used for the fires on the first and second floors at $T = 0$ and $\Delta T = +12$ minutes, however, the actual record that was used was roughly 10% of that. The reason for this difference was a geometrical error, instead of the roof of the vehicle being a flat plate and allowing the fire to fully develop, the roof was a solid block. (See Figure 4-113) Time and circumstances did not allow the analysis to be repeated with the correct geometry, and analysis of the results of the Analysis 8 was performed with knowledge of the error. The incorrect heat flux on the third floor did not introduce error into the results generated for floors 1 or 2.

Slice images showing temperature distribution through the structure are shown in Figures 4-116 to 4-120. The slice is located directly above the burning vehicles centered between the double-tee webs at x = 11.25m. The separate ignitions of each vehicle are seen, as is the heat buildup on the upper floors prior to the ΔT timed ignition of the vehicles. Images are shown at 6 minute intervals.

Once again, time-temperature plots taken from thermocouples throughout the structure are shown in Figures 4-121 to 4-126 and are broken into two series: longitudinal time-temperature plots (Figures 4-123 to 4-125) and a single vertical time-temperature plot (Figure 4-126).

The longitudinal time-temperature plots are shown for thermocouple locations centered between the double-tee webs in the cavity above the burning vehicle. Figure 4-123 shows four thermocouples distributed on the first floor from y = 0.25m to y = 18m. The highest temperature recorded was 984 degrees Celsius at y = 15.25m. Figure 4-124 shows a similar set of thermocouple time-temperature plots to Figure 4-123, but these are shown for the opposite side of the center wall on the second floor with a peak recorded temperature of 1217 degrees Celsius at y = 21.0m directly above the burning vehicle. Finally, Figure 4-125 shows another set of thermocouples arrayed on the third floor just as those on the first floor. The peak recorded temperature for the third floor was 370 degrees Celsius at y = 18.0m.

The final time-temperature plot shown for Analysis 8 is a comparison between thermocouple locations on the first, second, and third floors (See Figure 4-126). The readings were taken centered above the burning vehicle on the first floor and mirrored on the second and third floor in anticipation of comparison with data from Analysis 5-7.

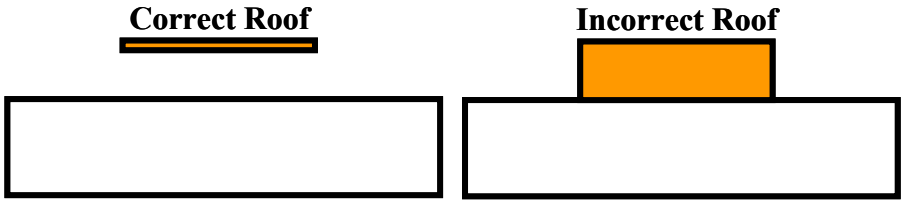

Figure 4-113: Analysis 8 roof geometry error.

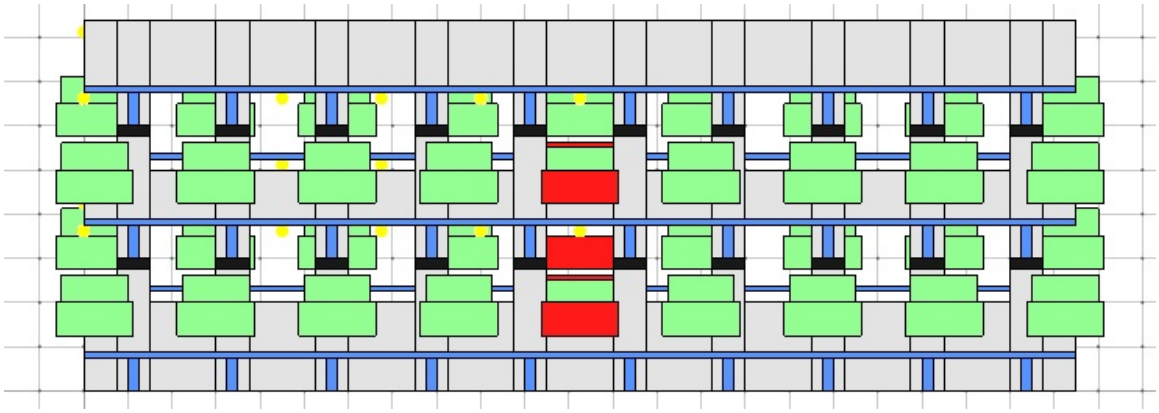

Figure 4-114: View of the center wall of Analysis 8 model.

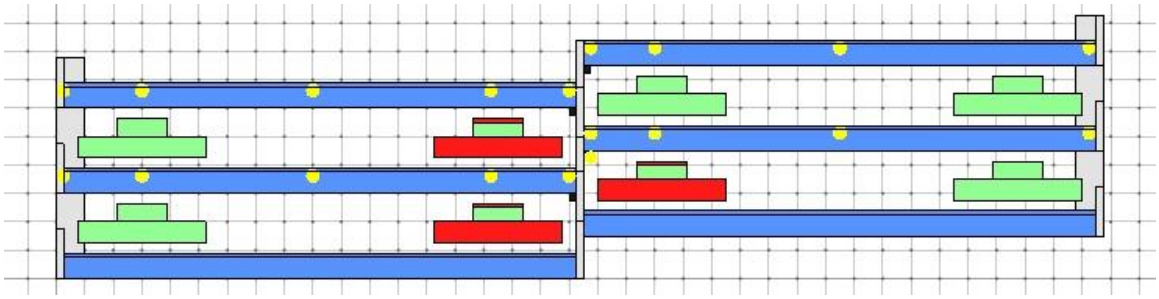

Figure 4-115: Elevation view of the Analysis 8 model showing the burning vehicles positioned next to the center wall on the first, second, and third floors.

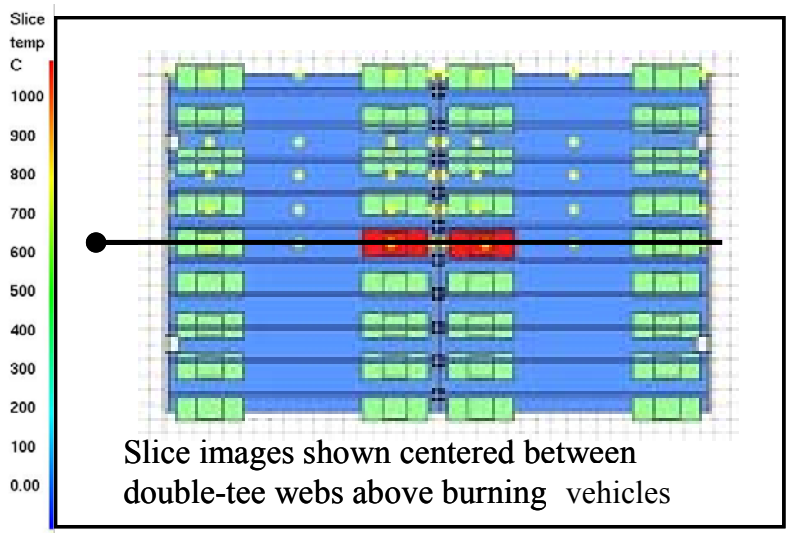

Figure 4-116: Slice images for Analysis 8 showing temperature distribution centered between double-tee webs above burning vehicles (x = 11.25m). Images shown at 6 minute intervals (360sec) from time = 6 to 84 minutes. (360-5040sec) Temperature scale in degrees Celsius. Continued in Figures 4-117 to 4-120.

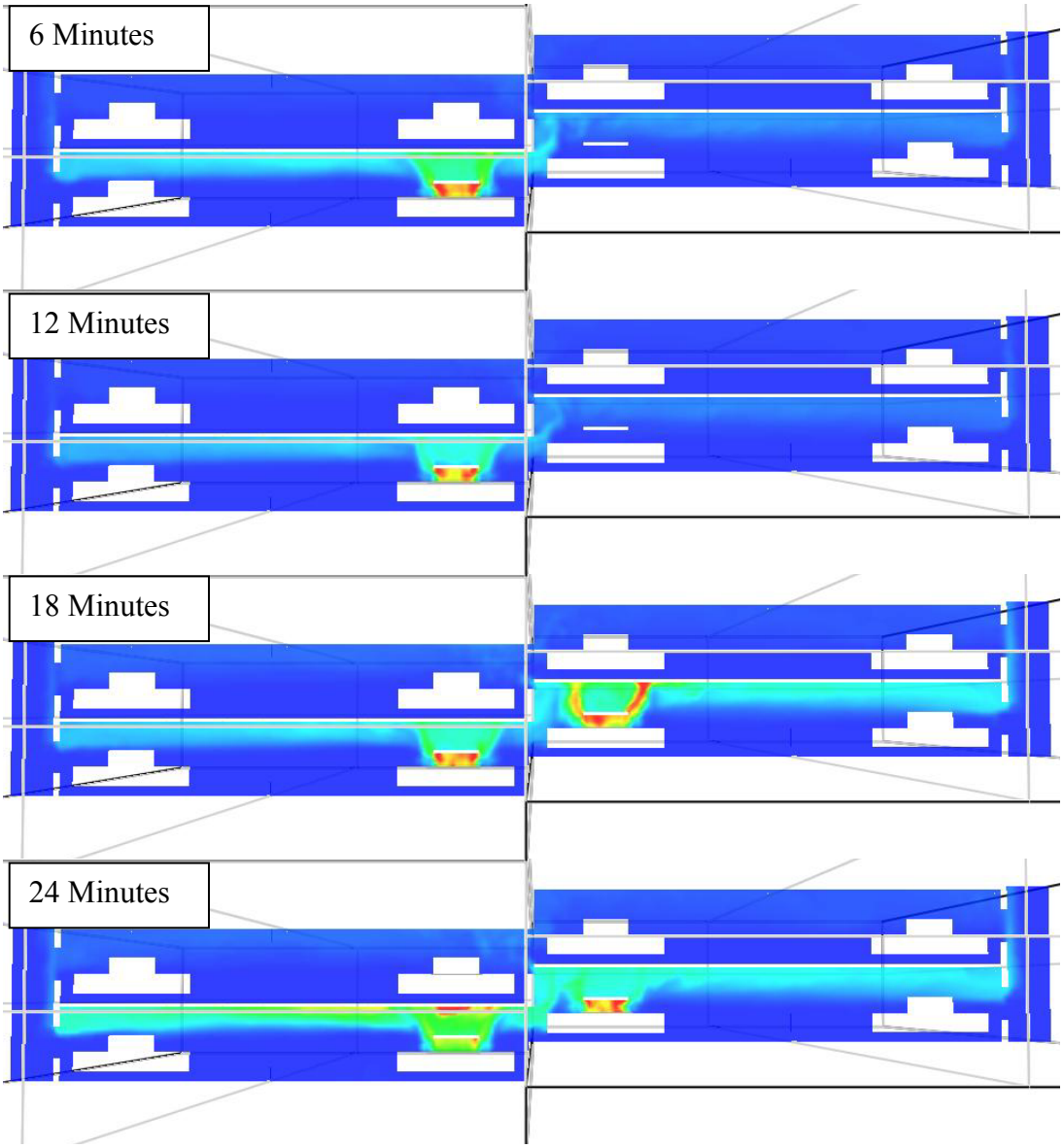

Figure 4-117: Continued from Figure 4-116.

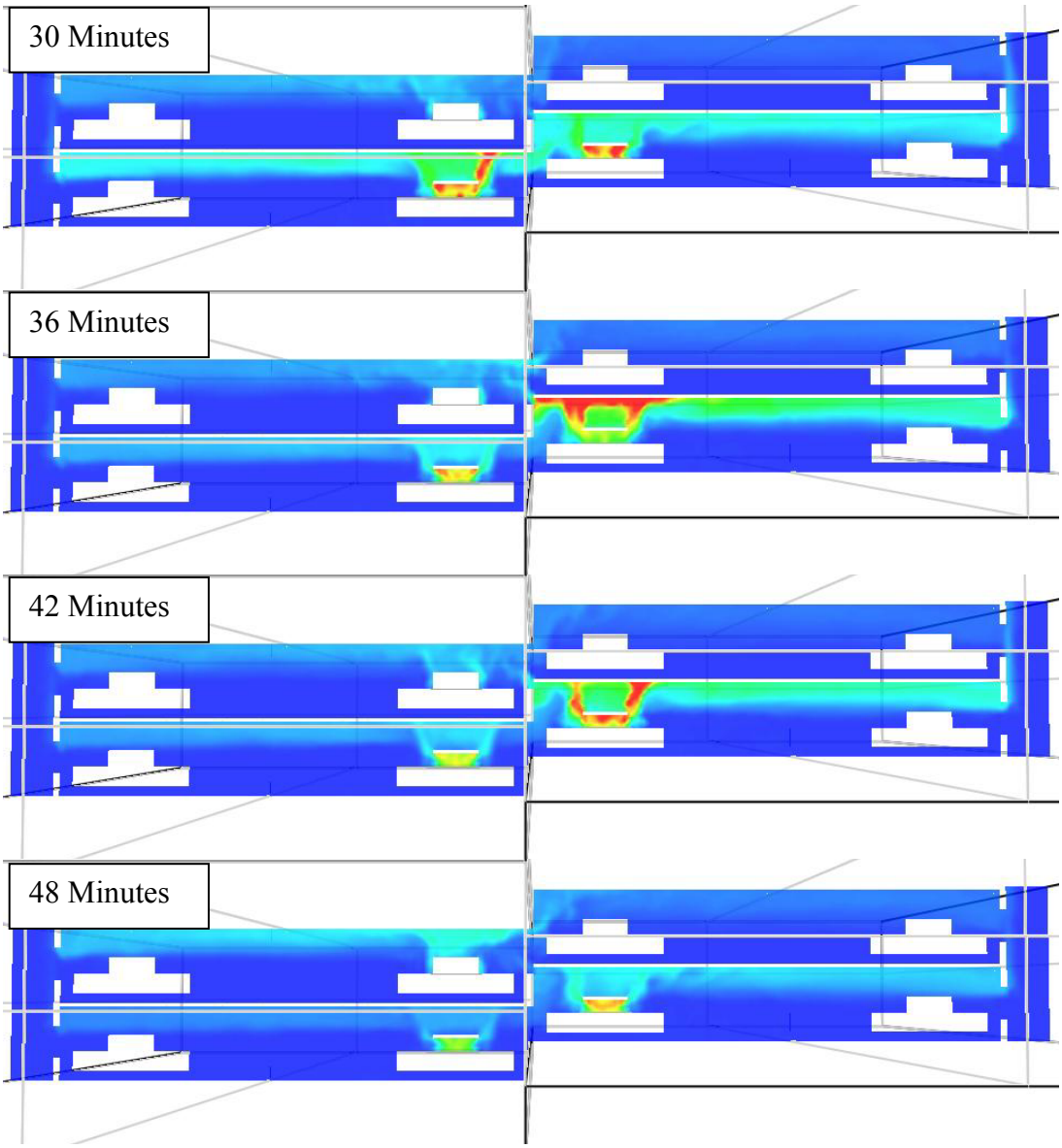

Figure 4-118: Continued from Figure 4-117.

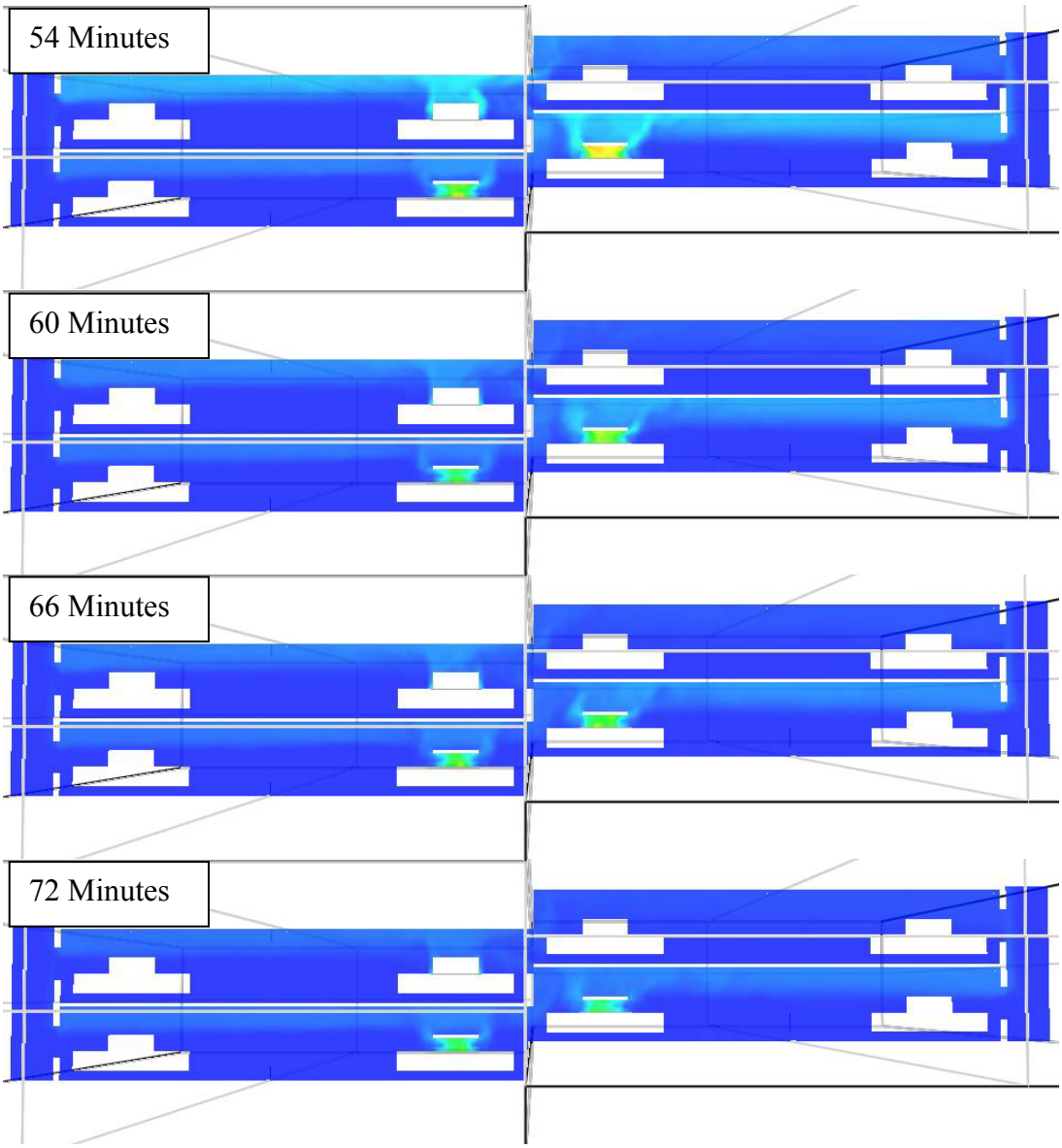

Figure 4-119: Continued from Figure 4-118.

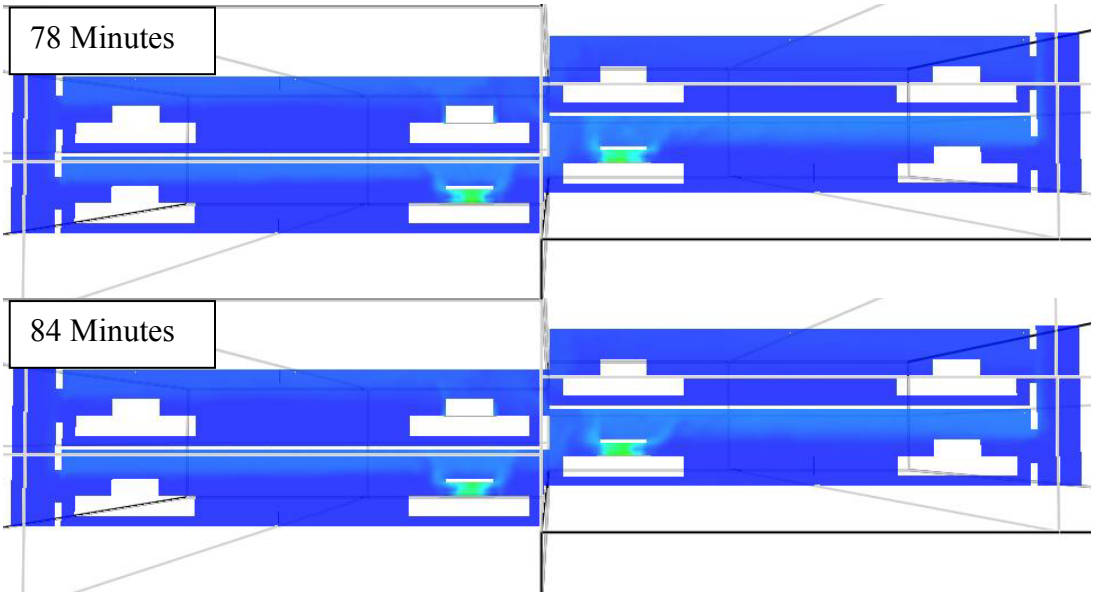

Figure 4-120: Continued from Figure 4-119.

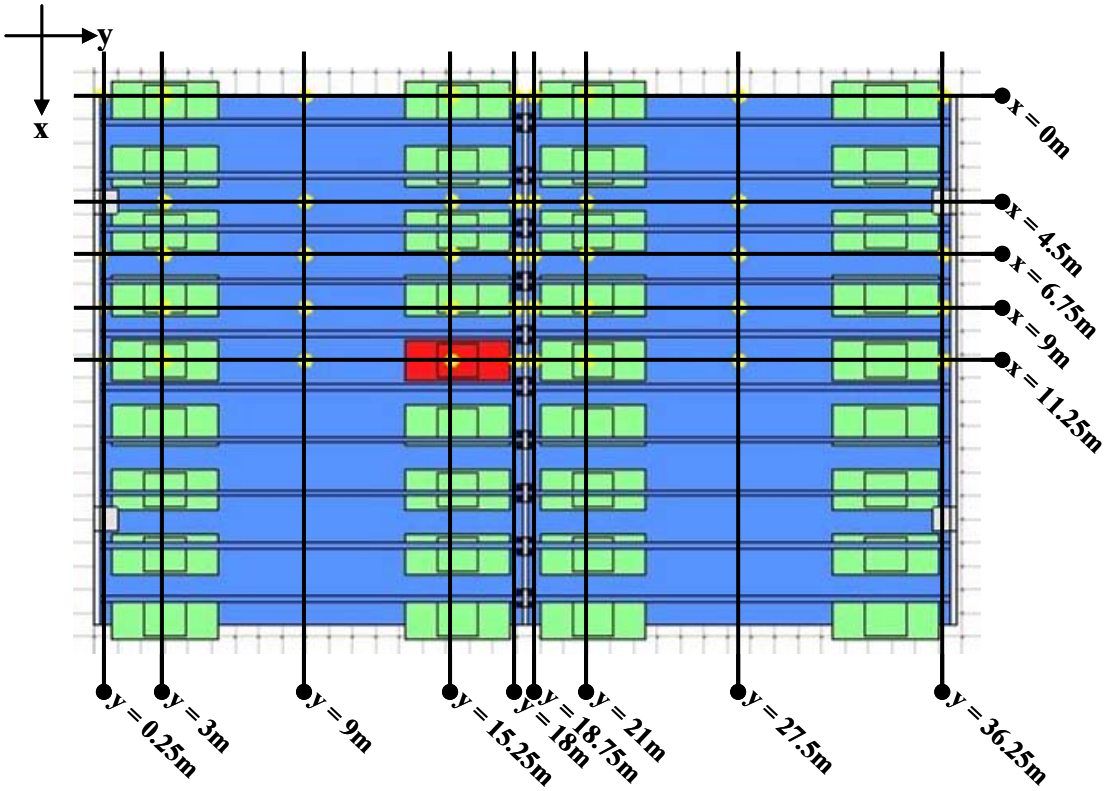

Figure 4-121: Plan view location key for thermocouples.

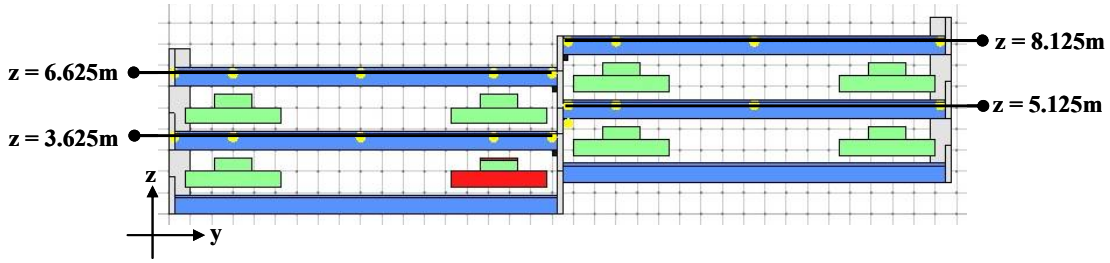

Figure 4-122: Elevation view location key for thermocouples.

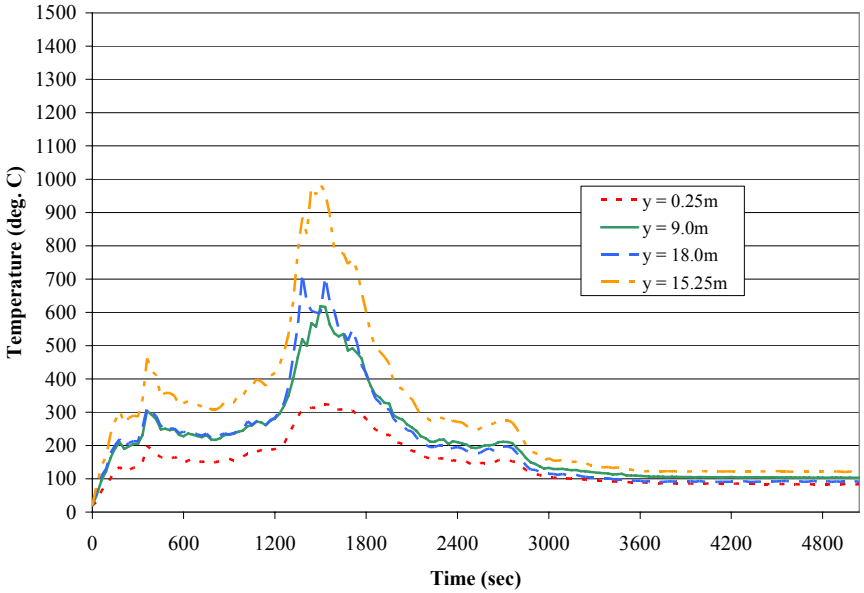

Figure 4-123: Time-temperature histories for Analysis 8 centered between double-tee webs above burning vehicle on floor 1 at x = 11.25m; y = 0.25m, 9.0m, 15.25m, 18.0m; z = 3.625m.

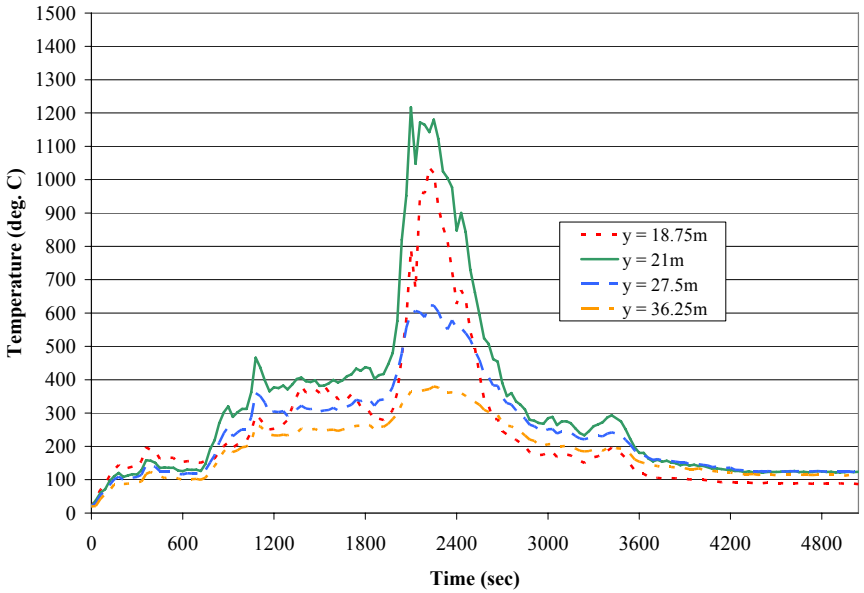

Figure 4-124: Time-temperature histories for Analysis 8 centered between double-tee webs on the opposite side of the center wall from the burning vehicle on floor 2 at x = 11.25m; y = 18.75m, 21.0m, 27.5m, 36.25m; z = 5.125m.

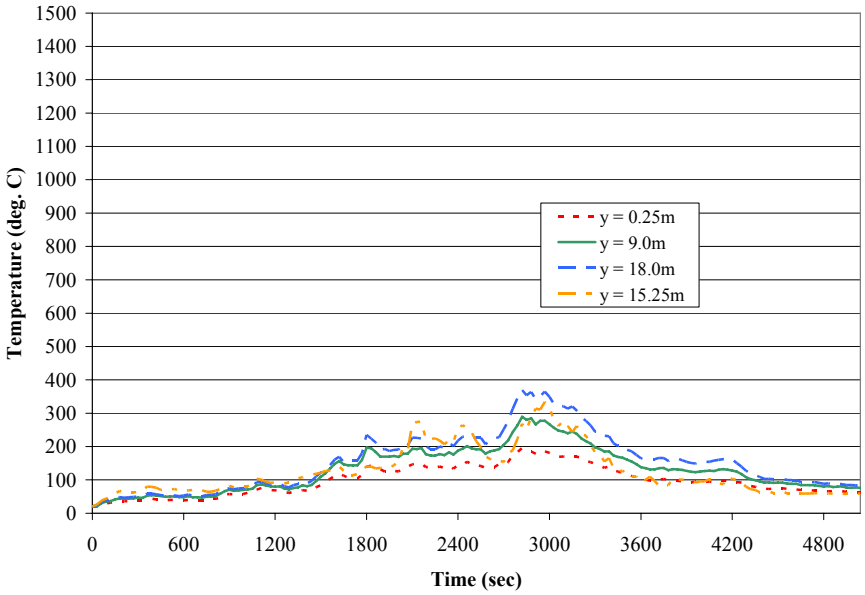

Figure 4-125: Time-temperature histories for Analysis 8 centered between double-tee webs on floor 3 at x = 11.25m; y = m, 18.75m; z = 3.625m.

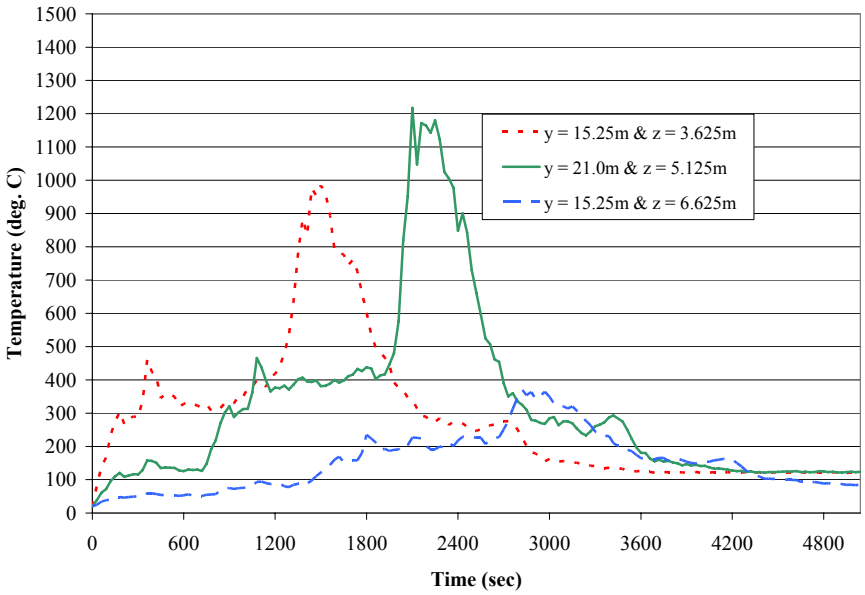

Figure 4-126: Time-temperature histories for Analysis 8 on floors 1, 2, and 3 at x = 11.25m; y = 15.25m/z = 3.625m, y = 21.0m/z = 5.125m; y = 15.25m/z = 6.625m.

4.3.9 Analysis 9: Spread Analysis

The Analysis 9 model involves a total of seven vehicles in sequential ignition on a single floor. The fire starts in position 23 and spreads to positions 22 and 24 at ΔT = +12 minutes, positions 21 and 25 at ΔT = +24 minutes, and positions 20 and 26 at ΔT = +36 minutes. Other than the difference in vehicle ignition, the geometry of Analysis 9 is identical to that of the Analysis 2. The material properties and analysis parameters used conformed to those explained in Chapter 3.

Slice images showing temperature distribution through the structure are shown in Figures 4-129 to 4-135. Images are shown at 12 minute intervals, and the slice location is shown by Figure 4-129. The temperature slice is located just below the slab above the burning vehicle at z = 3.625m. It is observed that the heat builds up longitudinally between the double-tee webs with some heat spilling over into adjacent double-tee cavities prior to the next ignition in the sequence. Little or no heat is allowed to flow through the center wall, and, once again, peak temperatures are reached above the burning vehicles.

Time-temperature plots taken from thermocouples throughout the structure are shown in Figures 4-136 to 4-143 and are broken into two series: longitudinal time-temperature plots (Figures 4-138 to 4-140), and transverse time-temperature plots (Figures 4-141 to 4-143).

The longitudinal time-temperature plots are shown for thermocouple locations centered between the double-tee webs in the cavity above the burning vehicle. Figure 4-138 shows four thermocouples distributed from y = 0.25m to y = 18m. The highest temperature recorded was 890 degrees Celsius at y = 15.25m. Figure 4-139 shows a similar set of thermocouple time-temperature plots to Figure 4-138, but these are shown for the opposite side of the center wall. Finally, Figure 4-140, shows two time-temperature plots, one on either side of the center wall.

The transverse time-temperature plots are shown in Figures 4-141 to 4-143 to show the how the heat spills under the double-tee webs from one cavity to the next.

The maximum gas temperatures reached in this analysis are higher than those recorded in the fire analyses by Bennets et al., which was 750 degrees Celsius, and lower than those recorded by Zhao and Kruppa (2004), which was 1000 degrees Celsius.

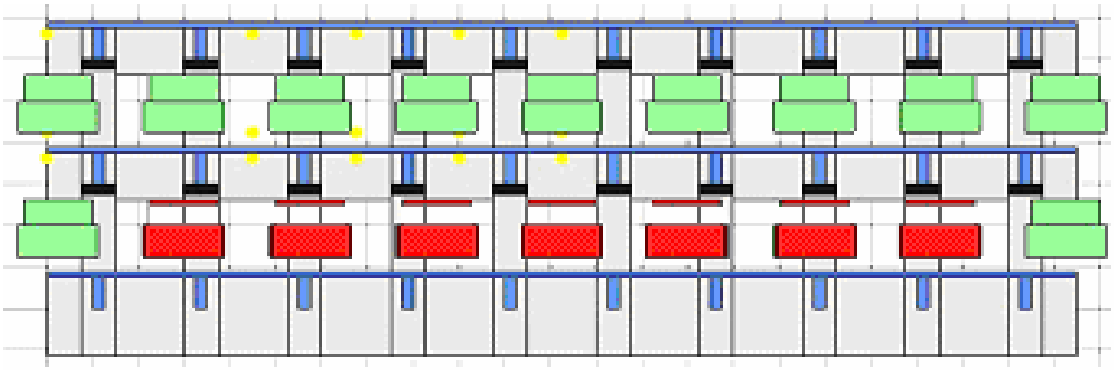

Figure 4-127: View of the center wall of the Analysis 9 model showing center wall opening position and burning vehicles.

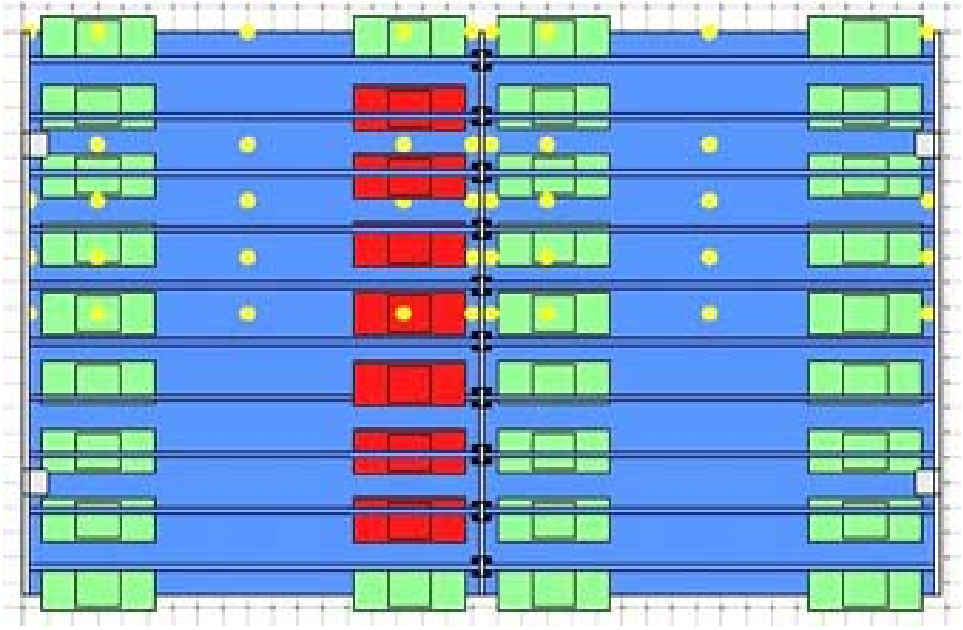

Figure 4-128: Plan view of the Analysis 9 model.

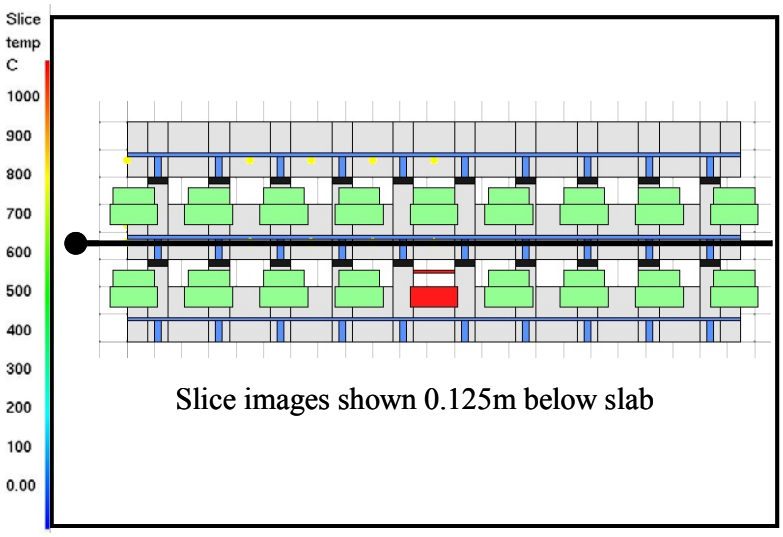

Figure 4-129: Slice images for Analysis 9 showing temperature distribution 0.125m below slab above burning vehicles. Images shown at 6 minute intervals (360sec) from time = 0 to 96 minutes. (0-5760sec) Temperature scale in degrees Celsius. Continued in Figures 4-130 to 4-135.

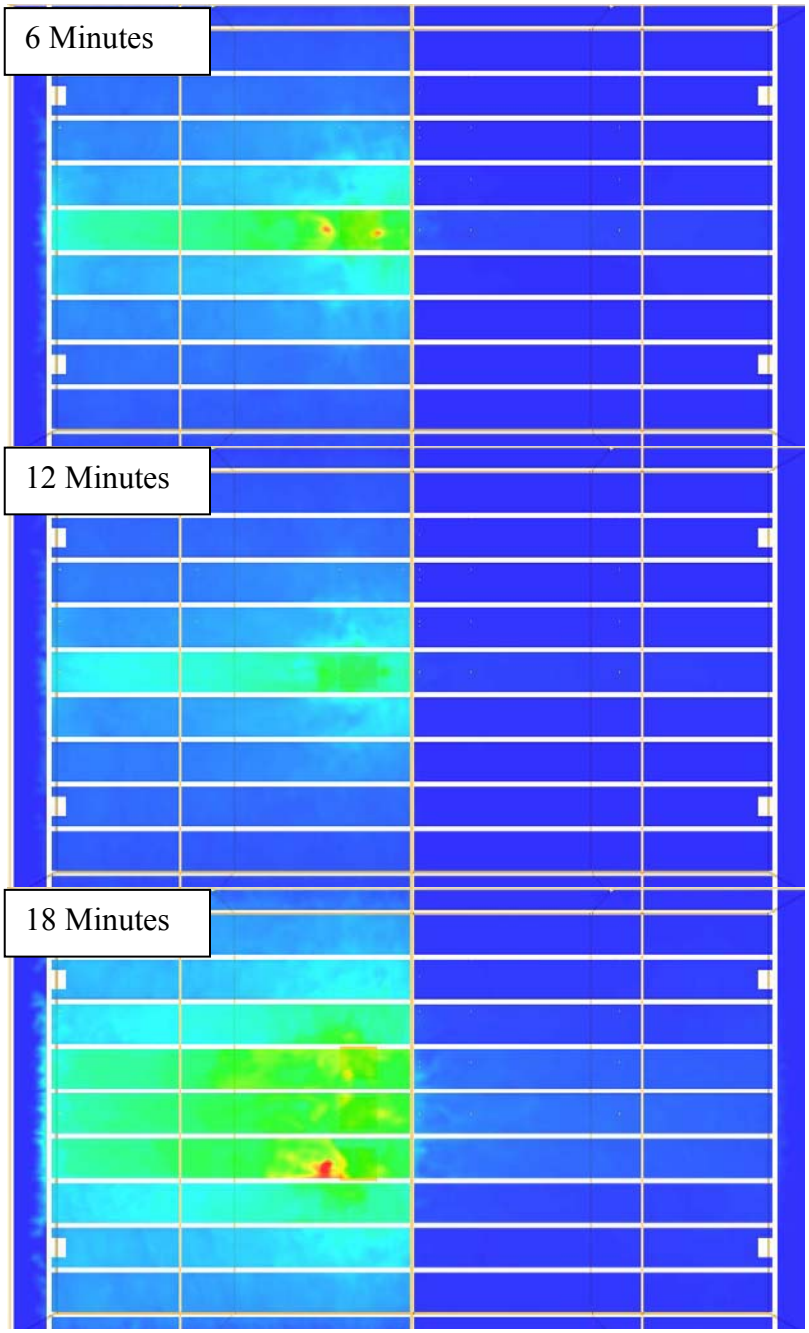

Figure 4-130: Continued from Figure 4-129.

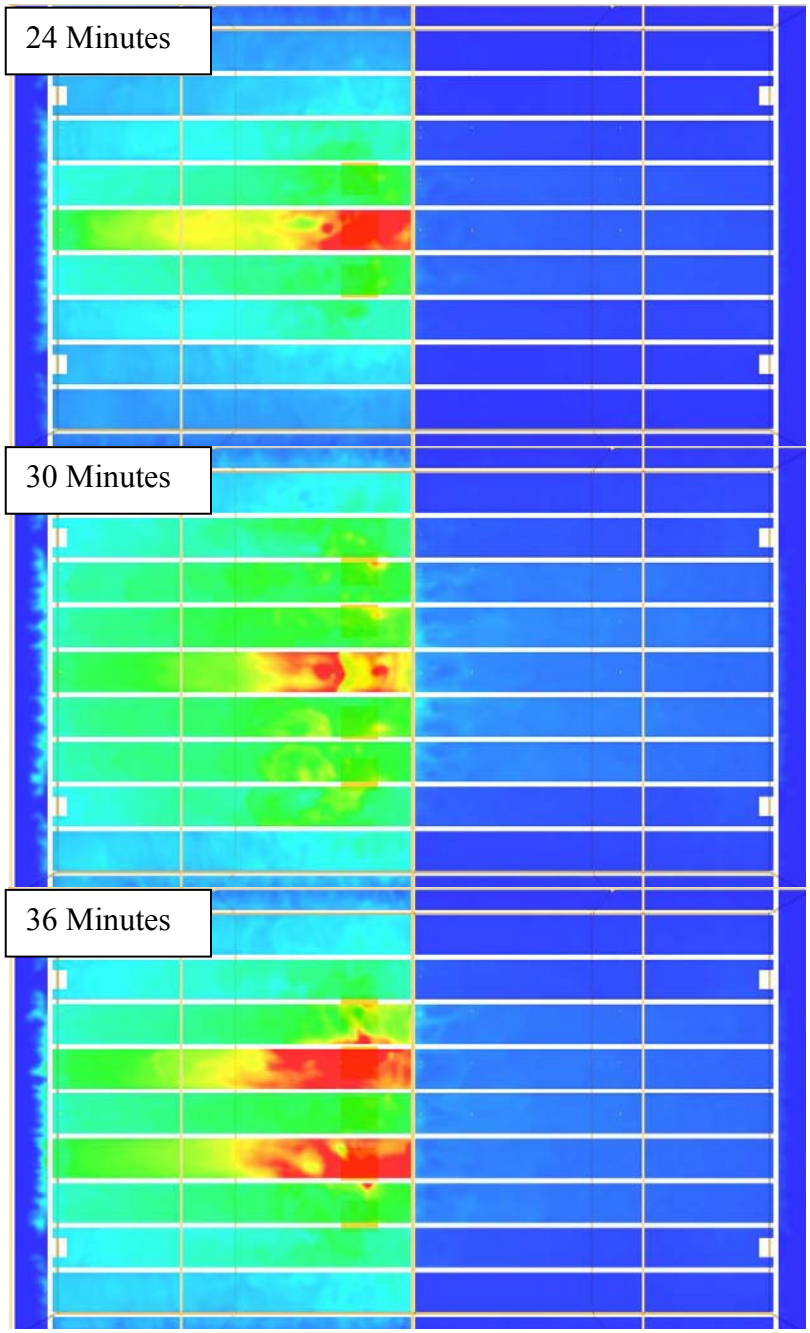

Figure 4-131: Continued from Figure 4-130.

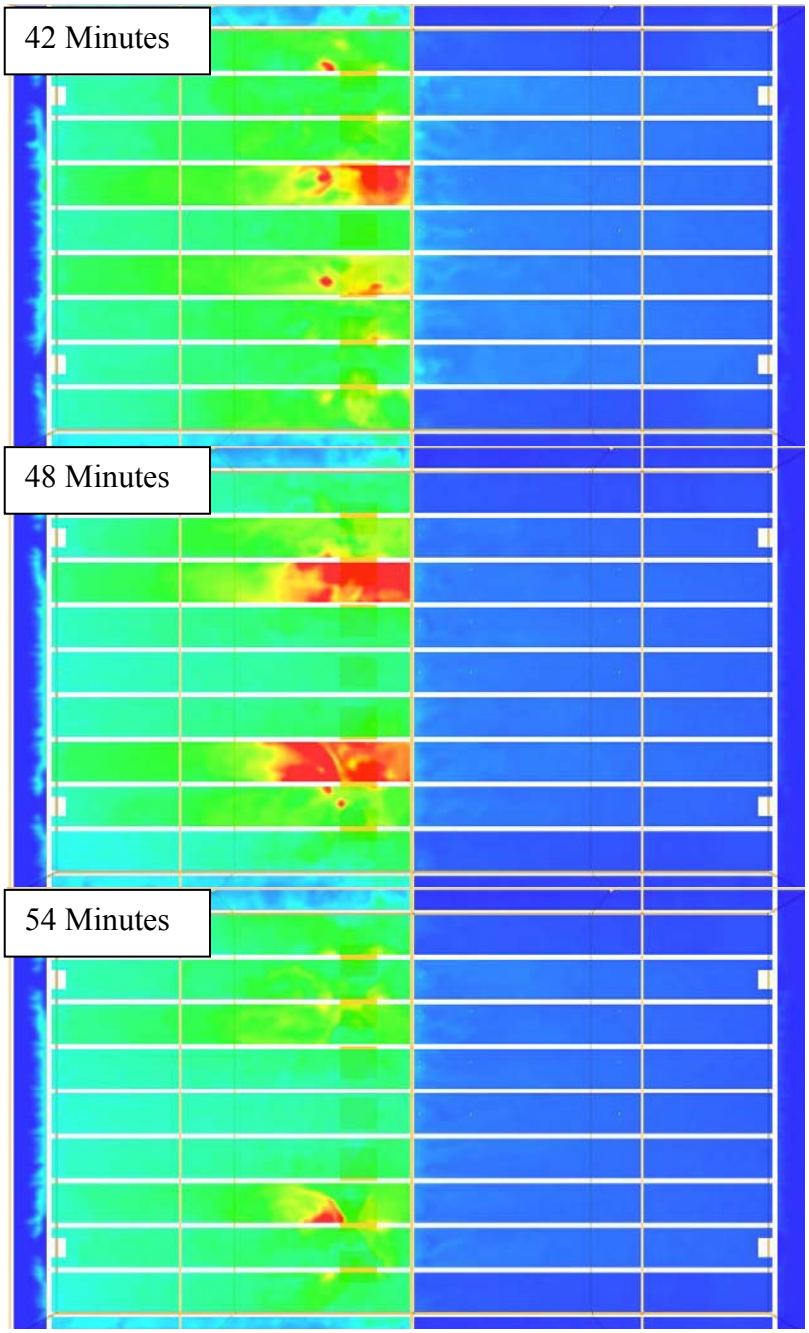

Figure 4-132: Continued from Figure 4-131.

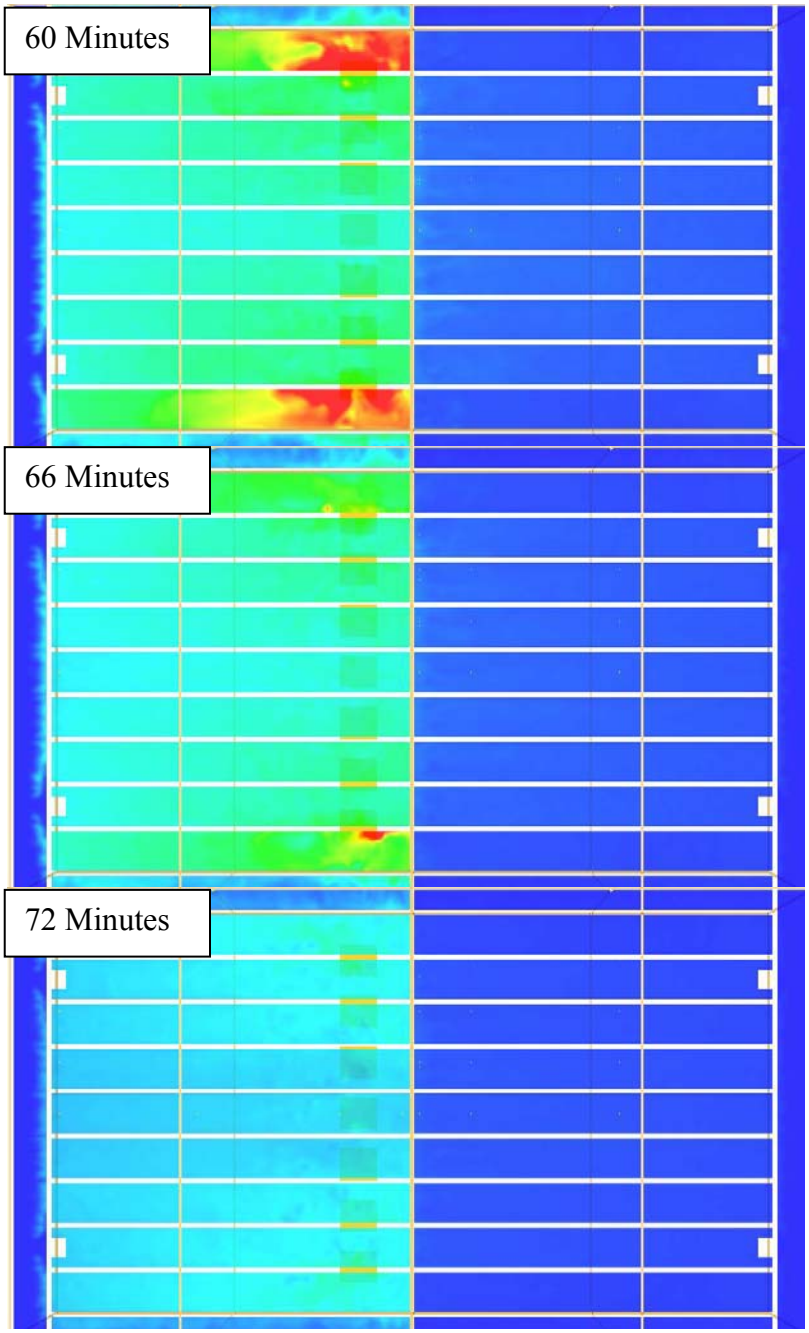

Figure 4-133: Continued from Figure 4-132.

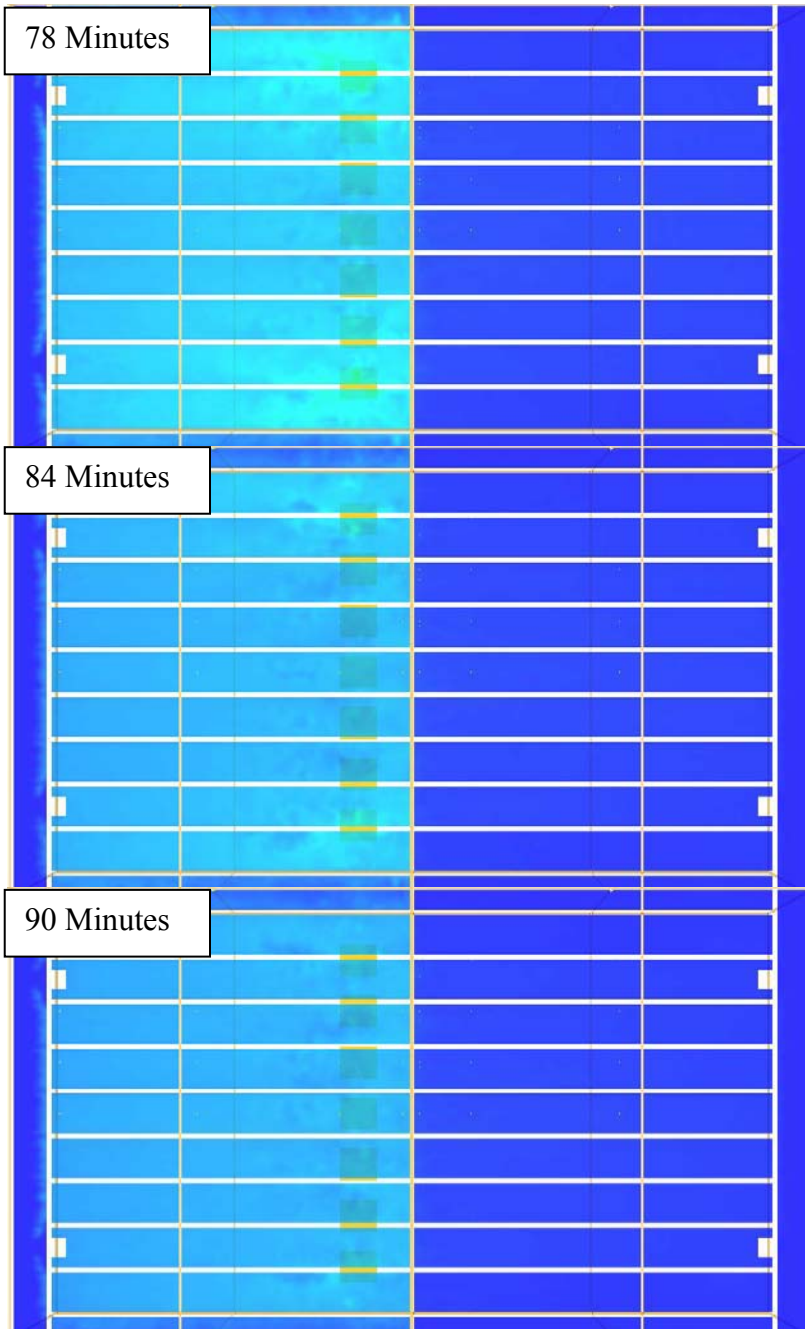

Figure 4-134: Continued from Figure 4-133.

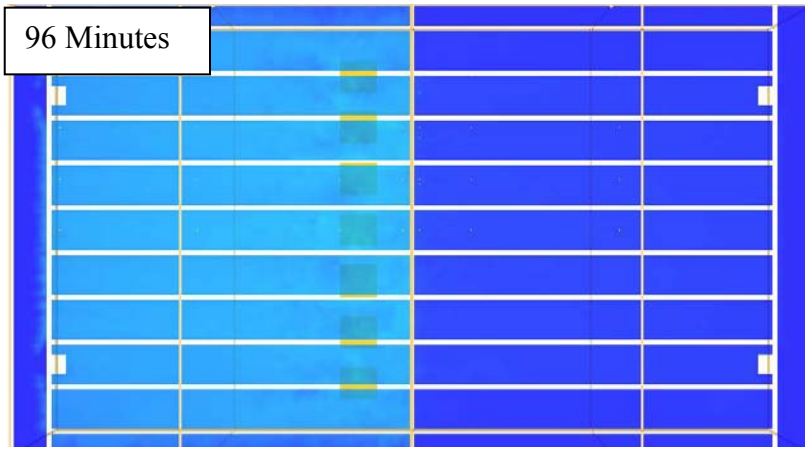

Figure 4-135: Continued from Figure 4-134.

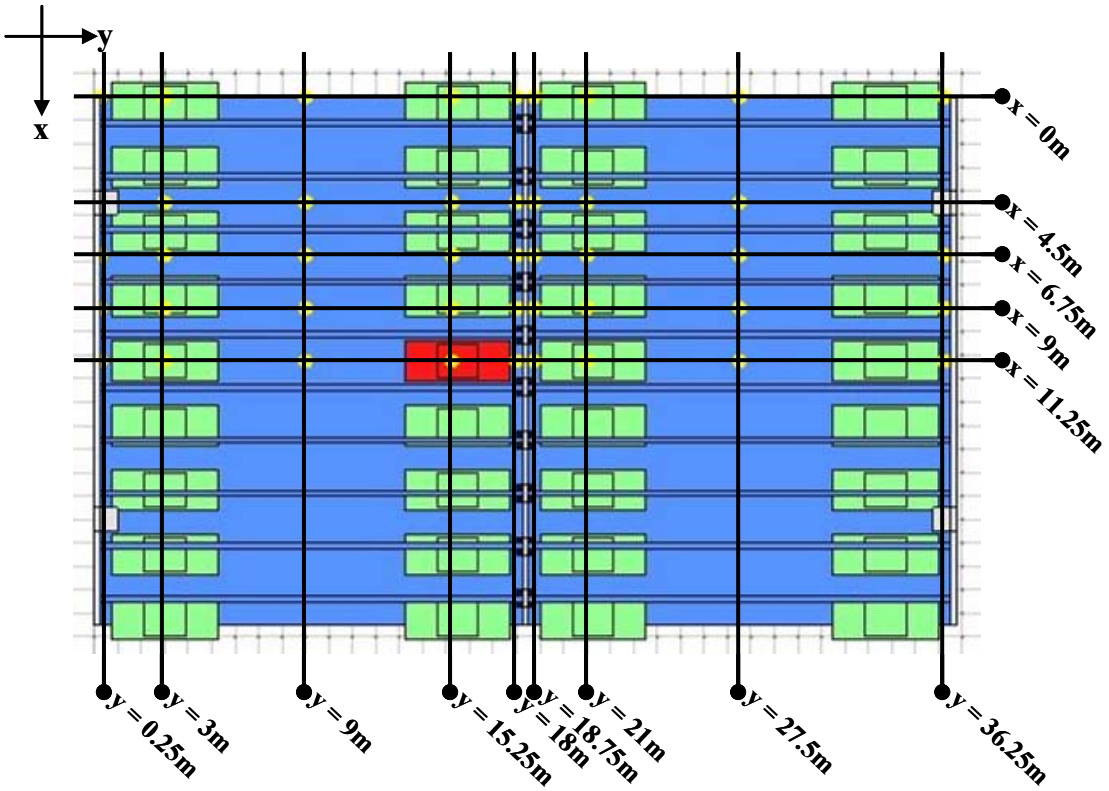

Figure 4-136: Plan view location key for thermocouples.

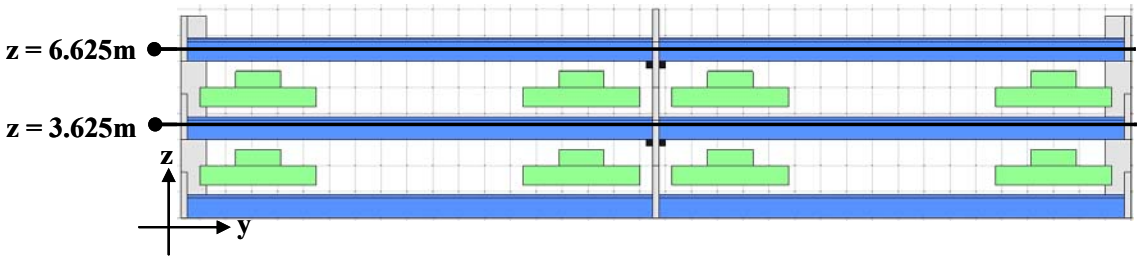

Figure 4-137: Elevation view location key for thermocouples.

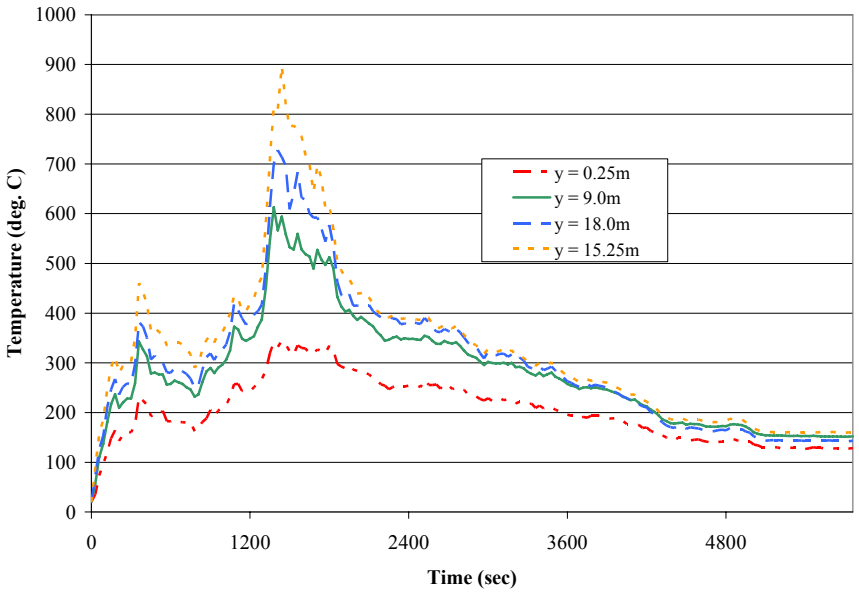

Figure 4-138: Time-temperature histories for Analysis 9 centered between double-tee webs above burning vehicle at x = 11.25m; y = 0.25m, 9.0m, 15.25m, 18.0m; z = 3.625m.

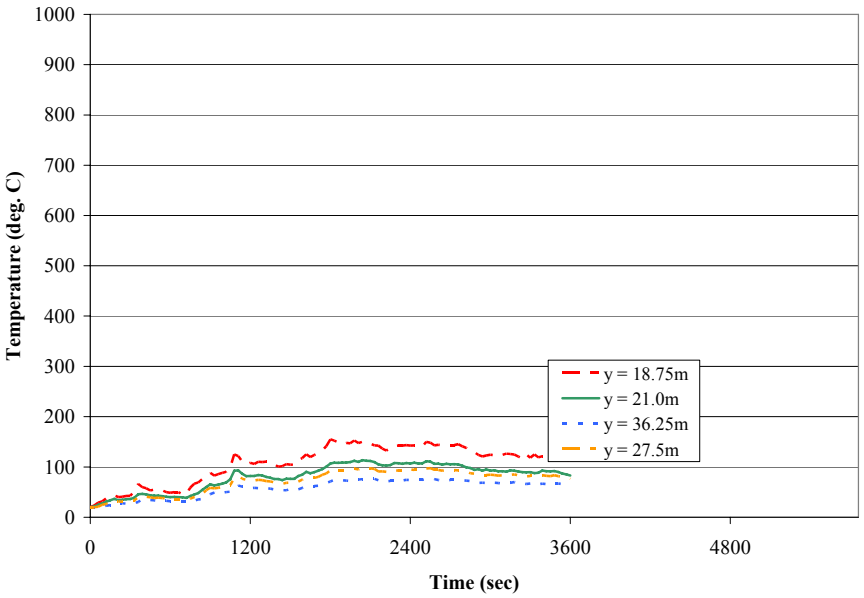

Figure 4-139: Time-temperature histories for Analysis 9 centered between double-tee webs above burning vehicle at x = 11.25m,; y = 18.75m, 21.0m, 27.5m, 36.25m; z = 3.625m.

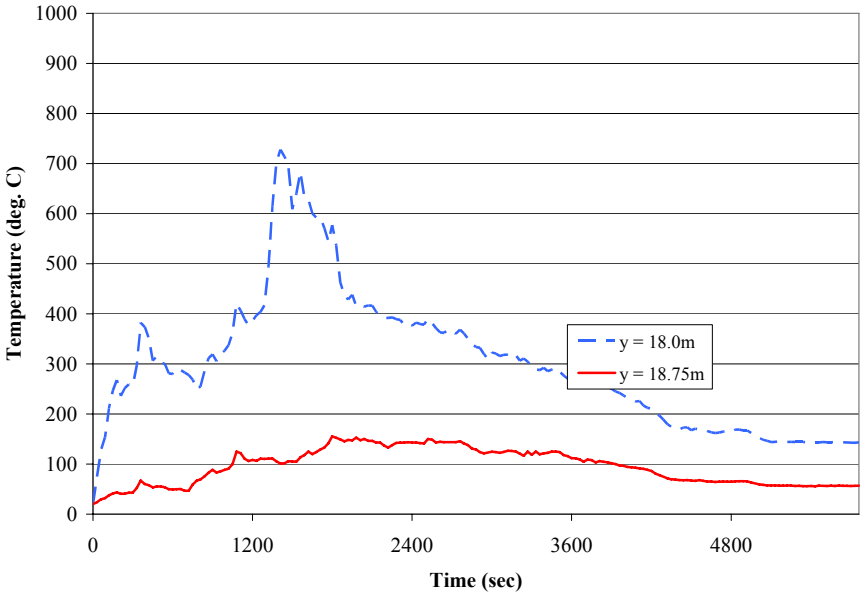

Figure 4-140: Time-temperature histories for Analysis 9 centered between double-tee webs above burning vehicle at x = 11.25m; y = 18.0m, 18.75m; z = 3.625m.

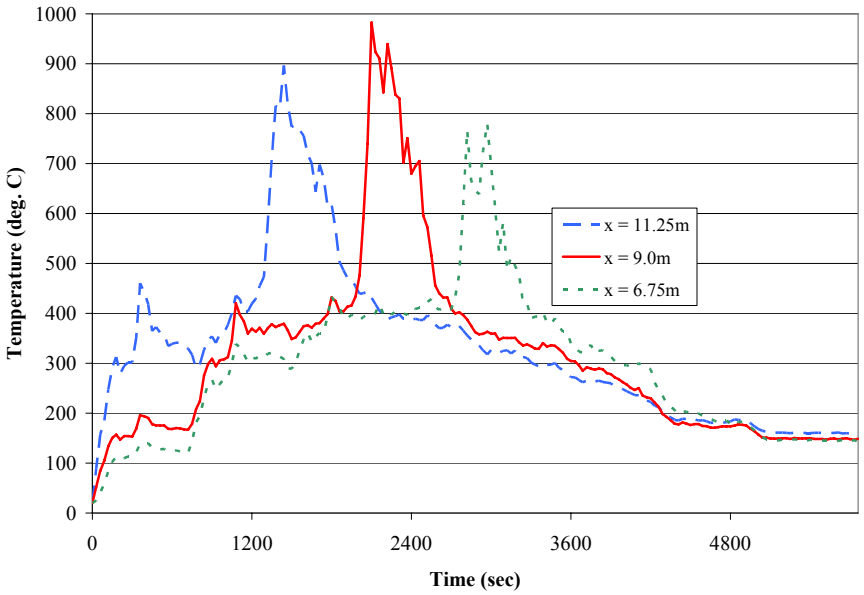

Figure 4-141: Time-temperature histories for Analysis 9 across double-tee webs at x = 11.25m, 9.0m, 6.75m; y = 15.25m; z = 3.625m.

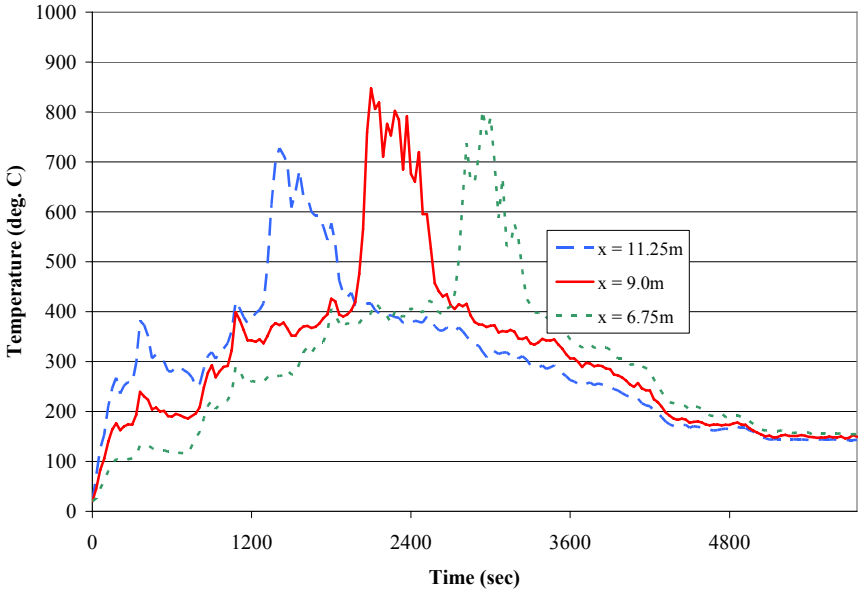

Figure 4-142: Time-temperature histories for Analysis 9 across double-tee webs at x = 11.25m, 9.0m, 6.75m; y = 18.0m; z = 3.625m.

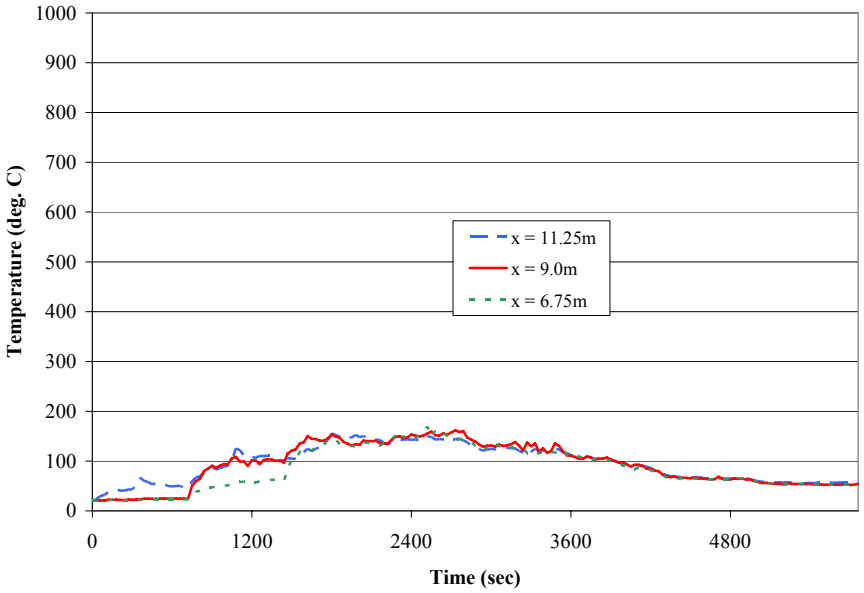

Figure 4-143: Time-temperature histories Analysis 9 across double-tee webs at x = 11.25m, 9.0m, 6.75m; y = 18.75m; z = 3.625m.

CHAPTER 5

ANALYSIS AND DISCUSSION OF RESULTS

This chapter presents a detailed analysis and discussion of the results of the FDS analyses. As stated previously, the broad objective of this research is the development of realistic fire loads (time-temperature or time-heat flux relationships) for structures. More specifically, this research focuses on fire loads for precast concrete parking structures, and investigates the influence of structure geometry and fire characteristics in the resulting fire loading. The following discussion therefore addresses geometry and fire characteristics by grouping the FDS analyses into five sets with some analyses appearing in more than one set.

Section 5.1 discusses the influence of opening position and floor elevation geometry on the fire loading and is broken into four sections: Section 5.1.1 examines the effects of center wall opening position on heat transfer on a single floor using Analyses 1 and 2. Section 5.1.2 uses Analyses 3, 5, and 6 to address geometrical influence on heat transfer between floors. Section 5.1.3 continues the discussion in Section 5.1.2 to examine the potential preheating of upper floors prior to ignition using Analyses 5-8. Lastly, Section 5.1.4 addresses the concept of 'channeling' of heat away from the fire using Analyses 1, 2, and 9.

The effects of fire characteristics are addressed in Section 5.2. The first variable is vehicle burn sequence and is addressed in Section 5.2.1. Next, Section 5.2.2 uses Analysis 3 and 4 as the basis for a discussion of the effects of different heat flux input records.

Section 5.3 discusses the implications of the results of the fire analyses performed in this project to structural design. First, Section 5.3.1 uses the ASTM E119 standard gas time-temperature curve as a comparative tool. Next, Section 5.3.2 discusses the implications of the concrete temperature results obtained by the ABAQUS analyses.

The slice and thermocouple locations used in this chapter are shown in Figures 5-1 and 5-2. The black dots indicate thermocouple locations, and the black lines indicate slice locations. Specific coordinates and a complete explanation of instrumentation is included in Section 3.6.

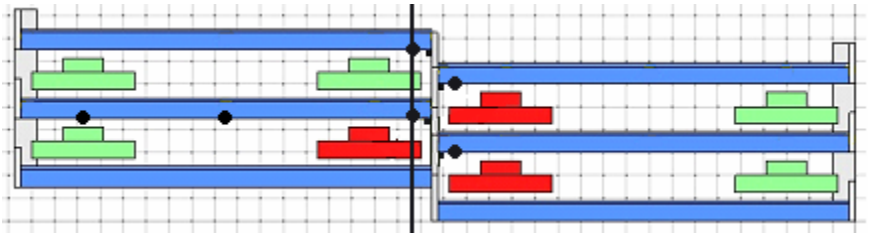

Figure 5-1: Slice and thermocouples used in Chapter 5 discussions (Elevation view).

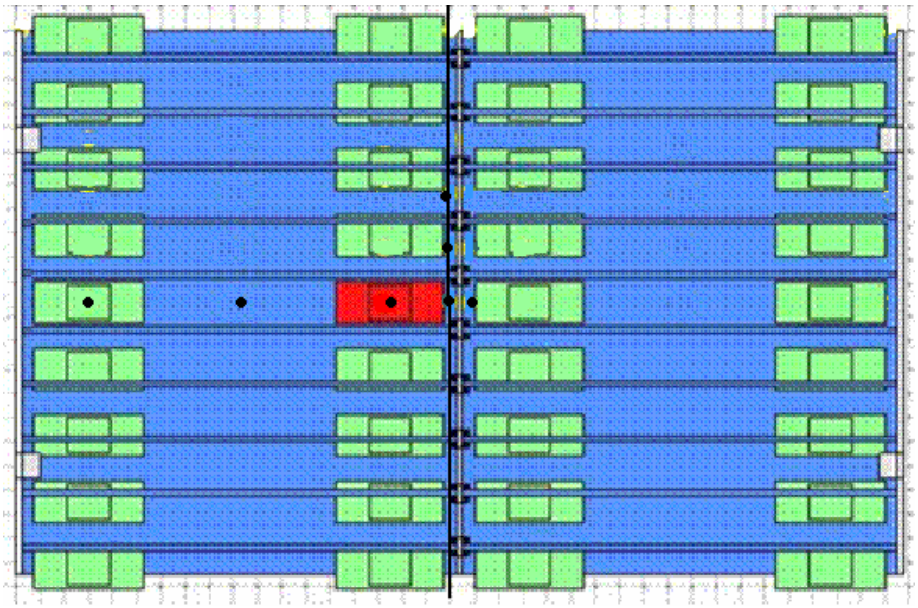

Figure 5-2: Slice and thermocouples used in this chapter (Plan view).

5.1 Geometric Effects on Fire Loading

As explained in Chapter 3, the center wall of the Campus Square parking garage contains a series of regular openings as part of the precast concrete structural system. These openings and their position in relation to the ramped double-tees provide an opportunity for the combustion gases and fire to spread through the center wall from one side of the garage to the other and from one from floor to the next. Analyses 1-3, 5, and 6 are used to investigate the geometrical effects of center wall opening position and floor elevation. The observed heat flow through each of the models follows the pattern one might expect using a conceptual understanding of fluid dynamics when the buoyant characteristics of heated gas are taken into account. Summarizing, the heat flows vertically upward until it encounters an obstruction, then spreads laterally through the cavity and vertically downward until that space is filled, and then the heat spills over into the next cavity.

5.1.1 Heat Transmission through the Center Wall

Starting with a comparison between Analyses 1 and 2 it is seen that center wall opening position greatly affects the transmission of heat from the side of the garage where a fire is burning to the opposite side.

In Analysis 1, the opening is positioned flush with the underside of the double-tee flange. It is expected the opening will allow the heat to flow freely along the underside of the double-tee slabs through the center wall. The only obstruction to heat flow through the center wall openings are at the sides where small protrusions from the columns extend past the double-tee webs. A finer mesh in the FDS model and a different set of output variables might show some turbulence and interference from the columns at the sides. This effect is assumed to be negligible for the larger model results for this project.

The anticipated results for heat to flow freely through the center wall are supported by the results as shown in Figure 4-15. Figure 4-15 is plot of time-temperature histories from thermocouples on either side of the center wall (11.25m, 18m, 3.625m and 11.25m, 18.75m, 3.6.25m) from Analysis 1. In the figure, very little temperature drop from over the 0.75m between the two thermocouples shown, which are 0.25m away from the center wall on either side. The slight increase in temperature from one thermocouple to the next (y = 18.0m to y = 18.75m) is what would be reasonably expected for the distance covered.

Analysis 2 shows how lowering the position of the center wall opening can reduce the heat transmission from one side of the garage to the other. The Analysis 2 model included the opening as low in relation the bottom of the slab as possible and creating an obstruction to heat flow that extends well below the lower edge of the double-tee webs. It was anticipated that heat would build up in the cavity between the double-tee webs staying on the side of the garage where the fire occurs, and the results support the predictions. Little heat is allowed to flow through the wall as shown in slice images Figures 4-23 and 4-24, instead, the heat flows away from the center wall toward the exterior of the garage.

Comparing Analyses 1 and 2, the effect of the structure geometry may be more clearly seen. Because the geometry of the model in Analysis 2 traps the heat on one side of the center wall, the gas temperature rises higher than that in Analysis 1 where the heat is allowed to freely flow through the center wall openings (See Figure 5-3). The higher intensity of the Analysis 2 heat into the surface of the concrete results in a higher concrete temperature at the level of the first prestressing strand (See Figure 5-4).

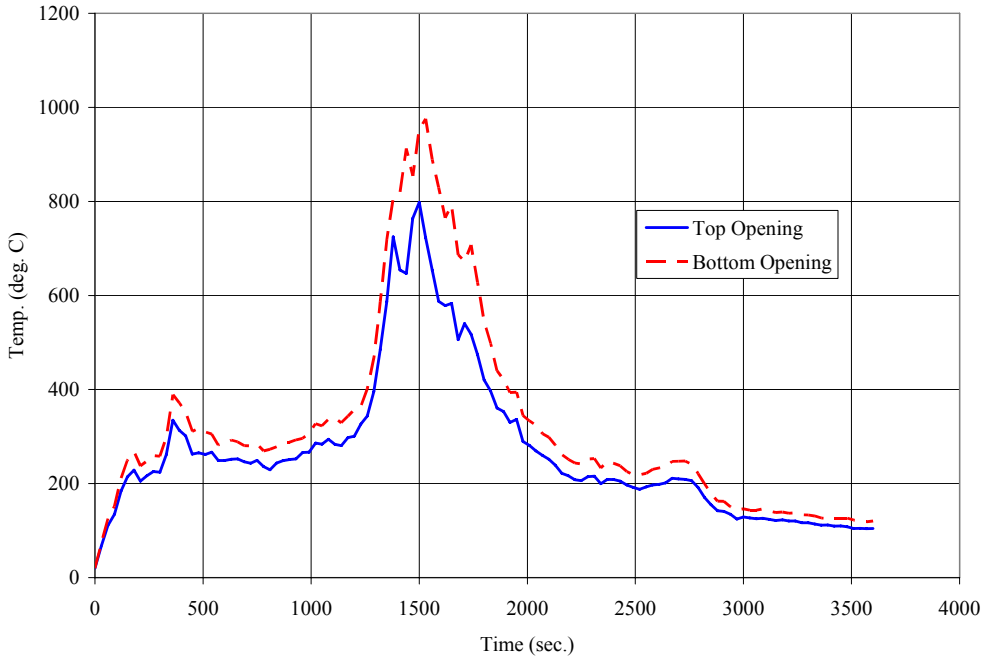

Figure 5-3: Gas temperature comparison between Analyses 1 and 2 next to the center wall (11.25, 18, 3.625).

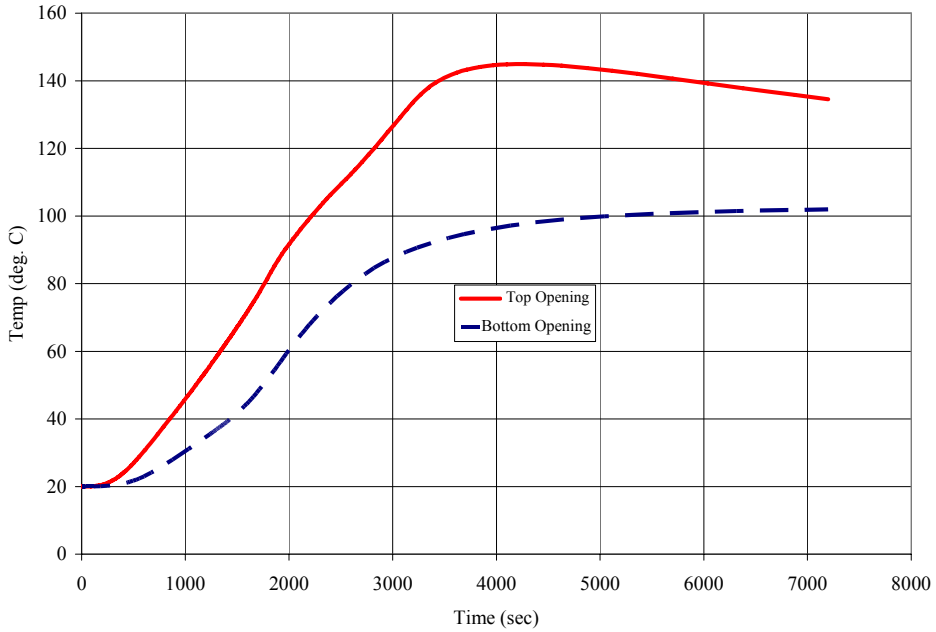

Figure 5-4: Concrete temperature at level of first prestressing strand above burning vehicle at 11.25,15.25,3.625m in Top and Bottom Opening Analyses.

Additionally, the difference between effect of the top and bottom opening positions is seen by the gas temperature record at the far end of the double-tee away from the fire at (11.25, 0.25, 3.625). (See Figure 5-5)

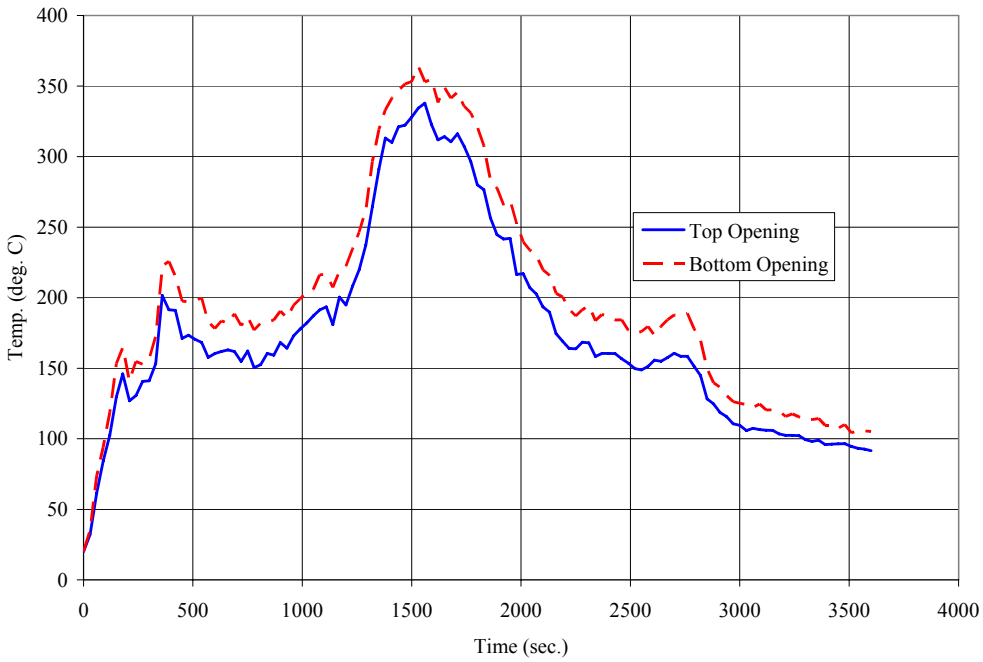

Figure 5-5: Gas temperature comparison at the exterior end of the double-tee away from the fire (11.25,0.25,3.625).

It is seen that, because the heat is forced to stay on the same side of the parking garage in the Analysis 2 model, the temperature at the exterior end of the double-tee is higher than in the Analysis 1 model.

5.1.2 Heat Transmission Between Floors

Heat flow between floors was investigated using Analyses 3, 5, and 6. Section 5.1.2.1 focuses on Analysis 5 and 6 to examine the heat flow between floors with staggered elevation, and Section 5.1.2.2 uses Analysis 3 for a similar discussion when floors are at level elevation.

5.1.2.1 Heat Flow Between Floors with Staggered Elevation

Analysis 5 was constructed specifically to allow heat transmission from one floor to the next through the center wall. The center wall openings were positioned in the same

manner as the Analysis 5 model for floors 1 and 3 to allow free heat flow through the center wall, and the floors were evenly staggered to simulate even spacing of the ramped double-tees resulting in a different opening position for floors 2 and 4. (See Figure 5-6)

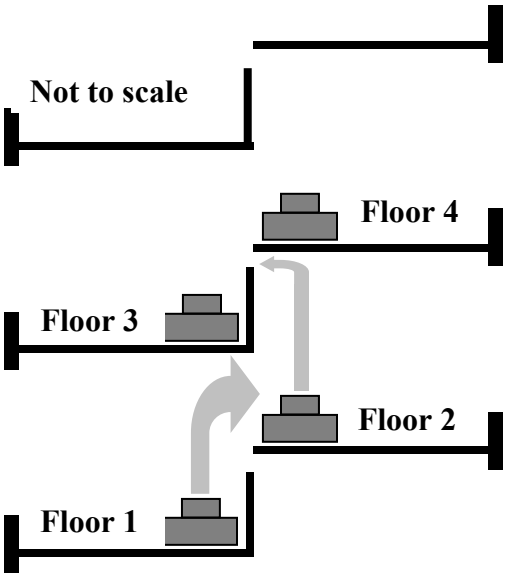

Figure 5-6: Analysis 5-8 geometry showing concrete in black, and potential heat flow from one floor to the next in gray arrows.

The preheating of the upper floors due to this geometry is discussed in Section 5.1.3. The results from this analysis with regard to center wall opening position are similar to those recorded in Analysis 1 because the same position was used (See Figure 5-12). Heat is allowed to flow freely through the opening in the center wall, but there is some difference shown in the peak of the time-temperature history recorded at the center wall on the side of the fire. The temperature in the Analysis 5 model appears to oscillate for a period of three minutes at peak. Differences in behavior between the models could be attributed to turbulence effects as the gas changes flow direction in the Analysis 5 and Analysis 3 models but does not do so in the Analysis 1 model. For this project, however, the sampling rate, which is 30 seconds for temperature readings in this project is likely not fine enough to draw a supported conclusion regarding this specific behavior. For the purpose of this project, the responses are taken to be the same.

As expected, the temperature rise on the second floor in the Analysis 5 model is significantly higher than that recorded in the Analysis 3 model. A comparison of the gas temperatures recorded on the second floor in the two models in shown in Figure 5-7.

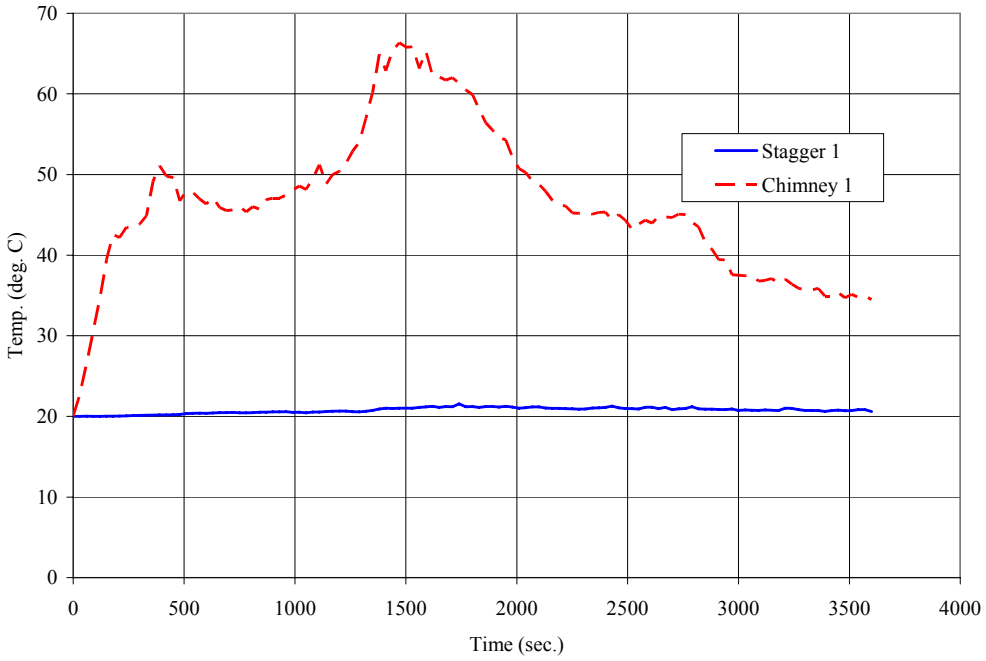

Figure 5-7: Comparison of gas temperature on second floor of Analysis 5 (11.25, 18.75, 5.125) and Analysis 3 (11.25, 18.75, 6.625).

The concrete temperatures that result from the heat transmission to the second floor in both the Analysis 5 and Analysis 3 models are shown in Figure 5-8. The small gas temperature increase in the Analysis 3 model results in essentially no increase in concrete temperature, while the Analysis 5 curve shows a smooth concrete temperature increase throughout the analysis to a peak of 43 degrees Celsius.

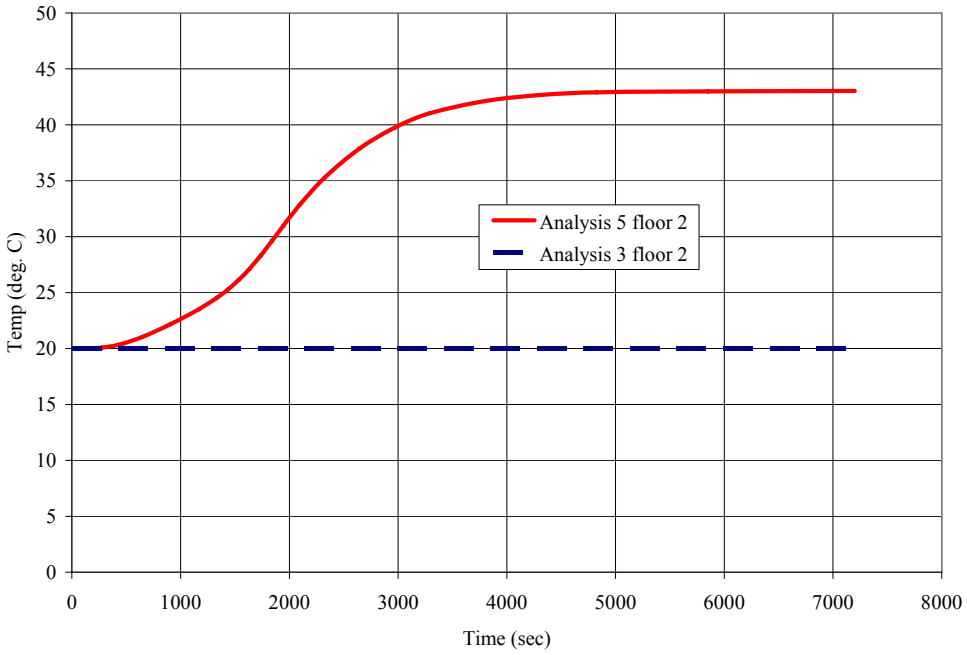

Figure 5-8: Concrete temperature on the second floor comparing Analysis 5 and Analysis 3 models.

In addition to the heat flow between floors 1 and 2, vertical heat flow is also observed between floors 2 and 3. The gas and concrete temperature predictions from Analyses 5 and 6 are shown in Figures 5-9 and 5-10 respectively.

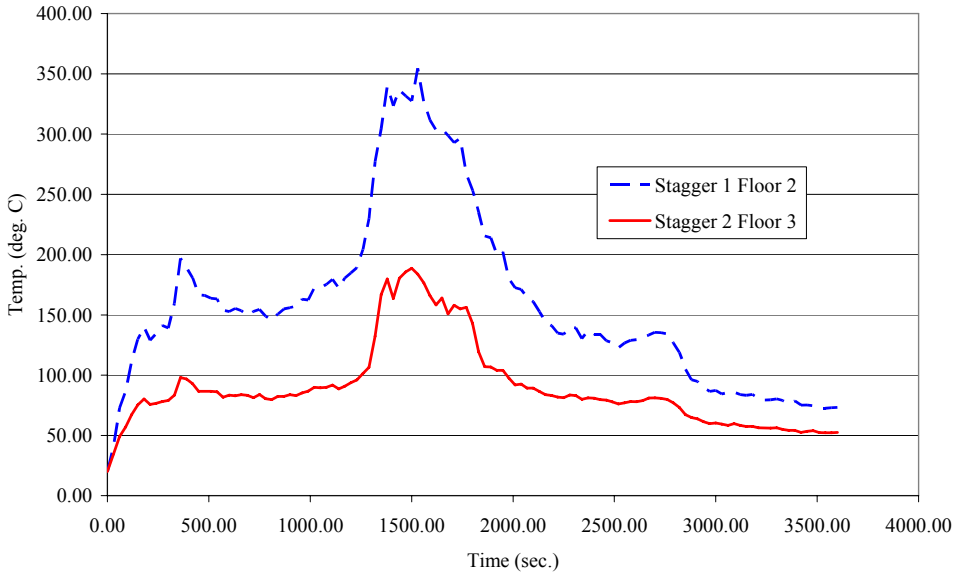

Figure 5-9: Comparison between floor-to-floor gas temperature rise in Analysis 5 and Analysis 6.

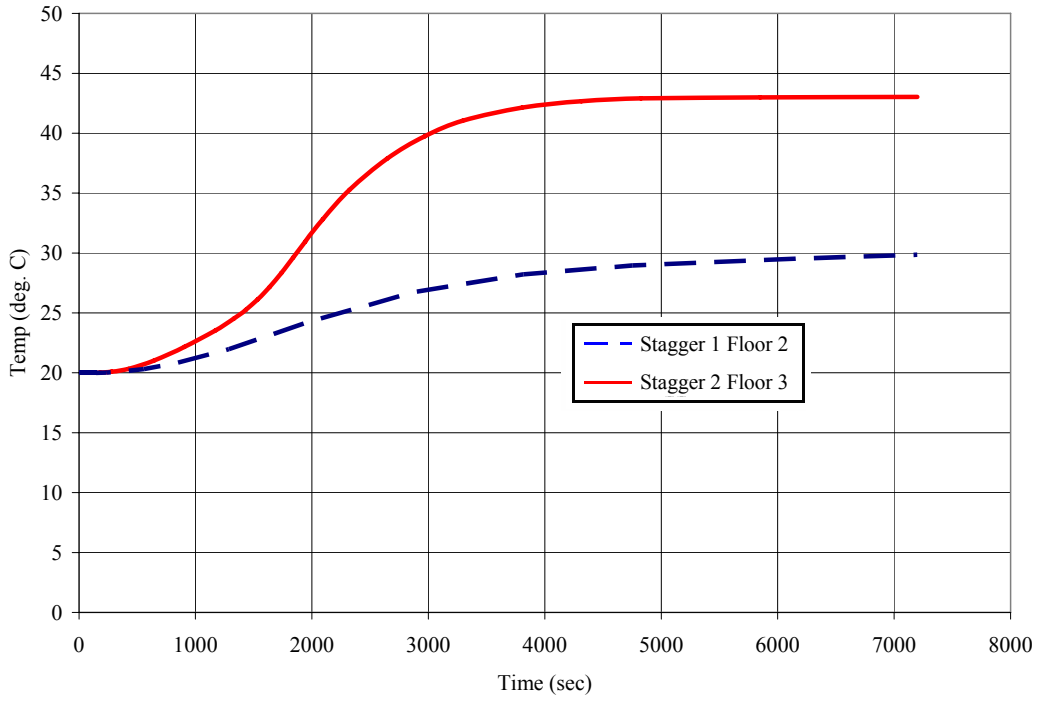

Figure 5-10: Comparison between floor-to-floor concrete temperature rise in Analysis 5 and Analysis 6.

Because of the difference in the center wall opening position between floors 1 to 2 and 2 to 3, as shown in Figure 5-6, the temperature difference is seen. The smaller opening between the second and third floors results in half of the temperature increase seen for the same fire in the same relative position seen between the first and second floors. In addition, a significantly decreased concrete temperature is seen comparing Analysis 5 floor 2 to Analysis 6 floor 3.

5.1.2.2 Heat Flow Between Floors at Level Elevation

In Analysis 1 the center wall opening straddles the double-tee slab and creates a 'chimney' opening in the center wall between the slabs that is the width of the center wall opening and the depth of the center wall itself for a total area of 0.375 square meters. This scenario can occur in the garage at a point where the ramps cross each other in the approximate center of the garage so that the floors are at essentially the same level. This situation may also occur at openings of limited size in the floor slab for grates or utilities. Because of the limited size of the 'chimney,' the amount of heat transferred to the upper floor is low as shown by the thermocouple temperature records in Figure 4-54, which show a peak temperature on the upper floor of less than 75 degrees Celsius. The small temperature rise recorded in the upper floor would suggest that openings of limited size in the double-tee slabs, do not pose a major path for heat flow with a parking garage.

With the exception of the small amount of heat that escapes to the next floor, and subsequently a slightly higher peak temperature, the Analysis 3 model results are similar to those collected from the Analysis 1 model (See Figure 5-11). This similarity is likely caused by the fact that the center wall opening extends below the bottom edge of the double-tee webs, and free flow of heat along the underside of the double-tee slab through the center wall is allowed in much the same way as the Analysis 1 model.

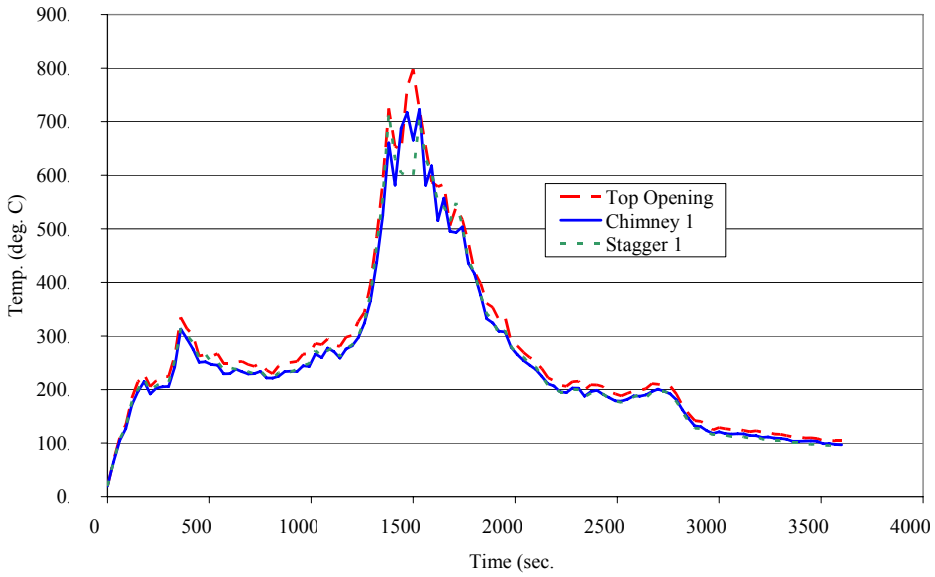

Figure 5-11: Gas temperature comparison next to center wall (11.25, 18, 3.625).

Summarizing the findings from the models discussed in this section, the geometry of the precast concrete parking structure has a significant impact on the transmission of combustion gases in the structure. The center wall opening position relative the floor location results in significant effect on the heat transmission through the structure. By lowering or raising the opening position when the floors are at the same level (Analyses 1-3) gas and concrete temperatures may be caused to build up on one side of the center wall when the opening is low or distribute more evenly through the wall when the opening is high. When the floors are staggered to simulate the driving ramps, the center wall opening position also plays a major role in heat transmission by trapping or allowing heat to flow to upper floors.

5.1.3 Preheating of Upper Floors due to Geometry

One of the questions addressed in this project was if a fire on a lower floor of the parking garage might cause significant preheating on an upper floor prior to the ignition of a fire on that floor. Section 5.1.2 explained that heat does flow to the upper floors if the center

wall opening positions allow, so it was hypothesized that this preheating could create longer durations of heating or higher temperatures causing greater risk to the structure than a single vehicle fire. In order to investigate the preheating effect, four models were used: Analysis 5-8. Each of the single-vehicle fire models (Analysis 5-7) was run separately as if it the ignition occurred at time = 0 and compared to the sequential burn (Analysis 8) by offsetting the output records by the appropriate ΔT.

By comparing the temperature records from Analysis 5 floor 2 and Analysis 8 floor 2 the preheating effect on the gas temperature may be seen. (See Figure 5-12)

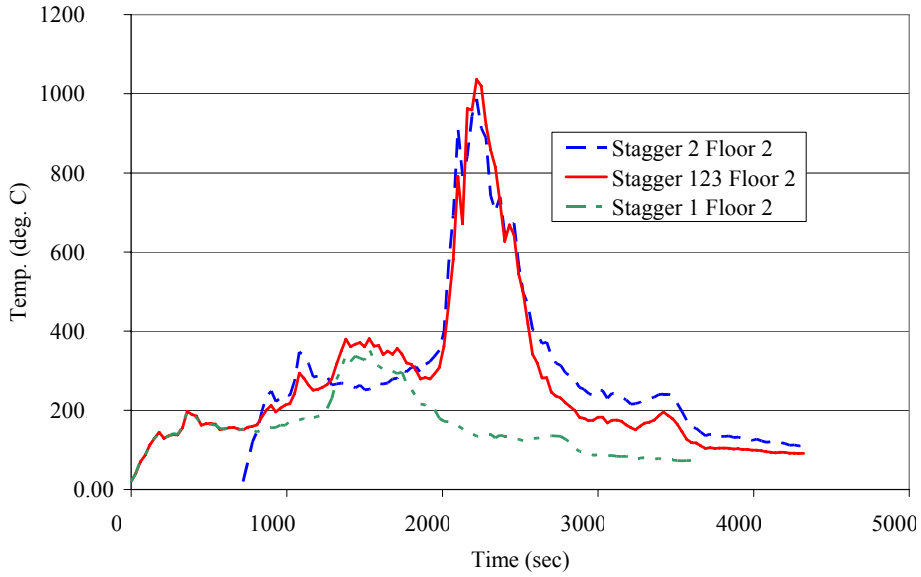

Figure 5-12: Preheating effect on gas temperature on floor 2 in the Analysis 5-8 models.

Prior to fire ignition on floor 2 at ΔT = 12 minutes (720 seconds), the temperature is seen to rise because of the heat transmission through the center wall openings (Stagger 123 Floor 2 – solid line). From 720 seconds to about 1800 seconds, the temperature record for Stagger 123 is shown to closely follow a combination of the actual fire on the second floor (Stagger 2 floor 2) and the heat transmission effect from the fire on the first floor (Stagger 1 floor 2). The two fires create this effect on temperature on the second floor as expected because they are both heat sources, one direct, and one through the center wall up to the second floor. After the effect of the fire on floor 1 is finished at about 2000 seconds, the temperature record follows a very similar curve to that of the single fire on the second floor. Even though the gas was preheated by the lower floor fire, there is little long-range effect on the temperature record, and no difference in peak temperature.

Gas temperature alone provides an incomplete picture of the results. To understand the influence of preheating on the behavior of the structure, the concrete temperature also is

examined. Figure 5-13 compares the concrete temperature on floor 2 at the level of the first prestressing strand in Analyses 6 and 3 just above the burning vehicle.

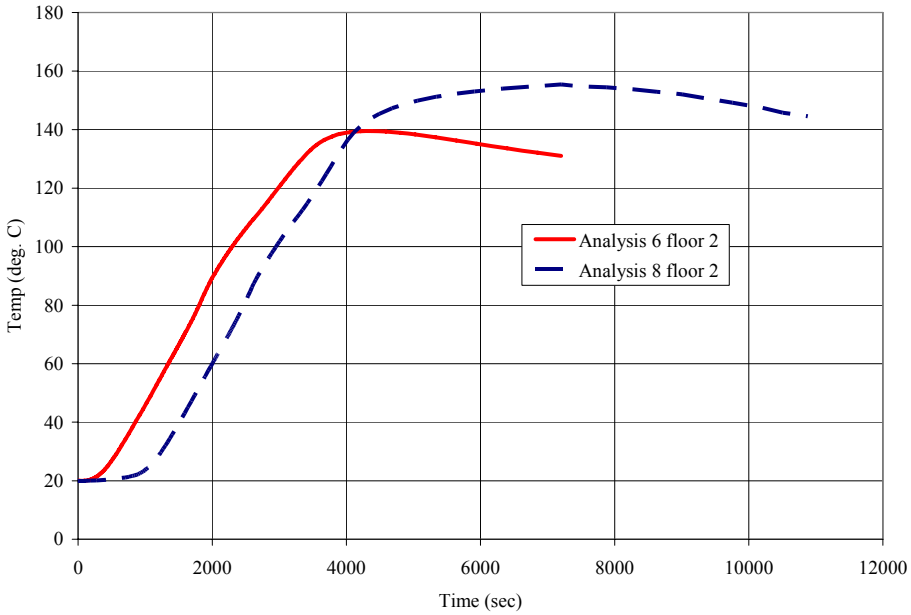

Figure 5-13: Concrete temperature at level of first prestressing strand on floor 2.

Figure 5-13 shows that the preheating on floor 2 because of the fire on floor 1 causes an increase in the concrete time-temperature curve. The temperature is seen to increase by an average of 20 degrees over the course of the fire due to preheating.

Because of the difference in center opening position between floors 2 and 3 in the Analysis 5-8 models, it was shown in Section 5.1.2 that significantly less heat flows to from the floor 2 to 3 as compared to floor 1 to 2. Similarly, the preheating effect on floor 3 is less than that on floor 2 when the temperature records from Analysis 8 are compared (See Figure 5-15).

In Figure 5-14, the preheating gas time-temperature curves are shown, and the significantly lower temperature at any point in time on floor 3 is observed. The fire on floor 2 starts at 720 seconds, ending the preheating and starting the combined heat sources, and the fire on floor 3 starts 720 seconds later at 1440 seconds. Because of the effect of the center wall opening position causing lower heat transmission to the third floor, the greater fire loading to the structure is on the second floor.

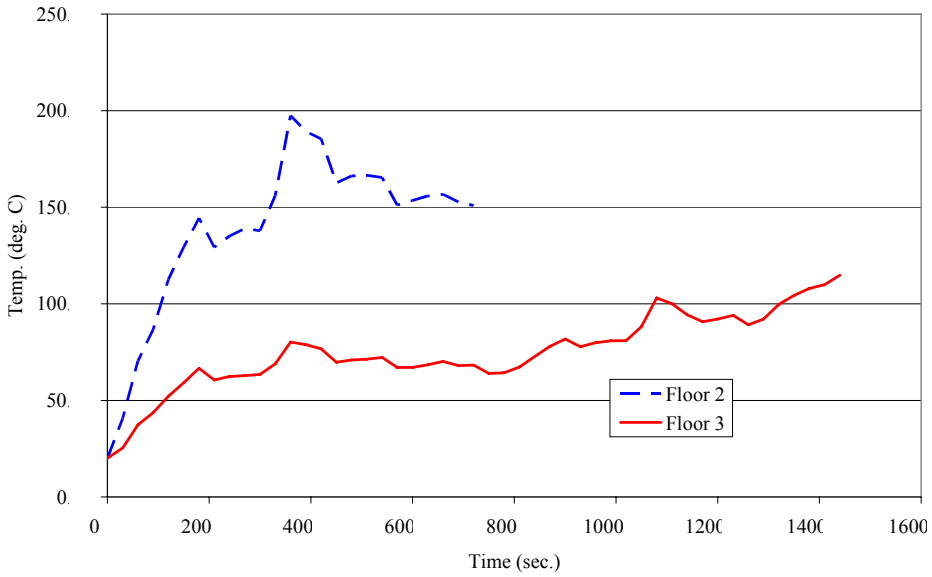

Figure 5-14: Preheating effect in Analysis 8 on floors 2 and 3 comparison.

5.1.4 Effects of Geometry in Channeling Heat Away from the Fire

As discussed previously, a vehicle fire in a parking garage could be characterized as a plume fire impinging on a horizontal surface. The horizontal surface in this case is the underside of the double-tee slab, which is broken at regular intervals by the webs of the double-tees. If the webs were not present, the flames and heat would spread radially outward from the center of the fire. The webs serve to longitudinally 'channel' the heat away from the fire and largely prevent the heat from spilling over transversely.

The 'channeling' effect caused by the double-tee webs is present in all models tested for this project, but this discussion focuses on three models: Analyses 1, 2, and 9.

Comparing the results from the Analysis 1 and 2 models, the 'channeling' effect is clearly present. The Analysis 1 model shows free longitudinal flow between the double-tee webs on both sides of the center wall with very little heat spilling over the webs. In the Analysis 2 model, the center wall opening position forces some of the heat to spill over the webs and prevents much of the heat from flowing through to the other side of the model. Despite the redirection of some of the heat, longitudinal heat flow is still the primary convection mechanism due to the geometry of the double-tees. Figure 5-15 to 5-17 show gas temperature distribution images from the Analysis 1, Analysis 2, and Analysis 9 models. The darker shading indicates higher temperatures, and all three images show that the heat is trapped between the double-tee webs, effectively "channeling" it longitudinally through the structure.

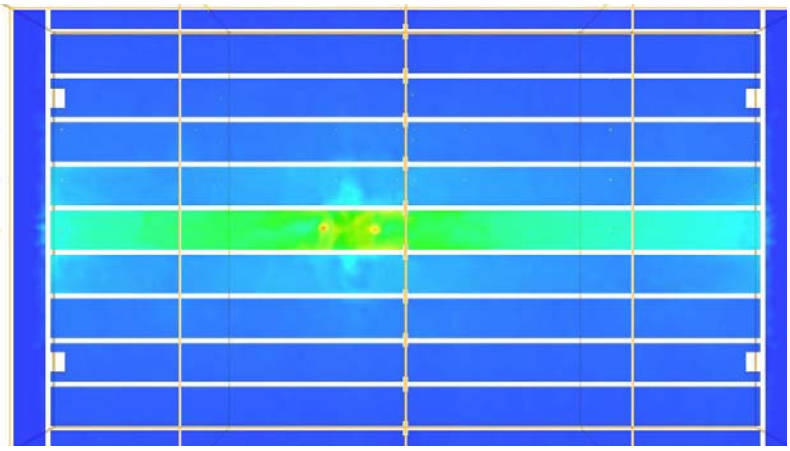

Figure 5-15: Analysis 1 gas temperature image at 1800 seconds.

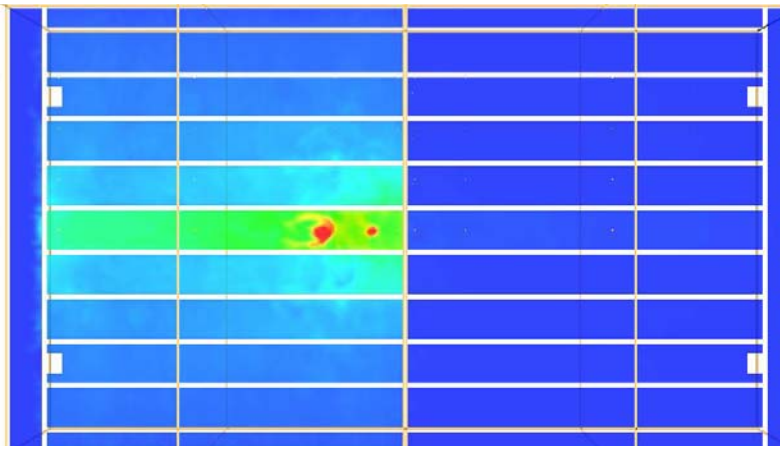

Figure 5-16: Analysis 2 gas temperature image at 1800 seconds.

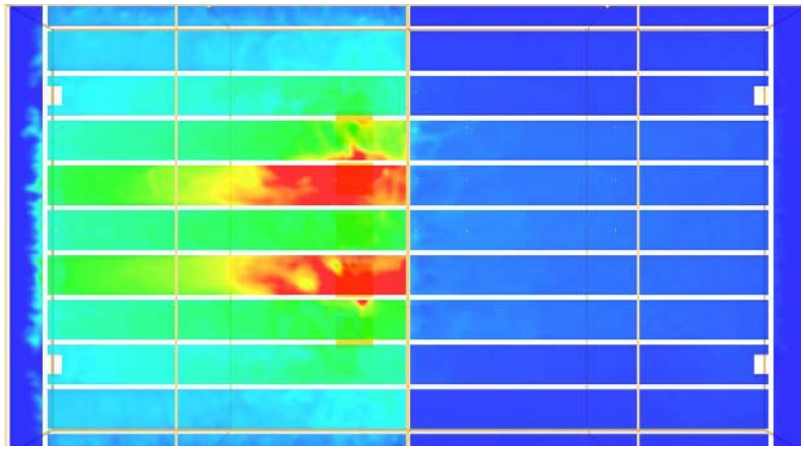

Figure 5-17: Analysis 9 gas temperature image at 2160 seconds.

The implication of the "channeling" effect is that the heat flows away from the fire longitudinally, mostly staying between the double-tee webs, and potentially helping to keep the overall temperature and subsequent risk to the structure down. This idea is supported by the gas temperature records shown in Figure 5-18.

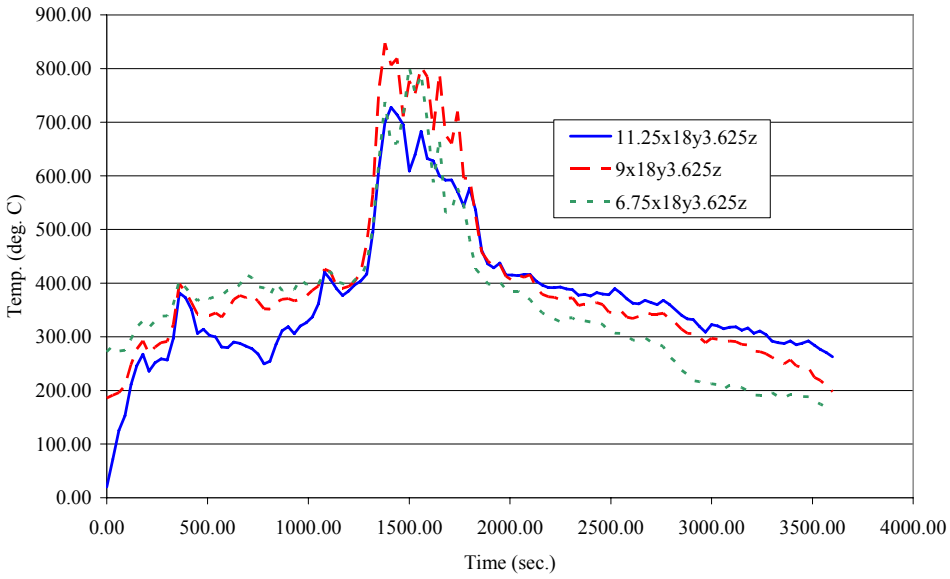

Figure 5-18: Shifted gas temperatures for Analysis 9.

The gas temperature records in Figure 5-18 have been shifted so the times line up for comparison. The curve for x = 9m is shifted -720 seconds and the curve for x = 6.75m is shifted -1440 seconds to correspond to the fire ignition times of ΔT = 720 and 1440 seconds respectively. It is seen that, even though there are additional vehicles burning under adjacent double-tee cavities, the gas temperature records for x = 11, 9, and 6.75m are very similar with peak temperatures of less than 100 degrees Celsius difference.

Summarizing the findings discussed in this section regarding the channeling of the heat by the geometry of the double-tee webs: the geometry causes heat to be trapped between the double-tee webs and helps to force convection longitudinally along the double-tee cavities.

5.2 Effects of Fire Characteristics on Fire Loading

5.2.1 Fire Burn Sequence

For this project, the sequence of ignition of each vehicle in the two multiple vehicle burn analyses (Analyses 8 and 9) was chosen as a standard time offset (ΔT). Since this value was fixed, the effects of the burn sequence are actually geometric and not a function of fire characteristics as would have been the case if ΔT was allowed to vary. For Analysis 8, the fire burn sequence is taken into account in the preheating geometric considerations (Section 5.2), and for Analysis 9, the effects are taken into account in the channeling considerations (Section 5.3).

5.2.2 Fire Heat Flux

The Analysis 3 and 4 models were built partly to investigate the potential differences in heat flow and temperature response in the model when two very different heat flux inputs were used. For Analysis 3 the vehicle 1 fire record was used, which is the same input that was used for all other analyses except Analysis 4. For Analysis 4, the vehicle 2 record was used.

The peak heat flux of vehicle 2 is more than 1500 kW higher than that of Vehicle 1. More qualitatively, the profiles of each of the histories exhibit very different characteristics as shown in Figure 5-19. The Vehicle 1 history shows two distinct peaks, the first is sharp, occurring at 360 seconds and 3000 kW, and the second building at approximately the same rate, but staying at a 5000 kW peak for almost 200 seconds before gradually decaying. In contrast, the Vehicle 2 fire builds to 3000 kW at approximately the same growth rate as the other fire, but once it reaches this point, the fire plateaus before rising to a sharp peak of 6763 kW at 2100 seconds.

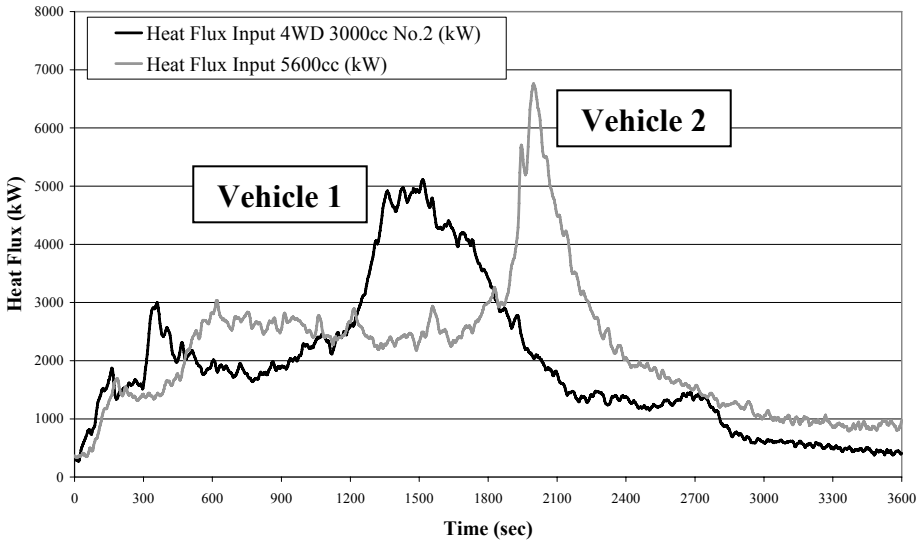

Figure 5-19: Comparison between heat flux inputs used for models.

The output from model follows the profile of the original heat flux input as in the rest of the analyses performed (See Figures 5-20 and 5-21).

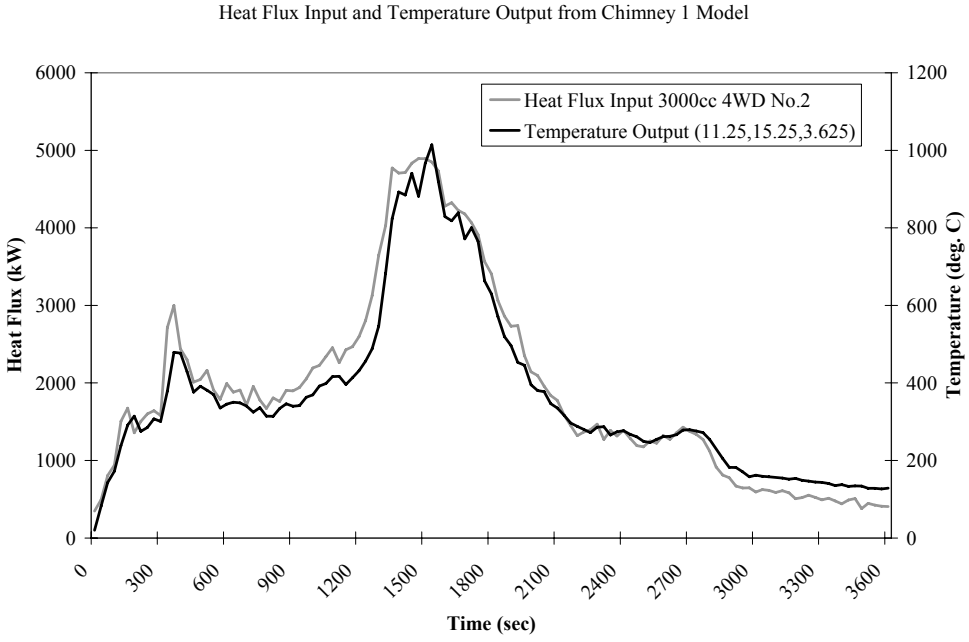

Figure 5-20: Heat flux input comparison to temperature output for Analysis 3.

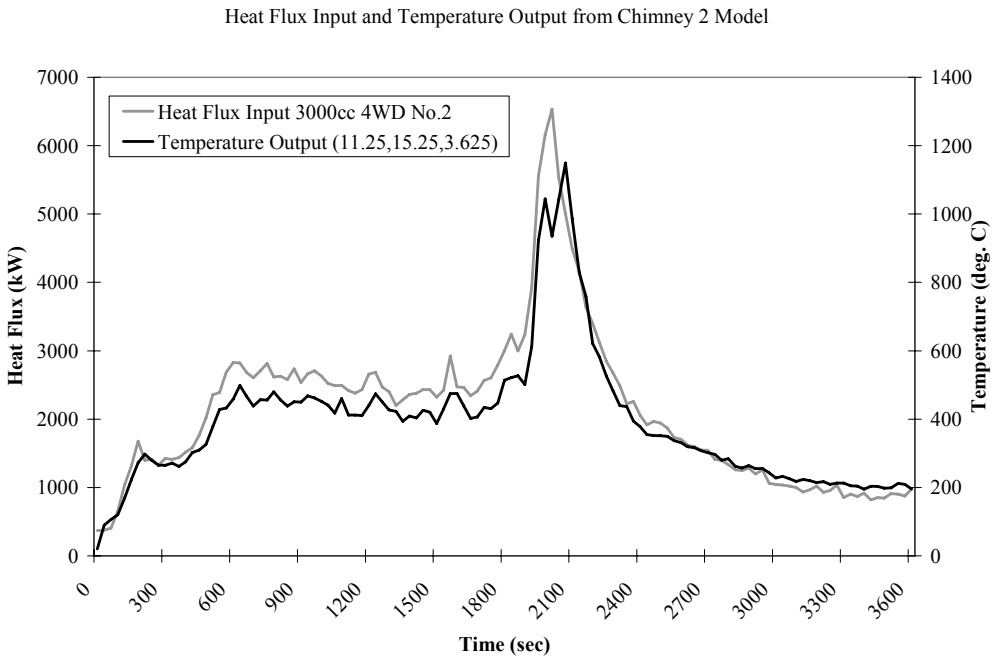

Figure 5-21: Heat flux input comparison to temperature output for Analysis 4.

In order to try to distinguish between the two vehicle fire models, a non-linear heat transfer analysis was performed following the procedures in Chapter 3. The concrete time-temperature curve at the level of the first prestressing strand was recorded for each of the Analysis 3 and 4 models and is shown in Figure 5-22.

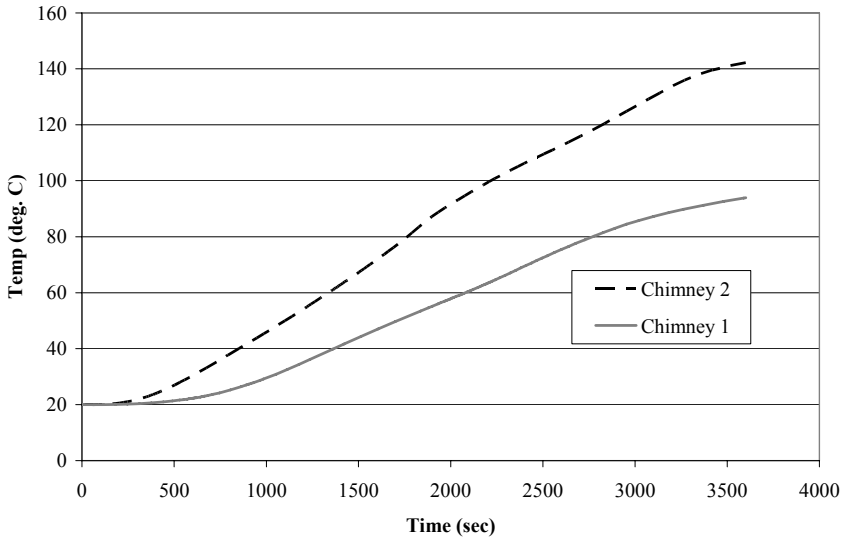

Figure 5-22: Time-temperature curves for Analysis 3 and 4 at the level of the first prestressing strand.

The time-temperature curve for Analysis 4 is significantly lower than that of the Analysis 3 model, which supports the idea that higher total energy release over the same time period results in higher heat flux into the structure and higher concrete temperatures.

5.3 Implications of Fire Analyses

The fire analyses performed for this project are applicable to an open parking garage under various vehicle configurations and fire ignition sequences according to the geometry and fire characteristics applied as variables. This section compares the results of the analyses to the ASTM E119 standard time-temperature curve (Section 5.3.1). This section also discusses the structural significance of the concrete temperatures predicted for the various analysis cases (Section 5.3.2).

5.3.1 ASTM E119 Fire Comparisons

The ASTM E119 standard fire time-temperature curve was discussed in detail previously in Section 2.2. For the sake of this analysis, it is important to reiterate, that the standard curves, including ASTM E119 and ISO 834, are intended for comparative purposes and are generalizations. That being understood, standard time-temperature curves are used in many furnace analyses of structural elements, so it is useful to compare the results of the FDS analyses to the standard curve for comparative purposes. Figures 5-23 to 5-34 show comparisons between the ASTM E119 curve and the select thermocouple records from each of the analyses. These figures show clearly that in all cases for single vehicles fires (Analyses 1-7) the time-temperature record does not approach the ASTM E119 curve

until the peak just above or slightly offset from the fire, where the FDS analysis record exceeds the standard curve by as much as 250 degrees Celsius. It is also seen that as the time-temperature histories are recorded further from the fire, both longitudinally and vertically (in the case of Analysis 5-8), the records do not approach the standard curve.

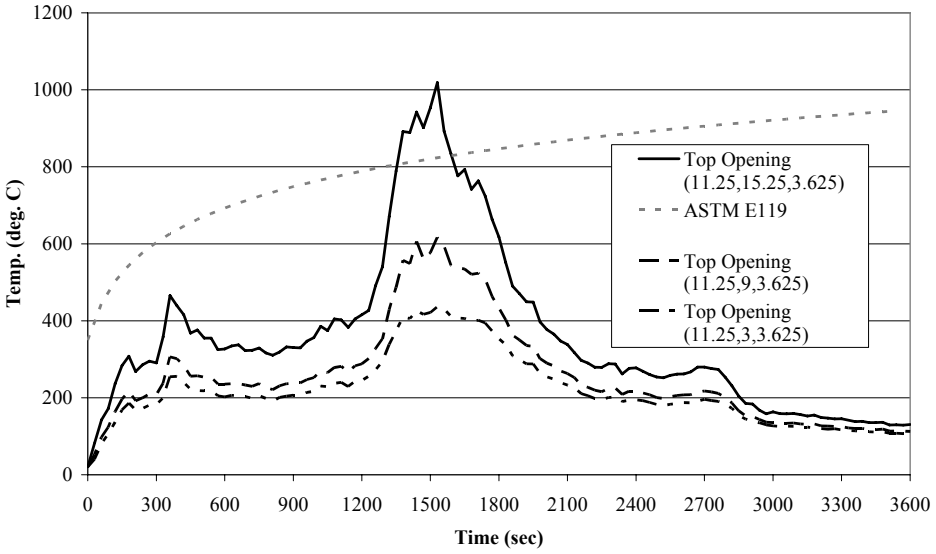

Figure 5-23: Analysis 1 comparison between select thermocouple records and ASTM E119 curve.

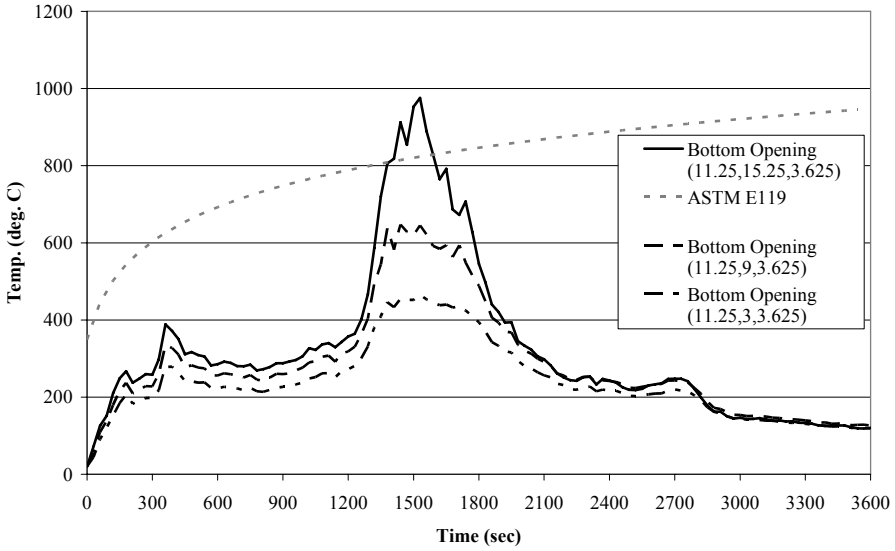

Figure 5-24: Analysis 2 comparison between select thermocouple records and ASTM E119 curve.

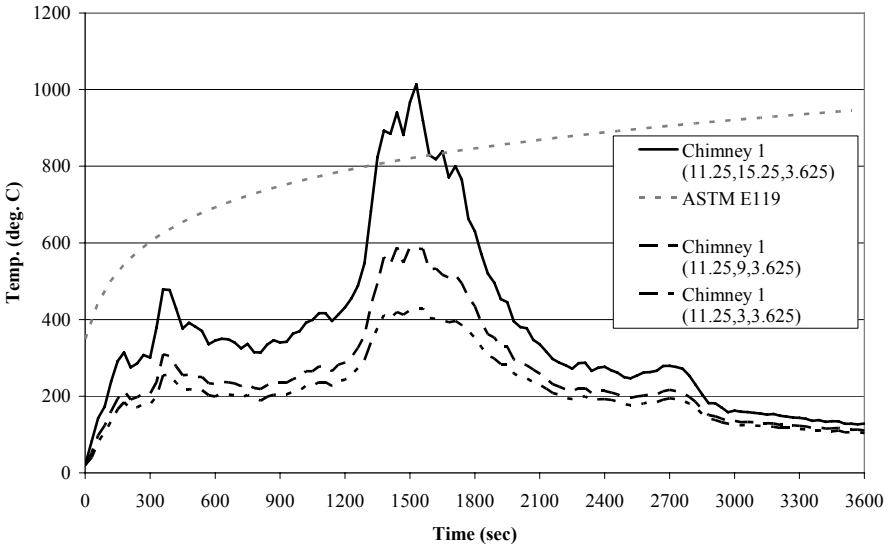

Figure 5-25: Analysis 3 comparison between select thermocouple records and ASTM E119 curve.

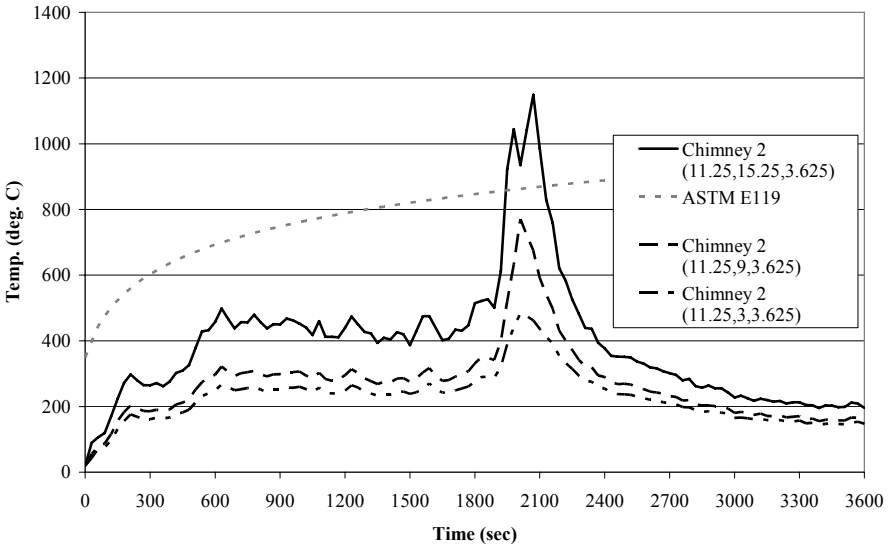

Figure 5-26: Analysis 4 comparison between select thermocouple records and ASTM E119 curve.

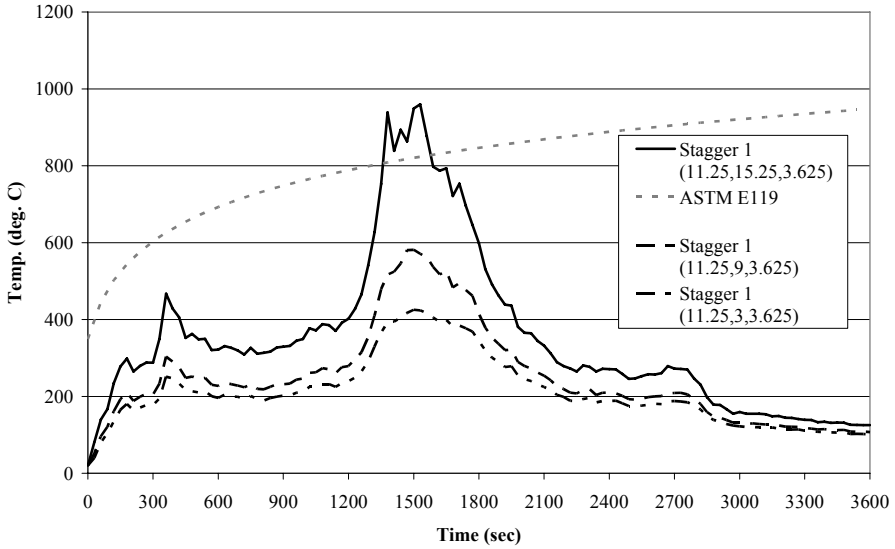

Figure 5-27: Analysis 5 comparison between select thermocouple records and ASTM E119 curve.

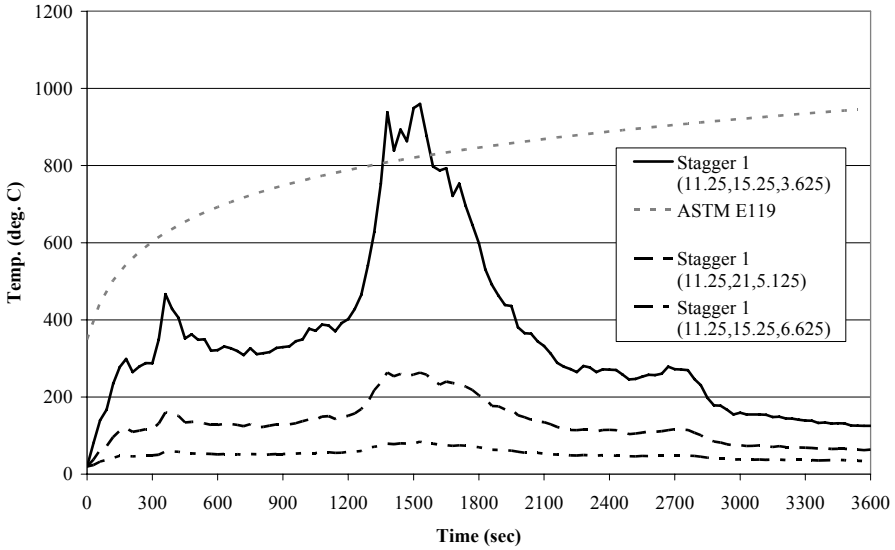

Figure 5-28: Analysis 5 multi-level comparison between select thermocouple records and ASTM E119 curve.

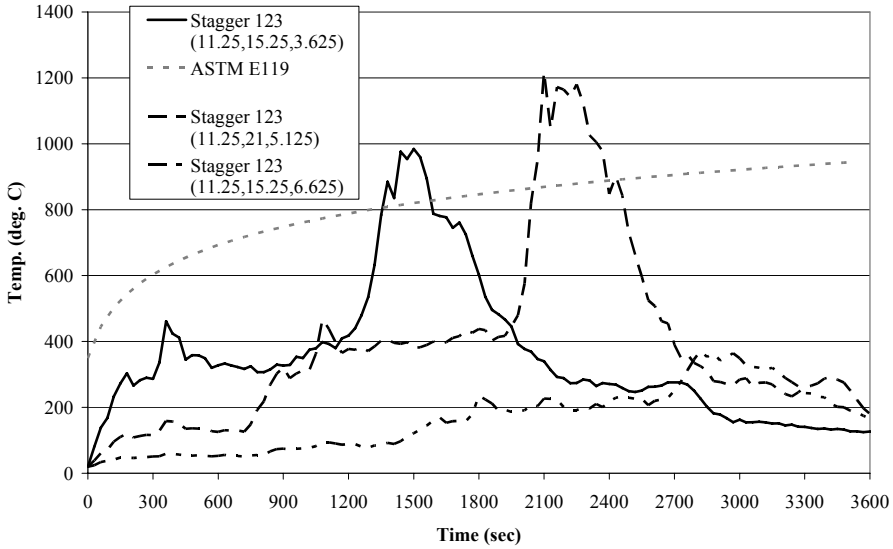

Figure 5-29: Analysis 8 multi-level comparison between select thermocouple records and ASTM E119 curve.

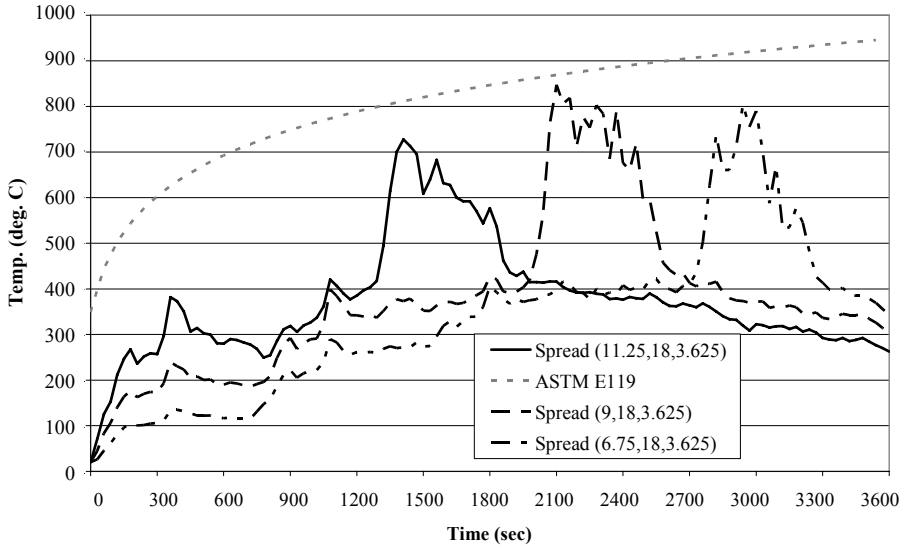

Figure 5-30: Analysis 9 comparison between select thermocouple records and ASTM E119 curve.

For the multiple vehicle fire models (e.g. Analyses 8 and 9), the gas temperature is seen to approach the ASTM E119 standard curve in a similar manner to the single vehicle burns, that is, the temperature is well below the ATSM curve except for a short time period where the peak nears or exceeds the standard. This suggests that, for precast concrete parking garage structures similar to the structure treated in this study, the standard fire curves represent a more severe fire loading than would be expected from actual vehicle fires.

5.3.2 Prestressing Steel Temperature

A non-linear heat transfer analysis using ABAQUS was performed on each of the fire analysis models following the procedures in Chapter 3. Fore each model, the concrete time-temperature curve at the level of the first prestressing strand was calculated. The thermal history used was located centered above the burning vehicle in one of the double-tee webs for each model. The maximum temperatures achieved for the analysis models are shown in Table 5-1.

Using the equations for reduction in strength in prestressing steel from the Eurocode 1 (2002) the impact of the fire loading is seen. The stress-strain curves for the steel are shown in Figure 5-32.

Simulation Name	Max. Steel Temp. (deg. C)	f_{pu} (Mpa)	f_{puo}/f_{pu}
At Ambient Temp.	**20**	**1860**	**1.00**
Top	142	1747	0.94
Bottom	94	1842	0.99
Chimney 1	93	1843	0.99
Chimney 2	142	1747	0.94
Stagger 1 Floor 1	129	1761	0.95
Stagger 2 Floor 2	136	1776	0.95
Stagger 3 Floor 3	120	1796	0.97
Stagger 123 Floor 2	149	1732	0.93
Spread	214	1579	0.85

Table 5-1: Maximum temperature at level of first prestressing strand in Analyses 1-9.

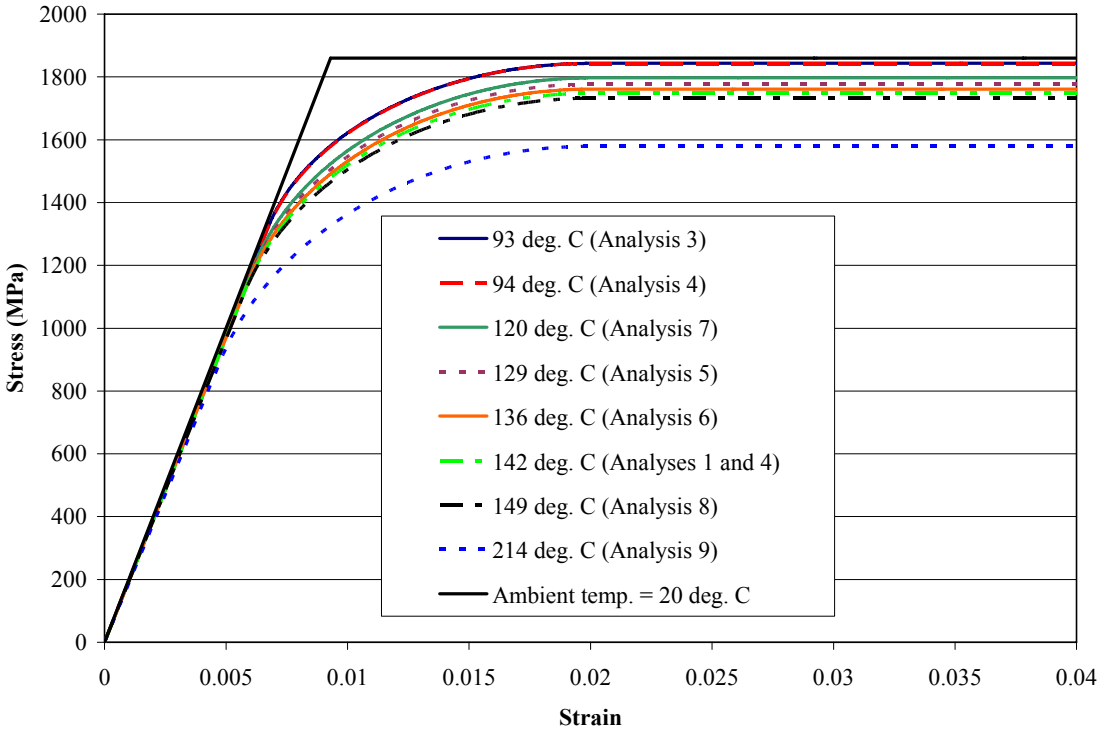

Figure 5-31: Temperature dependent stress-strain curves for prestressing steel.

For the maximum temperature reached in the concrete in any model tested for this project, 214 degrees Celsius in Analysis 9, the strength reduction in of the prestressing steel is about 15%. For the rest of the models, the temperature in at the level of the strand is much lower than 214 degrees, with a maximum temperature recorded anywhere in the structure no more than about 150 degrees Celsius or about an 8% reduction in prestressing steel strength.

CHAPTER 6

CONCLUSIONS AND FUTURE WORK

Vehicle fires in precast parking garages provide a simple starting point for an investigation of realistic fire loading for precast concrete structures. Because the structures themselves are non-combustible, the fuel loads are fairly well-defined. And the open parking garage design means the ventilation conditions are defined and constant throughout the analyses. These characteristics allow for a systematic development of different fire analysis models to investigate a number of analysis variables related to the geometry and fire characteristics. The effects of the precast double-tee construction geometry were examined by varying the location of the openings in the center wall and the relative location of the floors due to ramping of the double-tees. Additionally, the potential effects of different heat flux records from actual vehicle fire analyses were studied. The following sections provide conclusions based on the results of this research (Section 6.1) and provide a list of potential areas for continued study (Section 6.2).

6.1 Conclusions

The following are conclusions drawn from the results of this project:

1. The geometric effects of openings in the center wall have a significant impact on the heat transmission through the structure. Depending on the relative position of the opening to the floor slabs, heat may be trapped on one side of the garage or allowed to flow freely from one side to the other or from one floor to the next.
2. Fires on lower floors can create a preheating effect on upper floors if the heat is allowed to flow from floor-to-floor by the center wall openings. This preheating effect causes an increase in the concrete temperature over the course of the fire. The peak gas temperature may not show a significant difference, so the increased concrete temperature is due in part to the longer heating duration.
3. The webs of the double-tee in a precast concrete construction trap the heat from the vehicle fires and "channel" it away from the fire.
4. The ASTM E119 standard time-temperature curve is not representative of the time-temperature curve that is produced by a single or multiple vehicle fire in a precast concrete parking garage.
5. For the fire scenarios considered, vehicle fires do not cause the temperature of the prestressing strand in the concrete to increase significantly. Vehicle fires cause the strength of the prestressing steel to vary from $0.99f_{pu}$ to $0.85f_{pu}$.

6.2 Future Work

This project addresses a new area of research for Lehigh University, and indeed this is the first research project at Lehigh on the topic of fire loadings. Accordingly additional research is needed in many areas. The research work presented in this report was not intended to provide a complete understanding of all the phenomena present during vehicle fires in precast parking garages. Instead, the expectation is that the results of this project will provide the foundation for future that investigate additional fire scenarios that address fundamental geometric and fire behavioral characteristics. There are several directions for future projects that are specifically suggested by the methods, results, and analysis of this project:

1. Further models are needed to completely understand the effect of opening position relative to the floor position. These models might be similar to the Stagger Analysis analyses, but relative position of the floors might be varied along with the center wall opening position.
2. Further research into the effects of differences in fire heat flux records is needed. Not only would this help to better understand structural effects, further classification of fires may potentially help to standardize the fuel loading for precast concrete parking structures.
3. Conducting similar studies of vehicle fires in parking structures with different ventilation conditions are important. Parking structures are not always completely open as in this project, and the closed boundaries presented by walls or foundations might present different results. Ambient wind conditions could also be treated as a parameter in such analyses.
4. Actual fire analyses on real precast concrete parking structures would help to clarify the potential for multiple-vehicle fires. Sequence and timing of ignition might be one focus.
5. Further investigation into the structural effects of vehicle fires in precast structures much like those explained in Okasha (2006) would be another closely related area of research.
6. Finally, other types of structures such as precast office buildings, hospitals, or apartment buildings might be investigated using a similar set of investigational principles. Clearly, those analyses will present even greater challenges, given the additional uncertainties in fuel loads, ventilation conditions, etc.

REFERENCES

Bennetts, I.D., Proe, D., Lewins, R., and I.R. Thomas. "Open-vehicle park fire analyses," Proceedings of the Pacific Structural Steel Conference, Aukland New Zealand, August 1986, pp.83-97.

Chow, W.K. "Analysis of vehicle park fires using zone models," Journal of Fire Protection Engineering, vol. 7, no. 2, (1995):65-74.

Cooke, G.M.E. "Behaviour of precast concrete floor slabs exposed to standardized fires," Fire Safety Journal, vol. 36, no. 5, (2001):459-475.

Cooke, G.M.E. "Deflections of concrete floor slabs exposed to standardized fires and some implications for design," The Structural Engineer, vol. 79, no. 12, (2001):26-34.

European Committee for Standardization. Eurocode 1: Actions on Structures, British Standard, 2002.

Fitzgerald, R.W. Building Fire Performance Analysis – A Way of Thinking, Chichester: John Wiley and Sons, 2003.

Fleming, R.P. "Assuming the ultra-fast fire," NFPA Journal, September/October 2003.

Gustaferro, A.H., and T.D. Lin, "Rational design of reinforced concrete members for fire resistance," Fire Safety Journal, vol. 11, no. 1, (1987):85-98.

Harmathy, T.Z. and M.A. Sultan. "Correlation between the severeities of the ASTM E19 and ISO 834 fire exposures," Fire Safety Journal, vol.13, no. 2-3 (1988): 163-168.

International Building Code Council (IBC). International Building Code, IBC, 2003.

Janssens, M.L. "Heat Release Rate of Motor Vehicles," 5th International Conference on Performance-Based Codes and Fire Safety Design Methods, Luxemburg, 6-8 October 2004. (Conference Presentation), 22pp.

Khono, M., kouno-m92ta@nilim.go.jp "Vehicle Fire Research," 8 November 2005, Personal e-mail (8 November 2005).

Klote, J.H. "Design fires: what you need to know," HPAC Engineering Interactive Feature, September 2002. http://www.hpac.com/member/feature/2002/0209/0209klote.htm. (23 August 2005).

Li, Y. “Assessment of Vehicle Fires in New Zealand Parking Buildings,” M.Eng. Thesis, Department of Civil Engineering, University of Canterbury, Christchurch, New Zealand, 2004, 174pp.

Mangs, J. “On the fire dynamics of vehicles and electrical equipment,” Academic Dissertation, Department of Physical Sciences, University of Helsinki, Helsinki, Finland, 2004, 62pp.

Mangs, J. and O. Keski-Rahkonen. “Characterization of the Fire Behavior of a Burning Passenger Vehicle. Part I: Vehicle Fire Experiments,” Fire Safety Journal 23 (1994): 17-35.

Mangs, J. and O. Keski-Rahkonen. “Characterization of the Fire Behavior of a Burning Passenger Vehicle. Part II: Parametrization of Measured Rate of Heat Release Curves,” Fire Safety Journal, 23 (1994): 37-49.

McGratten, K. ed. NIST Special Publications 1018: Fire Dynamics Simulator (Version 4) Technical Reference Guide, National Institute of Standards and Technology, Washington: U.S. Government Printing Office, 2005a.

McGratten, K and G. Forney. NIST Special Publications 1019: Fire Dynamics Simulator (Version 4) User’s Guide, National Institute of Standards and Technology, Washington: U.S. Government Printing Office, 2005b.

Milke, J.A. ed. NFPA 92B: Guide for Smoke Management Systems in Malls, Atria, and Large Areas, Quincy: NFPA, 2005.

Minkowycz, W.J. and E.M. Sparrow, ed. Advances in Numerical Heat Transfer: Volume 2, New York: Taylor and Frances, 2000.

Oertel, H., ed. Prandtl’s Essentials of Fluid Mechanics, 2nd ed. Germany: Springer-Verlag, 2004.

Okasha, N. “Development of Restraint Mechanisms in Precast Concrete Structures Under Fire Loading,” Master’s Thesis, Department of Civil and Environmental Engineering, Lehigh University, Bethlehem, PA, (2006).

Quintiere, J.G., Chairman. Engineering Guide – Fire Exposures to Structural Elements, Bethesda: Society of Fire Protection Engineers, 2004.

Schleich, J.B. “Numerical Analyses, A more realistic fire safety approach in structural stability,” New technology to reduce fire losses and costs conference, Luxembourg (Conference Paper) (1986):203-210.

Shipp, M., and M. Spearpoint. “Measurements of the Severity of Fires Involving Private Motor Vehicles,” Fire and Materials, vol. 19, (1995): 143-151.

Steinert, C. “Experimental Investigation of Burning and Fire Jumping Behavior of Automobiles,” VFDB Journal (2000), 4:163-172.

Stroup, D.W., DeLauter L., Lee, J., and G. Roadamarmel. “Passenger minivan analyses,” U.S. Department of Commerce, National Institute of Standards and Technology, Report of Analysis (FR 4011). 1 December 2001. 26pp.

Thomas, L.C. Heat Transfer – Professional Version, 2nd ed. Tulsa: Capstone Publishing Corporation, 1999.

Wang, Y.C. Steel and Composite Structures: Behavior and Design for Fire Safety, Spon Press: London, 2002. pp. 196,197.

Zhao, B., and J. Kruppa. “Structural behavior of an open vehicle park under real fire scenarios,” Fire and Materials, vol. 28, (2004): 269-280.